

UC Berkeley

UC Berkeley Electronic Theses and Dissertations

Title

Toward the Systematic Design of Complex Materials from Structural Motifs

Permalink

<https://escholarship.org/uc/item/04g5p8ph>

Author

SMIDT, TESS Eleonora

Publication Date

2018

Peer reviewed|Thesis/dissertation

Toward the Systematic Design of Complex Materials from Structural Motifs

by

Tess Eleonora Smidt

A dissertation submitted in partial satisfaction of the
requirements for the degree of
Doctor of Philosophy

in

Physics

in the

Graduate Division

of the

University of California, Berkeley

Committee in charge:

Professor Jeffrey B. Neaton, Chair
Professor Ramamoorthy Ramesh
Professor Kristin Persson

Spring 2018

Toward the Systematic Design of Complex Materials from Structural Motifs

Copyright 2018
by
Tess Eleonora Smidt

Abstract

Toward the Systematic Design of Complex Materials from Structural Motifs

by

Tess Eleonora Smidt

Doctor of Philosophy in Physics

University of California, Berkeley

Professor Jeffrey B. Neaton, Chair

With first-principles calculations based on density functional theory, we can predict with good accuracy the electronic ground state properties of a fixed arrangement of nuclei in a molecule or crystal. However, the potential of this formalism and approach is not fully utilized; most calculations are performed on experimentally determined structures and stoichiometric substitutions of those systems. This in part stems from the difficulty of systematically generating 3D geometries that are chemically valid under the complex interactions existing in materials. Designing materials is a bottleneck for computational materials exploration; there is a need for systematic design tools that can keep up with our calculation capacity. Identifying a higher level language to articulate designs at the atomic scale rather than simply points in 3D space can aid in developing these tools.

Constituent atoms of materials tend to arrange in recognizable patterns with defined symmetry such as coordination polyhedra in transition metal oxides or subgroups of organic molecules; we call these structural motifs. In this thesis, we advance a variety of systematic strategies for understanding complex materials from structural motifs on the atomic scale with an eye towards future design.

In collaboration with experiment, we introduce the harmonic honeycomb iridates with frustrated, spin-anisotropic magnetism. At the atomic level, the harmonic honeycomb iridates have identical local geometry where each iridium atom octahedrally coordinated by oxygen hosts a $J_{eff} = 1/2$ spin state that experiences interactions in orthogonal spin directions from three neighboring iridium atoms. A homologous series of harmonic honeycomb can be constructed by changing the connectivity of their basic structural units.

Also in collaboration with experiment, we investigate the metal-organic chalcogenide assembly $[\text{AgSePh}]_{\infty}$ that hosts 2D physics in a bulk 3D crystal. In this material, inorganic AgSe layers are scaffolded by organic phenyl ligands preventing the inorganic layers from strongly interacting. While bulk Ag_2Se is an indirect band gap semiconductor, $[\text{AgSePh}]_{\infty}$ has a direct band gap and photoluminesces blue. We propose that these hybrid systems present a promising alternative approach to exploring and controlling low-dimensional physics due to their ease of synthesis and robustness to the ambient environ-

ment, contrasting sharply with the difficulty of isolating and maintaining traditional low-dimensional materials such as graphene and MoS₂.

Automated density functional theory via high throughput approaches are a promising means of identifying new materials with a given property. We automate a search for ferroelectric materials by integrating density functional theory calculations, crystal structure databases, symmetry tools, workflow software, and a custom analysis toolkit. Structural distortions that occur in the structural motifs of ferroelectrics give rise to a switchable spontaneous polarization. In ferroelectrics lattice, spin, and electronic degrees of freedom couple leading to exotic physical phenomena and making them technologically useful (e.g. non-volatile RAM).

We also propose a new neural network architecture that encodes the symmetries of 3D Euclidean space for learning the structural motifs of atomic systems. We describe how these networks can be used to speed up important components of the computational materials discovery pipeline and generate hypothetical stable atomic structures.

Finally, we conclude with a discussion of the materials design tools deep learning may enable and how these tools could be guided by the intuition of materials scientists.

To Mom and Dad

Contents

Contents	ii
List of Figures	v
List of Tables	xv
1 Introduction	1
1.1 Harmonic Honeycomb Iridates	3
1.2 Metal-organic Chalcogenide Assemblies (MOChAs)	7
1.3 Ferroelectrics	8
1.4 Deep learning for atomic systems	11
2 Methods	13
2.1 Density Functional Theory	13
3 Realization of a three-dimensional spin-anisotropic harmonic honeycomb iridate	17
3.1 Introduction	17
3.2 Results	18
3.3 Discussion	23
3.4 Methods	26
4 Ab initio Studies of Structural and Energetic Trends in the Harmonic Honeycomb Iridates	28
4.1 Introduction	28
4.2 Calculation Details	29
4.3 DFT Results	31
4.4 Conclusion	38
5 Silver Benzeneselenolate is a Self-Assembling Direct-Gap Metal-Organic Chalcogenide Assembly	43
5.1 Introduction	43
5.2 Results and Discussion	44

5.3	Conclusions and Prospects	51
6	An Automatically Curated First-Principles Database of Ferroelectrics	52
6.1	Background and Summary	52
6.2	Methods	54
6.3	Data Records	65
6.4	Technical Validation and Verification	67
6.5	Usage Details	76
7	Tensor Field Networks: Rotation- and Translation-Equivariant Neural Networks for 3D Point Clouds	79
7.1	Motivation	79
7.2	Related work	80
7.3	Representations and equivariance	81
7.4	Tensor field network layers	83
7.5	Demonstrations and experiments	88
7.6	Future work	93
8	Outlook	95
	Bibliography	98
A	Appendix for Realization of a three-dimensional spin-anisotropic harmonic honeycomb iridate	121
B	Appendix for Ab initio Studies of Structural and Energetic Trends in the Harmonic Honeycomb Iridates	138
C	Appendix for Silver Benzeneselenolate is a Self-Assembling Direct-Gap Metal-Organic Chalcogenide Assembly	143
C.1	General Information	144
C.2	Miscible Gram-Scale Synthesis of $[\text{AgSePh}]_{\infty}$	144
C.3	Immiscible Interface Synthesis of $[\text{AgSePh}]_{\infty}$	144
C.4	Fluorescence Imaging Methods	145
C.5	Calculation Methods	145
C.6	Calculation Details	146
D	A prototypical ferroelectric: BaTiO_3	155
E	Appendix for An Automatically Curated First-Principles Database of Ferroelectrics	157

F Isotropy Subgroups: How to check if two structure are continuously deformable	163
G A brief primer on deep learning	167
H Appendix for Tensor Field Networks	169
H.1 Proofs of general equivariance propositions	170
H.2 Motivating point convolutions	170
H.3 Proof of equivariance of point convolution layer	171
H.4 Details for gravitational accelerations and moment of inertia tasks	173
H.5 Proof of weighted point-averaging layer equivariance	174
H.6 Missing point task accuracies and MAE by epoch	175

List of Figures

1.1	The splitting of $5d$ orbitals for iridium atoms octahedrally coordinated by oxygen atoms. Crystal field splitting breaks the degeneracy of the $5d$ orbitals into a two-dimensional manifold E_g and a three-dimensional manifold T_{2g} . Spin-orbit coupling further splits the T_{2g} manifold with $L_{eff} = 1$ into $J_{eff} = 1/2$ and $J_{eff} = 3/2$ states.	5
1.2	In the harmonic honeycomb iridates, the IrO_6 edge-share with three nearest neighbors, forming three orthogonal planes defined by the Ir-O-Ir bonds. These planes are indicated with blue, red, and green shading. The Ir ions are indicated by the circles while the oxygens (not shown) lie on the edges of the polyhedra.	6
1.3	MOChAs can host inorganic structures of varying dimensionality and topology, from sheets and tubes (2D), to chains and rings (1D), to individual clusters (0D).	7
1.4	Different transition metals and organic ligands form MOChAs with various coordinations and topologies. (Top to Bottom) adamantane + copper give a nanotube structure made of triangular coordination polygons, carborane + lead give a chiral 1D chain of seesaw coordination polyhedra, carborane + mercury give a non-chiral 1D chain of seesaw coordination polyhedra.	9
1.5	Top) Three methods for making MOChAs: immiscible layered strategy, gram-scale bulk synthesis, and wafer-scale gas phase deposition. Middle row) Crystals produced from each method. Bottom row) All three methods produce different crystal morphologies but uniform emission energy.	9
1.6	a) A ferroelectric is a material with a spontaneous polarization that is switchable by applying an external electric field. b) The free energy written in terms of polarization has a double well, each well representing stable, switchable polar structures. c) A plot of the polarization of a ferroelectric versus the application of an electric field will produce a hysteresis loop.	10
1.7	A network with 3D translation- and 3D rotation-equivariance allows us to identify chemical motifs in any location or orientation using the same filters.	12

- 3.1 **Single crystal of ${}^{\mathcal{H}}\langle 1 \rangle$ -Li₂IrO₃ and the Ir lattice structure.** (A) Single crystal oriented to be parallel to the crystallographic axes shown in (C), (B) 3D view and (C) projection in the ab plane. In (B) gray shading emphasizes the Ir (purple balls) honeycomb rows that run parallel to the $\mathbf{a} \pm \mathbf{b}$ diagonals, alternating upon moving along the c -axis. For simplicity only Li ions (grey balls) located in the center of Ir honeycombs are shown. In (B) and (C) the rectangular box indicates the unit cell. Comparing (A) and (C) we note that the $\sim 70^\circ$ angle between honeycomb rows is evident in the crystalline morphology. 19
- 3.2 **The temperature dependence of the single-crystal magnetic susceptibility along the three principal crystalline directions.** The inset shows $1/\chi$ for all three axes χ_a , χ_b , and χ_c . The dashed line indicates the slope of the inverse Curie-Weiss susceptibility for a paramagnet with effective moment of $\mu_{eff} = 1.6\mu_B$, close to that expected of an Ir $J_{eff} = 1/2$ state if g -factor anisotropy is ignored. All three components of susceptibility show strong deviation from Curie-Weiss behavior as a function of temperature. 20
- 3.3 **Temperature dependence of the magnetic anisotropy.** (A) Each Ir is surrounded by one of two planar, triangular environments indicated by blue and red shaded triangles, located at $\sim 35^\circ$ either side of the b -axis. (B) The anisotropy of the magnetic susceptibility as measured by torque and the differences in (SQUID) susceptibilities (grey lines) are shown as a function of temperature for all three crystallographic directions. An anomaly indicates the onset of magnetic order at $T_N = 38$ K. (C) The ratios of the anisotropic susceptibility tend to simple fractional values dictated by the g -factor anisotropy of the local planar iridium environment. (D) $\sin(2\theta)$ fits to the anisotropy α_{bc} illustrating the change of sign at ~ 75 K. 22
- 3.4 **Low temperature magnetic properties of the ${}^{\mathcal{H}}\langle 1 \rangle$ -Li₂IrO₃.** (A) The Ir-O₂-Ir planes defining three orthogonal directions of the spin-exchange, one parallel to $\hat{\mathbf{b}}$ and the other two parallel to $\hat{\mathbf{a}} \pm \hat{\mathbf{c}}$, labelled + and - ($\hat{\mathbf{a}}$ is the unit vector along \mathbf{a}). This connects to the notation used to describe the Kitaev Hamiltonian in SI III. (B) Torque signal τ divided by the applied magnetic field H at a temperature of 1.5 K, illustrating a linear low-field dependence and a kink at H^* , which is strongly angle dependent (colors correspond to angles shown in (D)). (C) Magnetization vs magnetic field applied along the b -axis at a temperature of 15 K. (D) & (E) The angle dependence $\theta_{ab/ac}$ of the kink field H^* of the ordered state (full circles, left axes) with respect to the crystallographic axes a, b and c . H^* is correlated to the magnetization anisotropy α_{ij} (open circles, right axes) indicating a common moment at H^* in all field orientations. 24

- 3.5 **Introducing the harmonic honeycomb series.** (A) Two kinds of c -axis bonds (black links) in the harmonic honeycomb family $\mathcal{H}\langle N \rangle$ -Li₂IrO₃ are shown, one linking within a honeycomb plane (for example blue to blue, top) and one that rotates between honeycomb planes (for example red to blue, bottom). For undistorted octahedra, these links are locally indistinguishable, as can be observed by the local coordination of any Ir atom (also see Figure 3.3A). (B) These building blocks can be used to construct a series of structures. The end members include the theoretical $N = 0$ ‘hyper-honeycomb’ [160, 127, 146] and the $N = \infty$ layered honeycomb [189]. Here N counts the number of complete honeycomb rows in a section along the c -axis before the orientation of the honeycomb plane switches. 25
- 4.1 (a) Conventional unit cells of $\mathcal{H}\langle 0 \rangle$, $\mathcal{H}\langle 1 \rangle$, $\mathcal{H}\langle 2 \rangle$, and $\mathcal{H}\langle \infty \rangle$ [174]. $\mathcal{H}\langle \infty \rangle$, $\mathcal{H}\langle 0 \rangle$, $\mathcal{H}\langle 1 \rangle$, and $\mathcal{H}\langle 2 \rangle$ have 2, 4, 8, and 12 formula units in their primitive unit cell, respectively. Members of the harmonic honeycomb series have identical local geometry, only varying in the connectivity of their basic structural units, orthogonal edge-sharing iridium oxide octahedra. The two growth or bonding planes are normal to $a + b$ and $a - b$, where a and b are the orthorhombic lattice vectors (indicated by the axes at the bottom left). The harmonic honeycomb pattern builds along the orthorhombic c direction. Compared to Li₂IrO₃ structures, Na₂IrO₃ structures have greater distortion of iridium oxide octahedra and larger volume. (b-e) Exaggerated distortions in the harmonic honeycombs. (b-c) Two parallel faces of each iridium oxide octahedron twist opposite to each other. These faces are parallel to the growth plane. (c) Which faces twist changes at twisting bonds. (b) A bond that preserves the bonding plane. (c) A “twist” bond that changes the bonding plane. (d) The octahedra also compress along their twist axis. (e) The twisting and compression of the octahedra cause Ir-O-Ir bond angles to increase from their ideal 90° and the angle between bonding planes to be close to the undistorted value of $\arccos(1/3) \approx 70.5^\circ$ 39
- 4.2 Non-magnetic density of states normalized by the number of formula units per unit cell for Li₂IrO₃ and Na₂IrO₃ harmonic honeycomb structures. Density of states is similar across the series. 40
- 4.3 PBE+SOC+U density of states of $\mathcal{H}\langle \infty \rangle$ Li₂IrO₃ and $\mathcal{H}\langle \infty \rangle$ Na₂IrO₃ for non-magnetic (all magnetic moments fixed at zero μ_B) and ferromagnetic (along the $\mathcal{H}\langle \infty \rangle$ b direction or $\mathcal{H}\langle 0 \rangle$ c direction) magnetic orders are shown in (a). A gap opens in the density of states of both systems with a non-zero magnetic order. Differences in the Li₂IrO₃ and Na₂IrO₃ density of states are caused by distortions of the local environment more so than change in volume. Li₂IrO₃ and Na₂IrO₃ structures have Ir-O-Ir bond angles of 94° and 100°, respectively. 40

- 4.4 Plots of ratio of relaxed lattice parameters vs doping for PBE+U where $U=0,1.5,3.0,6.0$. The discontinuity indicates that when PBE gives asymmetric Ir-Ir bonds below a given Na doping. The discontinuity in the lattice parameters shifts toward more Li doping with increasing U, demonstrating that the performance of the functional is sensitive to localization of iridium 5d orbitals and closeness of iridium atoms. 41
- 4.5 Plots of Ir-Ir bond lengths and Ir-O-Ir bond angles as a function of Na doping of ${}^h\langle 0\rangle$ Li_2IrO_3 for PBE+U and PBE+SOC+U ($U = 3$ eV). While SOC is not sufficient to prevent discontinuities in bond length relaxations, it does give uniform bond length ($< \pm 0.01$ Å) and bond angles ($< \pm 1.5$ degree) for all relaxations. Note, if $U = 3$ eV is used for Li concentration $< 15\%$ and $U = 1.5$ eV for Li concentration $< 15\%$ there is no discontinuity. $(\text{Li}_{1-x}\text{Na}_x)_2\text{IrO}_3$ is metallic for $U = 1.5$ eV and $0.1 < x < 0.2\%$. According to VCA, the distortion is not linear in doping. 42
- 5.1 a) The monoclinic unit cell of solid silver benzeneselenolate contains two complete layers of hybrid chalcogenide 2D polymer. Silver is coordinated tetrahedrally by four selenium atoms. b,c) The multilayered structure isolates inorganic layers via the benzene moieties oriented above and below the silver selenide polymer layer. D) A single isolated layer has a thickness of 1.4 nm, each containing two layers of phenyl rings and one layer of silver selenolate. Silver is represented as the grey spheres, selenium in dark orange, and carbon in black. Aromatic rings are accented in blue. 45
- 5.2 a) A chartreuse deposit of silver benzeneselenolate forms at an immiscible liquid-liquid interface of organic and aqueous solutions of diphenyl diselenide and silver nitrate, respectively. b) Crystals of $[\text{AgSePh}]_\infty$ recovered have typical edge lengths between 1 and 4 microns. b) Scanning electron micrograph of a silver benzeneselenolate silver crystal reveals the layered structure of the crystal. Individual layers are resolved in high-resolution SEM images. c) Atomic force microscopy reveals highly uniform $[\text{AgSePh}]_\infty$ (001) terraces with measured step heights at 1.4 nm. 46
- 5.3 a) Confocal micrographs showing the color uniformity of photoluminescence in $[\text{AgSePh}]_\infty$. b) A single, intense emission of the solid at 467 nm is attributed to a direct-gap electronic transition. c,d) Optical and confocal micrographs of $[\text{AgSePh}]_\infty$ showing fluorescence scanning confocal images of several individual crystals of nearly the same size. e) Distribution of the intensity from 157 individual crystals plotted as a function of the area of the crystal and f) aspect ratio. The Pearson's r-value for each set of data was calculated by using linear least squares fitting (solid line); for both the plots of area (r-value of 0.07) and aspect ratio (r-value of 0.1) the Pearson's r-values indicate no correlation with intensity. Images are false colored according to emission wavelength. 48

- 5.4 a) DFT-HSE band structure and density of states of bulk $[\text{AgSePh}]_\infty$. See supporting information Figure C.6 for details. Band color signifies the fractional contribution of states centered on inorganic (Ag and Se, orange) and organic (C and H, black) atoms in the crystal. The total density of states is shown in gray. b) DFT-HSE band structure of a single layer of $[\text{AgSePh}]_\infty$ c) DFT-HSE band structure of a single layer of $[\text{AgSePh}]_\infty$ with the phenyls replaced by hydrogen. The hydrogen positions have been relaxed with PBE; see supporting information Figure C.5. The near-band edge character remains relatively unchanged when the phenyls are replaced by hydrogen, suggesting that the degree of 2D quantum confinement is unchanged by 3D crystallization. d) The Brillouin zone for the primitive cell of $[\text{AgSePh}]_\infty$. The path in the Brillouin zone used for the band structure is identified by orange lines and k-point labels. 49
- 5.5 Depictions of side and top views of $[\text{AgSePh}]_\infty$ with overlain charge density maps. The DFT-HSE computed valence band maximum (VBM) and conduction band minimum (CBM) at Γ are accented in yellow and blue, respectively. The minimal but non-negligible participation of carbon in the CBM state suggests tailoring of electronic properties via synthetic modification of ligand. 50
- 6.1 Diagram of entire automated ferroelectric search workflow. Databases are shown as purple cylinders. Processes are shown as rectangles: blue designates processes used to identify and perform ab initio calculations, green designates post-processing and validation, and orange designates the web-interface. Arrow directions indicate the flow of information. For example, the Workflow Database provides information to the Computing Resources for which calculations to compute and the Workflow Database is updated as calculations complete or errors occur on the Computing Resources. 56
- 6.2 Diagram of DFT workflow written with atomate and Fireworks. Blue and red boxes denote initial nonpolar and polar structures, respectively, green boxes denote DFT calculations, orange rhombuses denote decision steps, and purple ellipses denote exit steps. 60
- 6.3 Polarization curves for BaTiO_3 along the $[001]$ versus distortion from nonpolar to polar structure. Due to the change in lattice parameters and volume across the distortion, the quantum of polarization along the $[001]$ direction is different for each structure. This causes the spontaneous polarization for different branches to differ. The branch that starts at zero is the corrected branch. The branch that starts near $-600 \mu\text{C}/\text{cm}^2$ is the data from VASP. Note, while in this specific case, the calculated polarization values for all interpolations were on the same branch, this is not usually the case. 62

6.4	A visual demonstration of the same branch polarization algorithm demonstrated in 1D (rather than 3D) using BaTiO ₃ . As mentioned in Figure 6.3, VASP returns polarizations all along the branch starting at -600 $\mu\text{C}/\text{cm}^2$. However, to better demonstrate the algorithm, we will suppose that the values for the polarization for each interpolation are those circled in red. In the first panel, we move the nonpolar polarization to be on the branch closest to zero. In the second panel, we move the first interpolated polarization to be on the branch closest to the adjusted nonpolar polarization. In the third panel, we move the second interpolated polarization to be on the branch closest to the adjusted first interpolation polarization. If the algorithm finishes successfully, the adjusted polarizations will on the same branch.	64
6.5	The polarization reconstruction for CrO ₃ with workflow ID <code>wfid_1484694851.899452</code> . The polarization along the b lattice parameter is incorrectly reconstructed because the different polarization branches are closer than the change in polarization between structure interpolations. To correctly reconstruct this polarization with our existing algorithm, more structure interpolations would be needed between the nonpolar and polar structures.	65
6.6	Legend for Figure 6.7.	70
6.7	Validated ferroelectric candidates from our search. Spontaneous polarization plotted against nonpolar-polar energy difference, maximum atomic distortion, PBE band gap, and energy of polar structure above lowest energy polymorph reported in the Materials Project.	71
6.8	Distortion candidate point group relations.	72
6.9	Diagrams of polarization magnitude vs. point group.	72
6.10	Experimental vs. Calculated polarizations for ferroelectric materials in the Landolt-Börnstein series. Note, the plot is log-log. We give colored regions to show which experimental values are within ± 25 , ± 50 , and ± 75 of calculated values.	76
7.1	Example of $V_{acm}^{(l)}$ representing two point masses with velocities and accelerations. Colored brackets indicate the a (point), c (channel), and m (representation) indices. (l) is the key for the $V_{acm}^{(l)}$ dictionary of feature tensors.	84
7.2	Network diagram for learning gravitational accelerations and moment of inertia tensor. The input tensor has indices [channels , points , representation]. The input for the gravitational acceleration and moment of inertia tasks are point mass scalars, therefore the representation index is 1-dimensional. Convolution filters are indicated by blocks marked F and Clebsch-Gordan tensors are indicated by CG . The numbers along the arrows for the representation index indicate the l of that arrow, with CG blocks combining the input and filter l s to generate output of a specific l .	89
7.3	Radial function learned by $l = 1$ filter for gravity toy dataset. Minimum radial cutoff distance of 0.5 is chosen for randomly sampled points such that there are enough samples generated near the minimum distance.	90

7.4	3D Tetris shapes. Blocks correspond to single points. The third and fourth shapes from the left are mirrored versions of each other.	90
7.5	Network diagrams for shape classification task showing how information flows between tensors of different order. Clebsch-Gordan tensors are implied in the arrows indicating convolutions. The numbers above the self-interactions indicate the number of channels. Individual convolutions, indicated by arrows, each produce a separate tensor, and concatenation is performed after the convolutions.	91
7.6	A hypothetical example input and output of the missing point network. (A) A benzene molecule with hydrogen removed (B) The relative output vectors produced by the network, with arrows shaded by the associated probabilities.	92
A.1	X-ray diffraction pattern in the $(hk0)$ (top) and $(h1l)$ (bottom) planes. Raw data (AB) is well reproduced by calculations (CD) for the $Cccm$ structure (Table A.1), in contrast an $Fddd$ (hyper-honeycomb) structure (EF) can only explain the existence of less than half of the observed diffraction peaks.	122
A.2	Observed diffraction intensities plotted against those calculated in the refined (A) $Cccm$ (Table A.1) and (B) $Fddd$ structural models. The dashed lines indicate 1:1 agreement between data and model and error bars reflect the intensity uncertainties after averaging the observed intensities of reflections expected to be equivalent under orthorhombic symmetry. The three families of reflections discussed in the text are plotted as different symbols/colors (black circles, red squares, and blue triangles). Note that the $Fddd$ model predicts zero intensity at the observed (odd, odd, even) reflections and largely overestimates the intensities of (odd, odd, odd) peaks.	123
A.3	Crystal structure models described in the text, (A) $Cccm$ (Table A.1) and (B) $Fddd$, large brown balls - Ir, medium light gray balls - Li, small gray balls - O.	124
A.4	Preliminary measurements of the change in the lattice parameters along the crystallographic a , b and c direction on cooling below the magnetic transition at T_N . We do not observe any changes in the crystallographic symmetry, but the elastic response in each direction is highly anisotropic, with the b -axis changing roughly 10 times more than the a -axis.	125
A.5	The magnetic anisotropy extracted from the low field slope of the torque signal $\tau/\mu_0 H$, similar to that shown in Figure 3.4 B, taken for rotations through the three principal crystallographic planes and at different temperatures. The anisotropy is shown in units of μ_B per Ir, for (A) the $\chi_a - \chi_b$, (B) $\chi_a - \chi_c$ and (C) $\chi_b - \chi_c$. The only change of sign in the anisotropy is in (A) and an enlargement of this scale is shown in Figure 3D of the main text to emphasize this.	126

A.6	Torque signal taken at magnetic fields up to 35 T at the National High magnetic Field Laboratory. The field H^* is extremely clear at all angles. At angles away from the principal axes the torque signal is very clearly linear and follows a $\sin 2\theta$ dependence described by equation A.4. The larger asymmetry in this data set compared to that measured in the superconducting magnet, is due to the larger field gradient experienced by the sample.	127
A.7	(A) The two choices of edge shared bonds give rise to two kinds of links that are locally indistinguishable. These define two bonding planes (see Figure 3A of the main text) that are an angle $\phi_o \sim 70^\circ$ apart. (B) Links along the c -axis can either keep the same (S -links) or rotate (R -links) the honeycomb planes.	128
A.8	The harmonic honeycomb family is rich in structural possibilities that tune symmetry (depending on whether the number of N_R and N_S links is odd or even) and dimensionality (the extent of the N_S links). This table summarizes this observation. Note we assume that the IrO_6 octahedra have ideal cubic symmetry. Complex distortions may create systems of lower symmetry than that indicated.	129
B.1	Non-magnetic and ferromagnetic c band structures of relaxed unit cells of Li_2IrO_3 and $\text{Na}_2\text{IrO}_3^{\mathcal{H}} \langle 1 \rangle$ with PBE+SOC+U with path through k -space show at the bottom of (a). While the non-magnetic band structure is metallic (b), a gap opens up between $j = 1/2$ states with a magnetic order (d). The density of states for Li_2IrO_3 and $\text{Na}_2\text{IrO}_3^{\mathcal{H}} \langle 1 \rangle$ (and likewise for the entire harmonic honeycomb series) is dominated by oxygen p and iridium d orbitals (c and e).	140
C.1	Powder X-Ray diffractogram of $[\text{AgSePh}]_\infty$ overlapping the diffractogram calculated from Cuthbert et al. providing positive identification for silver benzeneselenolate. ²⁸	147
C.2	Larger $[\text{AgSePh}]_\infty$ crystal sizes, having dimensions in excess of $20 \mu\text{m}$, are observed in the gram-scale-reaction product.	147
C.3	Additional micrographs of $[\text{AgSePh}]_\infty$. Detail of step edges of the layered system down to single layer step edges are evident in the SEM micrographs.	148
C.4	Single particles of $[\text{AgSePh}]_\infty$ were selected from confocal microscopy images and their spectra were compared. Color was invariant regardless of size and aspect ratio. Thickness had no discernable effect but the precise thicknesses of crystals can be inferred only from total intensity. 100 isolated crystals were selected for this representation.	149
C.5	HSE band structures for bulk and single-layer $[\text{AgSePh}]_\infty$ and single layer $[\text{AgSePh}]_\infty$ with the phenyls replaced with hydrogens Dashed lines show the Fermi level (at 0 eV) and the HSE band gap for bulk and single-layer $[\text{AgSePh}]_\infty$. Color of band signifies the fraction of band occupations by inorganic atoms (Ag and Se) versus organic atoms (C and H). Bulk and single layer HSE band structures look identical. Single layer and hydrogen truncated AgSe look similar for Ag and Se dominated bands with small changes to the band gap and mobilities.	149

C.6	HSE, PBE, and df2 band structures for bulk $[\text{AgSePh}]_\infty$. Dashed lines show the Fermi level. Color of band signifies the fraction of band occupations by inorganic atoms (Ag and Se) versus organic atoms (C and H). Band occupations and shape remain similar across these three levels of theory. N , N_1 and Z are along the primitive lattice vectors a^* , b^* and c^* , respectively.	150
C.7	Parameters of Ag lattice used in relaxation table.	150
D.1	BaTiO_3 is the quintessential ferroelectric. BaTiO_3 has a cubic perovskite crystal structure at high temperatures. Both the barium and titanium are octahedrally coordinated by oxygen. Octahedra of similar center element share corners. . . .	155
D.2	BaTiO_3 goes through three phase transition as temperature is lowered: $Pm\bar{3}$ (221) $\rightarrow P4mm$ (99) $\rightarrow Amm2$ (38) $\rightarrow R3m$ (160). The red arrows in the diagram indicate the direction of the spontaneous polarization due to the displacement of the titanium atom and associated rearrangement of the oxygen atoms[273, 125].	156
F.1	Symmetry checks for isotropy subgroups the BaTiO_3 phase transition $Pm\bar{3}m$ (221) $\rightarrow R3m$ (160). a) cubic and rhombohedral BaTiO_3 structures. b) The maximal subgroup relations of the of the point group $4/m\bar{3}2/m$ (abbreviated as $m\bar{3}m$), modified from Figure 7.1 in [179] and reproduced with permission. The nonpolar point group ($4/m\bar{3}2/m$) is highlighted in green and the polar point group ($3m$) is highlighted in red. The point groups highlighted in blue ($\bar{4}3m$ and $\bar{3}2/m$) are the maximal subgroups between the nonpolar and polar point groups. c) A table, generated using the BCS tool CELLSUB (http://www.cryst.ehu.es/cryst/cellsub.html) [29], of the indices of the maximal polar subgroups of the cubic space group $Pm\bar{3}m$ with k -index of 1. We have highlighted those in red that correspond to subgroups shown in Figure D.2 d) A table of the possible transformation matrices for different chains of maximal subgroup from the nonpolar (221) to polar space group (160) for a group-subgroup index of 8. This table was generated using the BCS tool (http://www.cryst.ehu.es/cryst/symmodes.html) SYMMODES[56]. This transformation matrix is used to transform the lattice and Wyckoff positions.	165
F.2	Wyckoff splitting for BaTiO_3 from the cubic phase to tetragonal phase. While the cubic phase has 3 symmetrically unique positions, the tetragonal phase has 4.	166
F.3	Once we have possible transformation matrices for the group-subgroup relation of a given index that give the proper Wyckoff splitting, we transform the nonpolar lattice to the polar symmetry setting and compare to the polar lattice. If the lattices match within a generous tolerance of 3 Å and 10 degrees, we then check the distance the atoms have move during the distortion.	166
G.1	Diagrams for example neural networks a) Diagram for an arbitrary function f . b) A one-layer fully-connected network. c) A two-layer fully-connected network. d) A diagram for backpropagation through a fully-connected network.	168

H.1	Condition for layer rotation equivariance	171
H.2	Filter equivariance equation	172
H.3	Equivariance of Clebsch-Gordan coefficients. Note that each D may refer to a different irreducible representation.	173
H.4	Diagrammatic proof of point convolution rotation equivariance.	174
H.5	Radial function learned by $l = 0$ and $l = 2$ filters for moment of inertia toy dataset. The filters learn the analytical radial functions. For a collection of randomly generated point sets, the mean minimum distance is the average of the minimum distance between points in each point set. Distances smaller than the mean minimum distance might not have been seen by the network enough times to correct the radial filter.	175
H.6	Accuracy of missing point task by epoch of training	177
H.7	Distance MAE of missing point task by epoch of training	177

List of Tables

4.1	Comparison of experimental and DFT (PBE+SOC+U) lattice parameters and Wyckoff positions for $\mathcal{H}\langle\infty\rangle$ Li_2IrO_3 and $\mathcal{H}\langle\infty\rangle$ Na_2IrO_3 . Experimental Li_2IrO_3 structure is refined from powder diffraction data [190]. Position tolerance required to symmetrize DFT structures obtained from PBE+SOC+U is given below Wyckoff positions.	32
4.2	Comparison of experimental and DFT (PBE+SOC+U) lattice parameters and Wyckoff positions for $\mathcal{H}\langle 0\rangle$ Li_2IrO_3 and $\mathcal{H}\langle 0\rangle$ Na_2IrO_3 . Position tolerance required to symmetrize DFT structures obtained from PBE+SOC+U is given below Wyckoff positions.	33
4.3	Comparison of experimental and DFT (PBE+SOC+U) lattice parameters and Wyckoff positions for $\mathcal{H}\langle 1\rangle$ Li_2IrO_3 and $\mathcal{H}\langle 1\rangle$ Na_2IrO_3 . Position tolerance required to symmetrize DFT structures obtained from PBE+SOC+U is given below Wyckoff positions.	34
4.4	Comparison of experimental and DFT (PBE+SOC+U) lattice parameters and Wyckoff positions for $\mathcal{H}\langle 2\rangle$ Li_2IrO_3 and $\mathcal{H}\langle 2\rangle$ Na_2IrO_3 . Position tolerance required to symmetrize DFT structures obtained from PBE+SOC+U is given below Wyckoff positions.	35
6.1	Results obtained by applying our workflow to the Materials Project database. † indicates “in Materials Project database at time of search”. Boxes relate numbers by symmetry conditions, DFT calculations, and validation processes. Rows separated by a single line give the sum of the numbers given below it in the same box.	57
6.2	Key, value data type, and value description for <code>distortion.json</code> entries. . . .	68
6.3	JSON keys, value data type, and value description for <code>distortion</code> dictionary of <code>distortion.json</code> entries.	68
6.4	Key, value data type, and value description for <code>workflow_data.json</code> entries. . .	69

6.5	Comparison of this work to other ab initio studies of ferroelectric perovskites. † indicates the reference being compared to used the Local Density Approximation (LDA) functional in their calculations. LDA results tend to be smaller than results calculated with PBE (which we use in this work) due to smaller predicted lattice parameters by LDA than PBE. The workflow ids for entries in the table are (1) wfid_1476040944.53976 (2) wfid_1476040944.53976 and wfid_1476040947.794782 (3) wfid_1476040956.832394 (4) wfid_1476040982.95148 (5) wfid_1476041128.167316 (6) wfid_1476040384.215156 (7) wfid_1476040759.946834 (8) wfid_1484445148.273011 (9) wfid_1484445014.628732 (10) wfid_1476040851.179557.	77
7.1	Performance on missing point task	93
A.1	Fractional atomic coordinates for $\mathcal{H}\langle 1 \rangle$ -Li ₂ IrO ₃ extracted from single-crystal x-ray data at 300 K (<i>Cccm</i> space group, $a = 5.9119(3)$ Å, $b = 8.4461(5)$ Å, $c = 17.8363(10)$ Å, $Z = 16$). All sites are fully occupied and Li positions are fixed to nominal values such that edge-sharing IrO ₆ and LiO ₆ octahedra form a near-hexagonal arrangement in both $(\mathbf{a} + \mathbf{b}, \mathbf{c})$ and $(\mathbf{a} - \mathbf{b}, \mathbf{c})$ planes. The isotropic displacement parameter U for Li is also fixed to a value in the range found for the other atoms. Values in brackets show standard deviations in the fitted parameters.	130
B.1	Lattice parameters for various levels of theory for $\mathcal{H}\langle 1 \rangle$ and $\mathcal{H}\langle \infty \rangle$ Li ₂ IrO ₃ and $\mathcal{H}\langle 1 \rangle$ and $\mathcal{H}\langle \infty \rangle$ Na ₂ IrO ₃ . All calculations for a given structure type are initialized with identical magnetic order. $U = 1.5$ eV. The percentage difference between the relaxed and experimental lattice parameter is indicated by the color of the cell.	138
B.2	Total energy (eV) for constrained collinear magnetic orders on relaxed Li ₂ IrO ₃ structures.	139
B.3	Total energy (eV) for constrained collinear magnetic orders on relaxed Na ₂ IrO ₃ structures.	139
B.4	Bond lengths and angles for experimental and theoretical structures.	139
B.5	Table of total energy, Ir-Ir bond lengths, and Ir-O-Ir bond angles for Li ₂ IrO ₃ . . .	140
B.6	Table of total energy, Ir-Ir bond lengths, and Ir-O-Ir bond angles for Na ₂ IrO ₃ . .	140
B.7	Table of total energy, Ir-Ir bond lengths, and Ir-O-Ir bond angles for experimentally synthesized harmonic honeycomb iridates.	141
B.8	$\mathcal{H}\langle 1 \rangle$ Li ₂ IrO ₃ PBE+SOC+U lattice parameters for varying U . All calculations are initialized with the same magnetic order. The final magnetizations are not identical to one another. For PBE+SOC+U(0.25 eV) and PBE+SOC, the experimental lithium iridate structure is metallic. The relaxed PBE+SOC+U(0.25 eV) and PBE+SOC structures have gaps and relax to non-magnetic ground states.	141
B.9	PBE+SOC+U for various initial magnetizations. All relaxations have a magnetic order. Magnetic orders were initialized with magnetic moments of 1 Bohr magneton on each iridium atom.	141

B.10	PBE+U for various initial magnetizations. Calculations initialized with as a non-magnetic state relax to be non-magnetic and have similar lattice parameters to a non spin-polarized calculation.:	142
C.1	Calculated effected masses at the direct gap of bulk, single and hydrogen-truncated $[\text{AgSePh}]_{\infty}$. The effective masses at the direct gap are similar for bulk and single layer $[\text{AgSePh}]_{\infty}$ and $[\text{AgSePh}]_{\infty}$ truncated with hydrogens. Only two principle directions are given for 2D single layer calculations.	148
C.2	Relaxation Wyckoff tables:Lattice and Wyckoff position parameters for one phenyl configuration of Cuthberts crystal structure and DFT relaxations of that configuration.	151
C.3	Wyckoff table for experimental structure of $[\text{AgSePh}]_{\infty}$. Lattice and Wyckoff position parameters for one phenyl configuration of Cuthberts crystal structure.	151
C.4	Wyckoff table for LDA Relaxation of experimental structure of $[\text{AgSePh}]_{\infty}$. Lattice and Wyckoff position parameters for one phenyl configuration of Cuthberts crystal structure relaxed with LDA.	152
C.5	Wyckoff table for PBE Relaxation of experimental structure of $[\text{AgSePh}]_{\infty}$. Lattice and Wyckoff position parameters for one phenyl configuration of Cuthberts crystal structure relaxed with PBE.	153
C.6	Wyckoff table for df2 Relaxation of experimental structure of $[\text{AgSePh}]_{\infty}$. Lattice and Wyckoff position parameters for one phenyl configuration of Cuthberts crystal structure relaxed with df2.	154
E.1	Table of calculated versus experimentally measured polarizations as given in the Landolt-Börnstein - Group III: Condensed Matter - Ferroelectrics and Related Substances [227, 228, 229].	158
E.2	New high-quality candidates	159
E.3	New high-quality candidates	160
E.4	Known high-quality candidates	161
E.5	Known high-quality candidates	162
H.1	Performance on missing point task by atom type	176

Acknowledgments

To my advisor Prof. Jeff Neaton, thank you for making sure I was always asking scientifically important questions and supporting me even when I wanted to do something strange. Thank you for always having a smile when I walk through your office door, for being a role model for how to handle immense responsibility with composure and joviality, and for fostering a supportive research environment where we are held to high-standards of scientific merit, effective communication, and personal integrity.

Thank you to my collaborators: Kim A. Modic, Itamar Kimchi, Nicholas P. Breznay, Alun Biffin, Sungkyun Choi, Roger D. Johnson, Radu Coldea, Pilanda Watkins-Curry, Gregory McCandless, Julia Y. Chan, Felipe Gandara, Z. Islam, Ashvin Vishwanath, Arkady Shekhter, Ross D. McDonald, and James G. Analytis (Chapter 3), Sinead M. Griffin (Chapter 4), Mary S. Collins, Behzad Rad, Paul D. Ashby, and J. Nathan Hohman (Chapter 5), Sebastian E. Reyes-Lillio and Anubhav Jain (Chapter 6), and Nathaniel Thomas, Steve Kearnes, Lusann Yang, Li Li, Kai Kohlhoff, and Patrick Riley (Chapter 7). Thank you to those who helped edit this thesis: Nate, Sean, Ben, Alejandro, Sinead, and Stephanie.

My research was supported in part by a National Science Foundation Graduate Research Fellowship under Grant No. DGE 1106400, the Materials Project funded by the U.S. Department of Energy, Office of Science, Office of Basic Energy Sciences, Materials Sciences and Engineering Division under Contract No. DE-AC02-05-CH11231: Materials Project program KC23MP, the Molecular Foundry at Lawrence Berkeley National Lab, the Laboratory Directed Research and Development Program of Lawrence Berkeley National Laboratory under U.S. Department of Energy Contract No. DE-AC02-05CH11231, and an internship at Google. This research used resources of the National Energy Research Scientific Computing Center, a DOE Office of Science User Facility supported by the Office of Science of the U.S. Department of Energy under Contract No. DE-AC02-05CH11231. Additional calculations were conducted at the High Performance Computing clusters at Lawrence Berkeley Lab.

To my labmates, for the many “team-building exercises” at Celia’s and Free House and conversations around the red couch. To my housemates, for giving me a relaxing and supportive space to come home to and for sharing many laughs over bottles of wine. To my graduate school compatriots and close friends, for your company during the ups and downs, many shared tasty meals, conversations about life, the universe, and everything, and always being up for silliness and mischief. You all have made my life outrageously interesting.

To Meg, for everything you do for us Neatonians. I can never repay you with enough pickles, though I will try. To Marisa and Aricay, for wrangling Jeff’s unruly schedule. To Nate Hohman, Jeff Urban, and Anubhav Jain, for helping me find my research voice.

To Aimee and Tahnee, for always being a source of creative inspiration and absurdity. Thank you for all the airport pick ups and pilgrimages to Old Town and Extraordinary Desserts¹. To Adrian, for teaching me how to have an astronaut mentality and for 10 years of beginning of the semester lunches. To the triumvirate of extraordinarily classy gentlemen,

¹To the reader: If you are in San Diego, you MUST go to this restaurant.

Commodore Sukrit, King Philipp and Admiral of the Fleet Benjamin, for their exquisite tastes for the finer things of life and marvelous wit. To Yasaman, for being my companion in condensed matter physics and deep learning at Berkeley and at Google and for all the bunny pictures. To Grandma Sally, for your perspective, compassion, understanding, love, and all the penguins. Sean, for getting me to repeatedly lift heavy things and bringing out my inner 5-year old. Nate, for pushing me and thinking so carefully about what things in this world need the most doing. I treasure our adventures and walks in conversation. Mom and Dad, for raising me to believe I could do anything and for always being there to share in my successes and comfort me through the rough patches.

Chapter 1

Introduction

Humanity's increasing ability to manipulate matter across length scales has been one of the most influential factors in developing new technologies. Yet as far as we have come, we are still far from mastering arbitrary forms of matter at one of its most fundamental controllable level – atoms. Material synthesis and characterization remain laborious and resource-intensive processes; thus, it is important to prioritize efforts toward existing and newly-discovered materials that show the greatest promise for new phenomena and technological applications. In order to efficiently identify the most promising materials, we must understand how specific atomic arrangements give rise to desirable properties and use available means to predict arrangements with high likelihood of being synthesized.

The invention of the transistor, a technology made possible by the scientific understanding of solid state physics, has precipitated an exponential increase in computational power since the mid-20th century. Now in turn, the multidisciplinary process of materials discovery increasingly relies on computational methods. We can now rapidly screen materials for desirable properties by searching materials databases and performing high-throughput first-principles calculations. This approach has led to the identification of new functional materials that have been subsequently confirmed in the lab [58, 277, 268]. However, this model of computational materials discovery is limited to the structures we can provide to our first-principles methods. How can we systematically design materials to expand our search beyond the structures stored in databases?

For atomic systems (crystals, materials, molecules, proteins, etc), quantum mechanics provides an ultimate design constraint. The electronic and nuclear interactions in materials lead to laws that set rules for the possible geometries atoms can adopt. How these quantum mechanical rules dictate the resulting atomic configurations is central to this thesis.

The design space of stable atomic systems is much more limited than all possible arrangements of points in 3D space. Atoms in materials form geometric patterns and simple recurring arrangements. In inorganic crystals, we often identify units comprised of transition metal atoms coordinated by atoms such as oxygen or sulfur that form simple polyhedra such as tetrahedra or octahedra. For molecules, we identify subgroups that are prevalent in organic chemistry such as phenyl groups (benzene) and hydroxyl groups (OH^-). These

recurrent collections of atoms in a fixed structure that we define as *structural motifs* are the building blocks of atomic systems.

This thesis explores a variety of systematic strategies for understanding and designing complex materials from structural motifs on the atomic scale. These approaches for designing materials combine geometric, chemical, and physical intuition with calculations based on quantum theory (density functional theory) and symmetry analysis.

The primary features of structural motifs in materials are their geometry and topology: the shape of the motifs and how the motifs connect or otherwise relate to each other. For example, a transition metal atom may be octahedrally coordinated by oxygen but this coordination may be distorted away from the Platonic ideal. This distortion can greatly impact the electronic properties resulting from this motif. These octahedral motifs can connect to each other in various ways. They can share corners (as they do in Perovskites), edges (as they do in the Harmonic Honeycomb Iridates in Chapters 3 and 4) or faces (as they do in Corundum). For many systems, there is no unique way to meaningfully partition an atomic structure into structural motifs and some may be more useful in specific contexts than others. By breaking a structure into components that enable complex phenomena, we may be able to systematically design motifs and connectivities that lead to desirable properties, expediting our ability to explore the space of possible materials.

Some material classes share structural motifs but differ in the way those motifs connect. In the Chapters 3 and 4, we closely analyze how edge-sharing three-fold coordinated IrO_6 octahedra in the harmonic honeycomb iridates leads to exotic magnetism. We propose an infinite series of homologous structures that share the same basic structural units but differ in their connectivity. We suggest this class of complex correlated systems can be better understood using a series of homologous structures with an identical local structure but different connectivity.

In other material classes, structural motifs are defined by interactions between two diverse starting ingredients, enabling a range of geometries and connectivities. In Chapter 5, we explore metal-organic chalcogenide assemblies (MOChAs), bulk hybrid materials with low-dimensional inorganic structures that are scaffolded by organic ligands. In MOChAs, the formation of motifs is driven by the possible oxidation states of a transition metal and the packing of chalcogenide (S, Se, or Te) bonded organic molecules around that transition metal. These motifs connect through supramolecular assembly to form low-dimensional organic structures. In the case of silver benzene selenolate ($[\text{AgSePh}]_\infty$), the end product is a bulk system with two-dimensional electronic properties. We show how MOChAs lend themselves to geometric analysis and design.

In structural phase transitions the geometry of motifs may change while the topology of those motifs is maintained. Ferroelectrics are materials that undergo a structural transition that results in the appearance of a spontaneous polarization that can be switched due to the energetic adjacency of degenerate low-symmetry states. In Chapter 6 we demonstrate how symmetry analysis, density functional theory calculations, and post-processing analysis can be automated to search for ferroelectric candidates, identifying several previously-unknown ferroelectric candidates. We discuss the use of isotropy subgroups for relating structures via

symmetric distortions.

Ideally, we want a means to automate the understanding of materials from their atomic structure. However, it is difficult to hand-code, using physical and chemical intuition, all possible structural motifs. Deep learning is a machine learning method in which multiple layers of neural networks are trained using the backpropagation algorithm to learn important features of large datasets. These techniques have revolutionized computer vision, a field that previously used hand-crafted features to create models to identify objects in images. Deep learning models now exceed human performance on a variety of image classification tasks [94]. In materials informatics, it is currently common practice to hand-featurize atomic structures when building machine learning models of material properties because we lack a natural method of encoding these structures for neural networks [36, 279, 33]. If deep learning techniques can be adapted for atomic systems, they could be used to learn what structural motifs are chemically stable and give rise to desirable properties. In the Chapter 7, we present a new type of neural network architecture that can naturally handle 3D geometry and the mathematical objects that characterize physical systems. We contrast this network to existing work that focuses on creating input representations of atomic systems compatible with existing networks invented in computer vision or throwing out geometric information.

The remainder of this chapter gives an overview of the material systems, phenomena, and computational techniques described in later chapters.

1.1 Harmonic Honeycomb Iridates

The harmonic honeycomb iridates ($A_2\text{IrO}_3$ for $A \in \text{Na, Li}$) are a class of structures with exotic anisotropic quantum magnetism. At the atomic level, the harmonic honeycomb iridates form a class of structures with identical local geometry that differ in the connectivity of basic structural units. Some structures in this series have been synthesized while others have yet eluded experimental synthesis efforts.

In these materials, electron correlation, spin-orbit coupling, and crystal field effects have comparable energy scales. The result is anisotropic magnetism that originates from a single spin on each iridium in a $J_{eff} = 1/2$ state.

Due to their geometry and spin, these materials may exhibit magnetic interactions described by the Kitaev model, an analytically solvable Hamiltonian that gives rise to a quantum spin liquid. Even as the temperature approaches absolute zero, quantum spin liquids have disordered spin states - the spins never order but rather transition between energetically degenerate configurations.

Energy levels of a single IrO_6 octahedra

The dominant structural motif in harmonic honeycomb iridates are IrO_6 octahedra. The $5d$ orbitals of the iridium atoms are split due to the presence of the oxygen atoms into a two-fold degenerate manifold containing the $x^2 - y^2$ and $2z^2 - x^2 - y^2$ d orbitals called E_g

and a three-fold degenerate manifold containing the xy , yz , and zx d orbitals called T_{2g} . Since the E_g orbitals are closer to the oxygen atoms than the T_{2g} orbitals and the oxygen atoms have a negative valence, the E_g orbitals are higher and the T_{2g} orbitals are lower in energy, see the center of Figure 1.1. The energy difference between these orbitals due to the presence of the oxygen is called the crystal field splitting. Experimentally, octahedrally coordinated iridates have crystal field splitting, $\Delta_{CF} \approx 3$ eV [96].

In the presence of large crystal field splitting, the mixing of E_g and T_{2g} is too energetically expensive to occur. The matrix elements of the angular momentum operator $\mathbf{L} = (L_x, L_y, L_z)$ on the T_{2g} orbitals are identical to those of the p orbitals modulo a minus sign, therefore the T_{2g} orbitals have $L_{eff} = 1$ [239]. The corresponding matrix elements for E_g mixing is zero therefore E_g orbitals have $L_{eff} = 0$ and are said to be “quenched” [239].

As iridium is a heavy element, its electrons experience a large potential well from iridium’s nucleus and the energy scales involved begin to be comparable to the energy of the electron. Thus, the coupling between spin and orbital momentum, proportional to $(Z^4/n^3)\mathbf{L} \cdot \mathbf{S}$ where Z is the atomic number and n is the principal quantum number, becomes a non-negligible term of the Hamiltonian [47]. Spin and orbital angular momentum no longer commute and the quantum states of the electrons are eigenstates of total angular momentum, $\mathbf{J} = \mathbf{L} + \mathbf{S}$.

The T_{2g} orbitals have $L_{eff} = 1$. Since $1 \otimes 1/2 = 1/2 \oplus 3/2$, the T_{2g} orbitals split into two manifolds, a two-fold degenerate $J_{eff} = 1/2$ manifold and a four-fold degenerate $J_{eff} = 3/2$ manifold, see the right of Figure 1.1. If the operator $\mathbf{L} \cdot \mathbf{S}$ acts on the T_{2g} orbitals with spin components, we find that the $J_{eff} = 1/2$ are λ_{SO} higher in energy and $J_{eff} = 3/2$ are $\lambda_{SO}/2$ lower in energy [239]. λ_{SO} in iridates is close to 0.5 eV [96], for a total splitting of ≈ 0.75 eV.

Iridium has 9 $5d$ electrons and in the harmonic honeycomb iridates, iridium takes a +4 oxidation state. The energy of Hund’s coupling is smaller than the crystal field splitting energy ($J_H \approx 0.25$ eV $\ll \Delta_{CF} \approx 3.0$ eV [271]), so the 5 remaining Ir electrons fill the T_{2g} manifold such that $J_{eff} = 3/2$ is filled and $J_{eff} = 1/2$ is half filled.

Since the $J_{eff} = 1/2$ is half filled, we would expect the iridates to be metallic. However, d orbitals are more localized than s or p orbitals and electrons experience repulsion from electrons in other d orbitals. This repulsion can be described by the Hubbard model in which there is competition between a hopping interaction with coefficient t and the repulsion term with coefficient U [114, 114]. As $U/t \rightarrow 0$, the system is metallic and as $U/t \rightarrow \infty$ the system is insulating. This effect is large in $3d$ systems (with $U \approx 5$ eV) where orbitals are more tightly bound with little overlap and small in $5d$ orbitals ($U \approx 1.5 - 2$ eV in iridates) which are more diffuse, therefore overlapping more [167, 116]. Despite the effect being small, this results in the two $J_{eff} = 1/2$ states being further split, preventing a metallic state. When a gap in the electronic states at the Fermi level is caused by Hubbard repulsion, a material is said to be a Mott insulator. The Mott gap in the honeycomb iridates is ≈ 0.4 eV [96].

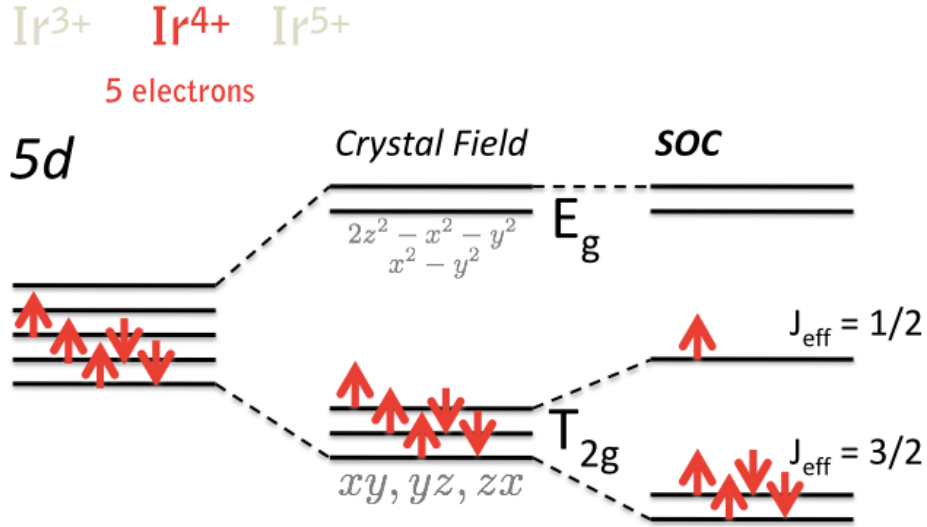


Figure 1.1: The splitting of $5d$ orbitals for iridium atoms octahedrally coordinated by oxygen atoms. Crystal field splitting breaks the degeneracy of the $5d$ orbitals into a two-dimensional manifold E_g and a three-dimensional manifold T_{2g} . Spin-orbit coupling further splits the T_{2g} manifold with $L_{eff} = 1$ into $J_{eff} = 1/2$ and $J_{eff} = 3/2$ states.

Interaction of edge-sharing IrO_6 octahedra

Magnetic interactions arise primarily from exchange symmetry, the requirement that wavefunctions of electrons must be antisymmetric under the exchange of any two electrons [48]. The Hamiltonian for the coupling of two spins can be written as $A\mathbf{S}_i \cdot \mathbf{S}_j$, where A is a constant, [49]. The simplest extension of this interaction to the case of many electrons is given by the Heisenberg model [48],

$$H_{\mathcal{H}} = \sum_{ij} J_{ij} \mathbf{S}_i \cdot \mathbf{S}_j, \quad (1.1)$$

where ij denotes neighbors. However, in general the magnetic Hamiltonian can have higher-order terms.

Given two IrO_6 octahedra sharing a single edge, there is a plane defined by the iridium centers and the two oxygen atoms the iridium share (which we will call the Ir-O-Ir bond plane). The magnetic iridium atoms interact via their shared oxygen through superexchange [48]. Given ideal octahedral geometry, there are two identical Ir-O-Ir bond exchange paths for the isotropic terms. The $J_{eff} = 1/2$ states destructively interfere along these paths causing the isotropic Heisenberg interaction to disappear, leaving a weak anisotropic interaction due to Hund's coupling [118]. This is called the Quantum Compass Model. Assuming the Ir-O-Ir bonds are in the xy -plane, the Hamiltonian further simplifies to

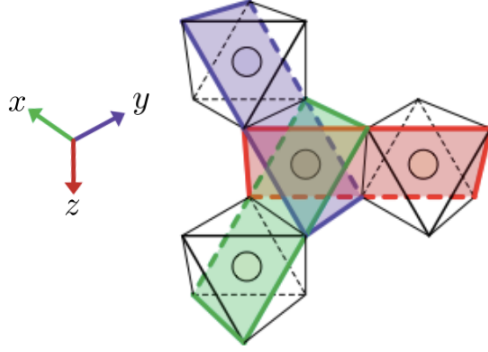


Figure 1.2: In the harmonic honeycomb iridates, the IrO_6 edge-share with three nearest neighbors, forming three orthogonal planes defined by the Ir-O-Ir bonds. These planes are indicated with blue, red, and green shading. The Ir ions are indicated by the circles while the oxygens (not shown) lie on the edges of the polyhedra.

$$H_{ij} = J_z S_i^z S_j^z. \quad (1.2)$$

The IrO_6 octahedra in harmonic honeycomb iridates edge-share with three nearest neighbor octahedra. These neighbors are maximally far apart from one another such that the three planes defined by the shared oxygen and central iridium atoms are orthogonal to each other, shown in Fig. 1.2. This gives a 3-fold orthogonal Quantum Compass Model known as the Kitaev Model, that is

$$H_K = -K_\gamma \sum_{\langle ij \rangle} S_i^\gamma S_j^\gamma. \quad (1.3)$$

where $\langle ij \rangle$ denotes, nearest neighbor iridium atoms that form a bonding plane perpendicular to γ .

Due to distortion of the IrO_6 octahedra, the magnetism of the harmonic honeycomb iridates is described by a Kitaev-Heisenberg model, where the distorted Ir-O-Ir exchange paths prevent complete destructive interference of the isotropic magnetic interaction.

In Chapter 3, we present the discovery of the first 3D harmonic honeycomb iridate and characterize its anisotropic magnetism. In Chapter 4 we compute the ground state structures of select members of the harmonic honeycomb homologous series with density functional theory-based methods (varying U and testing sensitivity to SOC) and investigate the effect of the alkali metal (Li or Na) on the distortion of IrO_6 octahedra.

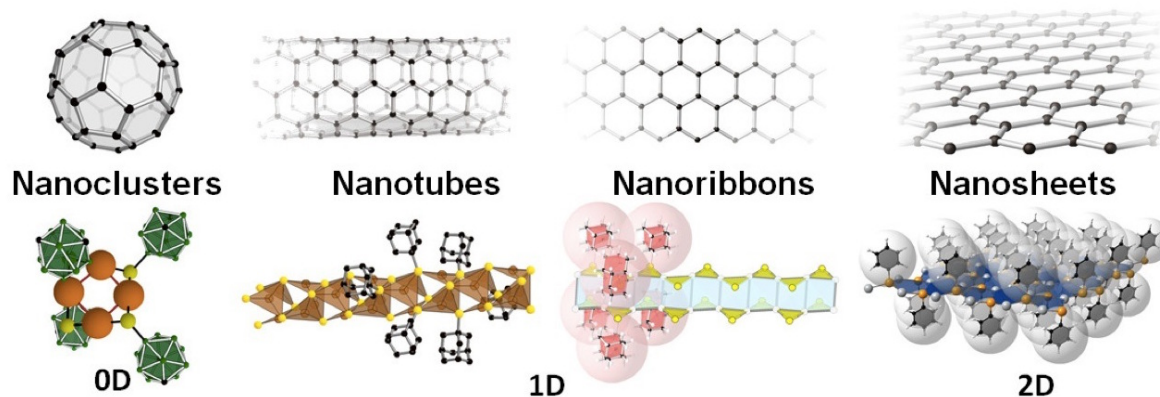


Figure 1.3: MOChAs can host inorganic structures of varying dimensionality and topology, from sheets and tubes (2D), to chains and rings (1D), to individual clusters (0D).

1.2 Metal-organic Chalcogenide Assemblies (MOChAs)

Metal-organic chalcogenides assemblies (MOChAs) are self-assembled hybrid crystals where low-dimensional transition metal chalcogenide structures are scaffolded by organic ligands [267]. Depending on the choice of organic ligand, the electronic structure near the Fermi level may be entirely dominated by the inorganic structure or influenced by the organic ligand. Due to the intrinsically insulating nature of many organic ligands, the geometry of MOChAs can be designed to yield bulk materials with low-dimensional electronic properties.

Electrons restricted in one or more dimensions have properties that differ from electrons in the bulk due to quantum confinement and the lack of screening by neighboring atoms. This is one of the driving motivations for research in modern nanoscience.

Two examples of this are graphene and MoS_2 ; both form 2D sheets as well as nanotubes. Graphene, a single layer of graphite, is the prototypical low-dimensional material comprised of an atomically-thin 2D hexagonal lattice of carbon atoms. While graphite is a semi-metal, graphene is a so-called Dirac semi-metal where electrons near the Fermi level behave relativistically. Layered transition metal dichalcogenides are comprised of edge sharing coordination polyhedra. These materials (e.g. MoS_2) are semiconductors and undergo an indirect-to-direct bandgap transition when exfoliated to a monocrystalline single-layer.

In both these examples, the bulk material is comprised of monolayers bonded by van der Waals interactions and the low-dimensional properties are only present in an isolated monolayer. Low-dimensional materials are often laborious to synthesize, isolate, and keep clean. MOChAs present an alternative approach to realizing materials with low-dimensional properties and to exploring low-dimensional phenomena. In contrast to isolated low-dimensional materials, MOChAs self-assemble at near room temperature and are robust to an ambient environment.

The synthesis of MOChAs is highly modular allowing for various combinations of metals, chalcogenides, and organic ligands to be readily explored. MOChAs are synthesized using a metal salt or metal wafer and organic groups attached via a dichalcogen bond (R-E-E-R) where R represents any organic ligand and E = S, Se, Te. The reaction between the metal ion and the organochalcogen drives molecular self-assembly, resulting in the formation of supramolecular hybrid structures. There are three primary synthetic routes for achieving self-assembly of these structures, shown in Figure 1.5: immiscible layered strategy, gram-scale bulk synthesis, and wafer-scale gas phase deposition. With care, it is possible to produce millimeter-scale single-crystals of spontaneously self-assembled hybrid compounds.

With metal-organic chalcogenides, we can harness the variety of geometry of organic molecules to tune the electronic properties of low-dimensional transition metal chalcogenide structures. Changing ligands and inorganic composition can yield diverse crystal geometries or variations of similar structures, see Figure 1.4.

Using MOChAs style synthesis, we can make low-dimensional transition metal chalcogenide structures of materials that do not form layered materials or other low-dimensional structures in the bulk. In Chapter 5, we focus on one such example, silver benzene selenolate, $[\text{AgSePh}]_\infty$ where the subscript ∞ denotes the bulk material is comprised of many van der Waals bonded layers of AgSePh. Bulk Ag_2Se is an indirect band gap semiconductor comprised of four- and five-fold selenium coordinated silver atoms; the coordination polyhedra edge-share along all three crystal lattice directions. In contrast, $[\text{AgSePh}]_\infty$ is comprised of 2D sheets of silver tetrahedrally coordinated by selenium with the sheets scaffolded by phenyl groups. Additionally, $[\text{AgSePh}]_\infty$ is a direct band gap semiconductor that photoluminesces blue light. In Chapter 5, we describe multiple synthetic avenues for creating $[\text{AgSePh}]_\infty$ and study the quantum confinement of its layers using photoluminescence measurements and density functional theory.

1.3 Ferroelectrics

When structural motifs are distorted, new electronic properties can arise that were previously forbidden by symmetry. One such property is ferroelectricity. Ferroelectric materials display couplings between magnetic, electronic, and lattice degrees of freedom, leading to exotic phenomena and making them technologically useful.

Macroscopically, a ferroelectric material has a spontaneous polarization that is switchable by an applied electric field [152] (see Figure 1.6a). At the atomic scale, ferroelectric switching is a structural transition between energetically degenerate structures with a spontaneous polarization resulting from the displacements of charged atoms.

Phenomenologically, these degenerate ferroelectric structures arise from the symmetry breaking of higher-symmetry structure without a spontaneous polarization. Materials can only host a spontaneous polarization if they have a space group symmetry with a polar point group. Out of the 32 crystallographic point groups, 10 are polar (1, 2, m , $mm2$, 3, $3m$, 4, $4mm$, 6 and $6mm$). The remaining point groups are nonpolar. A crystal with a nonpolar

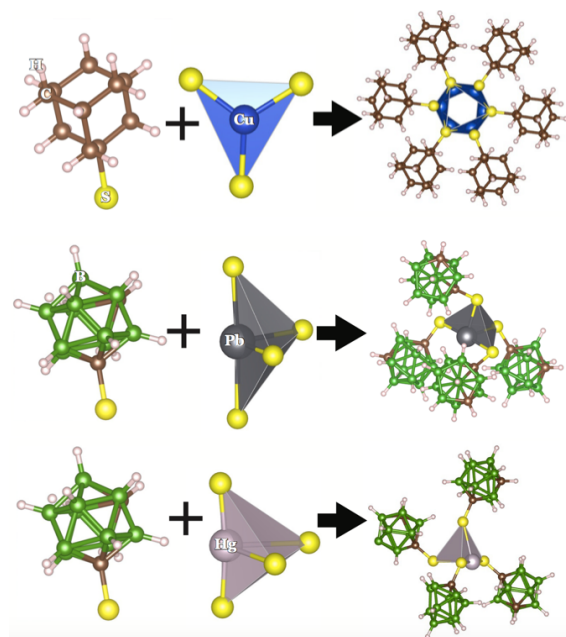


Figure 1.4: Different transition metals and organic ligands form MOChAs with various coordinations and topologies. (Top to Bottom) adamantane + copper give a nanotube structure made of triangular coordination polygons, carborane + lead give a chiral 1D chain of see-saw coordination polyhedra, carborane + mercury give a non-chiral 1D chain of see-saw coordination polyhedra.

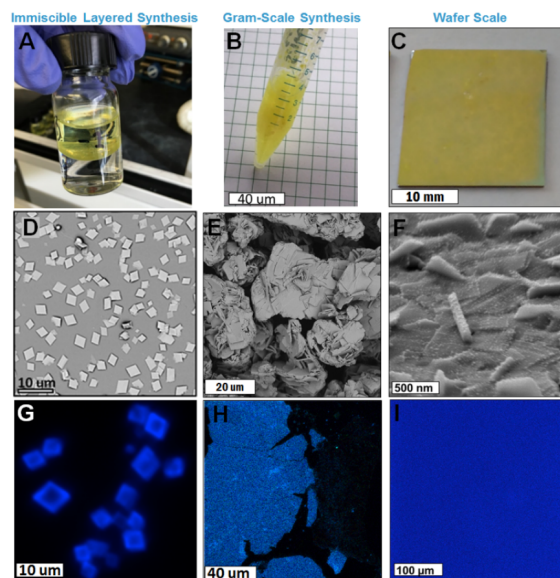


Figure 1.5: Top) Three methods for making MOChAs: immiscible layered strategy, gram-scale bulk synthesis, and wafer-scale gas phase deposition. Middle row). Crystals produced from each method. Bottom row) All three methods produce different crystal morphologies but uniform emission energy.

symmetry has a center of symmetry such that no vector quantity (such as a polarization vector) can be compatible with the crystal symmetry.

The high-symmetry structure that cannot host a spontaneous polarization belongs to a nonpolar space group; we call it the nonpolar structure.¹ The ferroelectric lower-symmetry structures belong to a polar space group; we call these degenerate structures the polar structures. See Appendix D for a concrete example of a prototypical ferroelectric, BaTiO₃. In Chapter 6, we use this symmetry criterion to find compatible pairs of nonpolar-polar structures to search for new ferroelectrics that may host new physics or be technologically useful.

¹It is common in the ferroelectric literature for it to be said the high-symmetry structure is required to have centrosymmetry, meaning having inversion symmetry; this is not necessarily correct. Nonpolar is a more general symmetry criterion. All point groups with inversion symmetry are nonpolar, but there are chiral, nonpolar point groups without inversion symmetry (222, 422, 622, 32, 23, and 432).

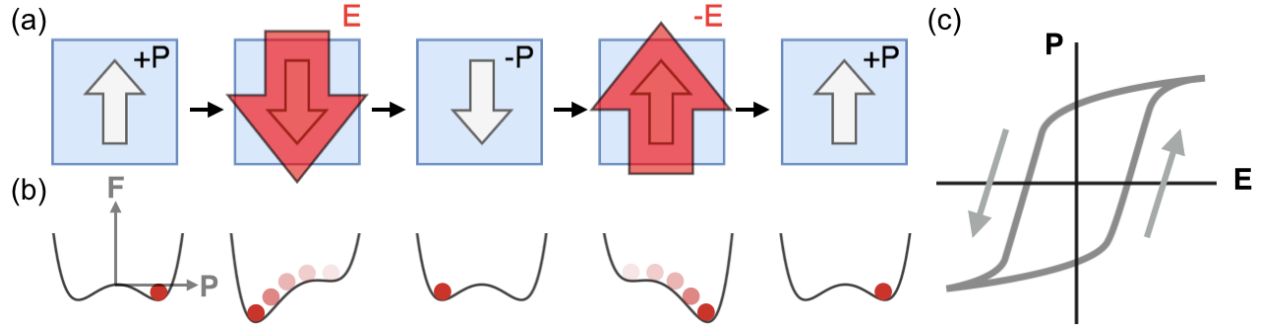


Figure 1.6: a) A ferroelectric is a material with a spontaneous polarization that is switchable by applying an external electric field. b) The free energy written in terms of polarization has a double well, each well representing stable, switchable polar structures. c) A plot of the polarization of a ferroelectric versus the application of an electric field will produce a hysteresis loop.

The structural transition from the nonpolar structure to one of multiple possible polar structures can be due to a phonon mode becoming “soft”, meaning it has become non-restorative, with decreasing temperature. In order to break the symmetries forbidding a spontaneous polarization to arise in the higher-symmetry nonpolar structure, the phonon mode itself must have a polar symmetry. One can search for ferroelectric materials by computing the phonon band structure for nonpolar structures and identifying polar phonon modes with negative energies. This method was used by Ref. [86] to search for ferroelectric candidates.

For our work in Chapter 6, we use a search method motivated by the Landau theory of phase transitions[60]. Near the structural phase transition between the high-symmetry nonpolar and low-symmetry polar structure, the free energy can be expanded using polarization, P , (in this case treated as 1D) as an order parameter as the following:

$$F = \frac{1}{2}a_0(T - T_c)P^2 + \frac{1}{4}bP^4 + \frac{1}{6}cP^6 - EP, \quad (1.4)$$

where a_0 , b , c are constants, T is temperature, T_c is the critical temperature of the phase transition, and E is the electric field.

Below a critical temperature T_c , the free energy of a ferroelectric expressed in terms of polarization has (in the case of a 1D polarization) a double well, with each well representing a stable, switchable structure with a spontaneous polarization (see Figure 1.6b). This transition is second order if the coefficient b is positive, and first order if it is negative [60].

In Chapter 6, we search for nonpolar-polar structure pairs that satisfy the symmetry requirements of Landau theory. In addition to the high(low)-symmetry structures being nonpolar(polar), we additionally require that they are continuously deformable into each other. This means that they satisfy group-subgroup relations and the polar structure must belong to an isotropy subgroup of the nonpolar structure; we go into detail about these

symmetry requirements in Chapter 6 and Appendix F. We then compute the polarization of structures along the distortion between nonpolar and polar structure in order to recover the spontaneous polarization. We must use intermediate structures to recover this quantity because polarization for a periodic system is defined on a lattice; it is not a single well-defined quantity and depends on the choice of unit cell [254]. It is the change in the polarization between the nonpolar and polar structure that is well-defined [205]. If one follows the change in the polarization value on the polarization lattice as it moves throughout the ferroelectric distortion, one can define a single-valued change in the spontaneous polarization that does not depend on the choice of unit cell.

This definition of polarization is compatible with what is seen experimentally. Experimentally, the polarization of a ferroelectric is not measured directly but instead determined by switching the polarization of a given sample with an external electric field and measuring the current that results from the polarization switching [153]. If one then plots the integrated current divided by the surface area of the sample (to obtain units of [charge]/[area] in common units ($\mu\text{Coulomb}/\text{cm}^2$)) as a function of electric field, one obtains a plot of the polarization versus electric field. This plot will have a hysteresis loop due to the switching. An ideal hysteresis loop would have a simple rectangular loop; above the critical electric field that is sufficient to oppose the existing polarization, the polarization would instantaneously switch to the opposite polarization. However, experimentally measured hysteresis loops look more like Figure 1.6c. The specific shape of the hysteresis loop is determined by the interactions of the ferroelectric domains (domains with differently oriented polarizations) inside a macroscopic material [153].

In Chapter 6, we design an automated workflow for finding ferroelectric candidates by harnessing symmetry analysis to find nonpolar-polar structure pairs and calculating the spontaneous polarization of these candidates using density functional theory calculations of intermediate structures between the nonpolar and polar structures. This workflow has been open-sourced and contributed to the *atomate* python package [165]. The data resulting from our first ferroelectric search using this workflow on the Materials Project databases [124] has been made publicly available at http://blondegeek.github.io/ferroelectric_search_site/.

1.4 Deep learning for atomic systems

Deep learning is a promising technique for expediting existing tools and creating new capabilities in computational materials exploration. It could potentially compute the properties of materials in an order of magnitude less time and propose hypothetical structures from experimentally known motifs. One of the challenges with applying deep learning techniques to materials and atomic systems generally is creating neural networks capable of operating on and producing the data types relevant to materials, such as 3D geometric configurations.

The community has approached this challenge in two ways: designing specialized input representations of atomic systems to use with existing neural network architecture [32, 33,

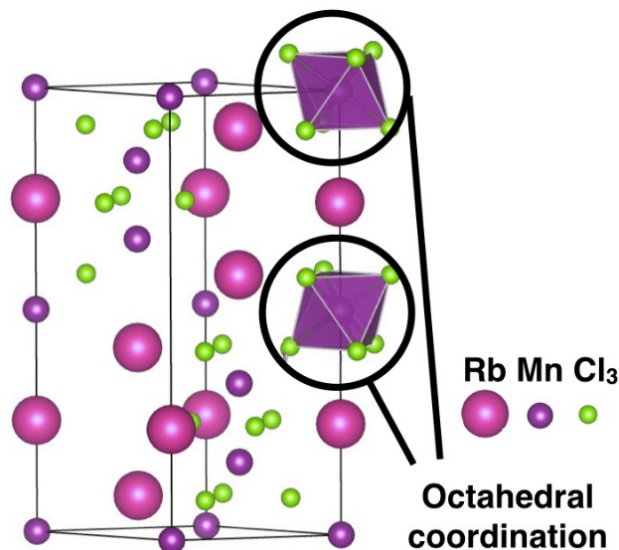


Figure 1.7: A network with 3D translation- and 3D rotation-equivariance allows us to identify chemical motifs in any location or orientation using the same filters.

36, 236, 92] and inventing new networks more tailored toward atomic structures [126, 83, 89, 222, 221].

These approaches have been used to predict properties of small molecules and crystals with chemical accuracy [202, 215, 62, 221] and to generate new molecules for applications such as drugs and devices [92]. However, these techniques either do not generalize to all types of atomic systems (molecules, crystals, polymers, nanocrystals, proteins, etc) or they throw out potentially useful geometric information. For example, Ref. [92] uses string representations of the topology of molecular graphs, called SMILES strings, as input to their network [262]. This input representation is not appropriate for material systems because materials have much more ambiguous bonding structures and a topological representation does not include any geometric information about the positions of the atoms. Ref. [126, 83, 89, 222, 221] use pairwise distances to encode atomic structures. Other rotation-invariant geometric information, such as bond angles can also be included, however this becomes expensive to encode.

Ideally, a neural network would use the atomic positions of the atomic system we are investigating and structural motifs could be identified at different locations and orientations within an example without the need for data augmentation, see Figure 1.7. In Chapter 7, we present a universal framework for deep learning on atomic systems that can naturally handle 3D geometry and features of physical systems. We call this framework *tensor field networks*.

Chapter 2

Methods

2.1 Density Functional Theory

The research presented in this dissertation uses density functional theory to understand the electronic structure of experimentally realized materials, evaluate hypothetical structures, and relate changes in the geometry of an atomic system to changes in its electronic properties.

Density functional theory (DFT) is a technique that has made quantum mechanical properties feasible to calculate for a wide variety of atomic systems, tens to thousands of atoms in size. Modern DFT relies on the Kohn-Sham equations which are solved self-consistently; expedient linear algebra libraries; and a generous application of compute power to calculate electronic properties.

The many body Schrödinger Equation in the Born-Oppenheimer approximation can be written as:

$$\hat{H}\Psi = \left[\hat{T} + \hat{V}_{ext} + \hat{V}_{int} + E_{II} \right] \Psi = E\Psi, \quad (2.1)$$

where T is the kinetic energy operator, \hat{V}_{ext} is potential energy associated with the nuclei, \hat{V}_{int} describes the electron-electron interactions, E_{II} is the classical interaction between nuclei, and E is the energy [162]. While such an equation is simple to write down, it is computationally infeasible to solve for more than tens of particles because the complexity scales exponentially with the number of particles [132].

Density functional theory (DFT) formalism relies on two theorems, known as the Hohenberg-Kohn theorems [109]. First, for a given system, $\hat{V}_{ext}(\mathbf{r})$ and thus the total energy of a system is a functional of the ground state charge density, $n(\mathbf{r})$, expressed as

$$E[n(\mathbf{r})] = \int d\mathbf{r} V_{ext}(\mathbf{r})n(\mathbf{r}) + F[n(\mathbf{r})] + E_{II}, \quad (2.2)$$

where $F[n(\mathbf{r})]$ includes kinetic energy and electron-electron interactions. Second, the density that minimizes the total energy is the ground state charge density. These two theorems have significant consequences; combined they imply the ground state total energy of a system

of interacting electrons and nuclei is determined by the ground state electron density. We only need to know the energy functional $E[n(\mathbf{r})]$ to solve for the ground state charge density variationally [163]. While a wavefunction has $3N$ variables, a charge density has only 3 (one for each spatial dimension). The greatly reduced number of degrees of freedom needed to describe the total energy and density of interacting many-body systems makes DFT a potentially powerful approach compared to more expensive wavefunction based methods.

While the Hohenberg-Kohn theorem proves the existence of a universal functional, it does not provide a way to determine this functional.¹ Fortunately, soon after the appearance of the Hohenberg-Kohn theorem in 1964, Kohn and Sham found a way to map the many-problem to that of a single electron in an external potential of non-interacting electrons in 1965 [133]. In this formulation, solving for the ground state charge density of this effective non-interacting system leads to the same ground state charge density of the true interacting many-body system; the ground state wavefunctions of the effective non-interacting system, obtained from the Kohn-Sham equations are used to determine ground state charge density of the many-body system. More explicitly, the Kohn-Sham approach reformulates the Hohenberg-Kohn expression for the ground state functional as:

$$E_{KS} = T_S[n] + \int d\mathbf{r} V_{\text{ext}}(\mathbf{r})n(\mathbf{r}) + E_{\text{Hartree}}[n] + E_{II} + E_{XC}[n] \quad (2.3)$$

where $T_S[n]$ is the kinetic energy of non-interacting electrons, $E_{\text{Hartree}}[n]$ is the mean-field Coulomb interaction energy of the electron density, and $E_{XC}[n]$ is the exchange-correlation functional. The first three terms of this equation are known and can be straightforwardly solved for. The $E_{XC}[n]$ term expresses the difference in kinetics and potential of an interacting versus a non-interacting system, which is readily seen in the following expression [163],

$$E_{XC}[n] = \langle \hat{T} \rangle - T_S[n] + \langle \hat{V}_{\text{int}} \rangle - E_{\text{Hartree}}[n], \quad (2.4)$$

and is in general unknown.

Density functionals

A major success of DFT is that approximate forms of E_{XC} have been developed that have been very effective. Different density functionals will treat exchange and correlation, $E_{XC}[n]$ differently. In this dissertation we use the LDA, PBE, and HSE functionals; these functionals are defined below.

In the local density approximation (LDA), one uses the exact exchange of a homogeneous electron gas as calculated from quantum Monte Carlo calculations [133]. The E_{XC} for the LDA depends linearly on the charge density,

¹Even if we were handed the universal functional, it may still be too expensive to feasibly compute.

$$E_{XC}^{\text{LDA}}[n] = \int d\mathbf{r} n(\mathbf{r}) \epsilon_{XC}^{\text{homogen.}}(n(\mathbf{r})). \quad (2.5)$$

Despite its simplicity, LDA has been successful at describing many material systems. The generalized gradient approximation (GGA) has lead to a class of functionals that depend on the charge density and its gradient,

$$E_{XC}^{\text{GGA}}[n] = \int d\mathbf{r} \epsilon_{XC}^{\text{GGA}}(n(\mathbf{r}), \nabla n(\mathbf{r})). \quad (2.6)$$

The functional by Perdew, Burke and Ernzerhof (PBE) is a specific functional based on the GGA that is widely used [193]. GGAs can improve on the LDA for certain classes of systems. Neither LDA nor GGA treat van der Waals dispersion interactions, a nonlocal correlation effect. LDA tends to overbind and PBE tends to underbind, resulting in structures that tend to have smaller and larger lattice parameters than experiment, respectively. Both LDA and PBE generally underestimate band gaps.

Hybrid functionals include a different fraction of exact Fock exchange. Range-separated hybrid functionals can include a fraction of exact exchange at short and long range. The exchange and correlation functional by Heyd, Scuseria, and Ernzerhof (HSE) includes a fraction of exact exchange for short range interactions and GGA exchange for longer range interactions distances and can be written as

$$E_{XC}^{\text{HSE}} = aE_X^{\text{HF,SR}}(\omega) + (1 - a)E_X^{\text{PBE,SR}}(\omega) + E_X^{\text{PBE,LR}} + E_C^{\text{PBE}} \quad (2.7)$$

where a is 0.25 and ω , the range separation parameter, is 0.2 [140]. Fortuitously, HSE tends to give better band gaps than LDA and PBE, due to the inclusion of some amount of exact exchange, but for accurate band gaps one needs to go beyond DFT to an excited state formalism such as many body perturbation theory.

Practically, one arrives at the ground state electron density through a self-consistent approach. For a given arrangement of nuclei, a starting guess for the charge density is made based on atomic orbitals. This charge density is then used to generate $V_{ext}(\mathbf{r})$ and $\Psi_i(\mathbf{r})$. We then update the wavefunctions based on the solutions of the Kohn-Sham equations. We repeat until the ground state energy and forces converge to desired values, typically $10^{-3} eV$ and $10^{-2} eV/\text{\AA}$.

Plane waves and pseudopotentials

To represent wavefunctions, one needs a basis set. In this dissertation, we focus on crystal systems so we use plane-waves. The plane-wave basis depends on the crystallographic lattice parameters of the input unit cell and an energy cutoff E_{cutoff} . For a given E_{cutoff} , all plane-waves satisfying the following equation are included

$$\frac{\hbar^2}{2m_e} |\mathbf{G} + \mathbf{k}|^2 < E_{\text{cutoff}}, \quad (2.8)$$

where \mathbf{G} is a reciprocal lattice vector and \mathbf{k} is a vector in reciprocal space.

For many systems, including those described in this thesis, it is computationally expensive to treat all electrons independently. Like all electrons, the wavefunctions of core electrons must be orthogonal to one another. Because core electrons exist in a rather confined region near the nucleus, this requires core electron wavefunctions to oscillate and defines their nodal structure. To accurately describe these core wavefunctions, one must use a basis that has a resolution comparable to these oscillations, which can be hundredths of Angstroms. For example, for $E_{\text{cutoff}} = 520$ eV, the resolution is approximately a tenth of an Angstrom.

$$\frac{\hbar^2}{2m_e} \left| \frac{1}{1.2 \times 10^{-11} \text{ meters}} \right|^2 \approx 520 \text{ eV} \quad (2.9)$$

To achieve a resolution of approximately a hundredth of an Angstrom, E_{cutoff} would have to be increased a hundred fold. Moreover, core electrons are highly localized and well-separated in energy from valence electrons, which are crucial to determining structural and electronic properties. Therefore, it is a good approximation to freeze them into an effective core and neglect core degrees of freedom in solving the Kohn-Sham equations. Thus, rather than treating core electrons directly, we use pseudopotentials which combine the nuclear and core electron contributions and create a smooth potential.

Treating on-site correlations associated with localized electrons with Hubbard U

In general, the most commonly used exchange-correlation functionals for the solid state, LDA and PBE, are most effective where the electron density is nearly uniform. Electrons in the Kohn-Sham DFT formalism neglecting exact exchange effectively experience spurious interactions with their contribution to the charge density when the many-body system is cast as an effective potential. This creates additional unphysical delocalization of the electron density; this can be highly problematic when describing more tightly bound d and f orbitals of transition-metals [164].

A computationally inexpensive approach that can improve treatment of such systems is to introduce a Hubbard U parameter penalizing electrons occupying the same site [26]. However, the value of U is usually empirically set; the use of U means the functional now depends on the density and occupation and the manner in which U is typically introduced leads to double counting errors, which can be serious in some cases [164]. Hybrid functionals such as HSE remove the need for such a parameter by including some amount of exact exchange. We use Hubbard U parameters in Chapters 4, 5 and 6 to treat materials comprised of transition-metals.

Chapter 3

Realization of a three-dimensional spin-anisotropic harmonic honeycomb iridate

The work described in this chapter has been published as Ref. [172].

Spin and orbital quantum numbers play a key role in the physics of Mott insulators, but in most systems they are connected only indirectly — via the Pauli exclusion principle and the Coulomb interaction. Iridium-based oxides (iridates) introduce strong spin-orbit coupling directly, such that the Mott physics has a strong orbital character. In the layered honeycomb iridates this is thought to generate highly spin-anisotropic magnetic interactions, coupling the spin orientation to a given spatial direction of exchange and leading to strongly frustrated magnetism. Here we report a new iridate structure that has the same local connectivity as the layered honeycomb and exhibits striking evidence for highly spin-anisotropic exchange. The basic structural units of this material suggest that a new family of three-dimensional structures could exist, the ‘harmonic honeycomb’ iridates, of which the present compound is the first example.

3.1 Introduction

Quantum spin systems are characterized by small moments where the spin orientation is decoupled from the crystal lattice, in contrast to Ising-like spin systems that often apply to higher spin states. In the Heisenberg model describing spin-isotropic exchange between neighboring spins, spatial anisotropies of the exchange suppress long-range order [170], but do not lead to anisotropy of the magnetic susceptibility. Striking examples of this are quasi-1D and -2D systems where the exchange differs by orders of magnitude for neighbors along distinct crystallographic directions [234, 91]. The spin-orbit interaction introduces magnetic anisotropy by coupling the spin to the symmetry of the local orbital environment. Although

in spin- $1/2$ systems the crystal field does not introduce single-ion anisotropy (due to Kramer’s protection of the spin- $1/2$ doublet), it can — via spin-orbit — introduce spin-anisotropies in the g -factor and in the exchange interactions. The strength of the spin-orbit coupling varies by orders of magnitude between the $3d$ and $5d$ transition metals. In the former, quenching of the orbital moment decouples the orbital wavefunction from the spin, giving a g -factor anisotropy that is typically small and an even smaller spin-anisotropy. For example, spin- $1/2$ copper in a tetragonal crystal field has a g -factor anisotropy of order 10%, whereas the spin-anisotropy of exchange is of the order of 1% [91].

The stronger spin-orbit coupling of the $5d$ transition metals is known to give rise to larger magnetic anisotropies. In materials with edge-shared IrO_6 octahedra, spin-anisotropy of the exchange between neighboring effective spin- $1/2$ states is enhanced by the interference of the two exchange paths across the planar Ir-O₂-Ir bond. Jackeli and Khaliullin (JK) suggested that in the honeycomb iridates this may lead to extreme spin-anisotropy of the exchange coupling, where in the limiting case, the only non-vanishing interaction is for the spin component normal to the Ir-O₂-Ir plane [119, 59, 3]. In the honeycomb lattice, such an interaction couples different orthogonal spin components for the three nearest neighbors; no single exchange direction can be simultaneously satisfied, leading to strong frustration. It is the possibility of engineering spin-anisotropy coupled to spatial exchange pathways that has spurred intense scientific research, particularly in connection to the search for quantum spin-liquids [130, 119, 59, 3]. However, whether the spin-anisotropic exchange interaction that is coupled to the Ir-O₂-Ir bonding plane is realized in such materials remains an intense subject of scientific debate [233, 3, 63, 97], highlighting the need for the discovery of new materials with related structures and strongly anisotropic exchange interactions.

We have synthesized single crystals of a new polytype of Li_2IrO_3 in which we reveal the effect of the spin-anisotropy of exchange from the temperature dependence of the anisotropic magnetic susceptibility.

3.2 Results

Crystal structure

Single crystals of Li_2IrO_3 were synthesized as described in Methods. As shown in Figure 3.1A, the crystals are clearly faceted and typically around $100 \times 100 \times 200 \mu\text{m}^3$ in size. In contrast to the monoclinic structure of the layered iridate, we find that these materials are orthorhombic and belong to the non-symmorphic space group $Cccm$, with lattice parameters $a = 5.9119(3) \text{ \AA}$, $b = 8.4461(5) \text{ \AA}$, $c = 17.8363(10) \text{ \AA}$ (see Appendix A for details of the crystallography). The structure (shown in Figure 3.1B and C) contains two interlaced honeycomb planes, the orientation of which alternate along the c axis. The x-ray refinement (see Appendix A and Figures A.1-A.4) is consistent with fully stoichiometric Li_2IrO_3 . In this case the Ir oxidation state is Ir^{4+} ($5d^5$), fixing the effective Ir local moment $J_{\text{eff}} = 1/2$, which is consistent with the magnetic properties of our crystals (see Figure 3.2). In

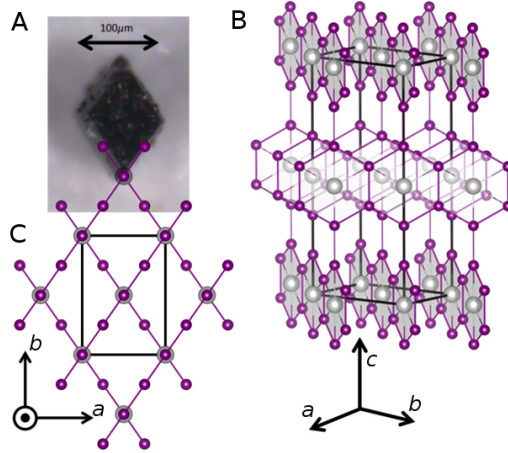


Figure 3.1: **Single crystal of $\mathcal{H}\langle 1 \rangle$ -Li₂IrO₃ and the Ir lattice structure.** (A) Single crystal oriented to be parallel to the crystallographic axes shown in (C), (B) 3D view and (C) projection in the ab plane. In (B) gray shading emphasizes the Ir (purple balls) honeycomb rows that run parallel to the $\mathbf{a} \pm \mathbf{b}$ diagonals, alternating upon moving along the c -axis. For simplicity only Li ions (grey balls) located in the center of Ir honeycombs are shown. In (B) and (C) the rectangular box indicates the unit cell. Comparing (A) and (C) we note that the $\sim 70^\circ$ angle between honeycomb rows is evident in the crystalline morphology.

addition, highly-sensitive single-crystal susceptibility and torque measurements (see below) observe sharp anomalies at the transition to magnetic order, with no measurable variability in this transition temperature between many crystals measured, indicating that the observed magnetic order is well-formed and intrinsic to the crystals. This suggests that if present, Li vacancy disorder is small, because such vacancies will lead non-magnetic Ir⁵⁺ $5d^4$ [52], whose presence is expected to give rise to spin-glass behavior [25] which we do not observe. Taken together, our experiments indicate that our crystals are representative of the high-purity, stoichiometric limit. We denote the crystal structure $\mathcal{H}\langle 1 \rangle$ -Li₂IrO₃, where $\mathcal{H}\langle 1 \rangle$ refers to the single, complete \mathcal{H} oneycomb row.

High temperature magnetic anisotropy

As can be seen in Figure 3.2, the raw magnetic susceptibility shows a magnetic anomaly at 38 K, most likely reflecting the bipartite nature of the structure, which alleviates the magnetic frustration. Due to the smallness of our samples and sensitivity to sample misalignment, the anisotropy at high temperatures could not be quantitatively resolved to high accuracy using SQUID magnetometry. To do so, we utilized torque magnetometry, which exclusively probes magnetic anisotropy (see discussion in Appendix A) and is sufficiently sensitive to measure single crystals of $\sim 10\mu\text{m}$ dimensions. Torque magnetometry was measured by attaching an oriented single crystal to a piezoresistive micro-cantilever [183] that measures mechanical

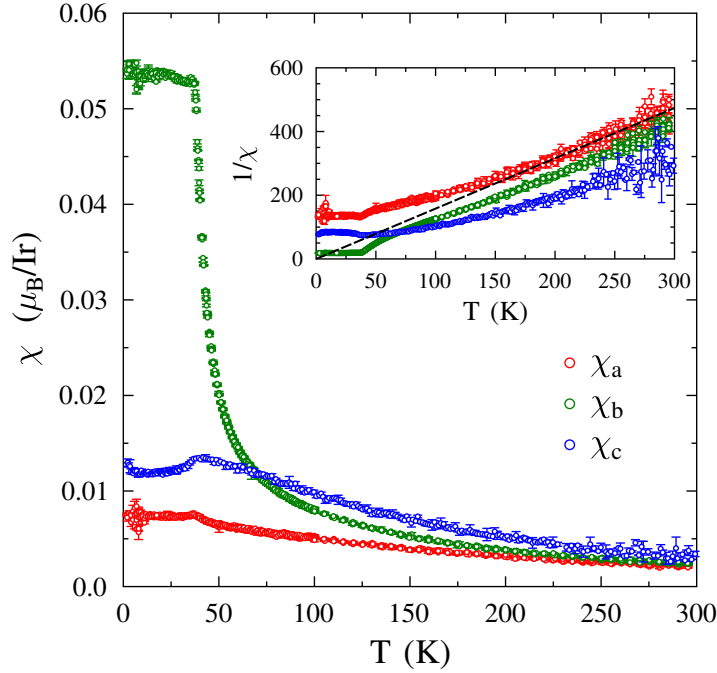


Figure 3.2: **The temperature dependence of the single-crystal magnetic susceptibility along the three principal crystalline directions.** The inset shows $1/\chi$ for all three axes χ_a , χ_b , and χ_c . The dashed line indicates the slope of the inverse Curie-Weiss susceptibility for a paramagnet with effective moment of $\mu_{eff} = 1.6\mu_B$, close to that expected of an Ir $J_{eff} = 1/2$ state if g -factor anisotropy is ignored. All three components of susceptibility show strong deviation from Curie-Weiss behavior as a function of temperature.

stress as the crystal flexes the lever to try to align its magnetic axes with the applied field. The mechanical strain is measured as a voltage change across a balanced Wheatstone Bridge and can detect a torque signal on the order of 10^{-13} Nm. The lever only responds to a torque perpendicular to its long axis and planar surface. As a result, the orientation of the crystal on the lever (determined by x-ray measurements and the diamond shaped morphology) defines the plane of rotation in field and which principal components of anisotropy, α_{ij} ($i, j \in a, b, c$) are measured. To achieve this the cantilever was mounted on a cryogenic goniometer to allow rotation of the sample with respect to magnetic field without thermal cycling. The low temperature anisotropy was confirmed on several similar sized single crystals. To measure $\alpha_{ij} = \chi_i - \chi_j$ between 1.5 K and 250 K, three discrete planes of rotation for the same crystal were used.

A magnetically anisotropic material experiences a torque when its magnetization is not aligned with the applied magnetic field; the deflection of the cantilever in a uniform magnetic

field is hence a direct measure of the magnetic anisotropy, $\vec{\tau} = \vec{M} \times \vec{H}$. At small fields, where the magnetic response is linear, the magnetic anisotropy is captured by a susceptibility tensor $M_i = \chi_{ij}H_j$. For an orthorhombic crystal, the magnetic axes coincide with the crystallographic directions, defining $\chi_{a,b,c}$. For example, for rotations in the $\mathbf{b-c}$ plane, the anisotropic magnetization $(M_b, M_c) = (\chi_b H_b, \chi_c H_c)$ creates a torque

$$\tau_a = \frac{(\chi_b - \chi_c)H^2 \sin 2\theta}{2} \quad (3.1)$$

where θ is the angle between a crystallographic axis (c in this case) and the applied magnetic field.

The geometry of the lattice is intimately connected to the magnetic anisotropy. Specifically, we note that the angle ϕ_0 between the honeycomb strips (see Figure 3.1C) is fixed by the geometry of the edge shared bonding of the IrO_6 octahedra (see Figures 3.3A). For cubic octahedra $\cos \phi_0 = 1/3$, namely $\phi_0 \approx 70^\circ$, as shown in Figure 3.3A. The magnetic axes can be uniquely identified from a complete angular dependence of the torque measurements, with the amplitude of the $\sin 2\theta$ dependence being proportional to the magnetic anisotropy α_{ij} . The observed magnetic axes are independent of temperature between 300 K and 1.5 K. The magnetic anisotropy, shown as data points in Figure 3.3B agrees well with the differences in the low temperature susceptibility data (grey lines in Figure 3.3B). At temperatures that are high relative to the exchange interaction energy scale, we expect that only the g -factor affects the magnetic anisotropy. We find that the ratio of the anisotropic susceptibilities α_{ij}/α_{jk} asymptotically approach simple fractions at high temperature (above ~ 100 K, see Figure 3.3C). Specifically, each Ir is in a three-fold local planar environment with (almost) equidistant neighbors and thus the Ir g -factor anisotropy can be captured by ascribing each honeycomb plane susceptibility components parallel, χ_{\parallel} and perpendicular, χ_{\perp} to the plane (consider Figure 3.3A). This uniaxial local iridium environment combined with the relative orientation of the iridium planes, $\cos \phi_0 = 1/3$, constrains the three components of susceptibility at high temperature to be equally spaced; $2\chi_b = \chi_a + \chi_c$ (see Appendix A) and the anisotropy ratios to be $\alpha_{ba}/\alpha_{ac} = -1/2$, $\alpha_{bc}/\alpha_{ac} = 1/2$, $\alpha_{bc}/\alpha_{ab} = 1$, just as we observe. This observation places constraints on the ordering of the principal components of the g -factor at all temperatures.

Reordering of the principal magnetic axes

The striking reordering of the principal components of susceptibility revealed in torque and SQUID magnetometry, is associated with a strong deviation from Curie-Weiss behavior as the temperature is lowered: α_{bc} changes sign at $T \approx 75$ K (Figure 3.3 D and Figures A.5-A.6). This is in stark contrast to spin-isotropic Heisenberg exchange systems where the low temperature susceptibility reflects the g -factor anisotropy observed at high temperatures, even in the presence of spatially-anisotropic exchange [91]. The change of sign of α_{bc} arises because χ_b softens, becoming an order of magnitude greater than χ_a and $\sim 5 \times \chi_c$ (Figure 3.2 and 3.3B). As a result, the susceptibility cannot be parameterized by a Curie-Weiss temperature:

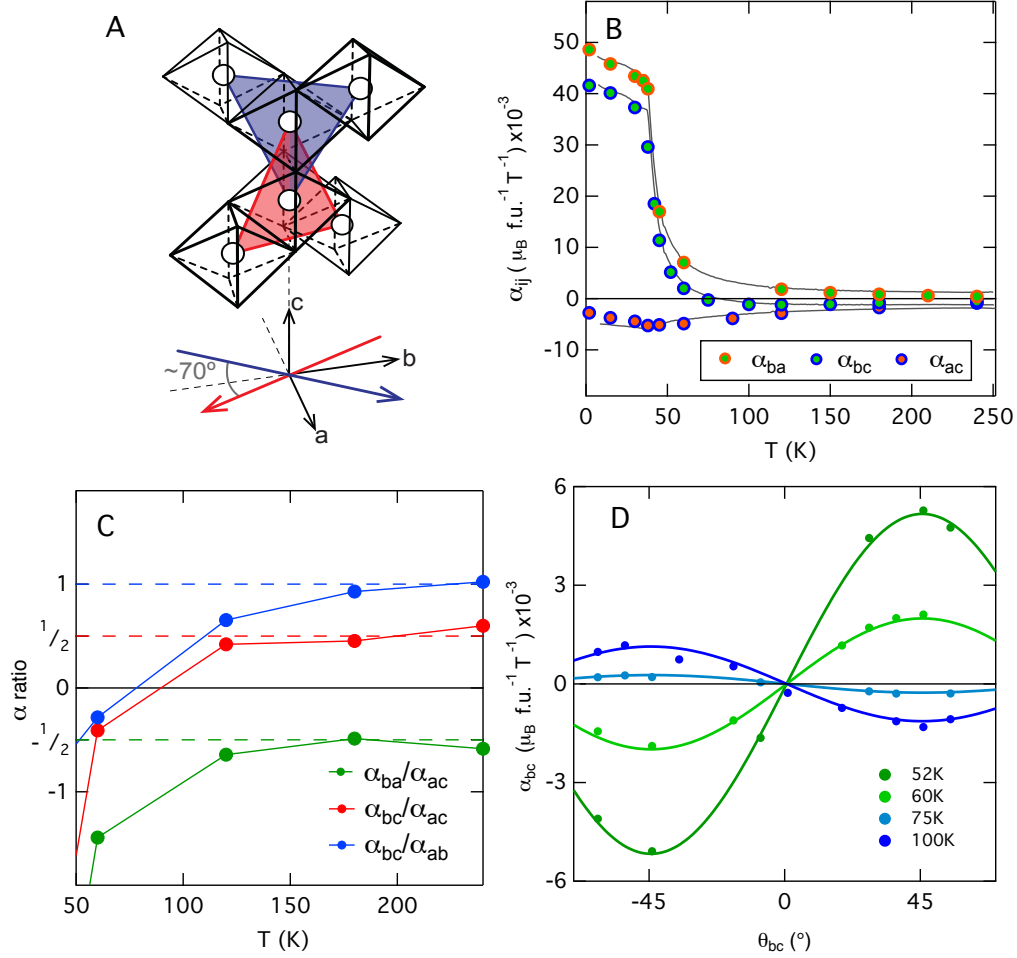


Figure 3.3: **Temperature dependence of the magnetic anisotropy.** (A) Each Ir is surrounded by one of two planar, triangular environments indicated by blue and red shaded triangles, located at $\sim 35^\circ$ either side of the b -axis. (B) The anisotropy of the magnetic susceptibility as measured by torque and the differences in (SQUID) susceptibilities (grey lines) are shown as a function of temperature for all three crystallographic directions. An anomaly indicates the onset of magnetic order at $T_N = 38 \text{ K}$. (C) The ratios of the anisotropic susceptibility tend to simple fractional values dictated by the g -factor anisotropy of the local planar iridium environment. (D) $\sin(2\theta)$ fits to the anisotropy α_{bc} illustrating the change of sign at $\sim 75 \text{ K}$.

the linear extrapolation of all three components of inverse susceptibility to the temperature axis depends strongly upon the temperature range considered. Between 50–150 K the extrapolation of all three components of inverse susceptibility is negative, consistent with the

absence of net moment in the ordered state. However, at higher temperatures (200–300 K) the inverse susceptibilities $1/\chi_b, 1/\chi_c$ extrapolate to positive temperature intercepts (see Figure 3.2) indicating a ferromagnetic component to the interactions. Above 200 K, $1/\chi$ the Curie-Weiss slope gives $\mu_{eff} \approx 1.6\mu_B$, consistent with a $J_{eff} = 1/2$ magnetism.

The observed ten fold increase in χ_b cannot be driven by the g -factor of the local iridium environment, whose geometric constraints are temperature independent (see Appendix A). The temperature dependence of χ_b must therefore arise from spin-anisotropic exchange. We note that all the c -axis bonds have the Ir-O₂-Ir plane normal to the b -axis, whether they preserve or rotate between the two honeycomb orientations (see the full structure in Figure A.3A and a schematic in Figure 3.4A - green shading indicate the Ir-O₂-Ir planes). This is the only Ir-O₂-Ir plane that is normal to a crystallographic axis. This coupling of the spin-anisotropy to the structure, provides evidence for spin-anisotropic exchange across the c -axis links, and by extension should be present in all Ir-O₂-Ir exchange paths. This likely arises from the interfering exchange mechanism suggested by JK in the context of the Kitaev model (see Appendix A).

Low temperature magnetic properties

The softening of χ_b is truncated at 38 K by a magnetic instability. Within the ordered state, the magnetization increases linearly with applied field (Figure 3.4C, τ/H in 3.4B and Figure A.6). At sufficiently high magnetic fields H^* , the magnetization kinks abruptly. This corresponds to an induced moment of $\approx 0.1\mu_B$. Above H^* , the finite torque signal reveals that the induced moment is not co-linear with the applied field, consistent with the finite slope observed at these fields in Figure 3.4C. This shows that in the phase above H^* the induced magnetization along the field direction is not yet saturated (the value is well below the expected saturated Ir moment of $\sim 1\mu_B$ for $J_{eff} = 1/2$). The angular dependence of both the slope of the linear regime and the kink field H^* , exhibit an order of magnitude anisotropy with field orientation (Figure 3.4D and 3.4E). Such strong anisotropy in a spin- $1/2$ system highlights the strong orbital character arising from the spin-orbit coupling, again in contrast to spin- $1/2$ Heisenberg anti-ferromagnetism [91].

3.3 Discussion

There is a very interesting connection between the layered honeycomb Li₂IrO₃ and the polytype studied here. The ${}^{\mathcal{H}}\langle 1 \rangle$ -Li₂IrO₃ is distinguished by its c -axis bond, which either preserves or rotates away from a given honeycomb plane (see Figure 3.5A and Figure A.7); in the case that all the bonds preserve the same plane, the resulting structure is the layered honeycomb system. Further polytypes can be envisioned by tuning the c -axis extent of the honeycomb plane before switching to the other orientation (see Figure 3.5B). We denote each polytype ${}^{\mathcal{H}}\langle N \rangle$ -Li₂IrO₃, where ${}^{\mathcal{H}}\langle N \rangle$ refers to the number of complete honeycomb rows (see Figure 3.5B and Figure A.8), and the family as the “harmonic”-honeycombs, so named

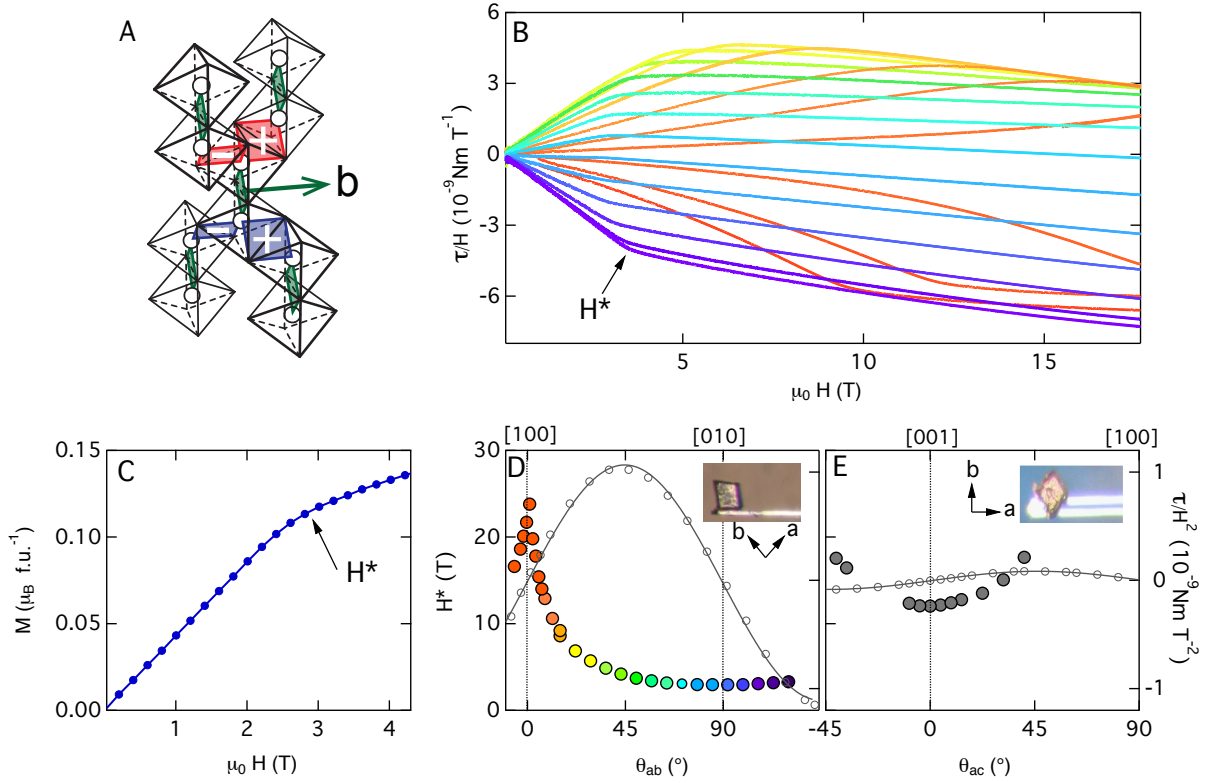


Figure 3.4: **Low temperature magnetic properties of the $\mathcal{H}\langle 1 \rangle$ - Li_2IrO_3 .** (A) The Ir-O₂-Ir planes defining three orthogonal directions of the spin-exchange, one parallel to \hat{b} and the other two parallel to $\hat{a} \pm \hat{c}$, labelled + and - (\hat{a} is the unit vector along \mathbf{a}). This connects to the notation used to describe the Kitaev Hamiltonian in SI III. (B) Torque signal τ divided by the applied magnetic field H at a temperature of 1.5 K, illustrating a linear low-field dependence and a kink at H^* , which is strongly angle dependent (colors correspond to angles shown in (D)). (C) Magnetization vs magnetic field applied along the b -axis at a temperature of 15 K. (D) & (E) The angle dependence $\theta_{ab/ac}$ of the kink field H^* of the ordered state (full circles, left axes) with respect to the crystallographic axes a, b and c . H^* is correlated to the magnetization anisotropy α_{ij} (open circles, right axes) indicating a common moment at H^* in all field orientations.

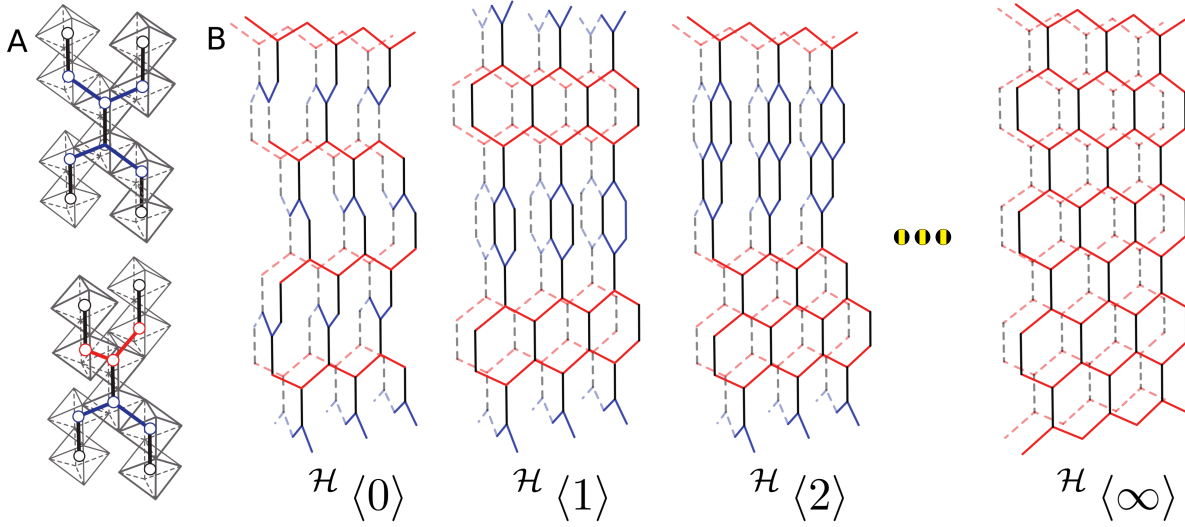


Figure 3.5: **Introducing the harmonic honeycomb series.** (A) Two kinds of c -axis bonds (black links) in the harmonic honeycomb family $\mathcal{H}\langle N \rangle$ - Li_2IrO_3 are shown, one linking within a honeycomb plane (for example blue to blue, top) and one that rotates between honeycomb planes (for example red to blue, bottom). For undistorted octahedra, these links are locally indistinguishable, as can be observed by the local coordination of any Ir atom (also see Figure 3.3A). (B) These building blocks can be used to construct a series of structures. The end members include the theoretical $N = 0$ ‘hyper-honeycomb’ [160, 127, 146] and the $N = \infty$ layered honeycomb [189]. Here N counts the number of complete honeycomb rows in a section along the c -axis before the orientation of the honeycomb plane switches.

to invoke the periodic connection between members. The layered compound, $\mathcal{H}\langle \infty \rangle$ - Li_2IrO_3 [189] and the hypothetical hyper-honeycomb structure, $\mathcal{H}\langle 0 \rangle$ - Li_2IrO_3 [127] are the end members of this family (see also SI IV). The edge-sharing geometry of the octahedra preserves the essential ingredients of the Kitaev model and this is universal for this family of polytypes. Each structure is a material candidate for the realization of a 3D spin liquid in the pure Kitaev limit (see Appendix A and for $\mathcal{H}\langle 0 \rangle$ - Li_2IrO_3 see Refs. [160, 146, 127]).

Finally, we speculate on the consequences and feasibility of making other members of the $\mathcal{H}\langle N \rangle$ - Li_2IrO_3 family. Both the layered $\mathcal{H}\langle \infty \rangle$ - Li_2IrO_3 and the $\mathcal{H}\langle 1 \rangle$ - Li_2IrO_3 are stable structures, implying that intermediate members may be possible under appropriate synthesis conditions. The building blocks shown in Figure 3.5A connect each member of the harmonic honeycomb series in a manner that is analogous to how corner sharing octahedra connect the Ruddlesden-Popper (RP) series. Indeed, despite the fact that members of the RP family are locally identical in structure, they exhibit a rich variety of exotic electronic states; including superconductivity and ferromagnetism in the ruthenates [169, 99], multiferroic behavior in the titanates [37], colossal magnetoresistance in the manganites [171] and high temperature

superconductivity in the cuprates [148]. The harmonic honeycomb family is a honeycomb analogue of the RP series, and its successful synthesis could similarly create a new frontier in the exploration of strongly spin-orbit coupled Mott insulators.

3.4 Methods

Synthesis

Powders of IrO_2 (99.99% purity, Alfa-Aesar) and Li_2CO_3 (99.9% purity, Alfa-Aesar) in the ratio of 1:1.05, were reacted at 1000°C , then reground and pelletized, taken to 1100°C and cooled slowly down to 800°C . The resulting pellet was then melted in LiOH in the ratio of 1:100 between $700\text{--}800^\circ\text{C}$ and cooled at 5°C/hr to yield single crystals of ${}^{\mathcal{H}}(1)\text{-Li}_2\text{IrO}_3$. The crystals were then mechanically extracted from the growth. Single crystal x-ray refinements were performed using a Mo-source Oxford Diffraction Supernova diffractometer. Please see Appendix A for a detailed analysis.

Magnetic measurements

Two complementary techniques were used to measure the magnetic response of single crystals of ${}^{\mathcal{H}}(1)\text{-Li}_2\text{IrO}_3$; a SQUID magnetometer was employed to measure magnetization and a piezoresistive cantilever to directly measure the magnetic anisotropy. The magnetization measurements were performed in a Cryogenic S700X. Due to the size of the single crystals, the high temperature magnetization was near the noise floor of the experiment. Nevertheless, SQUID measured anisotropies at high temperatures were close to those measured by torque, with absolute values of $\chi_a(300\text{K}) = 0.0021\mu_{\text{B}}/\text{T}$ f.u. and $\chi_b = 0.0024\mu_{\text{B}}/\text{T}$ f.u.. Curie-Weiss fits to the linear portion of the susceptibility yielded an effective moment of $\mu_{\text{eff}} = 1.6(1)\mu_{\text{B}}$, consistent with $J_{\text{eff}} = 1/2$ magnetism. However, the SQUID resolution was not adequate to determine the susceptibilities anisotropy at high temperature to the accuracy we required (see Figure 3.2). To resolve the magnetic anisotropy throughout the entire temperature range, we employed torque magnetometry, where a single crystal could be precisely oriented. Although the piezoresistive cantilever technique is sensitive enough to resolve the anisotropy of a $\sim 50\mu\text{m}^3$ single crystal, and hence ordering of susceptibilities at high temperature, the absolute calibration of the piezoresistive response of the lever leads to a larger systematic error than in the absolute value of the susceptibility measured using the SQUID at low temperature. To reconcile these systematic deficiencies in both techniques, the torque data was scaled by a single common factor of the order of unity, for all field orientations and temperatures, so as to give the best agreement with the differences between the low temperature susceptibilities as measured using the SQUID. The rescaled torque data was thus used to resolve the magnetic anisotropy at high temperature where the susceptibility is smallest.

Torque magnetometry was measured on a $50 \times 100 \times 40\mu\text{m}^3$ single crystal (5.95×10^{-9} mol Ir) employing a piezoresistive micro-cantilever [183] that measures mechanical stress as

the crystal flexes the lever to try to align its magnetic axes with the applied field. The mechanical strain is measured as a voltage change across a balanced Wheatstone Bridge and can detect a torque signal on the order of 10^{-13} Nm. Torque magnetometry is an extremely sensitive technique and is well suited for measuring very small single crystals. The cantilever was mounted on a cryogenic goniometer to allow rotation of the sample with respect to magnetic field without thermal cycling. The lever only responds to a torque perpendicular to its long axis and planar surface, such that the orientation of the crystal on the lever and the plane of rotation in field could be chosen to measure the principal components of anisotropy, α_{ij} . The low temperature anisotropy was confirmed on several similar sized single crystals. However to measure $\alpha_{ij} = \chi_i - \chi_j$ between 1.5 K and 250 K, three discrete planes of rotation for the same crystal were used. When remounting the sample to change the plane of rotation, care was taken to maintain the same center of mass position of the crystal on the lever to minimize systematic changes in sensitivity. Magnetic fields were applied using a 20 T superconducting solenoid and a 35 T resistive solenoid at the National High Magnetic Field Laboratory, Tallahassee, FL.

Chapter 4

Ab initio Studies of Structural and Energetic Trends in the Harmonic Honeycomb Iridates

Edge-sharing iridates present an exciting opportunity to study the competition of Mott insulator physics and strong spin-orbit coupling. These interactions also make these materials a challenge to study computationally. Harmonic honeycomb iridates are a recently discovered homologous series of stoichiometrically identical structures that host anisotropic magnetism and exotic spin ordering. We use density functional theory (DFT) to investigate structural and energetic trends in Li_2IrO_3 and Na_2IrO_3 harmonic honeycomb iridates. We predict the formation energies and distortion of as-yet unsynthesized series members to be degenerate for identical composition. We also demonstrate that DFT can accurately predict the structure of Li_2IrO_3 harmonic honeycomb iridates, but only if we account for strong spin-orbit coupling and electron-electron correlation at the level of a Hubbard U in these materials.

4.1 Introduction

Iridates have the ingredients believed to be necessary to host a spin-liquid state: crystal field splitting to create low spin states, strong spin-orbit interactions to couple spin and lattice degrees of freedom, and frustrated lattices to foster anisotropic magnetic interactions [35]. Systems as complex as iridates, it is invaluable to have a series of structures one can compare and tune to understand the ingredients driving local and long-range interactions.

The harmonic honeycomb iridates are a recently discovered series of crystal structures that are three-dimensional analogs to the two-dimensional honeycomb lattice [172]. The materials are spin-orbit Mott insulators, where strong spin-orbit coupling and electronic correlation result in the opening of a gap [172, 242, 45, 44]. Like iridates on kagome, hyperkagome, pyrochlore and honeycomb lattices, the harmonic honeycombs are geometrically frustrated which may give rise to new physics leading to a spin liquid state [35]. Direct

evidence of bond-directional interactions in layered honeycomb Na_2IrO_3 , suggest that a spin liquid state may be achievable in the harmonic honeycomb iridates if anisotropic interactions can be tuned through structural distortions or chemical substitutions [115].

The harmonic honeycomb structures are pictured in Figure 4.1. We use $^{\mathcal{H}}\langle\#\rangle$ to designate a particular structure, where $\#$ is the number of rows of completed hexagons along the orthorhombic c direction between alternating bonding planes. Single crystals of Li_2IrO_3 $^{\mathcal{H}}\langle 0\rangle$, Li_2IrO_3 $^{\mathcal{H}}\langle 1\rangle$, and Na_2IrO_3 $^{\mathcal{H}}\langle\infty\rangle$ and polycrystalline samples of Li_2IrO_3 $^{\mathcal{H}}\langle\infty\rangle$ have been synthesized [190, 231, 172, 242]. The magnetic order and anisotropy of these materials is sensitive to distortion and structure dimensionality¹. Not yet synthesized members may have the environment necessary to host exotic phases and can lend important clues to understand these materials' complex magnetic interactions.

Using density functional theory (DFT), we investigate whether as-yet unsynthesized members are energetically favorable and examine variations in magnetically relevant bond lengths and angles across the series. We find we can accurately predict these values by including spin-orbit coupling and Hubbard U-type corrections for Ir 5d orbitals in our calculations. Li_2IrO_3 is more sensitive to the inclusion of these interactions than Na_2IrO_3 due the Ir-Ir bond lengths being 5% shorter in Li_2IrO_3 than Na_2IrO_3 . We use the virtual crystal approximation (VCA) to demonstrate this sensitivity.

Our calculations indicate the harmonic honeycombs of Li_2IrO_3 are nearly degenerate in formation energy for various spin-orderings, likewise for Na_2IrO_3 . For a given alkali, the difference in energetics between phases corresponding to early members of this series do not exceed 20 meV per formula unit, small compared to the growth temperature of these materials of approximately 1300 K (112 meV). Thus, the lack of experimental evidence of other structures may not be an issue of energetics but of kinetics or growth conditions. For a given alkali, there is no notable change of Ir-Ir bond length or Ir-O-Ir bond angles across the relaxed harmonic honeycomb series. According to Ref. [120], the strength of local anisotropic interactions is sensitive to distortions of the iridium oxide octahedra. Since our calculations show that for a given composition these distortions are uniform across the series, differences in magnetism of the harmonic honeycomb iridates for a given alkali may indicate sensitivity to long-range structure. Our calculations suggest that the harmonic honeycomb iridates may provide a path for understanding and tuning long-range interactions.

4.2 Calculation Details

Our DFT calculations are performed using the Vienna Ab initio Software Package (VASP) with a plane wave basis [135, 137, 136]. We use the generalized gradient approximation

¹ Li_2IrO_3 $^{\mathcal{H}}\langle 0\rangle$, $^{\mathcal{H}}\langle 1\rangle$ and $^{\mathcal{H}}\langle\infty\rangle$ have been measured or postulated to have incommensurate spiral magnetic orders [44, 45, 209]. Na_2IrO_3 $^{\mathcal{H}}\langle\infty\rangle$ has a comparatively simple, commensurate “zigzag” collinear order [155, 64, 270]. The magnetic anisotropy of Li_2IrO_3 $^{\mathcal{H}}\langle 0\rangle$ and $^{\mathcal{H}}\langle 1\rangle$ dramatically reorders below the spin ordering temperature while the magnetic anisotropy of polycrystalline Li_2IrO_3 $^{\mathcal{H}}\langle\infty\rangle$ and single crystal Na_2IrO_3 $^{\mathcal{H}}\langle\infty\rangle$ do not exhibit this change across their transition temperature [172, 242, 231, 233, 55].

functional of Perdew, Burke, and Ernzerhof (PBE) [193], PAW pseudopotentials [46, 138] and an energy cutoff of 520 eV. Monkhorst k-point meshes of $9 \times 9 \times 5$, $9 \times 9 \times 3$, $9 \times 9 \times 1$, and $9 \times 9 \times 9$ are used for the ${}^h \langle 0 \rangle$, ${}^h \langle 1 \rangle$, ${}^h \langle 2 \rangle$ and ${}^h \langle \infty \rangle$ structures, respectively. Relaxations are performed with spin-orbit coupling and Hubbard U corrections to localized Ir 5d states following the approach in Ref. [81], unless otherwise specified, and allow unconstrained non-collinear magnetism as described in Ref. [108, 107]. When including these interactions during optimizations, non-collinear spin and structural contributions to the total energy have to be calculated iteratively, making these calculations computationally expensive.

Unit cell and ionic position relaxations are initialized with idealized harmonic honeycomb structures, where iridium oxide octahedra are undistorted such that Ir-O-Ir bond angles are 90° and all Ir-Ir bond lengths are taken to be equal and derived from average experimental values. Relaxations are not restricted to the spacegroup of the initial structure since spinor wavefunctions used in relativistic calculations transform under the appropriate spin spacegroup determined by the magnetic order [217]. Previous studies of the harmonic honeycomb iridates do not indicate structural transitions at low temperature [172, 233, 64]. Thus, we report re-symmetrized relaxed structures for ease of comparison using the Materials Project Python package (pymatgen) [187]. We confirm that there is no significant change in total energy between the relaxed and re-symmetrized structures. Relaxation results are converged such that Hellmann-Feynman forces on individual atoms in any direction are less than $0.01 \text{ eV}/\text{\AA}$, the energy difference between self-consistent electronic steps is less than 10^{-5} eV , and that the absolute value of the external pressure, computed as the trace of the stress tensor, is less than 0.5 kB . When referring to the level of theory of the calculation, we will use abbreviations to denote the functional used (in this case, PBE) and whether not spin-orbit coupling (SOC) and a Hubbard U correction to the 5d iridium orbitals (U) is included.

To relax the series for structural and energetic comparisons, we use PBE+SOC+U. The values for onsite U correction used in studying iridates spans from 0 to 4 eV, with most calculations using $U = 1.5 - 3 \text{ eV}$ [168, 272, 184, 155, 161, 150]. We find that lattice parameters, bond angles, and bond lengths of ${}^h \langle 1 \rangle \text{ Li}_2\text{IrO}_3$ are insensitive to U provided that U was at least 0.5 eV. We use $U = 1.5 \text{ eV}$ for all calculations, unless otherwise specified, to ensure that our calculations maintain a gap during relaxations and permit total energy comparisons between series members. Lattice parameters, bond lengths, and distortions of PBE+SOC+U relaxations are insensitive to initial magnetic configuration. Because of this, we initialized structural relaxations with a randomized spin ordering with a normalized magnetic moment of $1 \mu_B$ per Ir.

To evaluate different approximations to DFT for these systems, we compare (i) the ratio of lattice parameters, (ii) Ir-Ir bond lengths, and (iii) Ir-O-Ir bond angles with experimental values where possible. The first two metrics inform us whether there has been an anisotropic relaxation of the unit cell. Experimentally synthesized structures have Ir-Ir bond lengths that vary by less than $\pm 0.01 \text{ \AA}$. Thus, deviations from this trend indicate inaccuracies of a given approximation.

The third metric is a direct measurement of the distortion of the iridium oxide octahedra, see Figure 4.1(b-e). The distortion mode of experimental structures from idealized harmonic

honeycomb lattices is identical across the series for both Li_2IrO_3 and Na_2IrO_3 and preserves the spacegroup of the undistorted structure. The amplitude of the distortion is greater in Na_2IrO_3 than Li_2IrO_3 . The distortion is dominated by displacements of oxygen and alkali atoms and changes in the Ir-O-Ir bond parameterize the distortion of the iridium oxide octahedra.

4.3 DFT Results

Tables 4.1, 4.2, 4.3, and 4.4 show lattice parameters and Wyckoff positions for Li_2IrO_3 and Na_2IrO_3 $^{\mathcal{H}}\langle\infty\rangle$, $^{\mathcal{H}}\langle 0\rangle$, $^{\mathcal{H}}\langle 1\rangle$, and $^{\mathcal{H}}\langle 2\rangle$ relaxed with PBE+SOC+U(=1.5 eV).

The lattice parameters for Li_2IrO_3 and Na_2IrO_3 structures relaxed with PBE+SOC+U differ <2% from experimental values, out-performing other approximations tested. Our results for PBE+SOC+U for Na_2IrO_3 $^{\mathcal{H}}\langle\infty\rangle$ and Li_2IrO_3 $^{\mathcal{H}}\langle\infty\rangle$ agree with VASP GGA+SOC+U calculations in Ref. [161], where $U = 3.0$ eV. Ref. [161] similarly noted that GGA+SOC+U gave better agreement with lattice parameters than GGA.

From our structural relaxations of the atomic positions and volume of idealized unit cells of $^{\mathcal{H}}\langle 0\rangle$, $^{\mathcal{H}}\langle 1\rangle$, $^{\mathcal{H}}\langle 2\rangle$ and $^{\mathcal{H}}\langle\infty\rangle$ Li_2IrO_3 and Na_2IrO_3 , for a given alkali, we find no notable change of bond lengths and bond angles across the series. The distortion of the Ir-O-Ir bond angle is driven by the choice of alkali metal (Li or Na). The ratio of the radii of sodium and iridium is further from unity than the ratio of radii of lithium and iridium, thus causing greater distortion of the oxygen octahedra. Experimentally, angles between $92 - 97^\circ$ are seen in Li_2IrO_3 $^{\mathcal{H}}\langle 0\rangle$ and Li_2IrO_3 $^{\mathcal{H}}\langle 1\rangle$. Our calculations find angular variations of only one degree around average values of 94° for Li_2IrO_3 and 100° for Na_2IrO_3 .

The uniformity of distortion and bond lengths across the series results in similar band structures and densities of states for members of identical composition. For example, Figure 4.2 shows very little variation in the non-magnetic band structure and density of states across the series². A non-vanishing magnetic order is required to open up a gap in the harmonic honeycomb iridates. Figure 4.3 shows the nonmagnetic and ferromagnetic along c density of states of Na_2IrO_3 $^{\mathcal{H}}\langle\infty\rangle$ and Li_2IrO_3 $^{\mathcal{H}}\langle\infty\rangle$ relaxed with PBE+SOC+U. While the non-magnetic band structure is metallic, a magnetic order is able to open the gap for both $^{\mathcal{H}}\langle\infty\rangle$ structures.

Comparing the total formation energy of members of the series is challenging due to the complexity of incommensurate magnetic orders. In this chapter, we restrict our comparison to simple collinear orders: ferromagnetic and Néel antiferromagnetic (nearest neighbors have opposite magnetization) along $^{\mathcal{H}}\langle 0\rangle$ lattice parameters a , b , and c and non-magnetic. These magnetic orders map identically and unambiguously on inequivalent structures.

We apply a penalty term to the total energy functional to constrain the spin direction for a given order as described in Ref. [158] and implemented in VASP. For Ir, we used the an integration sphere of radius 1.423 Å, equalling the Wigner-Seitz radius for elemental Ir.

²Band structures of the harmonic honeycombs can be found in the S.I.

		$\mathcal{H}(\infty)$ Li_2IrO_3						$\mathcal{H}(\infty)$ Na_2IrO_3									
		Experiment [190]			PBE+SOC+U			Experiment [64]			PBE+SOC+U						
		a	b	c	a	b	c	a	b	c	a	b	c				
Spacegroup:		α	β	γ	α	β	γ	α	β	γ	α	β	γ				
C2/m (12)		90.00°	109.76°	90.00°	90.00°	109.78°	90.00°	90.00°	109.04°	90.00°	90.00°	109.33°	90.00°				
Atom	Site	x	y	z	x	y	z	x	y	z	x	y	z				
Li1/Na1	2a	0	0	0	0	0	0	0	0	0	0	0	0				
Li2/Na2	2d	0.5	0	0.5	0.5	0	0.5	0.5	0	0.5	0.5	0	0.5				
Li3/Na3	4h	0	0.191	0.5	0	0.161	0.5	0	0.160	0.5	0	0.160	0.5				
Ir1	4g	0	0.333	0	0	0.333	0	0	0.333	0	0	0.333	0				
O1	8j	0.248	0.816	0.241	0.252	0.826	0.234	0.252	0.822	0.211	0.252	0.817	0.206				
O2	8i	0.256	0	0.788	0.268	0	0.764	0.289	0	0.796	0.295	0	0.792				
						Tolerance: 5.1E-03 Å						Tolerance: 4.4E-03 Å					

Table 4.1: Comparison of experimental and DFT (PBE+SOC+U) lattice parameters and Wyckoff positions for $\mathcal{H}(\infty)$ Li_2IrO_3 and $\mathcal{H}(\infty)$ Na_2IrO_3 . Experimental Li_2IrO_3 structure is refined from powder diffraction data [190]. Position tolerance required to symmetrize DFT structures obtained from PBE+SOC+U is given below Wyckoff positions.

		$\mathcal{H} \langle 0 \rangle \text{Li}_2\text{IrO}_3$						$\mathcal{H} \langle 0 \rangle \text{Na}_2\text{IrO}_3$						
		Experiment [45]			PBE+SOC+U			PBE+SOC+U			PBE+SOC+U			
		a	b	c	a	b	c	a	b	c	a	b	c	
Spacegroup:		5.89	8.43	17.79	5.96	8.55	17.99	6.48	9.10	18.99				
Fddd (70)		α	β	γ	α	β	γ	α	β	γ	α	β	γ	
		90.00°	90.0°	90.00°	90.00°	90.0°	90.00°	90.00°	90.0°	90.00°	90.00°	90.0°	90.00°	
Atom	Site	x	y	z	x	y	z	x	y	z	x	y	z	
Li1/Na1	16g	0.125	0.125	0.875	0.125	0.125	0.877	0.125	0.125	0.880	0.125	0.125	0.880	
Li2/Na2	16g	0.125	0.125	0.042	0.125	0.125	0.045	0.125	0.125	0.046	0.125	0.125	0.046	
Ir1	16g	0.125	0.125	0.709	0.125	0.125	0.708	0.125	0.125	0.709	0.125	0.125	0.709	
O1	16e	0.856	0.125	0.125	0.863	0.125	0.125	0.831	0.125	0.125	0.831	0.125	0.125	
O2	32h	0.622	0.367	0.039	0.633	0.364	0.038	0.647	0.352	0.034	0.647	0.352	0.034	
							Tolerance: 2.3E-02 Å							
							Tolerance: 5.1E-03 Å							

Table 4.2: Comparison of experimental and DFT (PBE+SOC+U) lattice parameters and Wyckoff positions for $\mathcal{H} \langle 0 \rangle \text{Li}_2\text{IrO}_3$ and $\mathcal{H} \langle 0 \rangle \text{Na}_2\text{IrO}_3$. Position tolerance required to symmetrize DFT structures obtained from PBE+SOC+U is given below Wyckoff positions.

		$\mathcal{H} \langle 1 \rangle \text{Li}_2\text{IrO}_3$						$\mathcal{H} \langle 1 \rangle \text{Na}_2\text{IrO}_3$									
		Experiment [172]			PBE+SOC+U			PBE+SOC+U			PBE+SOC+U						
		a	b	c	a	b	c	a	b	c	a	b	c				
Spacegroup:		5.91	8.45	17.84	5.96	8.53	18.02	6.48	9.10	19.02							
Cccm (66)		α	β	γ	α	β	γ	α	β	γ	α	β	γ				
		90.00°	90.0°	90.00°	90.00°	90.0°	90.00°	90.00°	90.0°	90.00°	90.00°	90.0°	90.00°				
Atom	Site	x	y	z	x	y	z	x	y	z	x	y	z				
La1/Na1	8j	0	0.5	0.333	0	0.50	0.331	0	0.50	0.330	0	0.50	0.330				
La2/Na2	8k	0.75	0.25	0.25	0.75	0.25	0.248	0.75	0.25	0.245	0.75	0.25	0.245				
La3/Na3	8k	0.75	0.25	0.917	0.75	0.25	0.920	0.75	0.25	0.920	0.75	0.25	0.920				
La4/Na4	4c	0.5	0.5	0.5	0.5	0.5	0.5	0.5	0.5	0.5	0.5	0.5	0.5				
La5/Na5	4d	0.5	0	0	0.5	0	0	0.5	0	0	0.5	0	0				
Ir1	8k	0.25	0.25	0.084	0.25	0.25	0.083	0.25	0.25	0.084	0.25	0.25	0.084				
Ir2	8i	0.5	0.5	0.167	0.5	0.5	0.167	0.5	0.5	0.166	0.5	0.5	0.166				
O1	16m	0.773	0.515	0.087	0.742	0.510	0.087	0.729	0.523	0.092	0.729	0.523	0.092				
O2	8g	0.722	0.5	0.25	0.737	0.5	0.25	0.706	0.5	0.25	0.706	0.5	0.25				
O3	8l	0.006	0.262	0	0.014	0.252	0	0.044	0.252	0	0.044	0.252	0				
O4	16m	0.487	0.262	0.163	0.493	0.260	0.163	0.478	0.273	0.159	0.478	0.273	0.159				
						Tolerance: 2.6E-02 Å						Tolerance: 1.1E-02 Å					

Table 4.3: Comparison of experimental and DFT (PBE+SOC+U) lattice parameters and Wyckoff positions for $\mathcal{H} \langle 1 \rangle \text{Li}_2\text{IrO}_3$ and $\mathcal{H} \langle 1 \rangle \text{Na}_2\text{IrO}_3$. Position tolerance required to symmetrize DFT structures obtained from PBE+SOC+U is given below Wyckoff positions.

		$\mathcal{H} \langle 2 \rangle \text{Li}_2\text{IrO}_3$			$\mathcal{H} \langle 2 \rangle \text{Na}_2\text{IrO}_3$		
		PBE+SOC+U			PBE+SOC+U		
		a	b	c	a	b	c
Spacegroup:		5.96	8.52	54.12	6.48	9.10	57.07
C _{ccm} (66)		α	β	γ	α	β	γ
		90.00°	90.0°	90.00°	90.00°	90.0°	90.00°
Atom	Site	x	y	z	x	y	z
Li1/Na1	16g	0.125	0.125	0.874	0.125	0.125	0.873
Li2/Na2	16g	0.125	0.125	0.042	0.125	0.125	0.042
Li2/Na3	16g	0.125	0.125	0.432	0.125	0.125	0.433
Li3/Na4	16g	0.125	0.125	0.485	0.125	0.125	0.485
Li4/Na5	16g	0.125	0.125	0.708	0.125	0.125	0.708
Li5/Na6	16g	0.125	0.125	0.652	0.125	0.125	0.652
Ir1	16g	0.125	0.125	0.097	0.125	0.125	0.097
Ir2	16g	0.125	0.125	0.986	0.125	0.125	0.986
Ir3	16g	0.125	0.125	0.931	0.125	0.125	0.930
O1	32h	0.881	0.115	0.013	0.896	0.102	0.072
O2	32h	0.882	0.116	0.071	0.896	0.102	0.011
O3	32h	0.883	0.117	0.904	0.897	0.102	0.905
O4	32h	0.891	0.123	0.292	0.919	0.124	0.292
O5	16e	0.890	0.125	0.125	0.919	0.125	0.125
				Tolerance: 1.9E-0.2 Å	Tolerance: 1.0E-03 Å		

Table 4.4: Comparison of experimental and DFT (PBE+SOC+U) lattice parameters and Wyckoff positions for $\mathcal{H} \langle 2 \rangle \text{Li}_2\text{IrO}_3$ and $\mathcal{H} \langle 2 \rangle \text{Na}_2\text{IrO}_3$. Position tolerance required to symmetrize DFT structures obtained from PBE+SOC+U is given below Wyckoff positions.

The total moment on each site depends on the magnetic order and ranges from 0.2-0.4 μ_B for Li_2IrO_3 and 0.14-0.26 μ_B for Na_2IrO_3 . For a given magnetic order, the magnetic moment per site varies less than 0.02 μ_B across the series, thus we do not constrain the magnitude of the magnetic moments. The magnetic moment per site for Li_2IrO_3 structures has been measured to be 0.471 μ_B for ${}^{\mathcal{H}}\langle 0 \rangle$ [45]. Ref. [270] measured the magnetic moment per site for Na_2IrO_3 ${}^{\mathcal{H}}\langle \infty \rangle$ to be 0.22 μ_B .

Our iridium site magnetic moments for Na_2IrO_3 are approximately 0.1 μ_B smaller than those calculated in Ref. [166]. In VASP, an integration sphere radius is defined for each atomic species in the calculation. Any magnetic moment within that radius is then projected onto local atomic orbitals for a given site. Thus, the differences between Ref. [166] and our calculations of the local magnetic moment may be due to integration scheme. There is also an additional 10% contribution from the oxygen sites, as expected for itinerant magnetism, which we do not add to the total Ir magnetic moment. We do agree with Ref. [166] that we see roughly a halving of Ir magnetic moments between ferromagnetic and antiferromagnetic orders.

The reason for the disparity between the magnetic moments calculated for Li_2IrO_3 and experiment may be due to the fact that we are imposing magnetic structures (ferromagnetic and Néel antiferromagnetic) that are not the ground state (incommensurate spiral). As shown in Ref. [166], the magnitude of magnetic moment per iridium site is sensitive to magnetic order.

The relaxed Li_2IrO_3 structures vary by less than 5 meV and the relaxed Na_2IrO_3 structures vary by less than 20 meV, respectively. None of the Li_2IrO_3 or Na_2IrO_3 structures are calculated to be significantly lower in energy in comparison to other series members. Na_2IrO_3 ${}^{\mathcal{H}}\langle 0 \rangle$ is lower in energy for these particular spin orders in comparison to the other series members. Without comparing magnetic ground states, it may be difficult to differentiate whether DFT predicts an energetic favorite or if the structures are degenerate. Total energy differences between collinear orders do not provide substantial insight into the ground state magnetic orders due to their simplicity compared to experimentally measured ground states. However, the differences in total energy between calculated magnetic orders is small, varying less than 10 meV for a given structure. Tables of total energies for given magnetic orders are included in the Appendix B.

Importance of SOC and U for relaxations

We determine the sensitivity of our structural relaxations to the level of theory used in our DFT calculations by performing relaxations of idealized structures of Li_2IrO_3 and Na_2IrO_3 with different levels of theory (PBE, PBE+U, PBE+SOC, PBE+SOC+U). We find that for Li_2IrO_3 , it is necessary to use PBE+SOC with $U \geq 0.5$ eV to obtain structures with Ir-Ir bond lengths compatible with experiment. In contrast, Na_2IrO_3 structures are less sensitive to changes in the level of theory; however, PBE+SOC+U gives the best agreement with experiment.

Li_2IrO_3 relaxations with PBE+SOC+U (<0.5 eV), PBE+SOC, PBE+U (=0,1.5,3,6 eV), and PBE result in asymmetric Ir-Ir bond lengths (differing as much as 0.5 Å), disparate Ir-O-Ir bond angles and nonmagnetic orders as the lowest energy magnetic order by at least 100 meV per formula unit. 3D Li_2IrO_3 structures when relaxed with these levels of theory, compress along the orthorhombic c lattice direction which opens a gap in the nonmagnetic band structure, see Table B.1 for converged lattice parameters for Li_2IrO_3 and Na_2IrO_3 $^{\mathcal{H}}\langle 1 \rangle$ for a given level of theory. Relaxations of Li_2IrO_3 $^{\mathcal{H}}\langle \infty \rangle$ with these levels of theory resulted in structures that could not be symmetrized back into C2/m, even with a symmetry tolerance of 1 Å.

We believe the cause of this anisotropic compression in these cases is due to the need to break the degeneracy of the t_{2g} 5d-orbitals. In Na_2IrO_3 the ratio of Na and Ir atomic radii are sufficiently different as to induce large distortions. In this case, the octahedra are sufficiently distorted as to easily break the degeneracy of the t_{2g} 5d-orbitals. Since, Li and Ir have more similar radii, there is less distortion from purely electrostatic forces so distortion is additionally incurred through bending of the opposite atoms of the octahedra. This distortion easily induces a gap in Li_2IrO_3 band structure. The distortion lessens as levels of theory are introduced that break the t_{2g} degeneracy.

Virtual Crystal Approximation

We attribute the difference in sensitivity of Li_2IrO_3 and Na_2IrO_3 to level of theory to the differences in average Ir-Ir separation; in particular, the Ir-Ir sites, which are bridged by oxygen atoms, are 5% further apart for Na_2IrO_3 than in Li_2IrO_3 . This larger separation for Na_2IrO_3 in this case reduces superexchange interactions through a delocalization of the Ir 5d electrons via decreased hybridization with O p electrons, reducing the importance of Hubbard U and SOC corrections to spin-polarized PBE calculations.

We test this hypothesis by performing relaxations of $^{\mathcal{H}}\langle 0 \rangle$ with “hybrid” Li-Na atoms to approximate idealized doping (by continuously changing the alkali atomic radius) using the Virtual Crystal Approximation (VCA) implemented in VASP. VCA uses a linear combination of existing pseudopotentials to create a “new” atom, mimicking a solid solution with a given stoichiometry. For example, if one wishes to calculate the structure of 50% Li and 50% Na, each alkali metal site would be occupied 50% by a Li atom and 50% by a Na atom. During a relaxation, the linear combination of the forces experienced on a given site by the different occupying atomic species is used to calculate the next structure.

VCA approximates isotropic doping – meaning that all sites are equally likely to be replaced by the substituting ion. Experimentally, this is known to not be the case for the harmonic honeycomb iridates. Ref. [161] investigated the change of lattice parameters and preference of cation substitution in $^{\mathcal{H}}\langle \infty \rangle (\text{Na}_{1-x}\text{Li}_x)_2\text{IrO}_3$ and find that Li atoms anisotropically replace cation sites, causing local distortions. Thus, our VCA calculations should not be considered predictions of lattice parameters and bond lengths for doped materials.

Ref. [213] measured that for approximately equivalent Ir-Ir bond lengths, changes in the Ir-O-Ir bond angle due to distortion (or disorder) from doping can have a dramatic effect on

magnetic order.

We perform VCA calculations with PBE+U(=0,1.5,3,6 eV) and PBE+SOC+U(=3 eV) on idealized $(\text{Li}_{1-x}\text{Na}_x)_2\text{IrO}_3$ ³. For PBE+U for both $(\text{Li}_{1-x}\text{Na}_x)_2\text{IrO}_3$, we find a sharp doping transition at which the $^{\mathcal{H}}\langle 0 \rangle$ c axis collapses, resulting in asymmetric Ir-Ir bonds. This transition moves closer and closer to pure Li doping with increasing U, indicating that it is sensitive to the localization of the Ir 5d orbitals, see Figure 4.4. For Li_2IrO_3 ³, PBE+U(=6 eV) gives Ir-Ir bond lengths that differ by greater than ± 0.1 Å while PBE+SOC+U(=3 eV) gives Ir-Ir bond lengths that differ by less than ± 0.01 Å, see Figure 4.5.

We also performed VCA calculations with PBE+U(=0,1.5) on idealized $(\text{Li}_{1-x}\text{Na}_x)_2\text{RhO}_3$ ³ and saw similar discontinuities in plots of the Ir-Ir bond lengths as a function of doping. These discontinuities occurred at lower doping than for $(\text{Li}_{1-x}\text{Na}_x)_2\text{IrO}_3$ but showed the same shift to lower doping when a higher Hubbard U correction was applied.

4.4 Conclusion

Despite the complexity of the harmonic honeycomb iridates, our calculations accurately reproduce experimental structures and predict yet to be synthesized series members by including spin-orbit coupling and using Hubbard U corrections for iridium 5d orbitals. Including these interactions is crucial for accurately calculating properties of Li_2IrO_3 , although less so than Na_2IrO_3 . Using these calculations, we assess trends in formation energetics and structural distortion in the harmonic honeycomb iridates. These studies provide concrete insight helpful to experimental efforts. Our calculations demonstrate the importance of systematically testing the level of ab initio theory needed to accurately capture basic properties of complex material systems. The workflow we present can be used for future ab initio studies to investigate the effects of strain and pressure on the magnetism of the harmonic honeycomb iridates.

³PBE+SOC+U(=1.5 eV) was insufficient to produce symmetric Ir-Ir bonds for 5% Na and 10% Na so we used U=3.0 eV

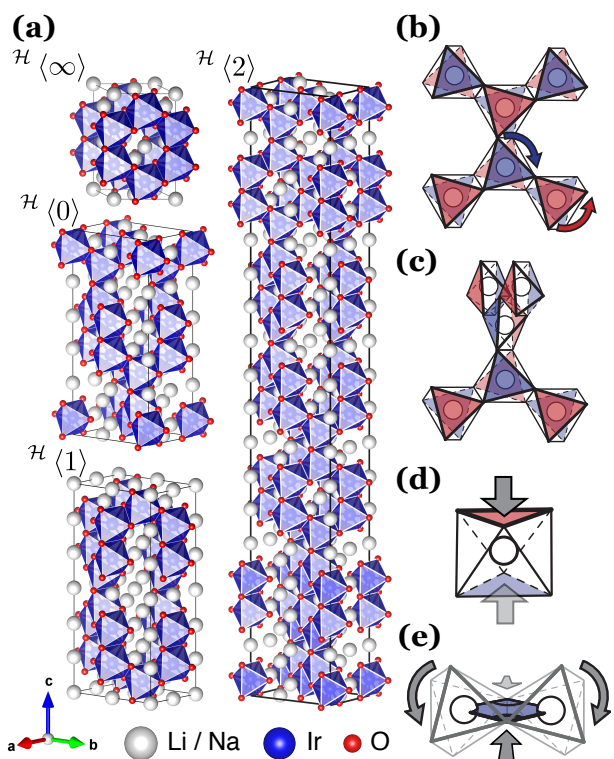


Figure 4.1: (a) Conventional unit cells of $\mathcal{H}\langle 0 \rangle$, $\mathcal{H}\langle 1 \rangle$, $\mathcal{H}\langle 2 \rangle$, and $\mathcal{H}\langle \infty \rangle$ [174]. $\mathcal{H}\langle \infty \rangle$, $\mathcal{H}\langle 0 \rangle$, $\mathcal{H}\langle 1 \rangle$, and $\mathcal{H}\langle 2 \rangle$ have 2, 4, 8, and 12 formula units in their primitive unit cell, respectively. Members of the harmonic honeycomb series have identical local geometry, only varying in the connectivity of their basic structural units, orthogonal edge-sharing iridium oxide octahedra. The two growth or bonding planes are normal to $a + b$ and $a - b$, where a and b are the orthorhombic lattice vectors (indicated by the axes at the bottom left). The harmonic honeycomb pattern builds along the orthorhombic c direction. Compared to Li_2IrO_3 structures, Na_2IrO_3 structures have greater distortion of iridium oxide octahedra and larger volume. (b-e) Exaggerated distortions in the harmonic honeycombs. (b-c) Two parallel faces of each iridium oxide octahedron twist opposite to each other. These faces are parallel to the growth plane. (c) Which faces twist changes at twisting bonds. (b) A bond that preserves the bonding plane. (c) A “twist” bond that changes the bonding plane. (d) The octahedra also compress along their twist axis. (e) The twisting and compression of the octahedra cause Ir-O-Ir bond angles to increase from their ideal 90° and the angle between bonding planes to be close to the undistorted value of $\arccos(1/3)$ 70.5° .

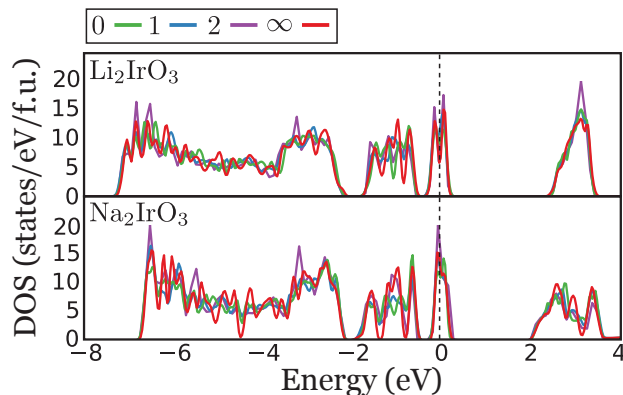


Figure 4.2: Non-magnetic density of states normalized by the number of formula units per unit cell for Li_2IrO_3 and Na_2IrO_3 harmonic honeycomb structures. Density of states is similar across the series.

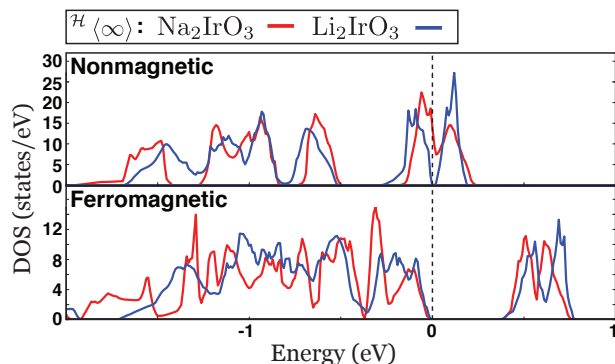


Figure 4.3: PBE+SOC+U density of states of ${}^{\mathcal{H}}\langle\infty\rangle$ Li_2IrO_3 and ${}^{\mathcal{H}}\langle\infty\rangle$ Na_2IrO_3 for non-magnetic (all magnetic moments fixed at zero μ_B) and ferromagnetic (along the ${}^{\mathcal{H}}\langle\infty\rangle$ b direction or ${}^{\mathcal{H}}\langle 0\rangle$ c direction) magnetic orders are shown in (a). A gap opens in the density of states of both systems with a non-zero magnetic order. Differences in the Li_2IrO_3 and Na_2IrO_3 density of states are caused by distortions of the local environment more so than change in volume. Li_2IrO_3 and Na_2IrO_3 structures have Ir-O-Ir bond angles of 94° and 100° , respectively.

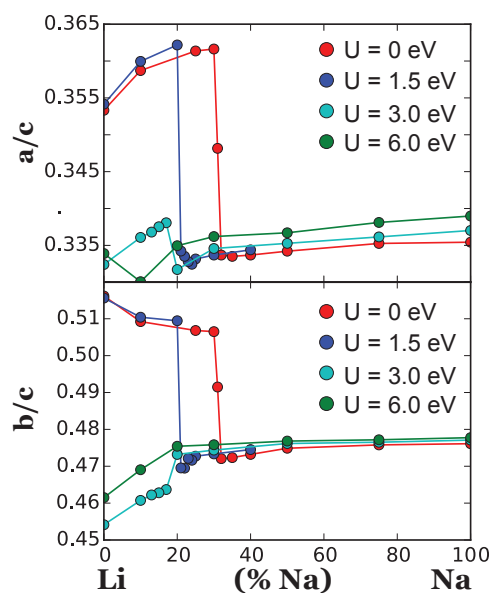


Figure 4.4: Plots of ratio of relaxed lattice parameters vs doping for PBE+U where $U=0,1.5,3.0,6.0$. The discontinuity indicates that when PBE gives asymmetric Ir-Ir bonds below a given Na doping. The discontinuity in the lattice parameters shifts toward more Li doping with increasing U , demonstrating that the performance of the functional is sensitive to localization of iridium 5d orbitals and closeness of iridium atoms.

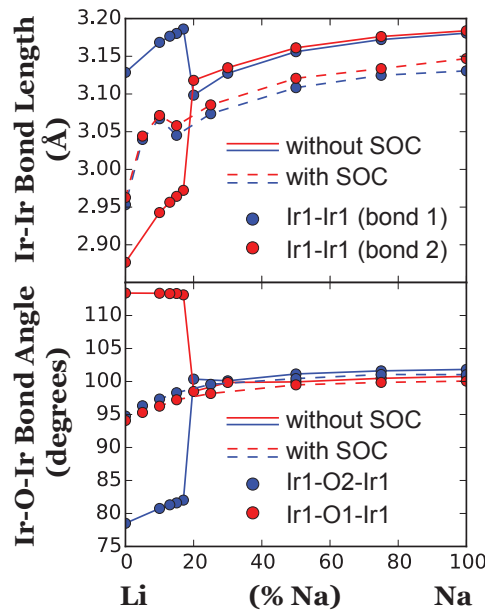


Figure 4.5: Plots of Ir-Ir bond lengths and Ir-O-Ir bond angles as a function of Na doping of ${}^{\mathcal{H}}\langle 0 \rangle$ Li_2IrO_3 for PBE+U and PBE+SOC+U ($U = 3$ eV). While SOC is not sufficient to prevent discontinuities in bond length relaxations, it does give uniform bond length ($< \pm 0.01$ Å) and bond angles ($< \pm 1.5$ degree) for all relaxations. Note, if $U = 3$ eV is used for Li concentration $< 15\%$ and $U = 1.5$ eV for Li concentration $< 15\%$ there is no discontinuity. $(\text{Li}_{1-x}\text{Na}_x)_2\text{IrO}_3$ is metallic for $U = 1.5$ eV and $0.1 < x < 0.2\%$. According to VCA, the distortion is not linear in doping.

Chapter 5

Silver Benzeneselenolate is a Self-Assembling Direct-Gap Metal-Organic Chalcogenide Assembly

Silver and diphenyl diselenide self-assemble into a blue-luminescent excitonic semiconducting crystalline hybrid lamellar van der Waals solid, silver benzeneselenolate ($[\text{AgSePh}]_{\infty}$). Each composite layer of the vdW solid is itself comprised of an ultrathin silver selenide layer having 2D connectivity and a supramolecular lattice of ordered phenyl rings. We find that the material has a strong blue photoluminescence at 467 nm. Density functional theory calculations imply significant quantum confinement of electronic carriers within inorganic layers. Three synthetic preparations for $[\text{AgSePh}]_{\infty}$ in different scales and form factors were developed.

5.1 Introduction

Single monolayers separated from layered van der Waals solids, like transition metal dichalcogenides (TMDs, e.g. MoS_2), usually exhibit semiconducting properties that are distinct from that of the bulk crystalline solid. For example, TMD monolayers possess direct band gaps and high electron mobilities, whereas their bulk crystalline counterparts are typically indirect band gap semiconductors [159, 88, 53, 43]. These and other interesting physical phenomena emerge from single layers due to quantum confinement and enhanced electron-electron interactions, and provide a variety of opportunities for technological exploitation [251, 220, 151, 54, 156]. However, the need to isolate monolayers from bulk crystals complicates their use in practical technology. Hybrid coordination polymers that combine an inorganic semiconducting polymer with a supramolecular matrix comprised of the covalently linked organic sidegroups have been considered as an alternate route for the preparation of

low-dimensional materials, with the inclusion of covalently linked ligands serving to isolate inorganic material systems [80, 111, 113, 112, 237, 260, 267, 252, 102, 143].

Here, we report that one such hybrid coordination polymer, silver benzeneselenolate ($[\text{AgSePh}]_\infty$, where the infinity subscript denotes a bulk crystal as opposed to a single monolayer), is a direct-gap semiconductor that expresses fully isolated 2D semiconducting properties in the bulk crystal. This compound exhibits a deep blue photoluminescence (467 nm) consistent with a direct-gap semiconductor. We developed two accessible-synthetic-routes to the single-crystal product: a single-step immiscible-interface method and a one-pot reaction with gram-scale yield, showcasing the ease at which this hybrid chalcogenide material is made by using commercially available small molecule precursor and mild reaction conditions. We will discuss our synthetic route, optical characterization of the direct gap semiconductor transition, and our companion density functional theory calculations. We then employ crystal engineering by way of design of discrete organic diselenide ligands and assemble them into analogous crystalline metal-organic chalcogenide assemblies. We find the properties of each are consistent with a propose that variance of organic ligand shape in the silver organoselenolate system presents a straightforward route towards the preparation of synthetically tailorable, self-assembling 2D materials from small molecule building blocks.

5.2 Results and Discussion

Synthesis and Characterization of $[\text{AgSePh}]_\infty$

The chemistry of metal organochalcogenolates[78, 68] present a rich chemical infrastructure for preparing layered, crystalline supramolecular assemblies. Silver, like many soft transition metals, can adopt a wide array of coordination geometries[219] while accommodating a broad variety of organic ligands. For example, both aryl and n-alkyl thiols assemble with silver into layered crystalline Ag-S 2D coordination polymers[191, 70, 110]. Selenium analogs of these compounds are less explored, in part because the use of harsh, odorous, or highly reactive selenium reagents is not ideal. Previous methods used to synthesize both discrete complexes and coordination polymers occur via chalcogenolysis, through cleavage of the Se-H bond[182], or the isolation of the reactive selenolate salt (-SeR)[50]. Corrigan and coworkers first reported the synthesis and single-crystal X-ray structure for a coordination polymer $[\text{AgSePh}]_\infty$ (Fig. 5.1) in 2002, during an effort to form silver selenolate polynuclear clusters, using a selenium lithiate as precursor[69]. The 2D lamellar structure of this product was characterized; however the application for this coordination polymer had not yet presented itself, as the interest in low-dimensional TMDs arrived only later.

We prepare single crystals of $[\text{AgSePh}]_\infty$ via crystallization between two immiscible solvents, water and toluene, at room temperature [267]. We employ the reagent diphenyl diselenide, a nonodorous, solid organoselenium source. This is dissolved in toluene (3 mM) and layered over a solution of silver nitrate in H₂O (3 mM). Cleavage of the diselenide by silver ion appears spontaneous, and coordination polymerization is restricted to the liquid-

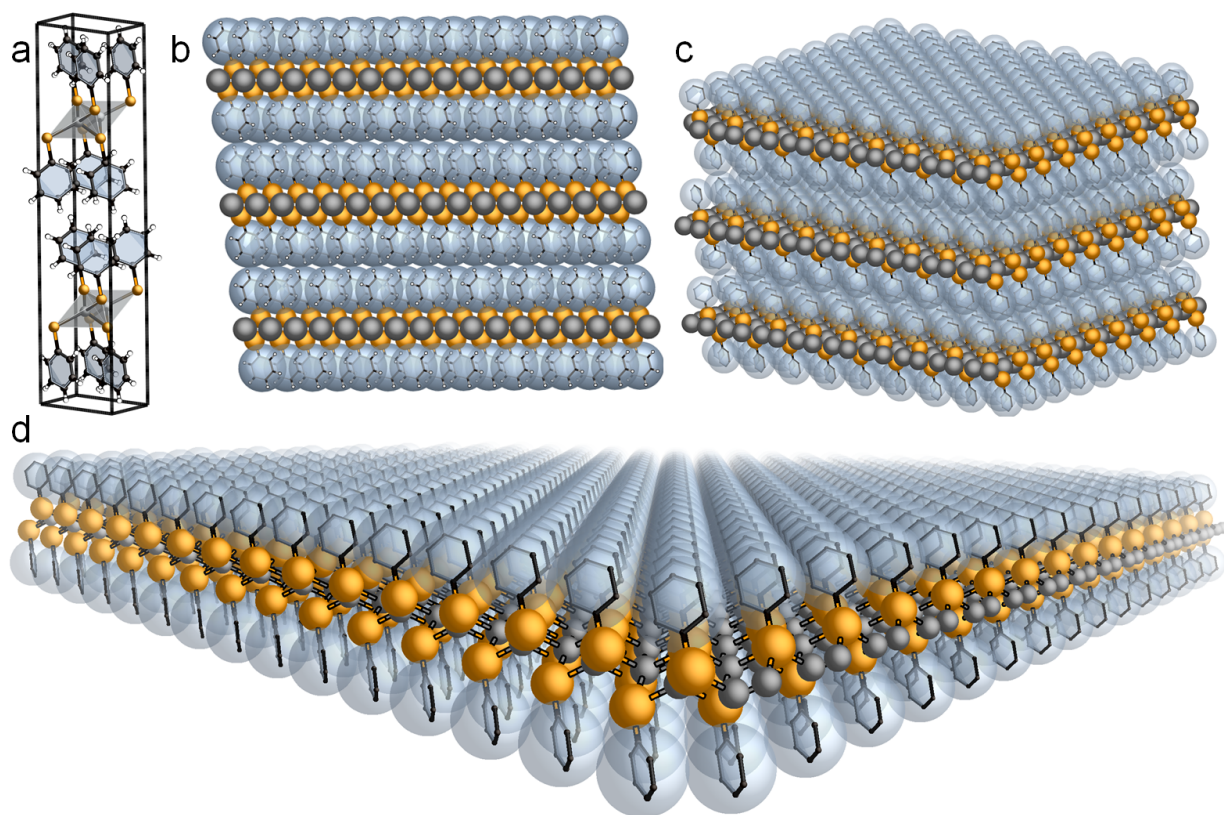


Figure 5.1: a) The monoclinic unit cell of solid silver benzeneselenolate contains two complete layers of hybrid chalcogenide 2D polymer. Silver is coordinated tetrahedrally by four selenium atoms. b,c) The multilayered structure isolates inorganic layers via the benzene moieties oriented above and below the silver selenide polymer layer. D) A single isolated layer has a thickness of 1.4 nm, each containing two layers of phenyl rings and one layer of silver selenolate. Silver is represented as the grey spheres, selenium in dark orange, and carbon in black. Aromatic rings are accented in blue.

liquid interface. Crystallization occurs readily without stirring over 1-3 days, with product manifesting as an opaque film, chartreuse in color, pinned between the two solvent layers (Fig 2a). The structure is confirmed by matching the powder X-Ray diffractogram of both products to the theoretical pattern derived from the known crystal structure (See supporting information, Figure C.1). Alternatively, a one-pot synthesis using triphenylphosphine to stabilize silver nitrate in tetrahydrofuran, similarly yields crystalline $[\text{AgSePh}]_{\infty}$ in high specificity at a gram scale with crystalline product dimensions in excess of tens of microns. The one-pot product contains considerably larger and thicker crystals relative to the immiscible layer approach, at the cost of increased polydispersity. Products produced by both routes are otherwise indistinguishable by the characterization methods employed above.

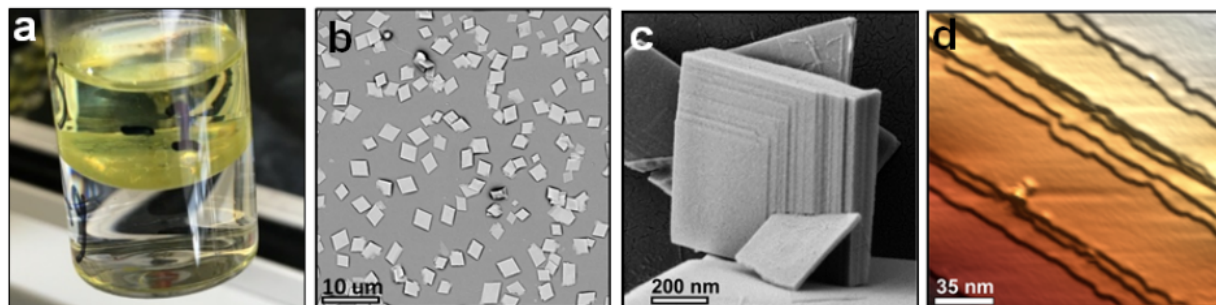


Figure 5.2: a) A chartreuse deposit of silver benzeneselenolate forms at an immiscible liquid-liquid interface of organic and aqueous solutions of diphenyl diselenide and silver nitrate, respectively. b) Crystals of $[\text{AgSePh}]_{\infty}$ recovered have typical edge lengths between 1 and 4 microns. b) Scanning electron micrograph of a silver benzeneselenolate silver crystal reveals the layered structure of the crystal. Individual layers are resolved in high-resolution SEM images. c) Atomic force microscopy reveals highly uniform $[\text{AgSePh}]_{\infty}$ (001) terraces with measured step heights at 1.4 nm.

The film is harvested by drawing a silicon wafer through the liquid-liquid interface at an angle. The precipitate adheres readily to silicon substrate. A layer of single crystals of $[\text{AgSePh}]_{\infty}$, each having edge lengths of 1-5 μm and a typical thickness of 100-200 nm, are shown in Figure 5.2b. Features of the crystal surface are examined by SEM and AFM in Figure 5.2c-d. The prominent 001 plane of the silver benzeneselenolate crystal is visible in Figure 5.2c as the large flat face. The smaller faces correspond to 010 and 100 facets, corresponding to exposed edges of the 2D hybrid crystalline polymer. Scanning electron microscopy resolves the individual molecular step edges, corresponding to the thickness of a single silver benzeneselenolate sheet (Fig. 5.2b). Atomic force microscopy (AFM) confirms the expected 1.4 nm step height of the (001) crystallographic plane. AFM images of these outermost layers of the $[\text{AgSePh}]_{\infty}$ crystal further reveal that the exposed terraces are virtually defect free over hundreds of nanometers, with no molecular vacancies are observed in our images at this scale.

Optical Characterization of the Semiconductor Direct-Gap

We note comparisons to two-dimensional TMDs, such as MoS₂, with some important distinctions due to the presence of the intervening organic groups and metal-metal interactions. MoS₂ is a layered indirect band gap semiconductor in the bulk, but has a direct band gap and high charge carrier mobilities as a single layer [159]. Similar to most TMD van der Waals (vdW) solids[248], adjacent 2D layers of silver benzeneselenolate are covalently decoupled. Unlike the TMD solids, the vdW coupling is strongest between the organic ligands, rather than between neighboring AgSe planes. As the transition metal chalcogenide layer is chemically decoupled from its neighboring layers, the bulk hybrid silver benzeneselenolate

system might be expected to be electrically decoupled as well, thereby exhibiting properties associated with monolayer-TMDs rather than with bulk-TMD systems. To test this hypothesis, we measured the photoluminescence (PL) spectroscopically and microscopically, and the results are shown in Figure 5.3.

On excitation with shorter wavelength light (380 nm), a single PL peak is observed at 2.65 eV, or 467 nm, a deep blue. To determine if the crystal size affects the PL color or intensity, we imaged single crystals by confocal microscopy using a 405 nm laser. Measuring the emission spectra, we find that each single crystal has an emission peak at 467 nm, consistent with the ensemble measurement (Figure 5.3, Figure C.4, Materials and Methods). Moreover, we observe no correlations between emission intensity and crystal aspect ratio or surface area (Figure 5.3e,f). The analysis at the single particle level suggests that the photoluminescence intensity is not dependent on the lateral size dimensions of the crystal at the microscale. Instead, emission intensity correlates with number of layers, or crystal thickness. Although absolute crystal thickness is not directly measured in this experiment, relative thicknesses may be inferred by visual inspection using the optical microscope (Figures 5.3c-d).

Band Structure Calculations

To understand the origin of the electronic properties of this system, we performed density functional theory (DFT) calculations with the VASP code [135, 137, 136, 138] using the hybrid functional of Heyd, Scuseria, and Ernzerhof (HSE), which includes approximate short-range exchange and correlation effects important for a balanced treatment of delocalized sp valent and localized d and π states in $[\text{AgSePh}]_\infty$.

Using experimental lattice parameters and atomic positions, we perform calculations on the following periodic structures: 1) bulk $[\text{AgSePh}]_\infty$, 2) single-layer $[\text{AgSePh}]_\infty$, and 3) a single-layer $[\text{AgSePh}]_\infty$ with the phenyls replaced by hydrogen atoms. We use 1) and 2) to demonstrate that the layers of $[\text{AgSePh}]_\infty$ are effectively electrically isolated and 3) to illustrate the impact of the ligand on the electronic structure. Our DFT band structures and density of states for these systems are summarized in Figure 5.4.

Our computed band structures of bulk and single layer $[\text{AgSePh}]_\infty$ are indistinguishable, demonstrating that the layers of bulk $[\text{AgSePh}]_\infty$ are electrically isolated. Within DFT-HSE, bulk and single layer $[\text{AgSePh}]_\infty$ have a direct band gap at Γ of 2.4 eV, in good agreement with the measured photoluminescence, despite the fact that DFT is not expected to yield quantitative gaps on formal grounds. To obtain quantitative optical gaps and spectra, a more advanced treatment of exchange and correlation effects, including electron-hole interactions, is required in addition to our calculations, e.g., the use of ab initio many-body perturbation theory (MBPT) within the GW approximation and the Bethe-Salpeter equation (BSE) approach [101, 211, 212]. The lowest-lying DFT-HSE conduction band of bulk $[\text{AgSePh}]_\infty$ is highly dispersive in plane, with electron effective masses of $1.13 m_e$ and $0.44 m_e$, respectively, at Γ (Figure C.6). Bands exhibit significantly less dispersion perpendicular to the *AgSe* planes and along the stacking direction of $[\text{AgSePh}]_\infty$, with an electron effective mass

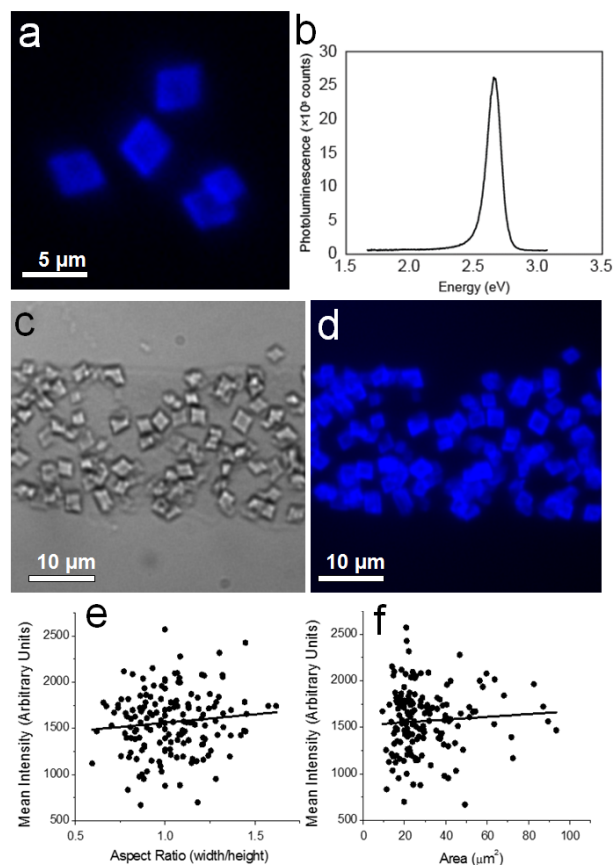


Figure 5.3: a) Confocal micrographs showing the color uniformity of photoluminescence in $[\text{AgSePh}]_{\infty}$. b) A single, intense emission of the solid at 467 nm is attributed to a direct-gap electronic transition. c,d) Optical and confocal micrographs of $[\text{AgSePh}]_{\infty}$ showing fluorescence scanning confocal images of several individual crystals of nearly the same size. e) Distribution of the intensity from 157 individual crystals plotted as a function of the area of the crystal and f) aspect ratio. The Pearson's r -value for each set of data was calculated by using linear least squares fitting (solid line); for both the plots of area (r -value of 0.07) and aspect ratio (r -value of 0.1) the Pearson's r -values indicate no correlation with intensity. Images are false colored according to emission wavelength.

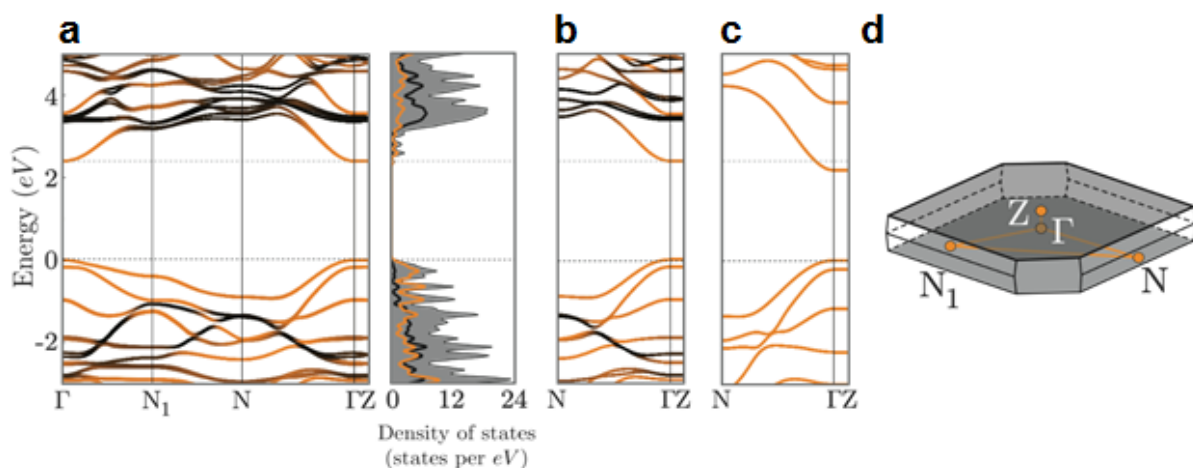


Figure 5.4: a) DFT-HSE band structure and density of states of bulk $[\text{AgSePh}]_\infty$. See supporting information Figure C.6 for details. Band color signifies the fractional contribution of states centered on inorganic (Ag and Se, orange) and organic (C and H, black) atoms in the crystal. The total density of states is shown in gray. b) DFT-HSE band structure of a single layer of $[\text{AgSePh}]_\infty$ c) DFT-HSE band structure of a single layer of $[\text{AgSePh}]_\infty$ with the phenyls replaced by hydrogen. The hydrogen positions have been relaxed with PBE; see supporting information Figure C.5. The near-band edge character remains relatively unchanged when the phenyls are replaced by hydrogen, suggesting that the degree of 2D quantum confinement is unchanged by 3D crystallization. d) The Brillouin zone for the primitive cell of $[\text{AgSePh}]_\infty$. The path in the Brillouin zone used for the band structure is identified by orange lines and k-point labels.

of $18.7 m_e$, reflecting weak (although non-negligible) interplanar coupling and indicating significantly lower mobility along the $[001]$ direction.

The electronic structure of bulk and single layer $[\text{AgSePh}]_\infty$ near the valence and conduction band edges is dominated by contributions from silver selenide. Figure shows isosurfaces of the square of the wavefunction for the bulk $[\text{AgSePh}]_\infty$ conduction band minimum and valence band maximum states at the Γ point. While the state at the valence band maximum exhibits directional bonding associated with Ag 4d and Se 3p character, the conduction band minimum is more delocalized, featuring significant Ag 5s character. As can be seen in Figure 5.5, the phenyl group p states contribute minimally to band edge states with valence band maximum and conduction band minimum isosurface density visible only on the carbon atoms adjacent to the AgSe layer.

The calculated density of states shows a separation of bands having organic (phenyl) and inorganic (Ag and Se) character near the band gap. The phenyl π and π^* states are largely grouped at energies well below and above the Ag- and Se-rich valence and conduction band edges, respectively, consistent with the relatively large benzene gap (Figure 5.4) and minimal carbon character at the band edges. Indeed, replacing the phenyl groups with hydrogen leads

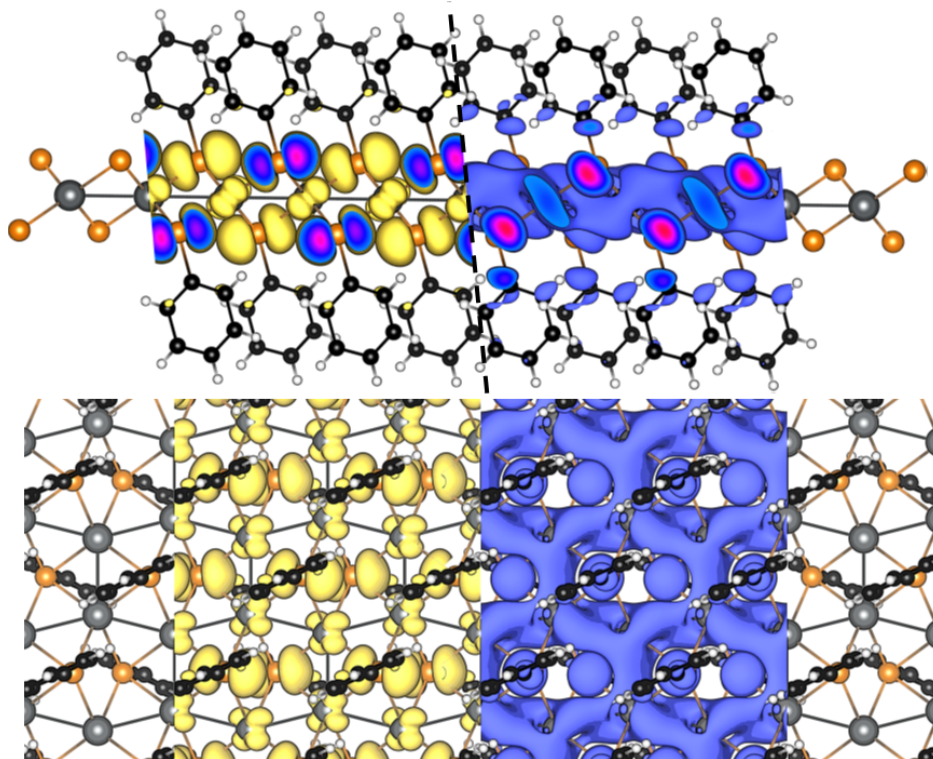


Figure 5.5: Depictions of side and top views of $[\text{AgSePh}]_{\infty}$ with overlain charge density maps. The DFT-HSE computed valence band maximum (VBM) and conduction band minimum (CBM) at Γ are accentuated in yellow and blue, respectively. The minimal but non-negligible participation of carbon in the CBM state suggests tailoring of electronic properties via synthetic modification of ligand.

to small changes in band gap and in-plane effective masses compared to the phenylated layer (Table C.1, Figure C.5). The relative alignment of the organic and inorganic states suggests an opportunity to tune the near-band edge character of each component via ligand choice. A ligand with a smaller band gap, such as pentacene, could contribute states hybridizing with those of silver selenide at the band edge. Thus, it may be possible to tune electronic properties of this system, as well as the coupling between layers, by ligand design. The use of ligands has been successfully used to tune the optoelectronic properties of quantum dots[216], we can apply the same principles to metal-organic crystalline systems described here.

Previous experiments and ab initio MBPT calculations on TMDs have established large exciton binding energies[199], novel screening effects[253], and trion formation[42]. Given the similarity of its atomic structure to that of 2D TMDs, and the added presence of the phenyl ligands, such excited state phenomena are also likely to emerge from this silver selenide system and will be explored in future work.

5.3 Conclusions and Prospects

Coordination polymers are often treated as kinetic side products en route to more elaborate, discrete organometallic clusters. However, the incorporation of organic side groups with inorganic polymers presents a straightforward approach to combine the chemical variety of organic chemistry with the compelling transport phenomena exhibited by 2D materials. Using metal-directed self-assembly, we synthesized silver benzeneselenolate, a material that expresses 2D semiconducting phenomena in its as-crystallized bulk state. The phenyl rings additionally appear to efficiently isolate the inorganic layers from one another, enabling the material to display monolayer-like properties in the bulk, and without need for exfoliation. The organization of this material is consistent with that of a multilayered single-crystal supramolecular quantum well. The 2.65 eV peak emission is attributed to a direct-gap transition. The straightforward synthesis from convenient reagents makes silver benzeneselenolate a notable candidate for studying high-binding-energy excitonic physics in as-synthesized crystalline 2D materials.

Crystal engineering applied to such low-dimensional semiconducting coordination polymers is accessible because of the robustness of silver/chalcogen coordination reactions. Because any ligand shape and composition can be varied over a broad range, molecular side group diversification enables a straightforward route to band level engineering between the organic and inorganic with ligand selection[274]. In this example, the inclusion of covalently attached ligands considerably alter the properties of the 2D AgSe-R polymer in comparison to Ag_2Se , which is a small bandgap near-infrared emitter[216, 276]. Using coordination polymers as the basis for 2D material systems opens synthetic avenues to the investigation of semiconducting inorganic systems that are not preexisting in nature, due to the variety of coordination geometries inherent to transition metals and the practically limitless design available through selection of organic ligands.

Chapter 6

An Automatically Curated First-Principles Database of Ferroelectrics

Ferroelectric materials have a wide-range of technological applications including non-volatile memory and optoelectronics. In this chapter, we integrate density functional theory, crystal structure databases, symmetry tools, workflow software, and a custom analysis toolkit to build a library of known and proposed ferroelectrics. With our automated workflow, we screen over 17,000 candidate structure pairs from the Materials Project structure database using symmetry relations between nonpolar and polar structures to generate a dataset of 239 ferroelectric candidates. Results are automatically parsed, stored in a database, and accessible via a web interface showing distortion animations and plots of polarization and total energy as a function of distortion. We provide the candidates found using our workflow on the Materials Project structure database. We benchmark these candidates against experimental data and other ab initio results. The data is available on FigShare and github. We also contribute our workflow and analysis code to the open-source python packages `atomate` and `pymatgen` so others can conduct their own symmetry driven searches for ferroelectrics and other phenomena.

6.1 Background and Summary

High-throughput screening of material databases integrated with first principles calculations has been increasingly successful in the discovery of new functional materials [268, 61, 71]. A remaining challenge is that while all the individual components for performing high-throughput searches exist, the infrastructure needed to connect and automate all the necessary components is still under development. In particular, the identification and curation of ferroelectrics has been an active area of research for the past half-century [154, 255, 2]. A ferroelectric material has a spontaneous polarization that is switchable between two or

more states by an applied electric field [152, 201]. Ferroelectrics are technologically useful, used in tunable capacitors and non-volatile RAM, and display couplings between magnetic, electronic, and lattice degrees of freedom [152, 201].

Ferroelectricity arises from a structural phase transition. This phase change results in the appearance of a spontaneous polarization [152]. In a conventional ferroelectric, the high-symmetry structure is nonpolar and the low-symmetry structure is polar, permitting a spontaneous polarization. The atomic structure distorts such that the new structure has a subset of the symmetries of the original structure, satisfying the requirements of a second-order phase transition [60].

Abrahams first proposed searching for pairs of nonpolar and polar structures related by symmetry to find ferroelectric candidates. In the late 1980s, he performed some of the earliest searches for ferroelectrics in crystallographic database using symmetry criteria [6, 7]. More recently, similar automated searches for new ferroelectric candidates have used symmetry arguments to identify nonpolar reference structures for existing polar materials [57, 117, 139]. Other papers have used a combination of group theoretic and first-principles calculations to propose ferroelectric candidates [241, 194, 235]. Bennett et al proposed using high throughput calculations to perform high-throughput substitution calculations on known classes of ferroelectrics [39, 40, 41]. Recent work used high-throughput phonon calculations to identify ferroelectric from polar, soft phonon modes [86].

However, previous works have focused on a limited number of compounds or families of compounds using few symmetry conditions. Furthermore, predictions were based on limited experimental data due to the screening approach, leading to predictions difficult to test experimentally. With shrinking computing costs, high-throughput material searches using density functional theory are on the rise. Ferroelectric databases and systematic screening of properties such as small band gaps, large polarizations, large volume expansion, high critical temperatures and coupling to magnetic and/or topological degrees of freedom may lead to new functional materials and potentially new physical phenomena [87].

In this chapter, we integrate density functional theory (DFT), crystal structure databases, symmetry tools, workflow software, and a custom analysis toolkit to build a workflow capable of generating libraries of known and proposed ferroelectrics. This workflow is general and can be performed on any crystal structure dataset. We present the results from performing this workflow on the Materials Project database of inorganic crystal structures [124]. We screen over 17,000 candidates using symmetry relations between nonpolar and polar structure pairs. We identify 239 ferroelectric candidates, 183 being classified as high-quality candidates by a stringent validation process. 78 of these high-quality candidates are known (anti)ferroelectrics or previously proposed, and 105 are new. Using the workflow developed here, this is the first automatically-curated ab initio dataset of diverse, multi-class known and new ferroelectrics calculated with a standardized method that permits straightforward comparison. This dataset can be used to develop new tools and criteria for studying ferroelectricity across diverse materials systems. In addition our code for conducting this search has been contributed to the open-source python packages `atomate` and `pymatgen` so others can conduct searches of their own and build directly on this work.

6.2 Methods

Ferroelectricity from First-Principles

The spontaneous polarization is not a direct observable; one can only measure the change in a material’s spontaneous polarization switching between two stable configurations [208]. Applying an electric field to a ferroelectric leads to a hysteresis loop in a plot of the polarization versus applied electric field. The half of the change in polarization is defined as the spontaneous polarization at a given field and temperature; the extrapolation of this quantity to zero field is the spontaneous polarization [152]. The spontaneous polarization can be directly predicted using ab initio methods.

We identify ferroelectrics as materials possessing two structural phases: a high-symmetry nonpolar structure and a low-symmetry polar structure that can support a polarization [128]. We automatize a search for compounds supporting two such phases and then compute the polarization difference between the two structures.

The polar and nonpolar symmetry criteria stems from the following. As a consequence of structural periodicity, the polarization of a crystal is a lattice vector. This means the polarization, \mathbf{P} , of a crystal is only defined modulo a “quantum of polarization”, [208, 238],

$$\mathbf{P} = \mathbf{P}_0 + \sum_{i \in \{a,b,c\}} n_i \frac{e\mathbf{R}_i}{\Omega}, \quad (6.1)$$

where e is the charge of the electron, n_i is an integer, \mathbf{R}_i is a lattice vector, and Ω is the unit cell volume.

In three dimensions, the only space groups compatible with leaving a 3D lattice vector invariant under its symmetry operations are those with polar point groups. Out of the 32 crystallographic point groups, 10 are polar; these polar point groups can keep points along specific lines (point groups 2, 3, 4, 6, mm2, 4mm, 3m, 6mm), planes (point group m), or all points in 3D space (point group 1) fixed [152]. All other point groups are nonpolar. We define polar structures as crystal structures with a polar space group, which is composed of a polar point group plus translations, likewise for nonpolar structures.

To recover a smooth polarization path, we ensure the nonpolar structure must be continuously deformable into the polar structure along a path that preserves the symmetry of the polar structure. We then perform calculations of multiple structures along the distortion path to compute the Berry phase polarization, which can be compared to the experimentally measured spontaneous polarization.

Antiferroelectrics

Antiferroelectrics, in contrast to ferroelectrics, exhibit double hysteresis loops in polarization versus electric-field measurements [200]. The field-induced phase transition is caused by energetically competing nonpolar and polar phases separated by a first order phase transition. The nonpolar phase is often referred to as “anti-polar” to distinguish it from the nonpolar

reference structure. Symmetry conditions for antiferroelectrics are described in Ref. [247]. For completeness, to find anti-ferroelectrics using ab initio techniques one would ideally find the reference nonpolar phase, the antipolar phase and the polar phase. However, one can also find antiferroelectric candidates by the same method as used to find ferroelectrics. In this case, the antipolar structure should be found to be lower in energy than the polar structure.

Workflow overview

We first describe the general workflow diagram shown in Figure 6.1. The complete workflow involves the passing of data between many separate calculations. To create an automated ferroelectric search, we automate the following tasks:

1. Identifying candidate materials possessing nonpolar-polar structure pairs related by a group-subgroup symmetry relation.
2. Performing DFT calculations of changes in total energy, band gap, and polarization across the nonpolar-polar distortion.
3. Post-processing calculation data to compute the spontaneous polarization.
4. Validating the calculation quality for each ferroelectric candidate.
5. Creating an interface for viewing the results for all candidates.

We start by choosing a crystal structure database on which to perform the search (see Structure Selection Symmetry Analysis) and perform a symmetry analysis to find candidate materials possessing nonpolar-polar structure pairs related by a continuous symmetry deformation. Any such pairs found to satisfy the symmetry criteria are stored in the Distortion Database as being deformable by symmetry. This criteria includes the following: The polar structure belongs to a space group that is a subgroup of the space group of the nonpolar structure. There exists a transformation matrix between the nonpolar structure in its high-symmetry setting to the low-symmetry setting of the polar structure.

We then prepare a workflow to perform DFT calculations on the candidate pairs to extract the changes in the band gaps, total energies, and polarization of the distortion (see Computational Methods). These workflows are stored in a Workflow Database that is then accessed by our Computing Resources where the calculations are performed.

Then, the information stored in the Distortion, Workflow, and Calculation Databases is used together to post-process quantities such as the spontaneous polarization and validate the candidates using experimental and previous ab initio results (see Post-processing and Spontaneous Polarization Values and Verification of computational methodology). The information needed to assess the quality and properties of the candidates is then added to the Candidate Database where it can be accessed by our web Interface for viewing the

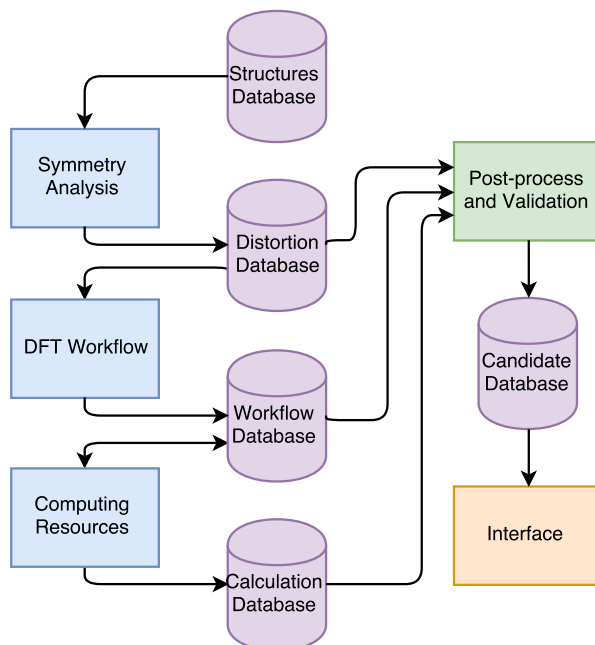


Figure 6.1: Diagram of entire automated ferroelectric search workflow. Databases are shown as purple cylinders. Processes are shown as rectangles: blue designates processes used to identify and perform ab initio calculations, green designates post-processing and validation, and orange designates the web-interface. Arrow directions indicate the flow of information. For example, the Workflow Database provides information to the Computing Resources for which calculations to compute and the Workflow Database is updated as calculations complete or errors occur on the Computing Resources.

candidates in aggregate (see Graphical Interface). We finally validate the candidates to ensure the polarization and energy profile across the nonpolar-polar distortion are smooth and continuous.

In the sections below, we describe in detail the methods used for creating an automatically curated dataset of ferroelectrics from the Materials Project database [124]. The Materials Project database is largely based on structures from the Inorganic Crystal Structure Database (ICSD) and also includes hypothetical structures created through stoichiometric substitution. The results from applying our workflow are described below and summarized in Table 6.1. We note that the workflow we create is modular and open-source, so it can be readily adapted and applied by others, expanding the search for ferroelectrics and multiferroics.

Table 6.1: Results obtained by applying our workflow to the Materials Project database. † indicates “in Materials Project database at time of search”. Boxes relate numbers by symmetry conditions, DFT calculations, and validation processes. Rows separated by a single line give the sum of the numbers given below it in the same box.

Symmetry	Structures [†]	~67,000
	Polar structures [†]	~15,000
	Distinct polar formula [†]	~10,000
	Nonpolar-polar pairs	~17,000
	Distinct nonpolar-polar pairs formula	~1,600
	Pairs with continuous transformation	414
DFT	Pairs with metallic endpoints	86
	Pairs with metallic interpolations	40
	Pairs with calculation errors	49
	Pairs that completed successfully	239
Valid.	High-quality ferroelectric candidates	183
	Known ferroelectrics in high-quality candidates	78
	New ferroelectrics in high-quality candidates	105

Structure Selection

The input to our workflow is a collection of a candidate nonpolar-polar structure pairs. There are several methods that can be used to create candidate nonpolar-polar structure pairs. For example, one can apply a polar distortion to an existing nonpolar structure or create a nonpolar reference structure for an existing polar structure. For this dataset, we require both the nonpolar and polar structures to exist in the Materials Project database.

To search for compatible nonpolar-polar structure pairs in the Materials Project dataset, we find structures that are in space groups that satisfy group-subgroup relations with a nonpolar high-symmetry space group and a polar low-symmetry space group. We also require that the number of sites in the nonpolar structure are less than or equal to the number of sites in the polar structure. We perform this query using `pymatgen`, `spglib`, and the Materials Project API [188, 250, 186]. We give the number of structures resulting from this query in the top box of Table 6.1.

At the time of this search, the Materials Project database has approximately 67,000 structures, approximately 15,000 of which are polar. We find approximately 17,000 nonpolar-polar structure pairs. These pairs contain approximately 1,600 materials out of the approximately 10,000 distinct polar compositions in the Materials Project database. All other polar compositions in the Materials Project do not have symmetry compatible nonpolar candidates in the database. We note that it is possible to propose hypothetical nonpolar reference structures for these polar candidates using group theoretic methods or large symmetry tolerances [57, 117, 139, 86]; this is left for future work.

Naming Conventions

We use the formula name output by the pymatgen `alphabetical_formula` method for the Composition class (with spaces and 1s removed) to output consistent formulas for our candidates. This method orders elements in such a way that does not match conventions in the literature. For example, we use O_3PbTi where the standard in the literature is PbTiO_3 . Compositions printed by pymatgen also differ from those used in mineralogy, such as for boracite, lawsonite and many other minerals in our dataset. In our datafiles, we also provide formula name output by the pymatgen `reduced_formula` method for the Composition class which sorts elements by electronegativity.

Symmetry Analysis

The automated nature of our ferroelectric search relies on strict symmetry criteria. As described in the Structure Selection section, we pre-screen our candidate nonpolar-polar structure pairs using the symmetry tools in pymatgen and spglib to ensure that these pairs already satisfy basic group-subgroup relationships. We then use symmetry tools provided by the Bilbao Crystallographic Server (BCS) to impose the symmetry criteria described in the Workflow Overview [31, 28, 30]. BCS has a freely available web interface for accessing a wide variety of symmetry tools. We create python scripts to automate interaction with and scrape returned data from BCS to perform our symmetry checks using the python package mechanize.

We use the BCS Structure Relations tool to obtain a transformation matrix connecting two group-subgroup related structures [225, 243, 240]. More details on this process are given in Appendix F. The Structure Relations tool checks for the following:

- 1.1 Compatible group-subgroup index relations. The index of a group-subgroup relation indicates how many ferroelectric domains (distinct polar structures) arise from the symmetry breaking of the high-symmetry structure.
- 1.2 There exists a path of maximal subgroups between the high symmetry structure and low symmetry structure.
- 1.3 The Wyckoff position splitting of the high symmetry structure is compatible with the Wyckoff positions of the low symmetry structure.
- 1.4 The lattice of the high-symmetry structure in the low-symmetry setting must be within a certain tolerance of the lattice of the low-symmetry structure
- 1.5 Each atom in the high symmetry structure in the low symmetry setting can be paired to an atom in the low symmetry structure such that no atom pairs are greater than a given tolerance apart.

Structure Relations takes Crystallographic Information Files (CIFs) high-symmetry and low-symmetry structures and tolerance thresholds as arguments. We use a lattice tolerance

of 3 Å and 10° for lattice parameters and angles, respectively. For the present work, we also use a maximum pairing distance of 1.5 Å, since few ferroelectrics have a distortion that results in any atom being displaced by more than 1.5 Å.

Out of the 17,000 structure pairs that we test with Structure Relations, 414 are found to be deformable by symmetry with maximum distortion less than or equal to 1.5 Å.

Symmetry precision

Symmetry precision is a tolerance factor used to assess whether an atom is equivalent to another after a symmetry operation up to a maximum distance. A symmetry precision between 10^{-1} and 10^{-5} Å is typically used.

In the Materials Project database, a symmetry tolerance of 10^{-1} Å is used for the reported space group stored in the database. We use this tolerance to generate CIFs sent to BCS Structure Relations. We evaluated how varying the symmetry tolerance changes the resolved space group for all the structures in the Materials Project. We were able to determine this efficiently by using binary search on a \log_{10} scale for a maximum symmetry tolerance of 10^{-1} Å and minimum tolerance of 10^{-5} Å. Out of the 67,000 structures we checked, 50,000(75%) of structures were resolved into one distinct space group for the entire symmetry precision range.

For additional discussion about the sensitivity of symmetry precision on resulting space groups in the search for ferroelectrics, see Refs. [86, 224].

DFT calculation details

We perform spin polarized DFT calculations using the Vienna Ab initio Software Package (VASP) [135, 137, 136]. We use the generalized gradient approximation functional of Perdew, Burke, and Ernzerhof (PBE) [193]. Our calculations use PAW pseudopotentials with an energy cutoff of 520 eV for the plane-wave basis [46, 138].

We use the Berry phase method from Ref. [129, 254, 205, 206, 207] as implemented in VASP to calculate the electronic part of the macroscopic polarization. We calculate the ionic part of the macroscopic polarization using the point charge dipole moment for each atom in the unit cell, see the `calc_ionic` function in `pymatgen.analysis.ferroelectricity.polarization` for details.

We use the default parameters VASP input defined in `pymatgen` (and used by Materials Project) and `atomate` [122, 121, 1]. For details on these parameters, see the documentation for `pymatgen.io.vasp.sets.MPStaticSet`. We use a Hubbard U correction to localize d states of select oxides and fluorides following the approach in Ref. [81]. To see the guidelines for which compounds we apply a U, see Ref. [124, 122, 121, 1]. We use a reciprocal k-point density of 50 for structural relaxations and 100 for static and polarization calculations. We use total energy convergence criteria of 5×10^{-5} eV per atom for the electronic self-consistent loop and 5×10^{-4} eV/Å per atom for the ionic relaxation loop for structural relaxations.

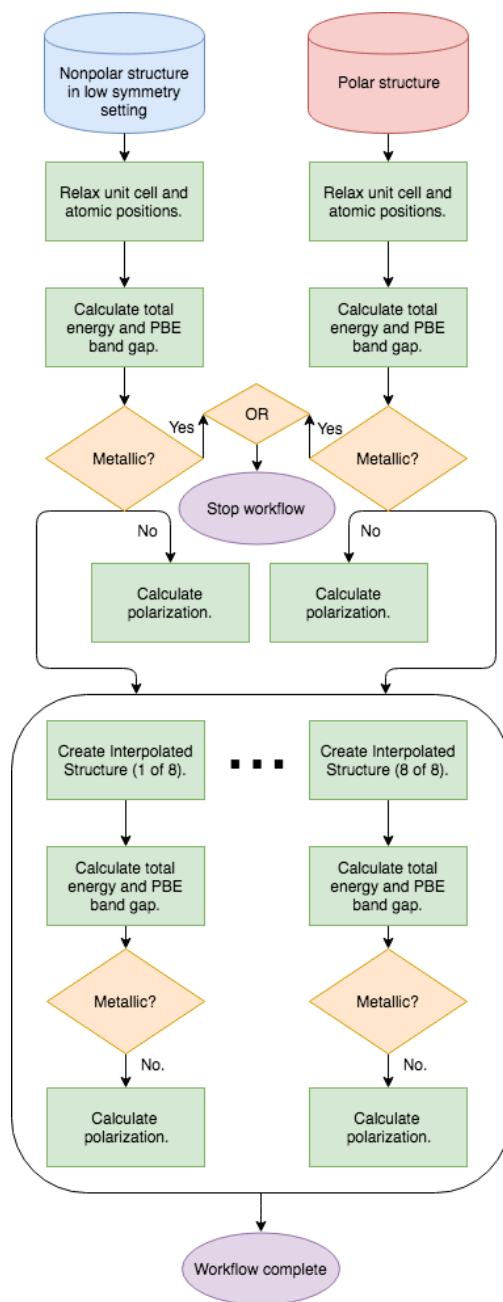


Figure 6.2: Diagram of DFT workflow written with atomate and Fireworks. Blue and red boxes denote initial nonpolar and polar structures, respectively, green boxes denote DFT calculations, orange rhombuses denote decision steps, and purple ellipses denote exit steps.

LDA is commonly used for polarization calculations because most known ferroelectrics are oxides and LDA tends to more accurately describe oxides. However, generalized gradient approximation (GGA) functionals such as PBE tend to generally perform better than LDA across a wider range of materials. We use PBE to compare to calculations in the Materials Project. We expect PBE and PBE+U to underestimate the band gap. Our results are in line with the typical overestimation of PBE for the lattice parameters, and therefore, we expect a similar overestimation of the polarization.

Scientific workflow packages

We construct the scientific workflows to perform the structural relaxations and calculations of energy, band gap, and polarization using the FireWorks and atomate python packages [123, 165]. FireWorks is built for managing computational scientific workflows. atomate is built for constructing workflows for multiple computational material science codes such as VASP. atomate uses FireWorks classes to build modules for performing common VASP calculations such as structural relaxations and self-consistent calculations of total energy. atomate also provides a framework for building custom modules, which we use to build our structural interpolations and polarization calculations modules.

DFT workflow

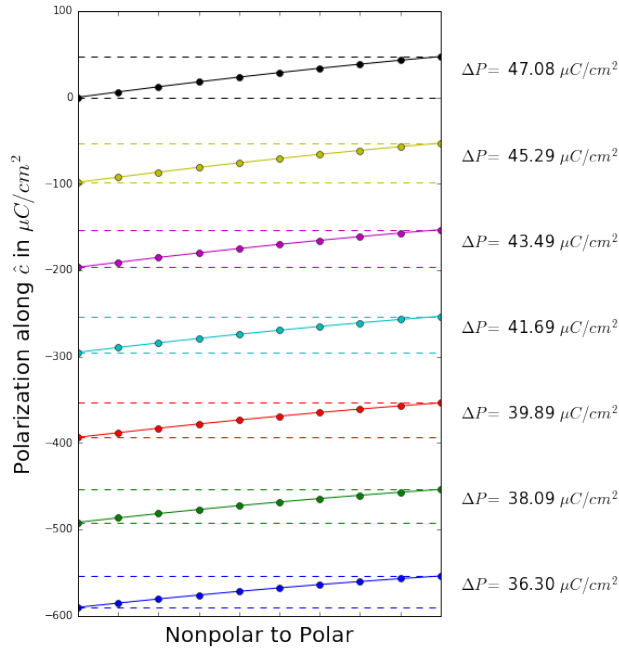
We perform the DFT workflow shown in Figure 6.2 for the 414 candidates with maximum distortions that do not exceed 1.5 Å and have structures returned from BCS that were able to be converted to pymatgen Structures objects. We use a maximum distortion cutoff of 1.5 Å because a distortion larger than this cutoff tends to be unphysical.

For each structure pair, we begin with the nonpolar structure in the low symmetry setting (obtained from BCS Structure Relations in the Symmetry Analysis step) and the polar structure. We use the nonpolar structure transformed into the low symmetry setting so we can perform structure interpolations and polarization calculations across similar lattices.

We perform relaxations of the unit cell and atomic positions of both of these structures two times, similar to what Materials Project performs on its database entries. We then fix the relaxed nonpolar and polar structures and perform a self-consistent calculation to compute the total energy and band gap. If either the nonpolar structure or polar structure is found to be metallic, which we define as having a band gap of less than 10 meV, we stop the workflow for that candidate.

If the polar and nonpolar structures are both not metallic, we compute the polarizations of both structures. 31 of the 414 structure pairs were found to have a metallic nonpolar structure but insulating polar structure, 2 were found to have a metallic polar structure but insulating nonpolar structure, and 51 were found to have both metallic polar and nonpolar structures. 2 additional structures have at least a metallic nonpolar structure, but these workflows were halted before the polar structures had their band gaps computed.

Figure 6.3: Polarization curves for BaTiO₃ along the [001] versus distortion from nonpolar to polar structure. Due to the change in lattice parameters and volume across the distortion, the quantum of polarization along the [001] direction is different for each structure. This causes the spontaneous polarization for different branches to differ. The branch that starts at zero is the corrected branch. The branch that starts near -600 $\mu\text{C}/\text{cm}^2$ is the data from VASP. Note, while in this specific case, the calculated polarization values for all interpolations were on the same branch, this is not usually the case.



We compute the total energy, band gap, and polarization of eight linear interpolations of the nonpolar to polar structures. We found eight interpolations to be sufficient for reconstructing a continuous same branch polarization for at least 75% of our candidates.

Unlike the previous step where a metallic calculation causes the workflow to stop, we instead allow interpolations to be metallic but in such cases do not attempt to calculate the polarization of that structure. 40 candidates were found to have metallic interpolations.

The DFT workflow is labeled as complete when all polarization calculations along the path have completed or have been skipped in the case of metallic interpolation.

Post-processing Spontaneous Polarization Values

Only polar space groups are compatible with polarization vectors of arbitrary length. Nonpolar space groups are also compatible with a polarization vector, but the polarization vector modulo quantum of polarization along each lattice direction must be zero or a half quantum. If we can find a reference nonpolar structure that is sufficiently similar to our polar struc-

ture, we can calculate the polarization of several interpolations between this initial reference nonpolar and final the ferroelectric, polar structure. This structure is used as a means to calculate the spontaneous polarization, it is not necessary for the nonpolar structure to exist for the polar material to be ferroelectric or for us to calculate a valid polarization.

Starting with the nonpolar structure, we can calculate its polarization which is either zero or a half quantum of polarization along the three lattice directions. Then we perform the same calculation for the first interpolation, and then the next, until we arrive at the final polar structure. If we have a sufficient number of interpolations between our structures, we will have hopefully traced out smooth, continuous paths in polarization space. Subtracting the vectors at the nonpolar beginning and the polar ending of these paths will give us the spontaneous polarization vector.

We perform the following steps to recovering the same branch polarization. We first construct a periodic lattice for each interpolation with lengths and angles corresponding to the quantum of polarization along each lattice direction; this corresponds to the second term of the polarization equation given in the section Ferroelectricity from first-principles. For calculating polarization, the lengths of the lattice vectors are divided by the volume of the unit cell and multiplied by conversion factors for electron charge and length scale. Because our polar and nonpolar structures can have different lattices, the quantum of polarization along the a, b, and c lattice parameters can differ for each structure. See Figure 6.3 for an example for BaTiO₃.

Our algorithm for adjusting the polarizations to be on the same branch is depicted in Figure 6.4. First, we take the nonpolar polarization, and choose the image of the polarization value in the nonpolar polarization lattice that is closest to Cartesian coordinates (0,0,0) which is one corner of the unit cell. The value of the nonpolar polarization along a, b, and c can either be zero or a half-quantum. Then, we find the image the of the first interpolation polarization value (using the first interpolation lattice) that is closest to the Cartesian coordinates (since lattices may differ) of the moved nonpolar polarization value. We continue this process until we get to the polar polarization.

This algorithm will find the polarization path with the smallest difference between polarizations of subsequent interpolations. This can cause the algorithm to find the incorrect same branch polarization in cases where the change in polarization between interpolations is larger than the quantum of polarization between branches. One example of this failure mode is polarization resolved for CrO₃ with workflow ID `wfid_1484694851.899452`, see Figure 6.5. In this example, the algorithm chooses a discontinuous path that has a smaller spontaneous polarization of 79.9 $\mu\text{C}/\text{cm}^2$ in red. However, the most continuous path uses the last three interpolations in the branch shown with a dashed red line give a polarization of 124.7 $\mu\text{C}/\text{cm}^2$.

Graphical Interface

To view the ferroelectric candidate data in aggregate, we create an interactive web site for viewing polarization and total energy plots, animations of the distortion, and other

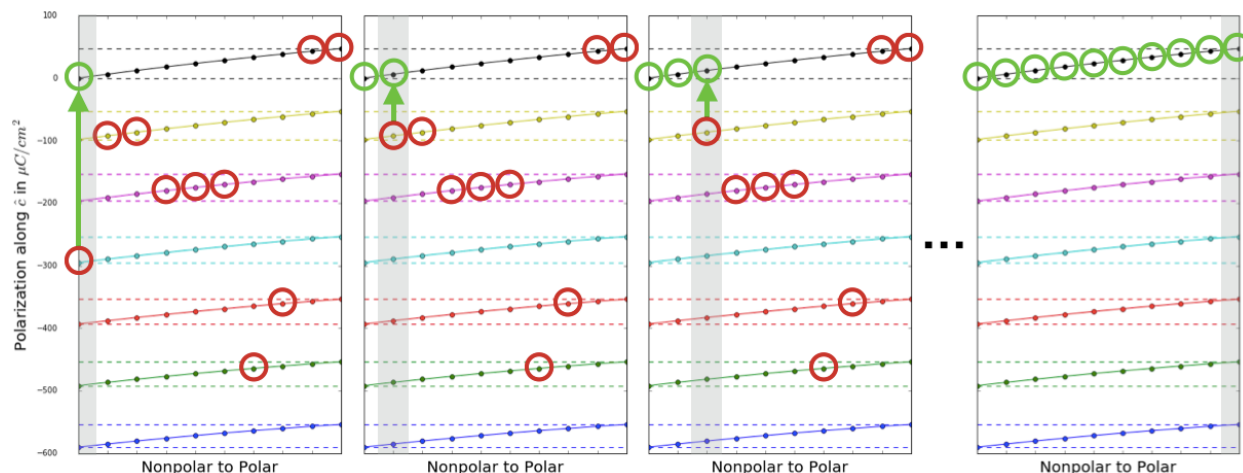


Figure 6.4: A visual demonstration of the same branch polarization algorithm demonstrated in 1D (rather than 3D) using BaTiO_3 . As mentioned in Figure 6.3, VASP returns polarizations all along the branch starting at $-600 \mu\text{C}/\text{cm}^2$. However, to better demonstrate the algorithm, we will suppose that the values for the polarization for each interpolation are those circled in red. In the first panel, we move the nonpolar polarization to be on the branch closest to zero. In the second panel, we move the first interpolated polarization to be on the branch closest to the adjusted nonpolar polarization. In the third panel, we move the second interpolated polarization to be on the branch closest to the adjusted first interpolation polarization. If the algorithm finishes successfully, the adjusted polarizations will be on the same branch.

data. The interface consists of two main pages: 1) a page containing a sortable table of ferroelectric candidates organized by category (whether the candidate had a polarization resolved and if so with what confidence) and 2) individual candidate pages that show energy and polarization plots, distortion animations, and other data specific to that candidate. This interface is available at https://blondegeek.github.io/\penalty\z@\ferroelectric_search_site/.

Code Availability

The Vienna Ab Initio Software Package (VASP) used to perform DFT calculations is a proprietary code. The Bilbao Crystallographic Server (BCS) is freely available on-line at <http://www.cryst.ehu.es>. Fireworks, atomate, and pymatgen are python packages accessible on GitHub. Fireworks and atomate are released under a modified BSD (Berkeley Software Distribution) License. pymatgen is released under a MIT (Massachusetts Institute of Technology) License. Both MIT and BSD licenses are open-source and permit both commercial and non-commercial use. Our workflow code is included in atomate version 0.6.7 and our analysis code is available in pymatgen since v4.7.4.

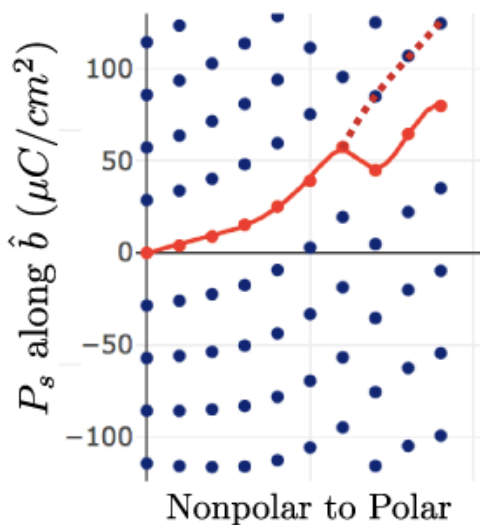


Figure 6.5: The polarization reconstruction for CrO_3 with workflow ID `wfid_1484694851.899452`. The polarization along the b lattice parameter is incorrectly reconstructed because the different polarization branches are closer than the change in polarization between structure interpolations. To correctly reconstruct this polarization with our existing algorithm, more structure interpolations would be needed between the nonpolar and polar structures.

Our code for recovering the same branch polarization from polarization calculations has been contributed to `pymatgen` under the `pymatgen.analysis.ferroelectricity` module. Our code for the DFT and polarization analysis workflows for performing polarization calculations has been contributed to `atomate` under the `atomate.vasp.workflows.base.ferroelectric` module. We also release a python package to automate interaction with several BCS's tools used in this search called `billbaocrystapi`. We also provide code for the interface that we used to view our candidates in aggregate. The web interface for the current work is hosted at http://blondegeek.github.io/ferroelectric_search_site/. The code for the interface can be found at http://github.com/blondegeek/penalty_z@ferroelectric_search_site.

6.3 Data Records

This dataset is available as two JSON files deposited in FigShare (doi:10.6084/m9.figshare.6025634 and doi:10.6084/m9.figshare.5048425) and our GitHub repository (http://github.com/blondegeek/ferroelectric_search_site). We also provide an interface for viewing the dataset at http://blondegeek.github.io/ferroelectric_search_site.

The JSON files provide details of the symmetry analysis performed for each candidate and data generated by DFT calculations and post-processing from the workflow.

VASP input and output files for each candidate are provided as a zip file on FigShare. The title of the zip file includes the workflow ID to correlate the VASP files to information in the JSON files provided.

File format

We contribute the following data:

1. JSON file with information describing all nonpolar-polar structure pairs with group-subgroup relations compatible with a second-order phase transition in the Materials Project determined with BCS Structure Relations and used in this search. See Tables 6.2 and 6.3 for details.
2. JSON file with information on workflow status of each calculated candidate and calculation details extracted from VASP inputs and outputs. This includes total energy, band gap, polarization, post-processed information and validation criteria for candidates with completed calculation. See Table 6.4 for details.
3. Zipped folders with the VASP INCAR, KPOINTS, OUTCAR, and POSCAR files.

Properties

For each candidate we provide an initial nonpolar-polar pair of structures, including the nonpolar structure in the nonpolar, high-symmetry setting and polar, low-symmetry setting. We also provide the displacements of each atom and other metrics provided by BCS Structure Relations.

For each successful calculation, we provide the structure used for calculation, the ionic and electronic polarization computed by VASP, the ionic polarization computed via the method of point charges, the energy and energy per atom of the structure, and other commonly computed quantities such as total magnetization, magnetization per atom, forces, and stresses. We also give details as to which calculations (out of the 22 computed) for a given candidate were completed.

For each set of completed calculations we also provide, the recovered spontaneous polarization using the algorithm described in the Method section and spline data characterizing the smoothness of the recovered polarization and energy trend across the nonpolar-polar distortion.

Graphical representation of results

In Figure 6.7, we partition the high-quality candidates into known and new ferroelectrics and further partition those ferroelectrics into subclasses. In 6.7 we see that known and new ferroelectric candidates are well mixed along the metrics of nonpolar-polar structure energy

difference, distortion maximum between nonpolar and polar structures, PBE band gap of polar structure, and energy above hull.

In the middle of Figure 6.7, the high performers denoted with red triangles are the perovskite family. Perovskites dominate the ferroelectric literature and we recover many known perovskite ferroelectrics in this search: LiNbO_3 , AlBiO_3 , BiInO_3 , KNbO_3 , BaO_3Ti , $\text{Bi}_2\text{Nb}_2\text{O}_9\text{Pb}$, $\text{Bi}_2\text{O}_9\text{SrTa}_2$, NaNbO_3 , $\text{Bi}_4\text{O}_{12}\text{Ti}_3$, CdO_3Ti , O_3PbTi , Bi_2MoO_6 , HfO_3Pb , O_3PbZr and $\text{Ca}_3\text{Mn}_2\text{O}_7$.

Other classes identified in the middle of Figure ?? are the organic $(\text{NH}_4)_2\text{SO}_4$ family in blue, boracites in green and structures already proposed by theory to be ferroelectric in purple. These show that there are many known and proposed ferroelectrics in the literature with polarizations of $10 \mu\text{C}/\text{cm}^2$ or less.

In the bottom row of Figure 6.7, we categorize new ferroelectric candidates into different trending compositions or structure types. There are several candidates containing fluorides, oxocarbons, and hydroxyl groups. We highlight these candidates because they are very different in composition from oxide ferroelectrics most common in the literature. We also point out some hypothetical non-magnetic hexagonal manganite-like structures found in the Materials Project database that have polarizations of approximately $10 \mu\text{C}/\text{cm}^2$ and half-quantum nonpolar polarizations.

In Figure 6.8, we show trends in the number of deformation candidates with given nonpolar point group - polar point group transitions. Each space group is comprised of translation and point group symmetry. There are 32 point groups; polar point groups are shown in red and nonpolar in blue. The thickness and color of line connecting nonpolar and polar point groups indicate the number of structures in the dataset with a deformation between those point groups. Point group transitions that correspond to orthorhombic structures such as $mmm \rightarrow mm2$, monoclinic structures such as $2/m \rightarrow 2$ or $2/m \rightarrow m$, and hexagonal $6/mmm \rightarrow 6mm$ are most prevalent.

In Figure 6.9, we show polarization of ferroelectric candidates plotted by polar point group, similar to the plot of piezoelectric tensor magnitudes in Ref. [71]. The majority of candidates have polarization less than $5 \mu\text{C}/\text{cm}^2$, shown on the right. The high performers in point group $4mm$ are perovskites with a reference structure with in point group $m - 3m$. The darkness of a radial cell is proportional to the the number of candidates in that region of the plot. For example, there are many candidates with polar point groups 2 and $mm2$ that have polarizations within $25 \mu\text{C}/\text{cm}^2$.

6.4 Technical Validation and Verification

Verification of computational methodology

Several checks are needed to ensure our automated calculations have completed satisfactorily and the information automatically extracted from them is reliable.

Table 6.2: Key, value data type, and value description for `distortion.json` entries.

Key	Type	Description
<code>_id</code>	<code>bson.ObjectId</code>	These ids are used to generate cid in <code>workflow_data.JSON</code> file
<code>pretty_formula</code>	<code>unicode</code>	Composition with elements sorted by electronegativity.
<code>polar_id</code>	<code>unicode</code>	Materials Project Id
<code>nonpolar_id</code>	<code>unicode</code>	Materials Project Id
<code>polar_icsd</code>	<code>float</code>	ICSD id number, if available
<code>nonpolar_icsd</code>	<code>float</code>	ICSD id number, if available
<code>polar_spacegroup</code>	<code>float</code>	Polar space group, integer between 1 and 230
<code>nonpolar_spacegroup</code>	<code>float</code>	Nonpolar space group, integer between 1 and 230
<code>bilbao_polar_spacegroup</code>	<code>float</code>	Polar space group from Bilbao Crystallographic Server, integer between 1 and 230
<code>bilbao_nonpolar_spacegroup</code>	<code>float</code>	Nonpolar space group from Bilbao Crystallographic Server, integer between 1 and 230
<code>distortion</code>	<code>dict</code>	Details pertaining to distortion between nonpolar and polar structure.
<code>polar_band_gap</code>	<code>float</code>	Materials Project computed band gap.
<code>nonpolar_band_gap</code>	<code>float</code>	Materials Project computed band gap.

 Table 6.3: JSON keys, value data type, and value description for `distortion.json` entries.

Key	Type	Description
<code>high_symm</code>	<code>dict of pymatgen.Structure</code>	Nonpolar structure in high-symmetry setting
<code>high_low_setting</code>	<code>dict of pymatgen.Structure</code>	Nonpolar structure in low-symmetry setting
<code>low_symm</code>	<code>dict of pymatgen.Structure</code>	Polar structure in low-symmetry setting
<code>high_pre</code>	<code>unicode</code>	Structure information as directly output by Bilbao Crystallographic Server website
<code>high_low_pre</code>	<code>unicode</code>	Structure information as directly output by Bilbao Crystallographic Server website
<code>low_pre</code>	<code>unicode</code>	Structure information as directly output by Bilbao Crystallographic Server website
<code>distortion</code>	<code>list</code>	Table of low-symmetry setting of Wyckoff position, the string “(x, y, z)”, species, distortion in x, y, and z, and the magnitude of distortion
<code>pairings</code>	<code>list</code>	Wyckoff splitting pairing between high symmetry and low symmetry structures.
<code>dmax</code>	<code>unicode</code>	Maximum distortion distance between nonpolar and polar structure.
<code>s</code>	<code>unicode</code>	Degree of lattice distortion (S) is the spontaneous strain (sum of the squared eigenvalues of the strain tensor divided by 3).
<code>dav</code>	<code>unicode</code>	Maximum distortion distance between nonpolar and polar structure.
<code>delta</code>	<code>unicode</code>	The measure of compatibility (Δ) (Bergerhoff et al. 1998)

Table 6.4: Key, value data type, and value description for `workflow_data.json` entries.

Key	Type	Description
<code>_id</code>	<code>bson.ObjectId.ObjectId</code>	The workflow id.
<code>wfid</code>	<code>unicode</code>	The alphanumeric portion of the string after <code>cid_</code> corresponds to the <code>bson.ObjectId.ObjectId</code> used in the distortion database
<code>cid</code>	<code>unicode</code>	Status of workflow denoted by FireWorks.
<code>workflow_status</code>	<code>unicode</code>	Composition with elements sorted alphabetically.
<code>alphabetical_formula</code>	<code>unicode</code>	Composition with elements sorted by electronegativity.
<code>pretty_formula</code>	<code>unicode</code>	Materials Project Id
<code>polar_id</code>	<code>unicode</code>	Materials Project Id
<code>nonpolar_id</code>	<code>unicode</code>	ICSD id numbers, if available.
<code>polar_icsd_ids</code>	<code>list of floats</code>	ICSD id numbers, if available.
<code>nonpolar_icsd_ids</code>	<code>list of floats</code>	Polar space group, integer between 1 and 230.
<code>polar_spacegroup</code>	<code>float</code>	Nonpolar space group, integer between 1 and 230.
<code>nonpolar_spacegroup</code>	<code>float</code>	Polar structure as referenced in distortion JSON file
<code>orig_polar_structure</code>	<code>dict of pymatgen.Structure</code>	Nonpolar structure as referenced in distortion JSON file
<code>orig_nonpolar_structure</code>	<code>dict of pymatgen.Structure</code>	Static calculation structures. Fully complete workflows have 10.
<code>structures</code>	<code>List of dicts of pymatgen.Structure</code>	Number of relaxation calculations performed. Fully complete workflows have 2.
<code>relaxation_len</code>	<code>float</code>	The task labels of the relaxation calculations performed.
<code>relaxation_task_labels</code>	<code>list of strs</code>	Number of static calculations performed. Fully complete workflows have 10.
<code>static_len</code>	<code>float</code>	The task labels of the static calculations performed.
<code>static_task_labels</code>	<code>list of strs</code>	The task labels of polarization calculations performed. Fully complete workflows have 10.
<code>polarization_len</code>	<code>float</code>	Number of polarization calculations performed. Fully complete workflows have 10.
<code>polarization_task_labels</code>	<code>list of strs</code>	The task labels of the polarization calculations performed.
<code>polarization_change_norm</code>	<code>float</code>	The Cartesian norm of the recovered spontaneous polarization.
<code>polarization_change</code>	<code>list of floats</code>	The vector along a, b, and c of the recovered spontaneous polarization.
<code>raw_electron_polarization</code>	<code>list of list of floats</code>	Raw electron polarization per polarization calculation structure from VASP
<code>raw_ionic_polarization_vasp</code>	<code>list of list of floats</code>	Raw ionic polarization per polarization calculation structure from VASP
<code>raw_ionic_polarization</code>	<code>list of list of floats</code>	Raw ionic polarization per polarization calculation structure from <code>calc.ionic</code> .
<code>polarization_quanta</code>	<code>list of list of floats</code>	Polarization quanta along a, b, and c lattice vectors for each polarization calculation structure
<code>same_branch_polarization</code>	<code>list of list of floats</code>	Same branch polarization along a, b, and c for each polarization calculation structure.
<code>polarization_max_spline_jumps</code>	<code>list of floats</code>	Max jump between spline and data for polarization along a, b, and c.
<code>polarization_smoothness</code>	<code>list of floats</code>	Average jump between spline and data for polarization along a, b, and c.
<code>energies</code>	<code>list of floats</code>	Energy in eV for each static calculation structure
<code>energies_per_atom</code>	<code>list of floats</code>	Energy per atom in eV for each static calculation structure
<code>energies_per_atom_max_spline_jumps</code>	<code>float</code>	Max jump between spline and data for energy per atom.
<code>energies_per_atom_smoothness</code>	<code>float</code>	Average jump between spline and data for energy per atom.
<code>calculated_max_distance</code>	<code>float</code>	Calculated max distortion distance. Compare to <code>dmax</code> in <code>distortion.json</code> entries.
<code>zval_dict</code>	<code>dict</code>	dict with keys of species and values of ZVAL in number of electrons.
<code>hubbards</code>	<code>dict</code>	dict with keys of species and values of Hubbard U correction in eV pairs.
<code>cbms</code>	<code>list of floats</code>	Conduction band minimum per static calculation computed structures
<code>vbms</code>	<code>list of floats</code>	Valence band maximum per static calculation computed structures
<code>stresses</code>	<code>list of list of floats</code>	stress tensor per static calculation computed structures
<code>charges</code>	<code>list of dict of floats</code>	Charges projected onto spd orbitals per atom per static calculation computed structures
<code>magnetization</code>	<code>list of list of floats</code>	Magnetization in Bohr magnetons per atom per static calculation computed structures
<code>total_magnetization</code>	<code>list of floats</code>	Total magnetization in Bohr magnetons per static calculation computed structures
<code>forces</code>	<code>list of list of floats</code>	Cartesian forces per atom per static calculation computed structures
<code>bandgaps</code>	<code>list of floats</code>	list of band gaps in eV for static calculation computed structures

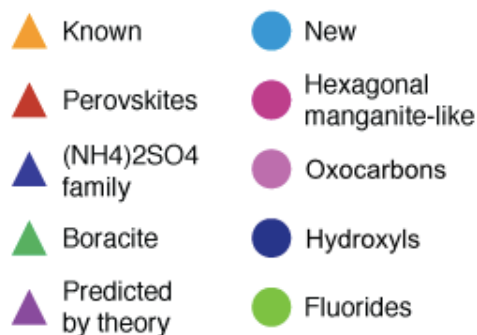


Figure 6.6: Legend for Figure 6.7.

Testing smoothness of energy and polarization trends with distortion

We want to flag any ferroelectric candidates whose calculations cannot be used to reliably assess the quality of the candidate. For example, if the trend in total energy is not continuous, we cannot be confident that we can extract a meaningful polarization trend. Similarly, if the same branch polarization is not continuous, we can not be confident that an accurate spontaneous polarization has been determined.

To assess the smoothness of trends in polarization and energy across a distortion, we use `UnivariateSplines` from `scipy.interpolate`. We use cubic splines for fitting polarizations and quartic splines for fitting total energies. We use the default smoothness parameter of 1.0. With this default, quartic splines sometimes fail for steep double wells. These splines can be generated using the `Polarization` class in `pymatgen.analysis.ferroelectricity.polarization`.

We found 13 materials to have several discontinuities in total energy (even when these calculations resulted in smooth polarizations). These materials were transition metal oxides, fluorides, carbonates, orthosilicates, and phosphates with alkali metals (Li, Na, and Ba for these specific examples), many being Li-ion battery cathode candidates. The transition metals in these materials (Co, Cr, Fe, Mn, Ni, V) can take multiple oxidation states. Because these discontinuities in energy were coincident with discontinuities in the total magnetization, we believe the cause of these jumps were caused by the transition metal species changing oxidation state through the distortion. To mitigate this, one might be able to constrain the total magnetization for each interpolation based on the interpolation of the initial nonpolar magnetization and final polar magnetization.

Metallic endpoints and metallic interpolations

Workflows that have either polar or nonpolar structures that are calculated to be metallic are halted. In the `workflow_data.json`, these workflows are designated by a `workflow_status` of “DEFUSED”. 86 structures have metallic endpoints. These candidates do not have interpolation calculations performed. Occasionally, interpolations between two nonmetallic

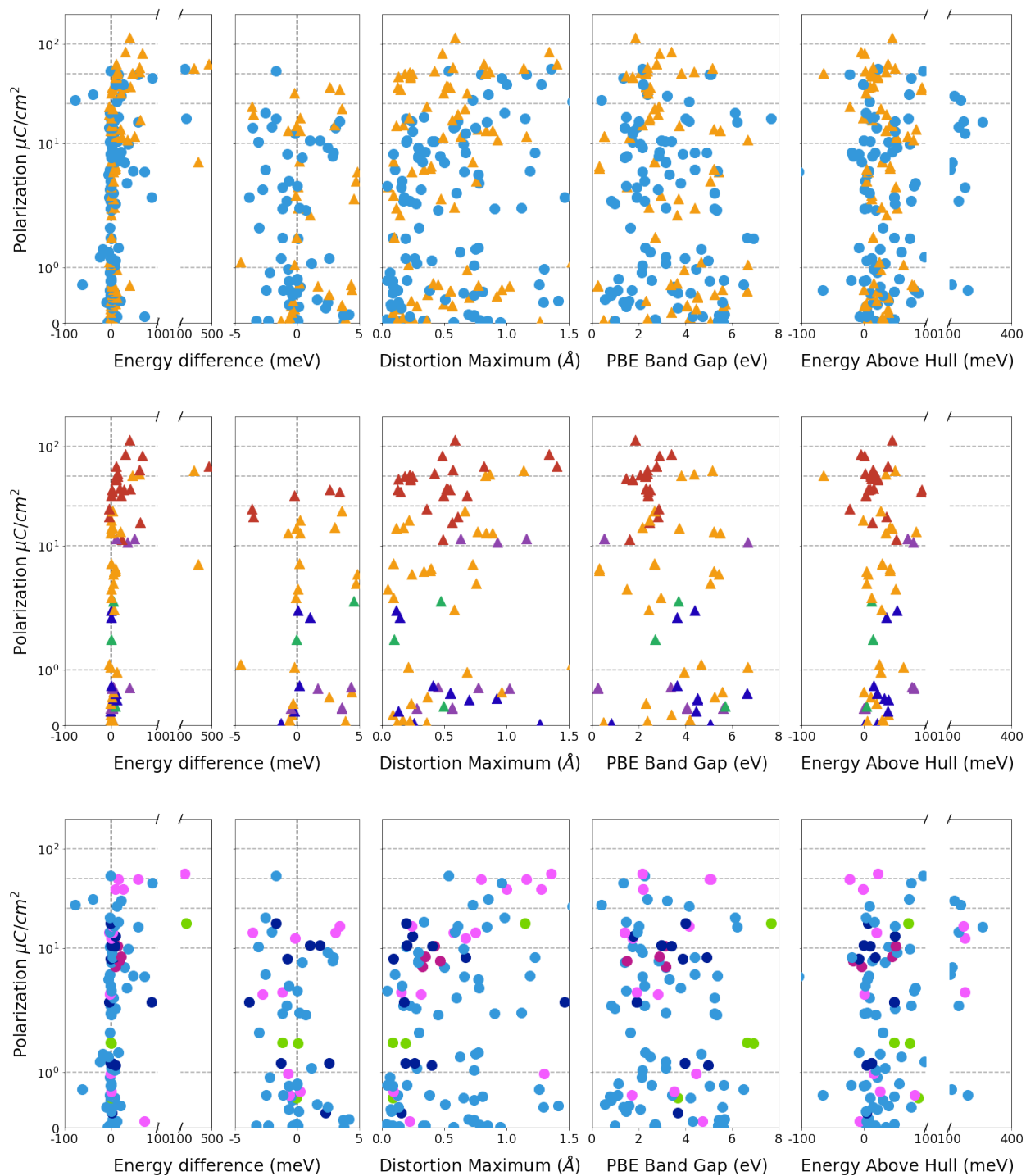


Figure 6.7: Validated ferroelectric candidates from our search. Spontaneous polarization plotted against nonpolar-polar energy difference, maximum atomic distortion, PBE band gap, and energy of polar structure above lowest energy polymorph reported in the Materials Project.

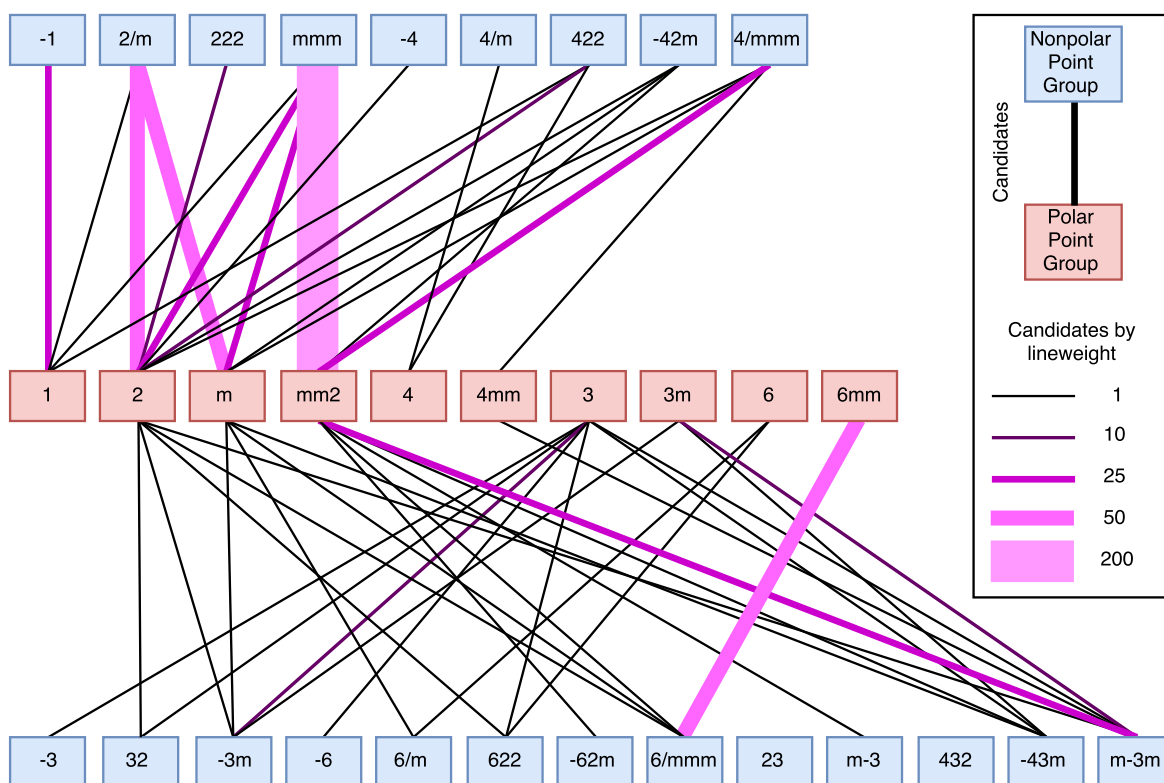


Figure 6.8: Distortion candidate point group relations.

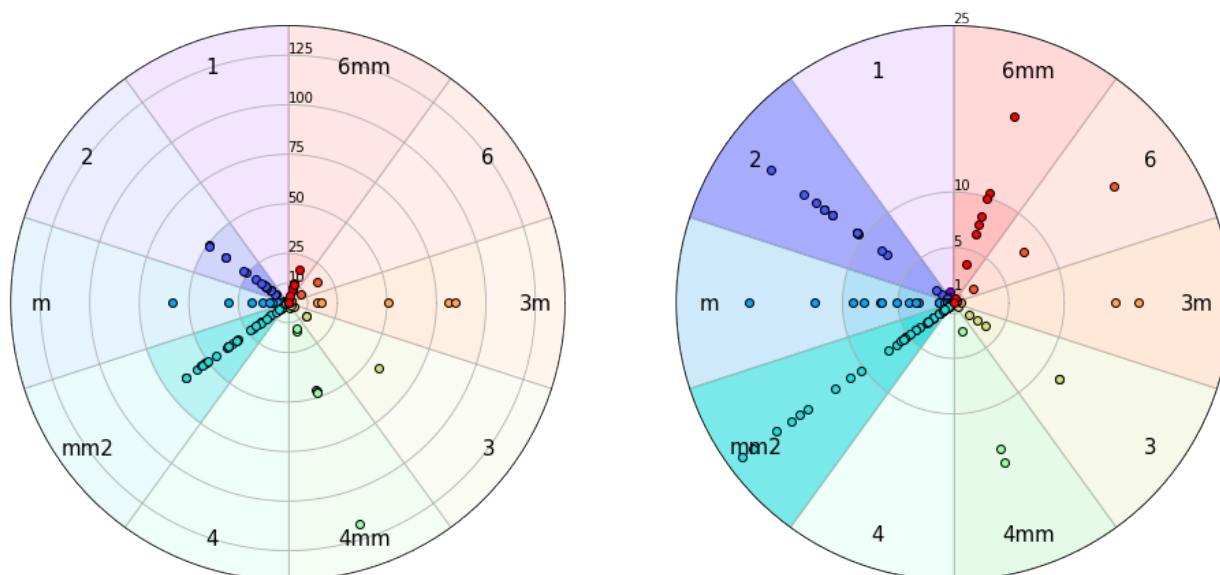


Figure 6.9: Diagrams of polarization magnitude vs. point group.

structures are metallic. Out of our 239 completed workflows, 40 of them had metallic interpolation structures. If any interpolation along the path from nonpolar to polar structure is metallic, the quality of automated analysis cannot be guaranteed. We include these candidates in our dataset, but they are noted as having a “polarization_len” of less than 10 or do not have a “polarization_change_norm” (in cases where some of the interpolated polarizations are None). If a candidate has a “polarization_len” equal to 10 and have a “polarization_change_norm”, all polarization calculations completed successfully.

Comparison of Materials Project to Relaxed Structures

Two structural relaxation steps are already performed on all structures in the Materials Project. We perform additional relaxations of the unit cell and atomic positions to ensure total energy convergence. We found only less than 5% (10%) of our relaxed structures have lattice parameter differences that differed larger than 3% (1%) from the original Materials Project structures. Because we perform relaxations of nonpolar structures transformed to the low symmetry polar setting, we compare the relaxed nonpolar structure to the low symmetry transformed structure output by BCS of the nonpolar structure from Materials Project.

Known and New Ferroelectrics

In any high-throughput search, there are calculations that complete perfectly and some that require further scrutiny to understand. We deem high-quality candidates as calculations where the polarization and total energy trends are smooth and continuous according to a max difference between the data and fitting spline to be $10^{-1} \mu C/cm^2$ for the spline fit to the same branch adjusted polarization and $10^{-2} eV$ for spline fit to the energy trend versus distortion.

Out of the 239 candidates, 183 pass through our stringent validation that ensures the polarization and energy trends across the ferroelectric distortion are smooth and continuous. The remaining candidates are still valid candidates; we recommend checking the polarization and energy trends by eye as the algorithms used for analysis may not have been able to reliably recover the spontaneous polarization in these cases.

The only factor that distinguishes known ferroelectrics from new ferroelectrics in our workflow is whether or not a given ferroelectric candidate is present in the literature. Thus, we perform a literature review by hand for every considered candidate. We leave automating such literature searches to future work. We find out of 183 high quality candidates, 78 are known or previously proposed and 105 are new ferroelectric candidates.

In Figure 6.7, we plot nonpolar-polar total energy difference, maximum distortion distance, PBE band gap, and energy difference between the polar structure and lowest energy polymorph reported in the Materials Project of known and proposed and new ferroelectric candidates versus the calculated spontaneous polarization. The legend for these is in Figure 6.6. We also provide tables of the new candidates in Tables E.2 and E.3 and of the known candidates in Tables E.4 and E.5.

As seen in the top of Figure 6.7, there are no trends in these quantities that distinguish known versus new ferroelectrics. The plots in the middle of Figure 6.7 demonstrate the variety of known ferroelectric candidates that we are able to recover, from perovskites and boracites to candidates in the organic $(\text{NH}_4)_2\text{SO}_4$ family and proposed by theory. The plots at the bottom of Figure 6.7 show categories of new ferroelectric candidates we find in the Materials Project, some from previously known ferroelectric classes such as hexagonal manganite-like structures and surprising categories such as fluorides, crystals containing oxocarbons, and crystals containing hydroxyl groups. We elaborate on these categories of known and new ferroelectrics in the Graphical representation of results.

Validation through comparison to hand-curated list of ferroelectrics in the Pauling File database

The Pauling File is a materials database accessible through SpringerMaterials [2]. In this database, there are materials tagged as ferroelectric and antiferroelectric. We use these tagged entries to estimate how many known (anti)ferroelectrics make it through our workflow.

In the Pauling Files, there are 955 distinct compositions tagged as (anti)ferroelectric, 306 of which are pure (not doped) compositions. Out of 306 pure compositions, 95 of those compositions are included in the Materials Project as polar materials. This does not necessarily mean that the Materials Project database contains the same ferroelectric polar structure as referenced in the Pauling Files, simply that there exists a polar structure in the Materials Project with the same composition as a tagged ferroelectric or antiferroelectric in the Pauling Files. 57 of these compositions have nonpolar-polar structures in the Materials Project, 42 of which are found to be deformable by BCS Structure Relations. 33 of the 42 are successfully identified by the workflow to have smooth polarizations. Out of the 9 candidates that did not successfully make it through the workflow, 6 of them (BiFeO_3 , CrO_3Y , Eu_2GeSe_4 , O_3W , CuLa_2O_4 , Cl_3CoTi) had metallic endpoints, 2 candidates (MnO_3Y and Br_3MnRb) had metallic interpolation structures, and for 1 candidate ($\text{Ge}_3\text{O}_{11}\text{Pb}_5$), there was a problem converting the BCS provided structures into a pymatgen Structure objects. This suggests that the primary impact to the robustness of our workflow is the level of DFT used; since PBE tends to underestimate band gaps, several of these candidates are experimentally insulating but are metallic in our calculations.

Validation through comparison to experimental measurements in Landolt-Börnstein series

Experimentally measured polarizations depend greatly on the quality of the sample and method used to measure the spontaneous polarization. For many ferroelectrics, there are experimental polarization measurements that have been made across decades that vary greatly depending on these factors. For example, measurements of single crystal BiFeO_3 in 1970 found the polarization to be less than $6.1 \mu\text{C}/\text{cm}^2$ [244]. Thin films of BiFeO_3 were measured to have a polarization 50-90 $\mu\text{C}/\text{cm}^2$ [259] in 2003. Then, first-principles calculations pre-

sented in 2005 predicted the polarization of single crystal BiFeO_3 to be 90-100 $\mu\text{C}/\text{cm}^2$ [180]. These first-principles results motivated further experimental investigation. Multiple teams studying ceramic BiFeO_3 found a small spontaneous polarization of less than 10 $\mu\text{C}/\text{cm}^2$ attributed to the high-conductivity of their samples causing a leakage current [196, 196]. Subsequent measurements of single crystal BiFeO_3 which conversely have high-resistivity permitted measuring a polarization that was in agreement with first-principle calculations [145].

We compare our calculated polarizations to ferroelectric materials referenced in the Landolt-Börnstein - Group III Condensed Matter - Ferroelectrics and Related Substances [227, 228, 229, 230]. This series classifies hundreds of ferroelectrics into a 72 class numbering scheme. We note that polarization values for ferroelectrics in the Landolt-Börnstein series volumes 36A, 36B and 36C may be superseded by more recent experimental measurements.

Plots of calculated vs. experimental spontaneous polarizations are shown in Figure 6.10 and tabulated in Table E.1. For experimental polarizations greater than 10 $\mu\text{C}/\text{cm}^2$, the majority of experimental polarizations are between 25% and -50% of those that we calculate. The exceptions are NaNbO_3 and $\text{Bi}_2\text{O}_9\text{SrTa}_2$, which are calculated to have polarizations much greater than their experimental values, and the polarization of $\text{Bi}_4\text{O}_{12}\text{Ti}_3$ which is calculated to be much lower than the experimental value. The multiple entries of a given formula on the plot indicate multiple calculations in our dataset for the same compound. Compounds with polarizations of less than or equal to 1 $\mu\text{C}/\text{cm}^2$ are not shown on the plot given the log-log scale. For polarizations less than 5 $\mu\text{C}/\text{cm}^2$, we see our calculations capture the general trends of the experimental polarizations.

We find that the PBE functional we use for our DFT calculations overestimates polarizations. This is partially due to unit cells relaxed with PBE having larger than experimental volumes and thus larger distortions.

Validation through comparison to DFT calculated polarizations

DFT calculated values for the ferroelectric polarization depends heavily on the structures and functional used in the calculation. For example, we relax the full geometry of our endpoint structures. Other references constrain the relaxed polar unit cell to have the same volume as the experimental structure. One such example is [27]; these calculated polarizations will be systematically smaller than ours due to PBE optimized structures having larger than experimental lattice parameters.

We compare to literature where a fully optimized (unit cell, volume, and atomic positions) relaxation procedure is used. The ferroelectric first-principles literature is largely dominated by studies of perovskites. We compare to calculations for the following perovskites: BaTiO_3 , PbTiO_3 , LiNbO_3 , $\text{SrBi}_2\text{Ta}_2\text{O}_9$, BiAlO_3 , CdTiO_3 , $\text{Ca}_3\text{Mn}_2\text{O}_7$, BiFeO_3 , and YMnO_3 . These comparisons are summarized in Table 6.5. We find our calculations in excellent agreement with the literature that use comparable methods, the only exception being BiFeO_3 , and YMnO_3 .

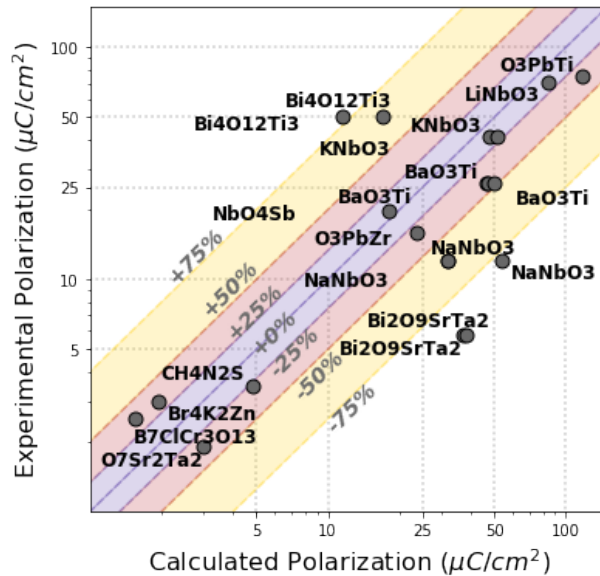


Figure 6.10: Experimental vs. Calculated polarizations for ferroelectric materials in the Landolt-Börnstein series. Note, the plot is log-log. We give colored regions to show which experimental values are within ± 25 , ± 50 , and ± 75 of calculated values.

BiFeO₃ candidates (of which there are 3) are found to have a metallic nonpolar structure and YMnO₃ candidates (of which there are 4) are found to have metallic intermediate structures by our workflow and thus do not have computed polarizations in this dataset. Ref. [275] notes difficulties in calculating polarizations for these structures due to LDA and PBE underestimating the gap. They attempt to calculate these polarizations at the level of PBE using a Hubbard U correction of 2 eV and 7.5 eV for the Fe in BiFeO₃ and Mn in YMnO₃, respectively. They are successful in calculating the polarization of BiFeO₃, but YMnO₃ is still metallic in their PBE calculations even with the Hubbard U correction. We used a Hubbard U correction of 5.3 eV for Fe and 3.9 eV for Mn. See [1] for elaboration on how Hubbard U's are chosen in our workflow. We have a metallic nonpolar structure for BiFeO₃ and several metallic interpolations for YMnO₃, thus we do not obtain the spontaneous polarization of either.

6.5 Usage Details

In this chapter, we present 414 nonpolar-polar structure pairs in the Materials Project database that are compatible with a second-order phase transition as ferroelectric candidates and perform DFT calculations of total energy, band gap and polarization for these structures pairs.

This dataset offers the first opportunity to compare many known and new ferroelectrics

Table 6.5: Comparison of this work to other ab initio studies of ferroelectric perovskites. † indicates the reference being compared to used the Local Density Approximation (LDA) functional in their calculations. LDA results tend to be smaller than results calculated with PBE (which we use in this work) due to smaller predicted lattice parameters by LDA than PBE. The workflow ids for entries in the table are (1) wfid_1476040944.53976 (2) wfid_1476040944.53976 and wfid_1476040947.794782 (3) wfid_1476040956.832394 (4) wfid_1476040982.95148 (5) wfid_1476041128.167316 (6) wfid_1476040384.215156 (7) wfid_1476040759.946834 (8) wfid_1484445148.273011 (9) wfid_1484445014.628732 (10) wfid_1476040851.179557.

Formula and Space Group		a (Å)	b (Å)	c (Å)	P_s ($\mu\text{C}/\text{cm}^2$)
BaTiO ₃ (99)	Ref. [257]	4.005	-	4.210	43.5
	Ref. [275]	4.000	-	4.216	47
	This work (1)	4.001	-	4.216	46.3
	This work (2)	4.000	-	4.225	47.1
PbTiO ₃ (99)	Ref. [275]	3.844	-	4.767	125.5
	This work (3)	3.867	-	4.600	117.2
LiNbO ₃ (161)	Ref. [275]	5.203	-	14.11	84.4
	This work (4)	5.216	-	14.11	84.1
SrBi ₂ Ta ₂ O ₉ (36)	Ref. [269]	5.55	5.55	25.10	34.1
	This work (5)	5.599	5.612	25.509	37.0
CdTiO ₃ (26)	Ref. [144] [†]	5.2498	5.3870	7.5699	21
	This work (6)	5.402	5.524	7.693	37.0
CdTiO ₃ (33)	Ref. [144] [†]	5.2392	5.3777	7.6192	29
	This work (7)	5.359	5.494	7.813	34.8
BiAlO ₃ (161)	Ref. [34] [†]	3.84 (cubic)	-	-	75.6
	This work (8)	3.845	-	-	81.1
Ca ₃ Mn ₂ O ₇ (36)	Ref. [38] [†]	-	-	-	5
	This work (9)	19.476	5.332	5.377	5.6
	This work (10)	19.457	5.334	5.380	5.9

side by side with the same methodology. We believe by setting strict criteria for ferroelectricity and casting a wide-net using high-throughput searches, we will find candidates that challenge and advance our understanding of ferroelectric phenomena. As seen in our candidates, there may be many candidate ferroelectrics waiting to be discovered that defy our expectations. This dataset will be useful for creating new tools and criteria for analyzing diverse ferroelectrics.

The infrastructure provided by the Bilbao Crystallographic Server, FireWorks, pymatgen, and atomate is crucial to being able to perform these types of searches efficiently. Thus, we also provide our code and data for these searches with the hope they will lower the barrier for others to perform similar searches.

Our code for performing structural interpolations and polarization calculations has been incorporated into the pymatgen and atomate packages. We also release a python package to automate interaction with several BCS's tools used in this search. We also provide code for the interface that we used to view our candidates in aggregate.

The workflow we have presented can be extended to any crystal structure database, experimental and hypothetical. Several small modifications can be made to this workflow to extend the scope of these searches. The same DFT workflow can be used to screen any experimentally measured polar structure by generating nonpolar reference structures with BCS Pseudosymmetry[57].

This workflow can also be adapted to perform species substitutions and find symmetry relations between structure types, classes of structures that share space group, Wyckoff positions, and other lattice similarities.

Chapter 7

Tensor Field Networks: Rotation- and Translation-Equivariant Neural Networks for 3D Point Clouds

The work described in this chapter was submitted to the 2018 International Conference on Machine Learning with the pre-print available as Ref. [246].

We introduce tensor field networks, which are locally equivariant to 3D rotations, translations, and permutations of points at every layer. 3D rotation equivariance removes the need for data augmentation to identify features in arbitrary orientations. Our network uses filters built from spherical harmonics; due to the mathematical consequences of this filter choice, each layer accepts as input (and guarantees as output) scalars, vectors, and higher-order tensors, in the geometric sense of these terms. We demonstrate how tensor field networks learn to model simple physics (Newtonian gravitation and moment of inertia), classify simple 3D shapes (trained on one orientation and tested on shapes in arbitrary orientations), and, given a small organic molecule with an atom removed, replace the correct element at the correct location in space.

7.1 Motivation

Convolutional neural networks are translation-equivariant, which means that features can be identified anywhere in a given input. This capability has contributed significantly to their widespread success.

In this chapter, we present a family of networks that enjoy much richer equivariance: the symmetries of 3D Euclidean space. This includes 3D rotation equivariance (the ability to identify a feature in any 3D rotation and its orientation) and 3D translation equivariance.

There are three main benefits. First, this is more efficient than data augmentation to obtain 3D rotation-invariant output, making computation and training less expensive. This

is significantly more important in 3D than 2D. Without equivariant filters like those in our design, achieving an angular resolution of δ would require a factor of $\mathcal{O}(\delta^{-1})$ more filters in 2D but $\mathcal{O}(\delta^{-3})$ more filters in 3D.¹ Second, a 3D rotation- and translation-equivariant network can identify local features in different orientations and locations with the same filters, which is helpful for interpretability. Finally, the network naturally encodes geometric tensors (such as scalars, vectors, and higher-rank geometric objects), mathematical objects that transform predictably under geometric transformations such as rotation. Here, and in the rest of this chapter, the word “tensor” refers to *geometric* tensors, not generic multidimensional arrays.

Our network differs from a traditional CNN in three ways:

- We operate on point clouds using continuous convolutions. Our layers act on 3D coordinates of points and features at those points.
- We constrain our filters to be the product of a learnable radial function $R(r)$ and a spherical harmonic $Y_m^{(l)}(\hat{r})$.
- Our filter choice requires the structure of our network to be compatible with the algebra of geometric tensors.

We call these *tensor field networks* because every layer of our network inputs and outputs tensor objects: scalars, vectors, and higher-order tensors at every geometric point in the network. Tensor fields are ubiquitous in geometry, physics, and chemistry.

Our motivation was to design a universal architecture for deep learning on atomic systems (such as molecules or materials), but our network design is quite general. We expect tensor field networks to be useful in many tasks involving 3D geometry. For example, tensor field networks could be used to process 3D images in a rotation- and translation-equivariant way. We mention other potential applications in Section 7.6.

In this chapter, we explain the mathematical conditions such a 3D rotation- and translation-equivariant network must satisfy, provide several examples of equivariant compatible network components, and give examples of tasks that this family of networks can uniquely perform.

7.2 Related work

Our work builds upon Harmonic Networks [265], which uses discrete convolutions and filters composed of circular harmonics to achieve 2D rotation equivariance, and SchNet [221], which presents a rotation-invariant network using continuous convolutions. The mathematics of rotation equivariance in 3D is much more complicated than in 2D because rotations in 3D do not commute; that is, for 3D rotation matrices A and B , $AB \neq BA$ in general (see Ref. [204] for more about the mathematics of tensors under 3D rotations). Ref. [65] introduce Spherical CNNs, which are equivariant models on spherical spaces. Our network differs from this work

¹This is because the manifold of orthonormal frames at a point in 2D (the group $O(2)$) has dimension 1 and in 3D ($O(3)$) has dimension 3.

because it is equivariant to all the symmetries of 3D Euclidean space, both 3D rotation and translation, and because it directly operates on more general data types, such as points. SchNet can be emulated by our network by only using $L = 0$ filters. Harmonic Networks is the 2D discretized analog of our 3D network. Our network and Spherical CNNs share much of the same mathematical underpinnings but differ in the learnable parameters for rotation-equivariant filters. Additionally, while Spherical CNNs use one convolution center, we use many.

Many other authors have investigated the problems of rotation equivariance in 2D, such as [278, 93, 149]. Typically these work by looking at rotations of a filter and differ in exactly which rotations and how that orientation information is preserved (or not) higher in the network.

Other authors have dealt with similar issues of invariance or equivariance under particular input transformations. G-CNNs [66] create invariance with *finite* symmetry groups (unlike the continuous groups in this work). Ref [65] use spherical harmonics and Wigner D -matrices but only address spherical signals (two dimensional data on the surface of a sphere). Ref. [134] use tensor algebra to create neural network layers that extend Message Passing Neural Networks [89], but they are permutation group tensors (operating under permutation of the indices of the nodes) not geometric tensors.

The networks presented in Ref. [197, 198] operate on point clouds and use symmetric functions to encode permutation invariance. Ref. [198] employ a randomized sampling algorithm to include pooling in the network. These networks do not include rotation equivariance.

Other neural networks have been designed and evaluated on atomic systems using nuclei centered calculations. Many of these capture 3D geometry just by including the pairwise distance between atoms (e.g. SchNet [222] and the graph convolutional model from Ref. [83]). Our work notably draws from SchNet [222] for the point convolutions, radial functions, and self-interaction layers. All models that rely only on pairwise distances or angles between points have the weakness (unlike this work) that they can not distinguish between chiral inputs (e.g. left hand and right hand), which have identical pairwise distances but are different shapes in 3D.

The other major approach to modeling 3D atomic systems is to voxelize the space [258, 51, 249]. In general, these are subject to significant expense, no guarantees of smooth transformation under rotation, and edge effects from the voxelization step.

An introduction to the concepts of steerability and equivariance in the context of neural networks can be found in Ref. [67], which focuses on discrete symmetries.

7.3 Representations and equivariance

A *representation* D of a group G is a function from G to square matrices such that for all $g, h \in G$,

$$D(g)D(h) = D(gh)$$

A function $\mathcal{L} : \mathcal{X} \rightarrow \mathcal{Y}$ (for vector spaces \mathcal{X} and \mathcal{Y}) is *equivariant* with respect to a group G and group representations $D^{\mathcal{X}}$ and $D^{\mathcal{Y}}$ if for all $g \in G$,

$$\mathcal{L} \circ D^{\mathcal{X}}(g) = D^{\mathcal{Y}}(g) \circ \mathcal{L}$$

Invariance is a type of equivariance where $D^{\mathcal{Y}}(g)$ is the identity for all g . We are concerned with the group of symmetry operations that includes isometries of 3D space and permutations of the points.

Composing equivariant networks \mathcal{L}_1 and \mathcal{L}_2 yields an equivariant network $\mathcal{L}_2 \circ \mathcal{L}_1$ (proof in Appendix H). Therefore, proving equivariance for each layer of a network is sufficient to prove (up to numerical accuracy) that a whole network is equivariant.

Furthermore, if a network is equivariant with respect to two transformations g and h , then it is equivariant to the composition of those transformations gh (by the definition of a representation). This implies that demonstrating permutation, translation, and rotation equivariance individually is sufficient to prove equivariance of a network to the group (and corresponding representations) containing all combinations of those transformations. As we describe shortly, translation and permutation equivariance are manifest in our core layers, so we will focus on demonstrating rotation equivariance.

Tensor field networks act on points with associated features. A layer \mathcal{L} takes a finite set S of vectors in \mathbb{R}^3 and a vector in \mathcal{X} at each point in S and outputs a vector in \mathcal{Y} at each point in S , where \mathcal{X} and \mathcal{Y} are vector spaces. We write this as

$$\mathcal{L}(\vec{r}_a, x_a) = (\vec{r}_a, y_a)$$

where $\vec{r}_a \in \mathbb{R}^3$ are the point coordinates and $x_a \in \mathcal{X}$, $y_a \in \mathcal{Y}$ are the feature vectors (a being an indexing scheme over the points in S). (To simplify the formulas here, we are assuming that inputs and outputs are at the same points in \mathbb{R}^3 , but this is not necessary.) This combination of \mathbb{R}^3 with another vector space can be written as $\mathbb{R}^3 \oplus \mathcal{X}$, where \oplus refers to the direct sum operation, where vectors in each space are concatenated and matrices acting on each space are combined into a larger block diagonal matrix.

We now describe the conditions on \mathcal{L} for equivariance with respect to different input transformations.

Permutation equivariance

$$\textit{Condition: } \mathcal{L} \circ \mathcal{P}_\sigma = \mathcal{P}_\sigma \circ \mathcal{L}$$

where $\mathcal{P}_\sigma(\vec{r}_a, x_a) := (\vec{r}_{\sigma(a)}, x_{\sigma(a)})$ and σ permutes the points to which the indices refer.

All of the layers that we will introduce in Section 7.4 are manifestly permutation-equivariant because we only treat point clouds as a *set* of points, never requiring an imposed order like in a list. In our implementation, points have an array index associated with them, but this index is only ever used in a symmetric way.

Translation equivariance

$$\text{Condition: } \mathcal{L} \circ \mathcal{T}_{\vec{t}} = \mathcal{T}_{\vec{t}} \circ \mathcal{L}$$

where $\mathcal{T}_{\vec{t}}(\vec{r}_a, x_a) := (\vec{r}_a + \vec{t}, x_a)$. This condition is analogous to the translation equivariance condition for CNNs. It is possible to use a more general translation equivariance condition, where the operator on the right-hand side of the equation also acts upon the \mathcal{Y} representation subspace, but we will not consider that in this chapter.

All of the layers in Section 7.4 are manifestly translation-equivariant because we only ever use differences between two points $\vec{r}_i - \vec{r}_j$ (for indices i and j).

Rotation equivariance

The group of proper 3D rotations is called $SO(3)$, which is a manifold that can be parametrized by 3 numbers (see Ref. [95]). Let $D^{\mathcal{X}}$ be a representation of $SO(3)$ on a vector space \mathcal{X} (and $D^{\mathcal{Y}}$ on \mathcal{Y}). Acting with $g \in SO(3)$ on $\vec{r} \in \mathbb{R}^3$ we write as $\mathcal{R}(g)\vec{r}$, and acting on $x \in \mathcal{X}$ gives $D^{\mathcal{X}}(g)x$.

$$\begin{aligned} \text{Condition:} \\ \mathcal{L} \circ [\mathcal{R}(g) \oplus D^{\mathcal{X}}(g)] &= [\mathcal{R}(g) \oplus D^{\mathcal{Y}}(g)] \circ \mathcal{L} \end{aligned} \tag{7.1}$$

where $[\mathcal{R}(g) \oplus D^{\mathcal{X}}(g)](\vec{r}_a, x_a) = (\mathcal{R}(g)\vec{r}_a, D^{\mathcal{X}}(g)x_a)$. (For layers in this chapter, only the action of $D^{\mathcal{Y}}(g)$ on \mathcal{Y} that will be nontrivial, so we will use a convention of omitting the \mathbb{R}^3 layer output in our equations.)

The key to attaining local rotation equivariance is to restrict our convolution filters to have a particular form. The features will have different types corresponding to whether they transform as scalars, vectors, or higher tensors.

To make our analysis and implementation easier, we decompose representations into irreducible representations. The irreducible representations of $SO(3)$ have dimensions $2l + 1$ for $l \in \mathbb{N}$ (including $l = 0$) and can be chosen to be unitary. We will use the term “rotation order” to refer to l in this expression. The rotation orders $l = 0, 1, 2$ correspond to scalars, vectors, and symmetric traceless matrices, respectively. The group elements are represented by $D^{(l)}$, which are called *Wigner D-matrices* (see Ref. [90]); they map elements of $SO(3)$ to $(2l + 1) \times (2l + 1)$ -dimensional complex matrices.

We could additionally have equivariance with respect to $O(3)$, the group of 3D rotations and mirror operations (a discrete symmetry). We would augment our convolution using the method for obtaining equivariance with respect to discrete symmetries described in Ref. [67]. We discuss this a bit more in Section 7.5.

7.4 Tensor field network layers

At each level of a tensor field network, we have a finite set S of points in \mathbb{R}^3 with a vector in a representation of $SO(3)$ (that has been decomposed into a direct sum of irreducible

$$V_{acm}^{(l)} = \{0: [[\mathbf{m0}], [\mathbf{m1}]], 1: [[\mathbf{v0x}, \mathbf{v0y}, \mathbf{v0z}], [\mathbf{a0x}, \mathbf{a0y}, \mathbf{a0z}]], [[\mathbf{v1x}, \mathbf{v1y}, \mathbf{v1z}], [\mathbf{a1x}, \mathbf{a1y}, \mathbf{a1z}]]\}$$

1: dictionary key, l
 [] point index, a
 [] channel index, c
 [] representation index, m

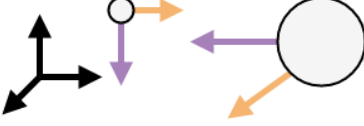


Figure 7.1: Example of $V_{acm}^{(l)}$ representing two point masses with velocities and accelerations. Colored brackets indicate the a (point), c (channel), and m (representation) indices. (l) is the key for the $V_{acm}^{(l)}$ dictionary of feature tensors.

representations) associated with each point. This is essentially a finite version of a tensor field, which was our inspiration for this network design.

At each point, we can have multiple instances of l -rotation-order representations corresponding to different features of that point. We will refer to these different instances as *channels*. We implement this object $V_{acm}^{(l)}$ as a dictionary with key l of multidimensional arrays each with shapes $[|S|, n_l, 2l + 1]$ (where n_l is the number of channels with representation l) corresponding to [point, channel, representation index]. See Figure 7.1 for an example of how to encode a simple system in this notation.

We will describe tensor field network layers and prove that they are equivariant. To prove that a layer is equivariant, we only have to prove rotation equivariance for a given rotation order. This requires showing that when the point cloud rotates and the input features are transformed, the output features transform accordingly. (All of these layers will be manifestly permutation-invariant and translation-equivariant.)

Point convolution

This layer is the core of our network and builds upon the pointwise convolutions in [221]. We start by considering the action of a general pointwise filter transformation

$$\sum_{b \in S} F_c(\vec{r}_a - \vec{r}_b) V_{bc}$$

Note that our design is strictly more general than standard convolutional neural networks, which can be treated as a point cloud S of a grid of points with regular spacing.

Spherical harmonics and filters

To design a rotation-equivariant point convolution, we want rotation-equivariant filters. The spherical harmonics, $Y_m^{(l)} : S^2 \rightarrow \mathbb{C}$ (where m can be any integer between $-l$ and l), are an orthonormal basis for functions on the sphere. These functions are equivariant to $SO(3)$;

that is, they have the property that for $g \in SO(3)$ and $\hat{r} \in S^2$,

$$Y_m^{(l)}(\mathcal{R}(g)\hat{r}) = \sum_{m'} D_{mm'}^{(l)}(g)Y_{m'}^{(l)}(\hat{r}).$$

For our filters to also be rotation-equivariant, we restrict them to the following form:

$$F_{cm}^{(l_f, l_i)}(\vec{r}) = R_c^{(l_f, l_i)}(r)Y_m^{(l_f)}(\hat{r})$$

where l_i and l_f are non-negative integers corresponding to the rotation order of the input and the filter, respectively; $R_c^{(l_f, l_i)} : \mathbb{R}_{\geq 0} \rightarrow \mathbb{R}$ are learned functions; and \hat{r} and r are the direction unit vector and magnitude of \vec{r} , respectively. Filters of this form inherit the transformation property of spherical harmonics under rotations because $R(r)$ is a scalar in m . This choice of filter restriction is analogous to the use of circular harmonics in Ref. [265] (though we do not have an analog to the phase offset because of the non-commutativity of $SO(3)$).

Combining representations using tensor products

Our filters and layer input each inhabit representations of $SO(3)$ (that is, they both carry l and m indices). In order to produce output that we can feed into downstream layers, we need to combine the layer input and filters in such a way that the output also transforms appropriately (by inhabiting a representation of $SO(3)$).

A *tensor product* of representations is a prescription for combining two representations l_1 and l_2 to get another representation $l_1 \otimes l_2$. If $u^{(l_1)} \in l_1$ and $v^{(l_2)} \in l_2$, then $u^{(l_1)} \otimes v^{(l_2)} \in l_1 \otimes l_2$ and

$$(u \otimes v)_m^{(l)} = \sum_{m_1=-l_1}^{l_1} \sum_{m_2=-l_2}^{l_2} C_{(l_1, m_1)(l_2, m_2)}^{(l, m)} u_{m_1}^{(l_1)} v_{m_2}^{(l_2)}$$

where C are called *Clebsch-Gordan coefficients* (see Ref. [98]). Note that l is any integer between $|l_1 - l_2|$ and $(l_1 + l_2)$ inclusive, and m is any integer between $-l$ and l inclusive.

The crucial property of the Clebsch-Gordan coefficients that we need to prove equivariance of this layer is

$$\begin{aligned} \sum_{m'_1, m'_2} C_{(l_1, m'_1)(l_2, m'_2)}^{(l_0, m_0)} D_{m'_1 m_1}^{(l_1)}(g) D_{m'_2 m_2}^{(l_2)}(g) \\ = \sum_{m'_0} D_{m_0 m'_0}^{(l)}(g) C_{(l_1, m_1)(l_2, m_2)}^{(l_0, m'_0)} \end{aligned} \tag{7.2}$$

(see, for example, Ref. [204]).

Layer definition

Filters inhabit one representation, inputs another, and outputs yet another. We need the Clebsch-Gordan coefficients to combine inputs and filters in such a way that they yield the desired output representation:

$$\begin{aligned} \mathcal{L}_{acm_O}^{(l_O)}(\vec{r}_a, V_{acm_I}^{(l_I)}) \\ := \sum_{m_F, m_I} C_{(l_F, m_F)(l_I, m_I)}^{(l_O, m_O)} \sum_{b \in S} F_{cm_F}^{(l_F, l_I)}(\vec{r}_{ab}) V_{bcm_I}^{(l_I)} \end{aligned} \quad (7.3)$$

where $\vec{r}_{ab} := \vec{r}_a - \vec{r}_b$ and the subscripts I , F , and O denote the representations of the input, filter, and output, respectively. A point convolution of an l_F filter on an l_I input yields outputs at $2 \max(l_I, l_F) + 1$ different rotation orders l_O (one for each integer between $|l_I - l_F|$ and $(l_I + l_F)$, inclusive), though in designing a particular network, we may choose not to calculate or use some of those outputs.

Using the equivariance of the filter F and the property of the Clebsch-Gordan coefficients Equation 7.2, we can show the rotation equivariance of point convolutions, Equation 7.1 (detailed proof in Appendix H, Section H.3):

$$\begin{aligned} \mathcal{L}_{acm_O}^{(l_O)}\left(\mathcal{R}(g)\vec{r}_a, \sum_{m'_I} D_{m_I m'_I}^{(l_I)}(g) V_{acm'_I}^{(l_I)}\right) \\ = \sum_{m'_O} D_{m_O m'_O}^{(l_O)}(g) \mathcal{L}_{acm'_O}^{(l_O)}(\vec{r}_a, V_{acm'_I}^{(l_I)}) \end{aligned} \quad (7.4)$$

This aspect of the design, and this proof of its correctness, is the core of our result.

Scalars ($l = 0$) and vectors ($l = 1$)

In this section, we attempt to demystify Wigner D -matrices, spherical harmonics, and Clebsch-Gordan coefficients by stating their values for a real representation of $l = 0$ (scalars) and $l = 1$ (vectors). (It can sometimes be simpler to use a complex representation, but we can always use a basis change to convert between real and complex versions.) The corresponding objects for $l > 1$ are more complicated.

The Wigner D -matrices are

$$D^{(0)}(g) = 1 \quad D^{(1)}(g) = \mathcal{R}(g),$$

where \mathcal{R} are the usual rotation matrices on \mathbb{R}^3 . The spherical harmonics are

$$Y^{(0)}(\hat{r}) \propto 1 \quad Y^{(1)}(\hat{r}) \propto \hat{r}$$

The Clebsch-Gordan coefficients are just the familiar ways to combine scalars and vectors: For $1 \otimes 1 \rightarrow 0$,

$$C_{(1,i)(1,j)}^{(0,0)} \propto \delta_{ij}$$

which is the dot product for 3D vectors. For $1 \otimes 1 \rightarrow 1$,

$$C_{(1,j)(1,k)}^{(1,i)} \propto \epsilon_{ijk}$$

which is the cross product for 3D vectors. The $0 \otimes 0 \rightarrow 0$ case is just regular multiplication of two scalars, and $0 \otimes 1 \rightarrow 1$ and $1 \otimes 0 \rightarrow 1$ corresponds to scalar multiplication of a vector.

Self-interaction

We follow Ref. [222] in using point convolutions to scale feature vectors elementwise and using self-interaction layers to mix together the components of the feature vectors at each point. Self-interaction layers are analogous to 1x1 convolutions, and they implicitly act like $l = 0$ (scalar) types of filters:

$$\sum_{c'} W_{cc'}^{(l)} V_{ac'm}^{(l)}$$

In general, each rotation order has different weights because there may be different numbers of channels n_l corresponding to that rotation order. For $l = 0$, we may also use biases. Putting a self-interaction layer after a one-hot encoding input is the same as the embedding layer described in Ref. [222].

The weight matrix W is a scalar transform with respect to the representation index m , so the D -matrices commute with W , straightforwardly implying that this layer is equivariant. Equivariance for $l = 0$ is straightforward because $D^{(0)} = 1$.

Concatenation

The most general way to combine incoming channels of the same rotation order before the next point convolution layer is to concatenate along the channel axis (increasing the number of input channels), then apply a self-interaction layer. This concatenation operation is equivariant because concatenation does not affect the representation index.

Nonlinearity

Our nonlinearity layer acts as a scalar transform in the l spaces (that is, along the m dimension). For $l = 0$ channels, we can use

$$\eta^{(0)}(V_{ac}^{(0)} + b_c^{(0)})$$

for some function $\eta^{(0)} : \mathbb{R} \rightarrow \mathbb{R}$ and biases $b_c^{(0)}$. For $l > 0$ channels, our nonlinearity has the form

$$\eta^{(l)}(\|V\|_{ac}^{(l)} + b_c^{(l)}) V_{acm}^{(l)}$$

where $\eta^{(l)} : \mathbb{R} \rightarrow \mathbb{R}$ can be different for each l and

$$\|V\|_{ac}^{(l)} := \sqrt{\sum_m |V_{acm}^{(l)}|^2}$$

(It may be necessary to regularize this norm near the origin for this layer to have desirable differentiability properties.)

Note that

$$\|D(g)V\| = \|V\|$$

because D is a unitary representation. Therefore, this layer is a scalar transform in the representation index m , so it is equivariant.

Global pooling

A global pooling operation that we use in our demonstrations is summing the feature vectors over each point. This operation is equivariant because D -matrices act linearly.

7.5 Demonstrations and experiments

We chose experiments that are simple enough to be easily understandable yet suggestive of richer problems. They each highlight a different aspect of our framework. Each of these tasks is either unnatural or impossible in existing frameworks.

We have focused on understanding how to construct and train these models in controlled tasks because of the complexity of the architecture. In future work, we will apply our network to more complicated and useful tasks.

In these tasks, we used radial functions identical to those used in Ref. [221]: We used radial basis functions composed of Gaussians, and two dense layers are applied to this basis vector. The number, spacing, and standard deviation of the Gaussians are hyperparameters. We used a shifted softplus activation function $\log(0.5e^x + 0.5)$ for our radial functions and nonlinearity layers. We implemented our models in TensorFlow [5]. Our code is available at <https://github.com/tensorfieldnetworks/tensorfieldnetworks>

Tensor outputs: acceleration vectors in Newtonian gravity and moment of inertia tensor

Network types: $0 \rightarrow 1$ and $0 \rightarrow 0 \oplus 2$

To demonstrate the simplest non-trivial tensor field networks, we train networks to calculate acceleration vectors of point masses under Newtonian gravity and the moment of inertia tensor at a specific point of a collection of point masses. These tasks only require a single layer of point convolutions to demonstrate. Furthermore, we can check the learned radial functions against analytical solutions.

The acceleration of a point mass in the presence of other point masses according to Newtonian gravity is given by

$$\vec{a}_p = -G_N \sum_{n \neq p} \frac{m_n}{r_{np}^2} \hat{r}_{np}$$

where we define $\vec{r}_{np} := \vec{r}_n - \vec{r}_p$. (We choose units where $G_N = 1$, for simplicity.)

The moment of inertia tensor is used in classical mechanics to calculate angular momentum. Objects generally have different moments of inertia depending on which axis they rotate about, and this is captured by the moment of inertia tensor (see Ref. [142]):

$$I_{ij} = \sum_p m_p \left[(\vec{r}_p \cdot \vec{r}_p) \delta_{ij} - (\vec{r}_p)_i (\vec{r}_p)_j \right]$$

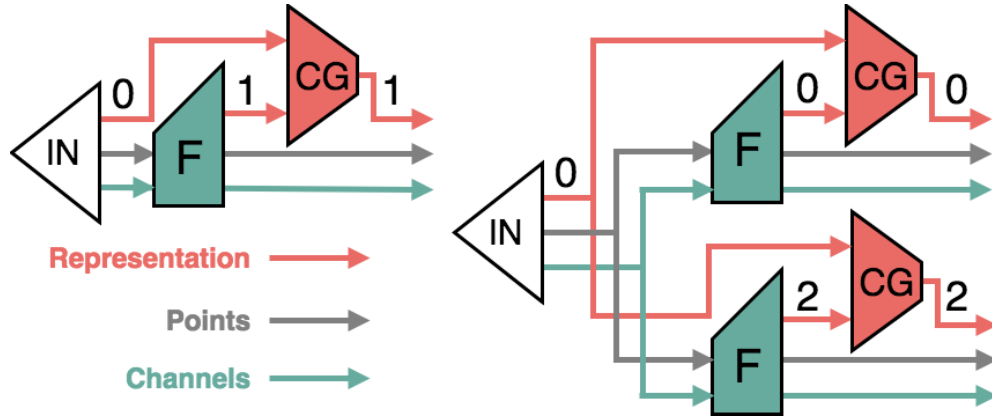


Figure 7.2: Network diagram for learning gravitational accelerations and moment of inertia tensor. The input tensor has indices [channels, points, representation]. The input for the gravitational acceleration and moment of inertia tasks are point mass scalars, therefore the representation index is 1-dimensional. Convolution filters are indicated by blocks marked F and Clebsch-Gordan tensors are indicated by CG . The numbers along the arrows for the representation index indicate the l of that arrow, with CG blocks combining the input and filter l s to generate output of a specific l .

The moment of inertia tensor is a symmetric tensor, so it can be encoded using a $0 \oplus 2$ representation. (Appendix H contains a more detailed explanation of how to go from irreducible representations to matrix tensor representation.)

For both of these tasks, we input to the network a set of random points with associated random masses. (Details of about how these points are generated and about the hyperparameters for our radial functions are given in Appendix H.) For the moment of inertia task, we also designate a different special point at which we want to calculate the moment of inertia tensor.

Our networks are simple: for learning Newtonian gravity, we use a single $l = 1$ convolution with 1 channel; for learning the moment of inertia tensor, we use a single layer comprised of $l = 0$ and $l = 2$ convolutions with 1 channel each. See Figure 7.2 for a diagram of these networks. We use elementwise summed $L2$ losses for the difference of the acceleration vectors and for the difference of the moment of inertia tensor. We get excellent agreement with the Newtonian gravity inverse square law after a 1,000 training steps and with the moment of inertia tensor radial functions after 10,000 steps.

In Figure 7.3, we show that the single radial filter is able to learn the $1/r^2$ law for gravitational accelerations. (Related figures for the moment of inertia task can be found in Appendix H.)

We could have obtained equivariant accelerations by using a pure $l = 0$ network to predict the gravitational potential $\phi : \mathbb{R}^3 \rightarrow \mathbb{R}$, a scalar field, and then taking derivatives of ϕ with respect to the point coordinates to obtain the forces and accelerations (as in,

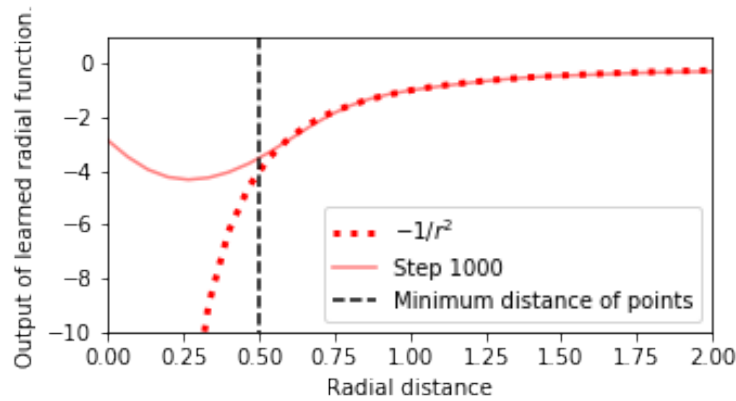


Figure 7.3: Radial function learned by $l = 1$ filter for gravity toy dataset. Minimum radial cutoff distance of 0.5 is chosen for randomly sampled points such that there are enough samples generated near the minimum distance.

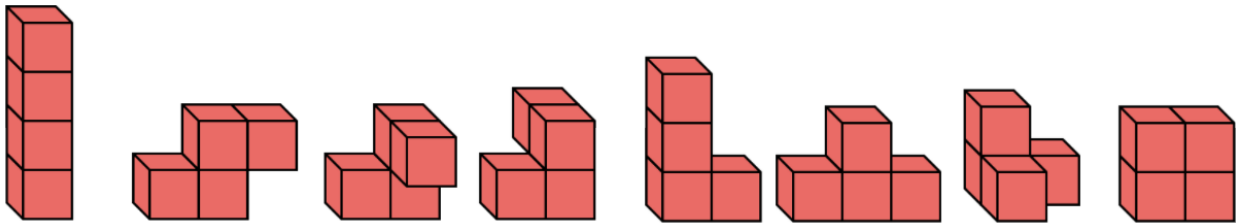


Figure 7.4: 3D Tetris shapes. Blocks correspond to single points. The third and fourth shapes from the left are mirrored versions of each other.

e.g., Ref. [222]). However, many important vector quantities, such as magnetic fields in electromagnetism, cannot be derived from scalar fields.

Shape classification

Network type: $0 \rightarrow 0$

In three dimensions, there are 8 unique shapes made of 4 adjacent cubes (up to translations and rotations); see Figure 7.4. We call these shapes *3D Tetris*, and represent them using points at the center of each cube.

We demonstrate the rotation equivariance of our network by classifying 3D Tetris pieces in the following way: During training, we input to the network a dataset of shapes in a single orientation, and it outputs a classification of which shape it has seen. To demonstrate the equivariance of the network, we test the network with shapes from the same dataset that have been rotated and translated randomly. Our network performs perfectly on this task.

We use a 3-layer network that includes the following for every layer: all possible paths

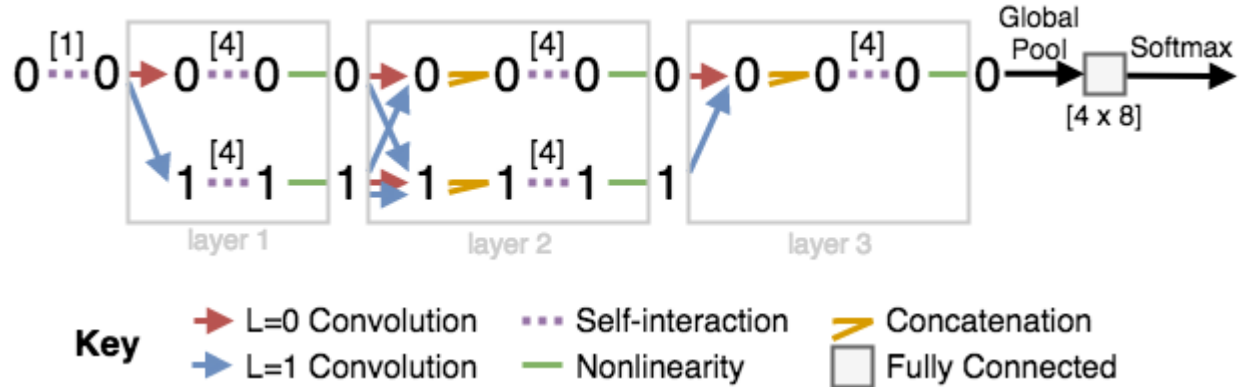


Figure 7.5: Network diagrams for shape classification task showing how information flows between tensors of different order. Clebsch-Gordan tensors are implied in the arrows indicating convolutions. The numbers above the self-interactions indicate the number of channels. Individual convolutions, indicated by arrows, each produce a separate tensor, and concatenation is performed after the convolutions.

with $l = 0$ and $l = 1$ convolutions, a concatenation (if necessary), a self-interaction layer, and a rotation-equivariant nonlinearity. We only use the $l = 0$ output of the network since the shape classes are invariant under rotation and hence scalars. To get a classification from the $l = 0$ output of the network, we sum over the output of all points (global pooling).

Chirality

There are two shapes in 3D Tetris that are mirrors of each other. Any network that relies solely upon distances (such as SchNet) or angles between points (such as ANI-1 [236]) cannot distinguish these shapes. Our network can.

A tensor field network that contains a path with an odd number of odd-rotation-order filters has the possibility of detecting local changes in handedness. This is because

$$Y^{(l)}(-\vec{r}) = (-1)^l Y^{(l)}(\vec{r}).$$

A tensor field network that does not include such paths will be invariant to mirror symmetry. As an example, a $0 \rightarrow 0$ network can correctly classify all 3D Tetris shapes except for the chiral shapes. The smallest network that can classify chiral shapes must include the path $0 \xrightarrow{1} 1 \xrightarrow{1} 1 \xrightarrow{1} 0$ (superscripts correspond to filter rotation order), which yields the vector triple product $\vec{F}_1 \cdot (\vec{F}_2 \times \vec{F}_3)$ of the filter vectors \vec{F}_i for each layer. This combination picks up a minus sign under mirror operations.

Missing point

Network type: $0 \rightarrow 0 \oplus 1$

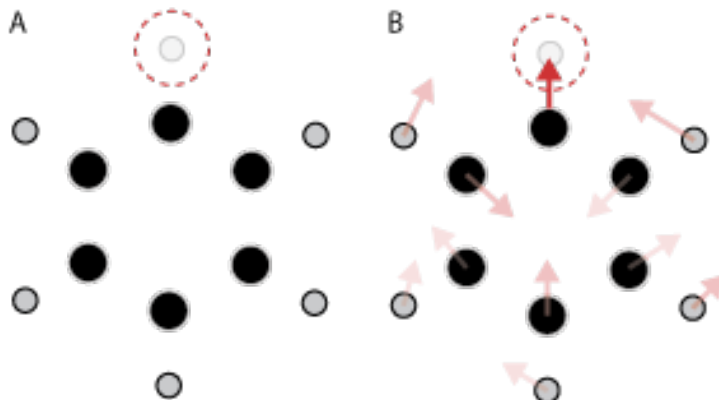


Figure 7.6: A hypothetical example input and output of the missing point network. (A) A benzene molecule with hydrogen removed (B) The relative output vectors produced by the network, with arrows shaded by the associated probabilities.

In this task, we randomly remove a point from a shape and ask the network to replace that point. This is a first step toward general isometry-equivariant generative models for 3D point clouds.

We output an array of scalars, a special scalar, and one vector at each point. The vector, $\vec{\delta}_a$, indicates where the missing point should be relative to the starting point \vec{r}_a (both direction and distance) and the array of scalars indicates the point type. The special scalar is put through softmax and used as a probability p_a measuring the confidence in that point’s vote. We aggregate votes for location using a weighted sum:

$$\sum_a p_a(\vec{r}_a + \vec{\delta}_a)$$

(See Appendix H for a proof that this is translation-equivariant.) This scheme is illustrated in Figure 7.6.

We train on molecular structures for this task because molecules can be comprised of a small number of atoms (making the task computationally easy to demonstrate) and because precise positions are important for chemical behavior.

We trained on structures in the QM9 dataset, a collection of 134,000 molecules with up to nine heavy atoms (C, N, O, F); including hydrogens, there are up to 29 atoms per molecule [203].

Our network is 3 layers deep, with 15 channels per rotation order at each layer. The input features to the network are a one-hot encoding of atom types at each point. We use 2-layer radial functions with 4 Gaussians with centers evenly spaced from 0 to 2.5 angstroms and variance that is half of the spacing. Most covalent bonds are 1-2 angstroms in length, so our radial functions are smaller than the diameter of the molecules of the QM9 dataset.

We train on a 1,000 molecule subset of molecules that have 5 to 18 atoms. In a single epoch, we train on each molecule in the training set (1,000 molecules with 5-18 atoms) with

Table 7.1: Performance on missing point task

Atoms	Number of predictions	Accuracy (%) ($\leq 0.5 \text{ \AA}$ and atom type)	Distance MAE in \AA
5-18 (train)	15863	91.3	0.16
19	19000	93.9	0.14
23	23000	96.5	0.13
25-29	25356	97.3	0.16

one randomly selected atom deleted (1,000 examples total per epoch). We then test the network on a random selection of 1,000 molecules with 19 atoms, 1,000 molecules with 23 atoms, and 1,000 molecules with 25-29 atoms.

For each epoch during training, we use each molecule once and randomly remove one atom. During evaluation, for each molecule, we make a prediction for every possible atom that could be removed. For example, for a molecule with 10 atoms, we will generate 10 predictions, each with a different atom missing. This is why the number of predictions is larger than the number of molecules.

We define an accurate placement of the missing atom position to be within 0.5 angstroms of the removed atom position with the correct atom type according to `argmax` of the returned atom type array. We choose the 0.5 angstrom cutoff because it is smaller than the smallest covalent bond, a hydrogen-hydrogen bond which has a length of 0.7 angstroms. We present the accuracy of our predictions in Table 7.1. We train for 225 epochs and show comparable prediction accuracy on the test sets of 19, 23, and 25-29 atoms as the training set of 5-18 atoms. We include a breakdown of the accuracy and distance mean absolute error (MAE) in the Appendix H.

Our network is most accurate for carbon and hydrogen missing atoms (over 90%), moderately accurate for oxygen and nitrogen (about 70-80%), and not accurate for fluorine atoms (since there are only 50 examples in our training set, they might not be seen during training due to random selection of the missing atom).

7.6 Future work

We have explained the theory of tensor field networks and demonstrated how they work on simple examples.

We hope that tensor field networks can be applied to a wide range of phenomena: In the context of atomic systems, we hope to train networks to predict properties of large and heterogeneous systems, learn molecular dynamics, calculate electron densities (as inputs to density functional theory algorithms), and hypothesize new stable structures. Ultimately, we hope to design new useful materials, drugs, and chemicals.

For more general physics, we see potential applications in modeling complex fluid flows, analyzing detector events in particle physics experiments, and studying configurations of stars and galaxies. We see other applications in 3D perception, robotics, computational geometry, and bioimaging.

Chapter 8

Outlook

In this thesis, we have understood the properties of a variety of atomic systems in terms of their structural motifs. We have classified these motifs based on their geometry, topology, and symmetry. We have also investigated potential methods for learning to identify structural motifs and relating those motifs to electronic properties using custom neural network architectures equivariant to 3D rotations and translations. While we have focused in this work on going from structural motifs to properties, the more challenging question is can we do the inverse?

A holy grail of computational materials discovery is a tool that, given desired material properties, can automatically generate corresponding atomic structures that host those properties [280]. However, before this tool can be feasible, we need an algorithm capable of generating stable atomic structures, regardless of properties. Such an algorithm does not currently exist.

High-throughput computational materials discovery pipelines are bottlenecked by our ability to systematically propose new structures. Generally, structures fed to high-throughput searches are already experimentally known or are just element substitutions of existing materials. Current approaches to computational materials discovery often presuppose that a material already exists and is awaiting identification. In contrast to this assumption, synthesis efforts (such as those at Berkeley Lab, including the Molecular Foundry and the Energy Sciences Area) regularly yield materials that differ substantially from the structures in databases of previously known materials.

An algorithm that could generate stable atomic structures could in the process learn a representation of the structural motifs atomic systems can host. This representation could be used as an *ab initio* materials map and as a similarity metric for comparing diverse atomic systems. There are many similarity metrics that exist for specific classes of material systems, especially molecules, but they cannot naturally be stitched together. Furthermore, these metrics do not necessarily allow for algebra on the metric – interpolations in metric space cannot necessarily be converted back into meaningful structures.

Genetic algorithms have been proposed as a means to generate hypothetical atomic structures, but they are generally constrained to explore a restricted space of structures

[261, 195, 157, 181]. Furthermore, it is difficult to understand why a given structure is generated by these algorithms.

With deep learning techniques specialized to deal with 3D geometry, we can learn a similarity metric out of the wealth of structural data, we already have available. Ref. [92], which focuses on molecules, demonstrates that learning such a representation is possible, although more work is needed to train a network on broader classes of atomic systems.

A computational tool that could generate new atomic-scale geometries would greatly accelerate materials discovery and innovation. This approach would also aid in resolving atomic structures from experimental data (such as data generated by users of the ALS) by reducing the time it takes to characterize new structures. MOChA style synthesis is amenable to combinatorial exploration through use of automated robotic synthesis. To better explore this synthesis space, it would be advantageous to have specific structures in mind to synthesize and quickly assess the relative structural stability and electronic properties of such structures. While hypothetical structures and density functional theory calculations in and of themselves cannot readily suggest specific synthetic pathways, due to the modularity of MOChA style synthesis, often just having components in mind gives direction to a synthetic search.

Existing tools will play an important role in creating structure generating algorithms. Contributors to the python package *atomate* have already started the process of building recipes for reliably calculating specific material properties with minimal user input [165]. These recipes are rapidly feeding databases of density functional theory calculations and will serve as crucial datasets for statistical methods. Deep learning techniques can expedite the calculation of properties traditionally computed with density functional theory and enable *ab initio* molecular dynamics for large systems (exceeding thousands of atoms) [89, 223]. It would also be very helpful to have open-source tools with modern APIs to transform and relate structures through symmetry. Bilbao Crystallographic Server and ISOTROPY are excellent tools. However, the fact that there is no open-source version of these codes and that they do not have modern APIs makes them difficult to modify and include for specific materials search efforts, including high-throughput first-principles workflows. Having easier access to these tools would make it much simpler to expand the automated ferroelectric workflow described in Chapter 6 by including nonpolar structures derived polar structures and vice versa.

In parallel with automated methods, we need better human-guided design tools to articulate the relationships of atomic systems. While software like Avogadro can help a user articulate a specific atomic system and test its feasibility, these tools do not make the intuitive leap that one atomic structure can imply many others, such as was the case in Chapters 3 [100]. This is the difference between design of individual systems to systematic design. Parametric models used in mechanical design could be immensely useful here if we can combine them with fast methods for testing the chemical feasibility of atomic structures. The popularity of Foldit, a video game built on the protein folding software Rosetta, demonstrates that it is possible to create interactive environments where quantitative chemical insights can be translated into tools that harness human visual intuition [131].

New tools are needed to bring us closer to the systematic design of atomic systems. These tools are emerging with the confluence of open-source software, robotic tools for synthesis and characterization, decreasing computational costs, systematized high-throughput first-principles calculations, and rapidly evolving deep learning techniques.

Bibliography

- [1] Materials Project Calculation Guide. <https://materialsproject.org/docs/calculations>.
- [2] Pauling file multinationals edition – 2012 in springermaterials. Copyright 2016 Springer-Verlag Berlin Heidelberg & Material Phases Data System (MPDS), Switzerland & National Institute for Materials Science (NIMS), Japan.
- [3] Zigzag Magnetic Order in the Iridium Oxide Na_2IrO_3 .
- [4] CS231n: Convolutional Neural Networks for Visual Recognition, 2018.
- [5] M. Abadi, A. Agarwal, P. Barham, E. Brevdo, Z. Chen, C. Citro, G. S. Corrado, A. Davis, J. Dean, M. Devin, S. Ghemawat, I. Goodfellow, A. Harp, G. Irving, M. Isard, Y. Jia, R. Jozefowicz, L. Kaiser, M. Kudlur, J. Levenberg, D. Mané, R. Monga, S. Moore, D. Murray, C. Olah, M. Schuster, J. Shlens, B. Steiner, I. Sutskever, K. Talwar, P. Tucker, V. Vanhoucke, V. Vasudevan, F. Viégas, O. Vinyals, P. Warden, M. Wattenberg, M. Wicke, Y. Yu, and X. Zheng. TensorFlow: Large-scale machine learning on heterogeneous systems, 2015. Software available from tensorflow.org.
- [6] S. C. Abrahams. Structurally Based Prediction of Ferroelectricity in Inorganic Materials with Point Group 6mm. *Acta Crystallographica Section B*, B44:585–595, 1988.
- [7] S. C. Abrahams. Structurally based predictions of ferroelectricity in seven inorganic materials with space group $P6_3$ and two experimental confirmations. *Acta Crystallographica Section B*, 45(3):228–232, 1989.
- [8] M. Adachi, Y. Akishige, T. Asahi, K. Deguchi, K. Gesi, K. Hasebe, T. Hikita, T. Ikeda, Y. Iwata, M. Komukae, et al. BaTiO_3 (cubic)[F] Survey, 1A-10. In *Oxides*, pages 1–9. Springer, 2001.
- [9] M. Adachi, Y. Akishige, T. Asahi, K. Deguchi, K. Gesi, K. Hasebe, T. Hikita, T. Ikeda, Y. Iwata, M. Komukae, et al. CdTiO_3 , 1A-9. In *Oxides*, pages 1–12. Springer, 2001.
- [10] M. Adachi, Y. Akishige, T. Asahi, K. Deguchi, K. Gesi, K. Hasebe, T. Hikita, T. Ikeda, Y. Iwata, M. Komukae, et al. KNbO_3 [F], 1A-2. In *Oxides*, pages 1–70. Springer, 2001.

- [11] M. Adachi, Y. Akishige, T. Asahi, K. Deguchi, K. Gesi, K. Hasebe, T. Hikita, T. Ikeda, Y. Iwata, M. Komukae, et al. LiNbO₃ [F] References, 2A-1. In *Oxides*, pages 1–14. Springer, 2001.
- [12] M. Adachi, Y. Akishige, T. Asahi, K. Deguchi, K. Gesi, K. Hasebe, T. Hikita, T. Ikeda, Y. Iwata, M. Komukae, et al. NaNbO₃ [(F) A], 1A-1. In *Oxides*, pages 1–36. Springer, 2001.
- [13] M. Adachi, Y. Akishige, T. Asahi, K. Deguchi, K. Gesi, K. Hasebe, T. Hikita, T. Ikeda, Y. Iwata, M. Komukae, et al. PbHfO₃ [(A)], 1A-16. In *Oxides*, pages 1–14. Springer, 2001.
- [14] M. Adachi, Y. Akishige, T. Asahi, K. Deguchi, K. Gesi, K. Hasebe, T. Hikita, T. Ikeda, Y. Iwata, M. Komukae, et al. PbTiO₃ [F], 1A-11. In *Oxides*, pages 1–77. Springer, 2001.
- [15] M. Adachi, Y. Akishige, T. Asahi, K. Deguchi, K. Gesi, K. Hasebe, T. Hikita, T. Ikeda, Y. Iwata, M. Komukae, et al. PbZrO₃ [A], 1A-15. In *Oxides*, pages 1–60. Springer, 2001.
- [16] M. Adachi, Y. Akishige, T. Asahi, K. Deguchi, K. Gesi, K. Hasebe, T. Hikita, T. Ikeda, Y. Iwata, M. Komukae, et al. Bi₄Ti₃O₁₂ [F], 9A-15. In *Oxides*, pages 1–26. Springer, 2002.
- [17] M. Adachi, Y. Akishige, T. Asahi, K. Deguchi, K. Gesi, K. Hasebe, T. Hikita, T. Ikeda, Y. Iwata, M. Komukae, et al. Cr₃B₇O₁₃Cl [F, A], 18A-2. In *Oxides*, pages 1–34. Springer, 2002.
- [18] M. Adachi, Y. Akishige, T. Asahi, K. Deguchi, K. Gesi, K. Hasebe, T. Hikita, T. Ikeda, Y. Iwata, M. Komukae, et al. Mg₃B₇O₁₃Cl [F], 18A-1. In *Oxides*, pages 1–37. Springer, 2002.
- [19] M. Adachi, Y. Akishige, T. Asahi, K. Deguchi, K. Gesi, K. Hasebe, T. Hikita, T. Ikeda, Y. Iwata, M. Komukae, et al. Mn₃B₇O₁₃I, 18A-20. In *Oxides*, pages 1–9. Springer, 2002.
- [20] M. Adachi, Y. Akishige, T. Asahi, K. Deguchi, K. Gesi, K. Hasebe, T. Hikita, T. Ikeda, Y. Iwata, M. Komukae, et al. PbBi₂Nb₂O₉ [(F)], 9A-10. In *Oxides*, pages 1–7. Springer, 2002.
- [21] M. Adachi, Y. Akishige, T. Asahi, K. Deguchi, K. Gesi, K. Hasebe, T. Hikita, T. Ikeda, Y. Iwata, M. Komukae, et al. SbNbO₄ [F,(A)], 5A-2. In *Oxides*, pages 1–9. Springer, 2002.

- [22] M. Adachi, Y. Akishige, T. Asahi, K. Deguchi, K. Gesi, K. Hasebe, T. Hikita, T. Ikeda, Y. Iwata, M. Komukae, et al. Sr₂Ta₂O₇ [F], 8A-6. In *Oxides*, pages 1–16. Springer, 2002.
- [23] M. Adachi, Y. Akishige, T. Asahi, K. Deguchi, K. Gesi, K. Hasebe, T. Hikita, T. Ikeda, Y. Iwata, M. Komukae, et al. SrBi₂Ta₂O₉ [F], 9A-12. In *Oxides*, pages 1–4. Springer, 2002.
- [24] A. Altomare, G. Cascarano, C. Giacovazzo, A. Guagliardi, M. C. Burla, G. Polidori, and M. Camalli. SIR92 – a program for automatic solution of crystal structures by direct methods. *Journal of Applied Crystallography*, 27(3):435, Jun 1994.
- [25] E. C. Andrade and M. Vojta. Magnetism in spin models for depleted honeycomb-lattice iridates: Spin-glass order towards percolation. *arXiv:1309.2951 [cond-mat]*, Sept. 2013.
- [26] V. I. Anisimov, J. Zaanen, and O. K. Andersen. Band theory and mott insulators: Hubbard u instead of stoner i. *Phys. Rev. B*, 44:943–954, Jul 1991.
- [27] R. Armiento, B. Kozinsky, M. Fornari, and G. Ceder. Screening for high-performance piezoelectrics using high-throughput density functional theory. *Phys. Rev. B*, 84:014103, Jul 2011.
- [28] M. I. Aroyo, A. Kirov, C. Capillas, J. M. Perez-Mato, and H. Wondratschek. Bilbao crystallographic server. II. representations of crystallographic point groups and space groups. *Acta Crystallographica Section A Foundations of Crystallography*, 62(2):115–128, mar 2006.
- [29] M. I. Aroyo, J. M. Perez-Mato, C. Capillas, E. Kroumova, S. Ivantchev, G. Madariaga, A. Kirov, and H. Wondratschek. Bilbao crystallographic server: I. databases and crystallographic computing programs. *Zeitschrift für Kristallographie - Crystalline Materials*, 221(1), jan 2006.
- [30] M. I. Aroyo, J. M. Perez-Mato, C. Capillas, E. Kroumova, S. Ivantchev, G. Madariaga, A. Kirov, and H. Wondratschek. Bilbao Crystallographic Server: I. Databases and crystallographic computing programs. *Zeitschrift für Kristallographie - Crystalline Materials*, 221(1), jan 2006.
- [31] M. I. Aroyo, J. M. Perez-Mato, D. Orobengoa, E. Tasci, G. de la Flor, and A. Kirov. Crystallography online: Bilbao Crystallographic Server. *Bulg. Chem. Commun.*, 43(2), jan 2011.
- [32] N. Artrith and A. Urban. An implementation of artificial neural-network potentials for atomistic materials simulations: Performance for tio₂. *Computational Materials Science*, 114(Supplement C):135 – 150, 2016.

- [33] N. Artrith, A. Urban, and G. Ceder. Efficient and accurate machine-learning interpolation of atomic energies in compositions with many species. *Phys. Rev. B*, 96:014112, Jul 2017.
- [34] P. Baettig, C. F. Schelle, R. LeSar, U. V. Waghmare, and N. A. Spaldin. Theoretical prediction of new high-performance lead-free piezoelectrics. *Chemistry of Materials*, 17(6):1376–1380, 2005.
- [35] L. Balents. Spin liquids in frustrated magnets. *Nature*, 464(7286):199–208, Mar. 2010.
- [36] J. Behler and M. Parrinello. Generalized neural-network representation of high-dimensional potential-energy surfaces. *Phys. Rev. Lett.*, 98(14):146401, 2007.
- [37] N. A. Benedek and C. J. Fennie. Hybrid improper ferroelectricity: A mechanism for controllable polarization-magnetization coupling. *Physical Review Letters*, 106(10):107204, Mar. 2011.
- [38] N. A. Benedek and C. J. Fennie. Hybrid improper ferroelectricity: A mechanism for controllable polarization-magnetization coupling. *Phys. Rev. Lett.*, 106:107204, Mar 2011.
- [39] J. W. Bennett. Discovery and Design of Functional Materials: Integration of Database Searching and First Principles Calculations. *Physics Procedia*, 34:14–23, 2012.
- [40] J. W. Bennett, K. F. Garrity, K. M. Rabe, and D. Vanderbilt. Hexagonal ABC semiconductors as ferroelectrics. *Physical Review Letters*, 109:167602, 2012.
- [41] J. W. Bennett and K. M. Rabe. Integration of first-principles methods and crystallographic database searches for new ferroelectrics: Strategies and explorations. *J. Solid State Chem.*, 195:21–31, 2012.
- [42] T. C. Berkelbach, M. S. Hybertsen, and D. R. Reichman. Theory of neutral and charged excitons in monolayer transition metal dichalcogenides. *Physical Review B*, 88(4):045318, 2013. PRB.
- [43] G. R. Bhimanapati, Z. Lin, V. Meunier, Y. Jung, J. Cha, S. Das, D. Xiao, Y. Son, M. S. Strano, V. R. Cooper, L. Liang, S. G. Louie, E. Ringe, W. Zhou, S. S. Kim, R. R. Naik, B. G. Sumpter, H. Terrones, F. Xia, Y. Wang, J. Zhu, D. Akinwande, N. Alem, J. A. Schuller, R. E. Schaak, M. Terrones, and J. A. Robinson. Recent advances in two-dimensional materials beyond graphene. *ACS Nano*, 9(12):11509–11539, 2015.
- [44] A. Biffin, R. Johnson, I. Kimchi, R. Morris, a. Bombardi, J. Analytis, a. Vishwanath, and R. Coldea. Noncoplanar and Counterrotating Incommensurate Magnetic Order Stabilized by Kitaev Interactions in γ -Li₂IrO₃. *Physical Review Letters*, 113(19):197201, Nov. 2014.

- [45] A. Biffin, R. D. Johnson, S. Choi, F. Freund, S. Manni, a. Bombardi, P. Manuel, P. Gegenwart, and R. Coldea. Unconventional magnetic order on the hyperhoneycomb Kitaev lattice in β -Li₂IrO₃. *Physical Review B*, 90(20):205116, Nov. 2014.
- [46] P. Blöchl. Projector augmented-wave method. *Physical Review B*, 50(24), 1994.
- [47] S. Blundell. *Magnetism in Condensed Matter (Oxford Master Series in Physics)*, chapter C.8. Oxford University Press, 2001.
- [48] S. Blundell. *Magnetism in Condensed Matter (Oxford Master Series in Physics)*, chapter 4. Oxford University Press, 2001.
- [49] S. Blundell. *Magnetism in Condensed Matter (Oxford Master Series in Physics)*, chapter 1. Oxford University Press, 2001.
- [50] P. J. Bonasia, G. P. Mitchell, F. J. Hollander, and J. Arnold. Synthesis and characterization of copper(i) and silver(i) tellurolates and selenolates. the x-ray crystal structures of Cu[SeC(SiMe₃)₃]PCy₃2 and the homoleptic silver selenolate ag₄[sec(sime₃)₃]₄. *Inorganic Chemistry*, 33(9):1797–1802, 1994.
- [51] W. Boomsma and J. Frellsen. Spherical convolutions and their application in molecular modelling. In I. Guyon, U. V. Luxburg, S. Bengio, H. Wallach, R. Fergus, S. Vishwanathan, and R. Garnett, editors, *Advances in Neural Information Processing Systems 30*, pages 3436–3446. Curran Associates, Inc., 2017.
- [52] M. Bremholm, S. Dutton, P. Stephens, and R. Cava. NaIrO₃ pentavalent post-perovskite. *Journal of Solid State Chemistry*, 184(3):601–607, Mar. 2011.
- [53] L. Britnell, R. M. Ribeiro, A. Eckmann, R. Jalil, B. D. Belle, A. Mishchenko, Y. J. Kim, R. V. Gorbachev, T. Georgiou, S. V. Morozov, A. N. Grigorenko, A. K. Geim, C. Casiraghi, A. H. C. Neto, and K. S. Novoselov. Strong light-matter interactions in heterostructures of atomically thin films. *Science*, 340(6138):1311–1314, 2013.
- [54] S. Z. Butler, S. M. Hollen, L. Cao, Y. Cui, J. A. Gupta, H. R. Gutierrez, T. F. Heinz, S. S. Hong, J. Huang, A. F. Ismach, E. Johnston-Halperin, M. Kuno, V. V. Plashnitsa, R. D. Robinson, R. S. Ruoff, S. Salahuddin, J. Shan, L. Shi, M. G. Spencer, M. Terrones, W. Windl, and J. E. Goldberger. Progress, challenges, and opportunities in two-dimensional materials beyond graphene. *Acs Nano*, 7(4):2898–2926, 2013.
- [55] G. Cao, T. F. Qi, L. Li, J. Terzic, V. S. Cao, S. J. Yuan, M. Tovar, G. Murthy, and R. K. Kaul. Evolution of magnetism in the single-crystal honeycomb iridates (Na_{1-x}Li_x)₂IrO₃. *Physical Review B*, 88(22):220414, Dec. 2013.
- [56] C. Capillas, E. Kroumova, M. I. Aroyo, J. M. Perez-Mato, H. T. Stokes, and D. M. Hatch. SYMMODES: a software package for group-theoretical analysis of structural phase transitions. *Journal of Applied Crystallography*, 36(3):953–954, may 2003.

- [57] C. Capillas, E. S. Tasci, G. de la Flor, D. Orobengoa, J. M. Perez-Mato, and M. I. Aroyo. A new computer tool at the Bilbao Crystallographic Server to detect and characterize pseudosymmetry. *Zeitschrift für Kristallographie*, 226(2):186–196, 2011.
- [58] G. Ceder, Y.-M. Chiang, D. R. Sadoway, M. K. Aydinol, Y.-I. Jang, and B. Huang. Identification of cathode materials for lithium batteries guided by first-principles calculations. *Nature*, 392(6677):694–696, apr 1998.
- [59] J. Chaloupka, G. Jackeli, and G. Khaliullin. Kitaev-Heisenberg Model on a Honeycomb Lattice: Possible Exotic Phases in Iridium Oxides $A_2\text{IrO}_3$. *Phys. Rev. Lett.*, 105:027204, Jul 2010.
- [60] P. Chandra and P. B. Littlewood. *A Landau Primer for Ferroelectrics*, pages 69–116. Springer Berlin Heidelberg, Berlin, Heidelberg, 2007.
- [61] R. Chen, H. C. Po, J. B. Neaton, and A. Vishwanath. Topological materials discovery using electron filling constraints. *Nature Physics*, 14(1):55–61, oct 2017.
- [62] S. Chmiela, A. Tkatchenko, H. E. Sauceda, I. Poltavsky, K. T. Schütt, and K.-R. Müller. Machine learning of accurate energy-conserving molecular force fields. *Science Advances*, 3(5), 2017.
- [63] S. K. Choi, R. Coldea, A. N. Kolmogorov, T. Lancaster, I. I. Mazin, S. J. Blundell, P. G. Radaelli, Y. Singh, P. Gegenwart, K. R. Choi, S.-W. Cheong, P. J. Baker, C. Stock, and J. Taylor. Spin Waves and Revised Crystal Structure of Honeycomb Iridate Na_2IrO_3 . *Physical Review Letters*, 108(12):127204, Mar. 2012.
- [64] S. K. Choi, R. Coldea, a. N. Kolmogorov, T. Lancaster, I. I. Mazin, S. J. Blundell, P. G. Radaelli, Y. Singh, P. Gegenwart, K. R. Choi, S.-W. Cheong, P. J. Baker, C. Stock, and J. Taylor. Spin Waves and Revised Crystal Structure of Honeycomb Iridate Na_2IrO_3 . *Physical Review Letters*, 108(12):127204, Mar. 2012.
- [65] T. Cohen, M. Geiger, J. Köhler, and M. Welling. Spherical CNNs. *International Conference on Learning Representations*, 2018.
- [66] T. Cohen and M. Welling. Group equivariant convolutional networks. In *Proceedings of the International Conference on Machine Learning (ICML)*, 2016.
- [67] T. Cohen and M. Welling. Steerable CNNs. In *International Conference on Learning Representations (ICLR)*, 2017.
- [68] J. F. Corrigan, O. Fuhr, and D. Fenske. Metal chalcogenide clusters on the border between molecules and materials. *Advanced Materials*, 21(18):1867–1871, 2009.
- [69] H. L. Cuthbert, A. I. Wallbank, N. J. Taylor, and J. F. Corrigan. Synthesis and Structural Characterization of $[\text{Cu}_{20}\text{Se}_4(3\text{-SePh})_{12}(\text{PPh}_3)_6]$ and $[\text{Ag}(\text{SePh})]_\infty$. *Zeitschrift für anorganische und allgemeine Chemie*, 628(11):2483–2488, 2002.

- [70] I. G. Dance, K. J. Fisher, R. M. H. Banda, and M. L. Scudder. Layered structure of crystalline compounds silver thiolates (agsr). *Inorganic Chemistry*, 30(2):183–187, 1991. doi: 10.1021/ic00002a008.
- [71] M. de Jong, W. Chen, H. Geerlings, M. Asta, and K. A. Persson. A database to enable discovery and design of piezoelectric materials. *Scientific Data*, 2:150053, 2015.
- [72] K. Deguchi, K. Hasebe, K. Gesi, and T. Asahi. 39A-1 (NH₄)₂SO₄ [F]. In *Inorganic Substances other than Oxides*, pages 1–53. Springer.
- [73] K. Deguchi, K. Hasebe, K. Gesi, and T. Asahi. 39A-16 K₂ZnBr₄ [F]. In *Inorganic Substances other than Oxides*, pages 1–10. Springer.
- [74] K. Deguchi, K. Hasebe, K. Gesi, and T. Asahi. 39A-2 K₂SeO₄ [F]. In *Inorganic Substances other than Oxides*, pages 1–39. Springer.
- [75] K. Deguchi, K. Hasebe, K. Gesi, and T. Asahi. 39A-7 Rb₂CoCl₄ [F]. In *Inorganic Substances other than Oxides*, pages 1–15. Springer.
- [76] K. Deguchi, K. Hasebe, K. Gesi, and T. Asahi. 39A-9 K₂ZnCl₄ [F]. In *Inorganic Substances other than Oxides*, pages 1–32. Springer.
- [77] K. Deguchi, K. Hasebe, K. Gesi, and T. Asahi. 39A-10 Rb₂ZnCl₄ [F]. In *Inorganic Substances other than Oxides*, pages 1–51. Springer, 2005.
- [78] S. Dehnen, A. Eichhfer, and D. Fenske. Chalcogen-bridged copper clusters. *European Journal of Inorganic Chemistry*, 2002(2):279–317, 2002.
- [79] M. Dion, H. Rydberg, E. Schrder, D. C. Langreth, and B. I. Lundqvist. Van der waals density functional for general geometries. *Physical Review Letters*, 92(24):246401, 2004. PRL.
- [80] L. Dou, A. B. Wong, Y. Yu, M. Lai, N. Kornienko, S. W. Eaton, A. Fu, C. G. Bischak, J. Ma, T. Ding, N. S. Ginsberg, L.-W. Wang, A. P. Alivisatos, and P. Yang. Atomically thin two-dimensional organic-inorganic hybrid perovskites. *Science*, 349(6255):1518–1521, 2015.
- [81] S. L. Dudarev, S. Y. Savrasov, C. J. Humphreys, and a. P. Sutton. Electron-energy-loss spectra and the structural stability of nickel oxide:An LSDA+U study. *Physical Review B*, 57(3):1505–1509, 1998.
- [82] I. Dzyaloshinsky. A thermodynamic theory of weak ferromagnetism of antiferromagnetics. *Journal of Physics and Chemistry of Solids*, 4(4):241–255, 1958.

- [83] F. A. Faber, L. Hutchison, B. Huang, J. Gilmer, S. S. Schoenholz, G. E. Dahl, O. Vinyals, S. Kearnes, P. F. Riley, and O. A. von Lilienfeld. Prediction errors of molecular machine learning models lower than hybrid DFT error. *Journal of Chemical Theory and Computation*.
- [84] L. J. Farrugia. WinGX and ORTEP for Windows: an update. *Journal of Applied Crystallography*, 45(4):849–854, Aug 2012.
- [85] A. Fonari and C. Sutton. Effective mass calculator for semiconductors. <http://afonari.com/emc/>.
- [86] K. F. Garrity. High-throughput first-principles search for new ferroelectrics. *Phys. Rev. B*, 97:024115, Jan 2018.
- [87] K. F. Garrity, K. M. Rabe, and D. Vanderbilt. Hyperferroelectrics: Proper Ferroelectrics with Persistent Polarization. *Phys. Rev. Lett.*, 112:127601, Mar 2014.
- [88] A. K. Geim and I. V. Grigorieva. Van der waals heterostructures. *Nature*, 499(7459):419–425, 2013.
- [89] J. Gilmer, S. S. Schoenholz, P. F. Riley, O. Vinyals, and G. E. Dahl. Neural message passing for quantum chemistry. In D. Precup and Y. W. Teh, editors, *Proceedings of the 34th International Conference on Machine Learning*, volume 70 of *Proceedings of Machine Learning Research*, pages 1263–1272, International Convention Centre, Sydney, Australia, 06–11 Aug 2017. PMLR.
- [90] R. Gilmore. *Lie groups, physics, and geometry: An introduction for physicists, engineers and chemists*. Cambridge University Press, 2008.
- [91] P. A. Goddard, J. Singleton, P. Sengupta, R. D. McDonald, T. Lancaster, S. J. Blundell, F. L. Pratt, S. Cox, N. Harrison, J. L. Manson, H. I. Southerland, and J. A. Schlueter. Experimentally determining the exchange parameters of quasi-two-dimensional heisenberg magnets. *New Journal of Physics*, 10(8):083025, Aug. 2008.
- [92] R. Gómez-Bombarelli, J. N. Wei, D. Duvenaud, J. M. Hernández-Lobato, B. Sánchez-Lengeling, D. Sheberla, J. Aguilera-Iparraguirre, T. D. Hirzel, R. P. Adams, and A. Aspuru-Guzik. Automatic chemical design using a data-driven continuous representation of molecules. *ACS Central Science*, 0(0):null, 0.
- [93] D. M. Gonzalez, M. Volpi, N. Komodakis, and D. Tuia. Rotation equivariant vector field networks. *CoRR*, abs/1612.09346, 2016.
- [94] I. Goodfellow, Y. Bengio, and A. Courville. *Deep Learning*. MIT Press, 2016. <http://www.deeplearningbook.org>.

- [95] R. Goodman and N. R. Wallach. *Representations and invariants of the classical groups*, volume 68. Cambridge University Press, 1998.
- [96] H. Gretarsson, J. P. Clancy, X. Liu, J. P. Hill, E. Bozin, Y. Singh, S. Manni, P. Gegenwart, J. Kim, A. H. Said, D. Casa, T. Gog, M. H. Upton, H.-S. Kim, J. Yu, V. M. Katukuri, L. Hozoi, J. van den Brink, and Y.-J. Kim. Crystal-Field Splitting and Correlation Effect on the Electronic Structure of $A_2\text{IrO}_3$. *Phys. Rev. Lett.*, 110:076402, Feb 2013.
- [97] H. Gretarsson, J. P. Clancy, Y. Singh, P. Gegenwart, J. P. Hill, J. Kim, M. H. Upton, A. H. Said, D. Casa, T. Gog, and Y.-J. Kim. Magnetic excitation spectrum of Na_2IrO_3 probed with resonant inelastic x-ray scattering. *Physical Review B*, 87(22):220407, June 2013.
- [98] D. J. Griffiths. *Introduction to quantum mechanics*. Cambridge University Press, 2017.
- [99] S. A. Grigera, R. S. Perry, A. J. Schofield, M. Chiao, S. R. Julian, G. G. Lonzarich, S. I. Ikeda, Y. Maeno, A. J. Millis, and A. P. Mackenzie. Magnetic field-tuned quantum criticality in the metallic ruthenate $\text{Sr}_3\text{Ru}_2\text{O}_7$. *Science*, 294(5541):329–332, Oct. 2001. PMID: 11598292.
- [100] M. D. Hanwell, D. E. Curtis, D. C. Lonie, T. Vandermeersch, E. Zurek, and G. R. Hutchison. Avogadro: an advanced semantic chemical editor, visualization, and analysis platform. *Journal of Cheminformatics*, 4(1):17, 2012.
- [101] L. Hedin. New method for calculating the one-particle green’s function with application to the electron-gas problem. *Physical Review*, 139(3A):A796–A823, 1965. PR.
- [102] C. H. Hendon, D. Tiana, T. P. Vaid, and A. Walsh. Thermodynamic and electronic properties of tunable II-VI and IV-VI semiconductor based metal-organic frameworks from computational chemistry. *Journal of Materials Chemistry C*, 1(1):95–100, 2013.
- [103] J. Heyd and G. E. Scuseria. Efficient hybrid density functional calculations in solids: Assessment of the heyd–scuseria–ernzerhof screened coulomb hybrid functional. *The Journal of Chemical Physics*, 121(3):1187–1192, jul 2004.
- [104] J. Heyd, G. E. Scuseria, and M. Ernzerhof. Hybrid functionals based on a screened coulomb potential. *The Journal of Chemical Physics*, 118(18):8207–8215, may 2003.
- [105] J. Heyd, G. E. Scuseria, and M. Ernzerhof. Erratum: “hybrid functionals based on a screened coulomb potential” [j. chem. phys. 118, 8207 (2003)]. *The Journal of Chemical Physics*, 124(21):219906, jun 2006.
- [106] T. Hikita. 35A-13 TlTiOPO_4 [(F)]. In *Inorganic Substances other than Oxides. Part 1: SbSI family... TAAP*, pages 1–9. Springer.

- [107] D. Hobbs and J. Hafner. Ab initio density functional study of phase stability and noncollinear magnetism in Mn. *Journal of Physics: Condensed Matter*, 13:L681–L688, 2001.
- [108] D. Hobbs, G. Kresse, and J. Hafner. Fully unconstrained noncollinear magnetism within the projector augmented-wave method. *Physical Review B*, 62(17):11556–11570, Nov. 2000.
- [109] P. Hohenberg and W. Kohn. Inhomogeneous electron gas. *Phys. Rev.*, 136:B864–B871, Nov 1964.
- [110] L. Hu, L. P. de la Rama, M. Y. Efremov, Y. Anahory, F. Schiettekatte, and L. H. Allen. Synthesis and characterization of single-layer silverdecanethiolate lamellar crystals. *Journal of the American Chemical Society*, 133(12):4367–4376, 2011.
- [111] X. Huang, Heulings, V. Le, and J. Li. Inorganicorganic hybrid composites containing mq (iivi) slabs: a new class of nanostructures with strong quantum confinement and periodic arrangement. *Chemistry of Materials*, 13(10):3754–3759, 2001.
- [112] X. Huang and J. Li. From single to multiple atomic layers: a unique approach to the systematic tuning of structures and properties of inorganicorganic hybrid nanostructured semiconductors. *Journal of the American Chemical Society*, 129(11):3157–3162, 2007.
- [113] X. Huang, J. Li, and H. Fu. The first covalent organicinorganic networks of hybrid chalcogenides: structures that may lead to a new type of quantum wells. *Journal of the American Chemical Society*, 122(36):8789–8790, 2000.
- [114] J. Hubbard. Electron correlations in narrow energy bands III. an improved solution. 281(1386):401–419, 1964.
- [115] S. Hwan Chun, J.-W. Kim, J. Kim, H. Zheng, C. Stoumpos, C. Malliakas, J. Mitchell, K. Mehlawat, Y. Singh, Y. Choi, T. Gog, a. Al-Zein, M. Sala, M. Krisch, J. Chaloupka, G. Jackeli, G. Khaliullin, and B. J. Kim. Direct evidence for dominant bond-directional interactions in a honeycomb lattice iridate Na₂IrO₃. *Nature Physics*, 11(May), 2015.
- [116] E. Şaşıoğlu, C. Friedrich, and S. Blügel. Effective coulomb interaction in transition metals from constrained random-phase approximation. *Phys. Rev. B*, 83:121101, Mar 2011.
- [117] J. M. Igartua, M. I. Aroyo, E. Kroumova, and J. M. Perez-Mato. Search for Pnma materials with high-temperature structural phase transitions. *Acta Crystallographica Section B Structural Science*, 55(2):177–185, 1999.

- [118] G. Jackeli and G. Khaliullin. Mott insulators in the strong spin-orbit coupling limit: From heisenberg to a quantum compass and kitaev models. *Physical Review Letters*, 102(1):017205, Jan. 2009.
- [119] G. Jackeli and G. Khaliullin. Mott insulators in the strong spin-orbit coupling limit: From heisenberg to a quantum compass and kitaev models. *Phys. Rev. Lett.*, 102:017205, Jan 2009.
- [120] G. Jackeli and G. Khaliullin. Mott Insulators in the Strong Spin-Orbit Coupling Limit: From Heisenberg to a Quantum Compass and Kitaev Models. *Physical Review Letters*, 102(1):017205, Jan. 2009.
- [121] A. Jain, G. Hautier, C. J. Moore, S. Ping Ong, C. C. Fischer, T. Mueller, K. A. Persson, and G. Ceder. A high-throughput infrastructure for density functional theory calculations. *Computational Materials Science*, 50(8):2295–2310, 2011.
- [122] A. Jain, G. Hautier, S. P. Ong, C. J. Moore, C. C. Fischer, K. A. Persson, and G. Ceder. Formation enthalpies by mixing GGA and GGA + U calculations. *Physical Review B - Condensed Matter and Materials Physics*, 84(4):1–10, 2011.
- [123] A. Jain, S. P. Ong, W. Chen, B. Medasani, X. Qu, M. Kocher, M. Brafman, G. Petretto, G.-M. Rignanese, G. Hautier, D. Gunter, and K. A. Persson. FireWorks: a dynamic workflow system designed for high-throughput applications. *Concurrency Computation Practice and Experience*, 27:5037–5059, 2015.
- [124] A. Jain, S. P. Ong, G. Hautier, W. Chen, W. D. Richards, S. Dacek, S. Cholia, D. Gunter, D. Skinner, G. Ceder, and K. a. Persson. The Materials Project: A materials genome approach to accelerating materials innovation. *APL Materials*, 1(1):011002, 2013.
- [125] H. Kay and P. Vousden. Xcv. symmetry changes in barium titanate at low temperatures and their relation to its ferroelectric properties. *The London, Edinburgh, and Dublin Philosophical Magazine and Journal of Science*, 40(309):1019–1040, 1949.
- [126] S. Kearnes, K. McCloskey, M. Berndl, V. Pande, and P. Riley. Molecular graph convolutions: moving beyond fingerprints. *Journal of Computer-Aided Molecular Design*, 30(8):595–608, Aug 2016.
- [127] I. Kimchi, J. G. Analytis, and A. Vishwanath. Three dimensional quantum spin liquid in 3d-honeycomb iridate models and phase diagram in an infinite-d approximation. arXiv e-print 1309.1171, Sept. 2013.
- [128] R. D. King-Smith and D. Vanderbilt. Theory of polarization of crystalline solids. *Phys. Rev. B*, 47:1651–1654, Jan 1993.

- [129] R. D. King-Smith and D. Vanderbilt. Theory of polarization of crystalline solids. *Physical Review B*, 47(3):1651–1654, jan 1993.
- [130] A. Kitaev. Anyons in an exactly solved model and beyond. *Annals of Physics*, 321(1):2–111, Jan. 2006.
- [131] R. Kleffner, J. Flatten, A. Leaver-Fay, D. Baker, J. B. Siegel, F. Khatib, and S. Cooper. Foldit standalone: a video game-derived protein structure manipulation interface using rosetta. *Bioinformatics*, 33(17):2765–2767, may 2017.
- [132] W. Kohn. Nobel lecture: Electronic structure of matter—wave functions and density functionals. *Rev. Mod. Phys.*, 71:1253–1266, Oct 1999.
- [133] W. Kohn and L. J. Sham. Self-consistent equations including exchange and correlation effects. *Phys. Rev.*, 140:A1133–A1138, Nov 1965.
- [134] R. Kondor, H. Truong Son, H. Pan, B. Anderson, and S. Trivedi. Covariant compositional networks for learning graphs. *ArXiv e-prints*, Jan. 2018.
- [135] G. Kresse and J. Furthmüller. Efficiency of ab-initio total energy calculations for metals and semiconductors using a plane-wave basis set. *Computational Materials Science*, 6(1):15–50, 1996.
- [136] G. Kresse and J. Furthmüller. Efficient iterative schemes for ab initio total-energy calculations using a plane-wave basis set. *Physical Review B*, 54(16), 1996.
- [137] G. Kresse and J. Hafner. Ab initio molecular dynamics for liquid metals. *Physical Review B*, 47(1):558–561, 1993.
- [138] G. Kresse and D. Jourbert. From ultrasoft pseudopotentials to the projector augmented-wave method. *Physical Review B*, 59(3):1758–1775, 1999.
- [139] E. Kroumova, M. I. Aroyo, and J. M. Perez-Mato. Prediction of new displacive ferroelectrics through systematic pseudosymmetry search. Results for materials with Pba 2 and Pmc 2 1 symmetry. *Acta Crystallographica Section B Structural Science*, 58(6):921–933, 2002.
- [140] A. V. Krukau, O. A. Vydrov, A. F. Izmaylov, and G. E. Scuseria. Influence of the exchange screening parameter on the performance of screened hybrid functionals. *The Journal of Chemical Physics*, 125(22):224106, dec 2006.
- [141] A. V. Krukau, O. A. Vydrov, A. F. Izmaylov, and G. E. Scuseria. Influence of the exchange screening parameter on the performance of screened hybrid functionals. *The Journal of Chemical Physics*, 125(22):224106, 2006.
- [142] L. D. Landau and E. M. Lifshitz. *Mechanics*, volume 1 of *Course of Theoretical Physics*. Elsevier, 1976.

- [143] C. Lavenn, N. Guillou, M. Monge, D. Podbevsek, G. Ledoux, A. Fateeva, and A. Demessence. Shedding light on an ultra-bright photoluminescent lamellar gold thiolate coordination polymer $[\text{Au}(\text{p-SPhCO}_2\text{Me})]_n$. *Chemical Communications*, 52(58):9063–9066, 2016.
- [144] A. I. Lebedev. Ferroelectric phase transition in orthorhombic CdTiO_3 : First-principles studies. *Physics of the Solid State*, 51(4):802–809, Apr 2009.
- [145] D. Lebeugle, D. Colson, A. Forget, and M. Viret. Very large spontaneous electric polarization in BiFeO_3 single crystals at room temperature and its evolution under cycling fields. *Applied Physics Letters*, 91(2):022907, 2007.
- [146] E. K.-H. Lee, R. Schaffer, S. Bhattacharjee, and Y. B. Kim. Heisenberg-kitaev model on hyper-honeycomb lattice. arXiv e-print 1308.6592, Aug. 2013.
- [147] K. Lee, E. D. Murray, L. Kong, B. I. Lundqvist, and D. C. Langreth. Higher-accuracy van der waals density functional. *Physical Review B*, 82(8):081101, 2010. PRB.
- [148] A. J. Leggett. Cuprate superconductivity: Dependence of $t_{\{c\}}$ on the c-axis layering structure. *Physical Review Letters*, 83(2):392–395, July 1999.
- [149] J. Li, Z. Yang, H. Liu, and D. Cai. Deep Rotation Equivariant Network. *ArXiv e-prints*, May 2017.
- [150] Y. Li, K. Foyevtsova, H. O. Jeschke, and R. Valentí. Analysis of the optical conductivity for A_2IrO_3 ($\text{A} = \text{Na, Li}$) from first principles. *Physical Review B*, 91(16):161101, 2015.
- [151] Y.-C. Lin, R. K. Ghosh, R. Addou, N. Lu, S. M. Eichfeld, H. Zhu, M.-Y. Li, X. Peng, M. J. Kim, L.-J. Li, R. M. Wallace, S. Datta, and J. A. Robinson. Atomically thin resonant tunnel diodes built from synthetic van der waals heterostructures. *Nat Commun*, 6, 2015.
- [152] M. E. Lines and A. M. Glass. *Basic Concepts*, chapter 1. Oxford University Press, Oxford, 2001.
- [153] M. E. Lines and A. M. Glass. *Domains, Imperfections, And Polarization Reversal*, pages 87–126. Oxford University Press, Feb 2001.
- [154] M. E. Lines and A. M. Glass. *Principles and Applications of Ferroelectrics and Related Materials*. Oxford University Press, Feb 2001.
- [155] X. Liu, T. Berlijn, W.-G. Yin, W. Ku, a. Tsvelik, Y.-J. Kim, H. Gretarsson, Y. Singh, P. Gegenwart, and J. P. Hill. Long-range magnetic ordering in Na_2IrO_3 . *Physical Review B*, 83(22):220403, June 2011.

- [156] T. Low, A. Chaves, J. D. Caldwell, A. Kumar, N. X. Fang, P. Avouris, T. F. Heinz, F. Guinea, L. Martin-Moreno, and F. Koppens. Polaritons in layered two-dimensional materials. *Nat Mater*, 16(2):182–194, 2017.
- [157] A. O. Lyakhov, A. R. Oganov, H. T. Stokes, and Q. Zhu. New developments in evolutionary structure prediction algorithm USPEX. *Computer Physics Communications*, 184(4):1172–1182, apr 2013.
- [158] P.-W. Ma and S. L. Dudarev. Constrained density functional for noncollinear magnetism. *Physical Review B*, 91(5):054420, 2015.
- [159] K. F. Mak, C. Lee, J. Hone, J. Shan, and T. F. Heinz. Atomically thin mos2: A new direct-gap semiconductor. *Physical Review Letters*, 105(13):136805, 2010. PRL.
- [160] S. Mandal and N. Surendran. Exactly solvable kitaev model in three dimensions. *Physical Review B*, 79(2):024426, Jan. 2009.
- [161] S. Manni, S. Choi, I. I. Mazin, R. Coldea, M. Altmeyer, H. O. Jeschke, R. Valentí, and P. Gegenwart. Effect of isoelectronic doping on the honeycomb-lattice iridate A_2IrO_3 . *Physical Review B*, 89(24):245113, June 2014.
- [162] R. M. Martin. *Electronic Structure: Basic Theory and Practical Methods*, chapter 3. Cambridge University Press, 2012.
- [163] R. M. Martin. *Electronic Structure: Basic Theory and Practical Methods*, chapter 6-9. Cambridge University Press, 2012.
- [164] R. M. Martin. *Electronic Structure: Basic Theory and Practical Methods*, chapter 8. Cambridge University Press, 2012.
- [165] K. Mathew, J. H. Montoya, A. Faghaninia, S. Dwarakanath, M. Aykol, H. Tang, I. heng Chu, T. Smidt, B. Bocklund, M. Horton, J. Dagdelen, B. Wood, Z.-K. Liu, J. Neaton, S. P. Ong, K. Persson, and A. Jain. Atomate: A high-level interface to generate, execute, and analyze computational materials science workflows. *Computational Materials Science*, 139(Supplement C):140 – 152, 2017.
- [166] I. I. Mazin, H. O. Jeschke, K. Foyevtsova, R. Valentí, and D. I. Khomskii. Na_2IrO_3 as a Molecular Orbital Crystal. *Physical Review Letters*, 109(19):197201, Nov. 2012.
- [167] I. I. Mazin, S. Manni, K. Foyevtsova, H. O. Jeschke, P. Gegenwart, and R. Valentí. Origin of the insulating state in honeycomb iridates and rhodates. *Phys. Rev. B*, 88:035115, Jul 2013.
- [168] I. I. Mazin, S. Manni, K. Foyevtsova, H. O. Jeschke, P. Gegenwart, and R. Valentí. Origin of the insulating state in honeycomb iridates and rhodates. *Physical Review B*, 88(3):035115, July 2013.

- [169] I. I. Mazin and D. J. Singh. Competitions in layered ruthenates: Ferromagnetism versus antiferromagnetism and triplet versus singlet pairing. *Physical Review Letters*, 82(21):4324–4327, May 1999.
- [170] N. D. Mermin and H. Wagner. Absence of ferromagnetism or antiferromagnetism in one- or two-dimensional isotropic heisenberg models. *Physical Review Letters*, 17(22):1133–1136, Nov. 1966.
- [171] A. I. Mihut, L. E. Spring, R. I. Bewley, S. J. Blundell, W. Hayes, T. Jestdt, B. W. Lovett, R. McDonald, F. L. Pratt, J. Singleton, P. D. Battle, J. Lago, M. J. Rosseinsky, and J. F. Vente. Physical properties of the n=3 ruddlesden - popper compound. *Journal of Physics: Condensed Matter*, 10(45):L727, Nov. 1998.
- [172] K. A. Modic, T. E. Smidt, I. Kimchi, N. P. Breznay, A. Biffin, S. Choi, R. D. Johnson, R. Coldea, P. Watkins-Curry, G. T. McCandless, J. Y. Chan, F. Gandara, Z. Islam, A. Vishwanath, A. Shekhter, R. D. McDonald, and J. G. Analytis. Realization of a three-dimensional spin-anisotropic harmonic honeycomb iridate. *Nature communications*, 5(May):4203, Jan. 2014.
- [173] K. Momma and F. Izumi. Vesta: a three-dimensional visualization system for electronic and structural analysis. *Journal of Applied Crystallography*, 41(3):653–658, 2008.
- [174] K. Momma and F. Izumi. VESTA3 for three-dimensional visualization of crystal, volumetric and morphology data. *Journal of Applied Crystallography*, 44(6):1272–1276, Dec 2011.
- [175] H. J. Monkhorst and J. D. Pack. Special points for brillouin-zone integrations. *Physical Review B*, 13(12):5188–5192, 1976. Phys. Rev. B ISI Document Delivery No.: BV088 Times Cited: 8161 Cited Reference Count: 6 AMERICAN PHYSICAL SOC COLLEGE PK.
- [176] T. Moriya. Anisotropic superexchange interaction and weak ferromagnetism. *Physical Review*, 120(1):91–98, Oct. 1960.
- [177] P. Muller. Crystal structure refinement: A crystallographer’s guide to shelxl. page 213, Jul 2006.
- [178] U. Müller. *Symmetry relations at phase transitions*, pages 196–215. Oxford University Press, apr 2013.
- [179] U. Müller. *Symmetry Relationships between Crystal Structures*. Oxford University Press, apr 2013.
- [180] J. B. Neaton, C. Ederer, U. V. Waghmare, N. A. Spaldin, and K. M. Rabe. First-principles study of spontaneous polarization in multiferroic BiFeO₃. *Phys. Rev. B*, 71:014113, Jan 2005.

- [181] A. R. Oganov, A. O. Lyakhov, and M. Valle. How evolutionary crystal structure prediction works—and why. *Accounts of Chemical Research*, 44(3):227–237, mar 2011.
- [182] D. Ohlmann, H. Pritzkow, H. Grutzmacher, M. Anthamatten, and R. Glaser. A hexanuclear copper arylselenolate: synthesis, structure and proposal for its rearrangement. *Journal of the Chemical Society, Chemical Communications*, (10):1011–1012, 1995.
- [183] E. Ohmichi and T. Osada. Torque magnetometry in pulsed magnetic fields with use of a commercial microcantilever. *Review of Scientific Instruments*, 73(8):3022–3026, Aug. 2002.
- [184] Y. Okada, D. Walkup, H. Lin, C. Dhital, T.-R. Chang, S. Khadka, W. Zhou, H.-T. Jeng, M. Paranjape, A. Bansil, Z. Wang, S. D. Wilson, and V. Madhavan. Imaging the evolution of metallic states in a correlated iridate. *Nature materials*, 12(8):707–13, Aug. 2013.
- [185] Y. Okamoto, M. Nohara, H. Aruga-Katori, and H. Takagi. Spin-liquid state in the $s=1/2$ hyperkagome antiferromagnet $\text{Na}_4\text{Ir}_3\text{O}_8$. *Physical Review Letters*, 99(13):137207, Sept. 2007.
- [186] S. P. Ong, S. Cholia, A. Jain, M. Brafman, D. Gunter, G. Ceder, and K. A. Persson. The materials application programming interface (API): A simple, flexible and efficient API for materials data based on REpresentational state transfer (REST) principles. *Computational Materials Science*, 97:209–215, feb 2015.
- [187] S. P. Ong, W. D. Richards, A. Jain, G. Hautier, M. Kocher, S. Cholia, D. Gunter, V. L. Chevrier, K. a. Persson, and G. Ceder. Python Materials Genomics (pymatgen): A robust, open-source python library for materials analysis. *Computational Materials Science*, 68:314–319, 2013.
- [188] S. P. Ong, W. D. Richards, A. Jain, G. Hautier, M. Kocher, S. Cholia, D. Gunter, V. L. Chevrier, K. a. Persson, and G. Ceder. Python Materials Genomics (pymatgen): A robust, open-source python library for materials analysis. *Computational Materials Science*, 68:314–319, 2013.
- [189] M. J. OMalley, H. Verweij, and P. M. Woodward. Structure and properties of ordered Li_2IrO_3 and Li_2PtO_3 . *Journal of Solid State Chemistry*, 181(8):1803–1809, Aug. 2008.
- [190] M. J. OMalley, H. Verweij, and P. M. Woodward. Structure and properties of ordered Li_2IrO_3 and Li_2PtO_3 . *Journal of Solid State Chemistry*, 181(8):1803–1809, Aug. 2008.
- [191] A. N. Parikh, S. D. Gillmor, J. D. Beers, K. M. Beardmore, R. W. Cutts, and B. I. Swanson. Characterization of chain molecular assemblies in long-chain, layered silver thiolates: A joint infrared spectroscopy and x-ray diffraction study. *The Journal of Physical Chemistry B*, 103(15):2850–2861, 1999. doi: 10.1021/jp983938b.

- [192] R. Penrose. Applications of negative dimensional tensors. In *Combinatorial Mathematics and its Applications*. Academic Press, 1971.
- [193] J. Perdew, K. Burke, and M. Ernzerhof. Generalized Gradient Approximation Made Simple. *Physical review letters*, 77(18):3865–3868, Oct. 1996.
- [194] J. M. Perez-Mato, R. L. Withers, A. K. Larsson, D. Orobengoa, and Y. Liu. Distortion modes and related ferroic properties of the stuffed tridymite-type compounds SrAl_2O_4 and BaAl_2O_4 . *Physical Review B - Condensed Matter and Materials Physics*, 79(6):1–12, 2009.
- [195] C. J. Pickard and R. J. Needs. Ab initio random structure searching. *Journal of Physics: Condensed Matter*, 23(5):053201, jan 2011.
- [196] A. K. Pradhan, K. Zhang, D. Hunter, J. B. Dadson, G. B. Loiu, P. Bhattacharya, R. Katiyar, J. Zhang, D. J. Sellmyer, U. N. Roy, Y. Cui, and A. Burger. Magnetic and electrical properties of single-phase multiferroic BiFeO_3 . *Journal of Applied Physics*, 97(9):093903, 2005.
- [197] C. R. Qi, H. Su, K. Mo, and L. J. Guibas. PointNet: Deep learning on point sets for 3D classification and segmentation. *arXiv preprint arXiv:1612.00593*, 2016.
- [198] C. R. Qi, L. Yi, H. Su, and L. J. Guibas. PointNet++: Deep hierarchical feature learning on point sets in a metric space. *arXiv preprint arXiv:1706.02413*, 2017.
- [199] D. Y. Qiu, F. H. da Jornada, and S. G. Louie. Optical spectrum of mos2: Many-body effects and diversity of exciton states. *Physical Review Letters*, 111(21):216805, 2013. PRL.
- [200] K. M. Rabe. Antiferroelectricity in Oxides: A Reexamination. In *Functional Metal Oxides*, pages 221–244. Wiley-VCH Verlag GmbH & Co. KGaA, jul 2013.
- [201] K. M. Rabe, M. Dawber, C. Lichtensteiger, C. H. Ahn, and J.-M. Triscone. Modern physics of ferroelectrics: Essential background. In *Physics of Ferroelectrics: A Modern Perspective*, pages 1–30. Springer Berlin Heidelberg.
- [202] R. Ramakrishnan, P. O. Dral, M. Rupp, and O. A. von Lilienfeld. Quantum chemistry structures and properties of 134 kilo molecules. *Scientific Data*, 1, 2014.
- [203] R. Ramakrishnan, P. O. Dral, M. Rupp, and O. A. von Lilienfeld. Quantum chemistry structures and properties of 134 kilo molecules. *Scientific Data*, 1, 2014.
- [204] M. Reisert and H. Burkhardt. Spherical tensor calculus for local adaptive filtering. *Tensors in Image Processing and Computer Vision*, pages 153–178, 2009.
- [205] R. Resta. Theory of the electric polarization in crystals. *Ferroelectrics*, 136(1):51–55, nov 1992.

- [206] R. Resta. Macroscopic polarization in crystalline dielectrics: the geometric phase approach. *Reviews of Modern Physics*, 66(3):899–915, jul 1994.
- [207] R. Resta. Berry phase in electronic wavefunctions. *Troisième Cycle de la Physique en Suisse Romande*, pages 899–915, Anne Académique 1995-1996.
- [208] R. Resta and D. Vanderbilt. *Theory of Polarization: A Modern Approach*, pages 31–68. Springer Berlin Heidelberg, Berlin, Heidelberg, 2007.
- [209] J. Reuther, R. Thomale, and S. Rachel. Spiral order in the honeycomb iridate Li_2IrO_3 . *Physical Review B*, 90(10):100405, Sept. 2014.
- [210] J. Rodriguez-Carvajal. Recent advances in magnetic structure determination by neutron powder diffraction. *Physica B: Condensed Matter (Amsterdam)*, 192:55, Oct 1993.
- [211] M. Rohlfing and S. G. Louie. Electron-hole excitations in semiconductors and insulators. *Physical Review Letters*, 81(11):2312–2315, 1998. PRL.
- [212] M. Rohlfing and S. G. Louie. Electron-hole excitations and optical spectra from first principles. *Physical Review B*, 62(8):4927–4944, 2000. PRB.
- [213] K. Rolfs, S. Toth, E. Pomjakushina, D. Sheptyakov, J. Taylor, and K. Conder. Spiral magnetic phase in Li-doped Na_2IrO_3 . *Physical Review B*, 91(18):5–8, 2015.
- [214] G. Román-Pérez and J. M. Soler. Efficient implementation of a van der waals density functional: Application to double-wall carbon nanotubes. *Physical Review Letters*, 103(9):096102, 2009. PRL.
- [215] L. Ruddigkeit, R. van Deursen, L. C. Blum, and J.-L. Reymond. Enumeration of 166 billion organic small molecules in the chemical universe database GDB-17. *Journal of Chemical Information and Modeling*, 52(11):2864–2875, nov 2012.
- [216] A. Sahu, A. Khare, D. D. Deng, and D. J. Norris. Quantum confinement in silver selenide semiconductor nanocrystals. *Chemical Communications*, 48(44):5458–5460, 2012.
- [217] L. M. Sandratskii and J. Kübler. Non-collinear magnetism: effects of symmetry and relativity. *Modern Physics Letters*, 10(189), 1996.
- [218] J. Schindelin, I. Arganda-Carreras, E. Frise, V. Kaynig, M. Longair, T. Pietzsch, S. Preibisch, C. Rueden, S. Saalfeld, B. Schmid, J.-Y. Tinevez, D. J. White, V. Hartenstein, K. Eliceiri, P. Tomancak, and A. Cardona. Fiji: an open-source platform for biological-image analysis. *Nat Meth*, 9(7):676–682, 2012. 10.1038/nmeth.2019.
- [219] H. Schmidbaur and A. Schier. Argentophilic interactions. *Angewandte Chemie International Edition*, 54(3):746–784, 2015.

- [220] H. Schmidt, F. Giustiniano, and G. Eda. Electronic transport properties of transition metal dichalcogenide field-effect devices: surface and interface effects. *Chemical Society Reviews*, 44(21):7715–7736, 2015.
- [221] K. T. Schütt, F. Arbabzadah, S. Chmiela, K. R. Müller, and A. Tkatchenko. Quantum-chemical insights from deep tensor neural networks. 8:13890 EP –, Jan 2017. Article.
- [222] K. T. Schütt, P.-J. Kindermans, H. E. Sauceda, S. Chmiela, A. Tkatchenko, and K.-R. Müller. SchNet: A continuous-filter convolutional neural network for modeling quantum interactions. *ArXiv e-prints*, June 2017.
- [223] K. T. Schütt, H. E. Sauceda, P.-J. Kindermans, A. Tkatchenko, and K.-R. Müller. SchNet – a deep learning architecture for molecules and materials. *The Journal of Chemical Physics*, 148(24):241722, jun 2018.
- [224] J. F. Scott. Searching for new ferroelectrics and multiferroics: A users point of view. *npj Computational Materials*, 1(July):15006, 2015.
- [225] B. C. Server. Structure relations, 2018. <http://www.cryst.ehu.es/cryst/rel.html>.
- [226] Y. Shiozaki and T. Asahi. 50A-1: 1-6 SC (NH₂)₂ [F]. In *Organic crystals, liquid crystals and polymers*, pages 1–48. Springer, 2006.
- [227] Y. Shiozaki, E. Nakamura, and T. Mitsui, editors. *Ferroelectrics and Related Substances: Oxides Part 1: Perovskite-type Oxides and LiNbO₃ Family*. Springer-Verlag, 2001.
- [228] Y. Shiozaki, E. Nakamura, and T. Mitsui, editors. *Ferroelectrics and Related Substances: Oxides Part 2: Oxides other than Perovskite-type and LiNbO₃ Family*. Springer-Verlag, 2002.
- [229] Y. Shiozaki, E. Nakamura, and T. Mitsui, editors. *Ferroelectrics and Related Substances: SbSI family ... TAAP*. Springer-Verlag, 2004.
- [230] Y. Shiozaki, E. Nakamura, and T. Mitsui, editors. *Ferroelectrics and Related Substances: Organic crystals, liquid crystals and polymers*. Springer Berlin Heidelberg, 2006.
- [231] Y. Singh and P. Gegenwart. Antiferromagnetic Mott insulating state in single crystals of the honeycomb lattice material Na₂IrO₃. *Physical Review B*, 82(6):064412, Aug. 2010.
- [232] Y. Singh and P. Gegenwart. Antiferromagnetic mott insulating state in single crystals of the honeycomb lattice material na-₂IrO-₃. *Physical Review B*, 82(6):064412, Aug. 2010.

- [233] Y. Singh, S. Manni, J. Reuther, T. Berlijn, R. Thomale, W. Ku, S. Trebst, and P. Gegenwart. Relevance of the heisenberg-kitaev model for the honeycomb lattice iridates $a_2\text{iro}_3$. *Phys. Rev. Lett.*, 108:127203, Mar 2012.
- [234] R. Skomski. *Simple models of magnetism*. Oxford University Press, Oxford New York, 2008.
- [235] E. H. Smith, N. A. Benedek, and C. J. Fennie. Interplay of Octahedral Rotations and Lone Pair Ferroelectricity in CsPbF_3 . *Inorganic Chemistry*, 54(17):8536–8543, 2015.
- [236] J. S. Smith, O. Isayev, and A. E. Roitberg. ANI-1: An extensible neural network potential with DFT accuracy at force field computational cost. *Chem. Sci.*, 8:3192–3203, 2017.
- [237] M. Sofos, J. Goldberger, D. A. Stone, J. E. Allen, Q. Ma, D. J. Herman, W.-W. Tsai, L. J. Lauhon, and S. I. Stupp. A synergistic assembly of nanoscale lamellar photoconductor hybrids. *Nature Materials*, 8(1):68–75, 2009. 10.1038/nmat2336.
- [238] N. A. Spaldin. A beginner’s guide to the modern theory of polarization. *Journal of Solid State Chemistry*, 195:2–10, 2012.
- [239] G. L. Stamokostas and G. A. Fiete. Mixing of t_{2g} - e_g orbitals in 4d and 5d transition metal oxides. *Physical Review B*, 97(8), feb 2018.
- [240] H. T. Stokes, D. M. Hatch, and B. J. Campbell. ISOTROPY Software Suite. iso.byu.edu.
- [241] H. T. Stokes, C. Sadate, D. M. Hatch, L. L. Boyer, and M. J. Mehl. Analysis of the ferroelectric phase transition in BaAl_2O_4 by group theoretical methods and first-principles calculations. *Physical Review B*, 65(6):064105, 2002.
- [242] T. Takayama, a. Kato, R. Dinnebier, J. Nuss, H. Kono, L. Veiga, G. Fabbris, D. Haskel, and H. Takagi. Hyperhoneycomb Iridate $\beta\text{-Li}_2\text{IrO}_3$ as a Platform for Kitaev Magnetism. *Physical Review Letters*, 114(7):2–6, 2015.
- [243] E. S. Tasci, G. de la Flor, and M. Aroyo. Obtaining the transformation matrix connecting two group-subgroup related structures. <http://sig9.ecanews.org/pdfs/19%20Emre%20Tasci%20-%20Structure%20Relations.pdf>.
- [244] J. R. Teague, R. Gerson, and W. James. Dielectric hysteresis in single crystal BiFeO_3 . *Solid State Communications*, 8(13):1073 – 1074, 1970.
- [245] H. Terauchi, K. Tanabe, H. Maeda, M. Hida, N. Kamijo, M. Takashige, T. Nakamura, H. Ozawa, and R. Uno. EXAFS Studies on Amorphous PbTiO_3 . *Journal of the Physical Society of Japan*, 50(12):3977–3979, 1981.

- [246] N. Thomas, T. Smidt, S. Kearnes, L. Yang, L. Li, K. Kohlhoff, and P. Riley. Tensor field networks: Rotation- and translation-equivariant neural networks for 3d point clouds, 2018.
- [247] P. Tolédano and M. Guennou. Theory of antiferroelectric phase transitions. *Phys. Rev. B*, 94:014107, Jul 2016.
- [248] S. Tongay, H. Sahin, C. Ko, A. Luce, W. Fan, K. Liu, J. Zhou, Y.-S. Huang, C.-H. Ho, J. Yan, D. F. Ogletree, S. Aloni, J. Ji, S. Li, J. Li, F. M. Peeters, and J. Wu. Monolayer behaviour in bulk res2 due to electronic and vibrational decoupling. *Nat Commun*, 5, 2014.
- [249] W. Torng and R. B. Altman. 3D deep convolutional neural networks for amino acid environment similarity analysis. *BMC Bioinformatics*, 18(1):302, Jun 2017.
- [250] A. Toyo. spglib, 2018. <https://atztogo.github.io/spglib/>.
- [251] M.-L. Tsai, S.-H. Su, J.-K. Chang, D.-S. Tsai, C.-H. Chen, C.-I. Wu, L.-J. Li, L.-J. Chen, and J.-H. He. Monolayer mos2 heterojunction solar cells. *ACS Nano*, 8(8):8317–8322, 2014.
- [252] D. L. Turner, T. P. Vaid, P. W. Stephens, K. H. Stone, A. G. DiPasquale, and A. L. Rheingold. Semiconducting leadsulfurorganic network solids. *Journal of the American Chemical Society*, 130(1):14–15, 2008.
- [253] M. M. Ugeda, A. J. Bradley, S.-F. Shi, F. H. da Jornada, Y. Zhang, D. Y. Qiu, W. Ruan, S.-K. Mo, Z. Hussain, Z.-X. Shen, F. Wang, S. G. Louie, and M. F. Crommie. Giant bandgap renormalization and excitonic effects in a monolayer transition metal dichalcogenide semiconductor. *Nat Mater*, 13(12):1091–1095, 2014.
- [254] D. Vanderbilt and R. D. King-Smith. Electric polarization as a bulk quantity and its relation to surface charge. *Physical Review B*, 48(7):4442–4455, aug 1993.
- [255] P. Villars and K. Cenzual, editors. *Crystal Structures of Inorganic Compounds*. Springer Berlin Heidelberg, 2009.
- [256] A. von Hippel, R. G. Breckenridge, F. G. Chesley, and L. Tisza. High dielectric constant ceramics. *Industrial & Engineering Chemistry*, 38(11):1097–1109, nov 1946.
- [257] R. Wahl, D. Vogtenhuber, and G. Kresse. SrTiO₃ and BaTiO₃ revisited using the projector augmented wave method: Performance of hybrid and semilocal functionals. *Phys. Rev. B*, 78:104116, Sep 2008.
- [258] I. Wallach, M. Dzamba, and A. Heifets. AtomNet: A deep convolutional neural network for bioactivity prediction in structure-based drug discovery. *CoRR*, abs/1510.02855, 2015.

- [259] J. Wang, J. B. Neaton, H. Zheng, V. Nagarajan, S. B. Ogale, B. Liu, D. Viehland, V. Vaithyanathan, D. G. Schlom, U. V. Waghmare, N. A. Spaldin, K. M. Rabe, M. Wuttig, and R. Ramesh. Epitaxial BiFeO₃ Multiferroic Thin Film Heterostructures. *Science*, 299(5613):1719–1722, 2003.
- [260] S. Wang and J. Li. Two-dimensional inorganicorganic hybrid semiconductors composed of double-layered ZnS and monoamines with aromatic and heterocyclic aliphatic rings: Syntheses, structures, and properties. *Journal of Solid State Chemistry*, (0), 2014.
- [261] Y. Wang, J. Lv, L. Zhu, and Y. Ma. Crystal structure prediction via particle-swarm optimization. *Phys. Rev. B*, 82:094116, Sep 2010.
- [262] D. Weininger. SMILES, a chemical language and information system. 1. introduction to methodology and encoding rules. *Journal of Chemical Information and Modeling*, 28(1):31–36, feb 1988.
- [263] S. Wemple, M. DiDomenico, and I. Camlibel. Dielectric and optical properties of melt-grown batio₃. *Journal of Physics and Chemistry of Solids*, 29(10):1797–1803, 1968.
- [264] S. Wemple, M. DiDomenico Jr, and I. Camlibel. Relationship between linear and quadratic electro-optic coefficients in linbo₃, litao₃, and other oxygen-octahedra ferroelectrics based on direct measurement of spontaneous polarization. *Applied Physics Letters*, 12(6):209–211, 1968.
- [265] D. E. Worrall, S. J. Garbin, D. Turmukhambetov, and G. J. Brostow. Harmonic networks: Deep translation and rotation equivariance. In *The IEEE Conference on Computer Vision and Pattern Recognition (CVPR)*, July 2017.
- [266] B. Wul and J. Goldman. Ferroelectric switching in batio₃ ceramics. *CR Acad. Sci. URSS*, 51:21, 1946.
- [267] H. Yan, J. N. Hohman, F. H. Li, C. Jia, D. Solis-Ibarra, B. Wu, J. E. P. Dahl, R. M. K. Carlson, B. A. Tkachenko, A. A. Fokin, P. R. Schreiner, A. Vailionis, T. R. Kim, T. P. Devereaux, Z.-X. Shen, and N. A. Melosh. Hybrid metal–organic chalcogenide nanowires with electrically conductive inorganic core through diamondoid-directed assembly. *Nature Materials*, 16(3):349–355, dec 2016.
- [268] Q. Yan, J. Yu, S. K. Suram, L. Zhou, A. Shinde, P. F. Newhouse, W. Chen, G. Li, K. A. Persson, J. M. Gregoire, and J. B. Neaton. Solar fuels photoanode materials discovery by integrating high-throughput theory and experiment. *Proceedings of the National Academy of Sciences*, 114(12):3040–3043, mar 2017.
- [269] Q. Yang, J. X. Cao, Y. Ma, and Y. C. Zhou. First principles study of polarization-strain coupling in SrBi₂Ta₂O₉. *AIP Advances*, 3(5):052134, 2013.

- [270] F. Ye, S. Chi, H. Cao, B. C. Chakoumakos, J. a. Fernandez-Baca, R. Custelcean, T. F. Qi, O. B. Korneta, and G. Cao. Direct evidence of a zigzag spin-chain structure in the honeycomb lattice: A neutron and x-ray diffraction investigation of single-crystal Na_2IrO_3 . *Physical Review B*, 85(18):180403, May 2012.
- [271] B. Yuan, J. P. Clancy, A. M. Cook, C. M. Thompson, J. Greedan, G. Cao, B. C. Jeon, T. W. Noh, M. H. Upton, D. Casa, T. Gog, A. Paramekanti, and Y.-J. Kim. Determination of Hund's coupling in $5d$ oxides using resonant inelastic x-ray scattering. *Phys. Rev. B*, 95:235114, Jun 2017.
- [272] M. A. Zeb and H.-Y. Kee. Interplay between spin-orbit coupling and Hubbard interaction in SrIrO_3 and related Pbnm perovskite oxides. *Physical Review B*, 86(8):085149, Aug. 2012.
- [273] H. Zhang. A theory for structural phase transitions in batio3 single crystal and pbzro3-xpbtio3 solid solution. *AIP Advances*, 3(4):042118, 2013.
- [274] Y. Zhang, G. M. Dalpian, B. Fluegel, S.-H. Wei, A. Mascarenhas, X. Y. Huang, J. Li, and L. W. Wang. Novel approach to tuning the physical properties of organic-inorganic hybrid semiconductors. *Physical Review Letters*, 96(2):026405, 2006. PRL.
- [275] Y. Zhang, J. Sun, J. P. Perdew, and X. Wu. Comparative first-principles studies of prototypical ferroelectric materials by LDA, GGA, and SCAN meta-GGA. *Phys. Rev. B*, 96:035143, Jul 2017.
- [276] Z. Zhao, S. Wang, A. R. Oganov, P. Chen, Z. Liu, and W. L. Mao. Tuning the crystal structure and electronic states of ag_2se : Structural transitions and metallization under pressure. *Physical Review B*, 89(18):180102, 2014. PRB.
- [277] L. Zhou, Q. Yan, A. Shinde, D. Guevarra, P. F. Newhouse, N. Becerra-Stasiewicz, S. M. Chatman, J. A. Haber, J. B. Neaton, and J. M. Gregoire. High Throughput Discovery of Solar Fuels Photoanodes in the $\text{CuO-V}_2\text{O}_5$ System. *Advanced Energy Materials*, 5(22):1500968, aug 2015.
- [278] Y. Zhou, Q. Ye, Q. Qiu, and J. Jiao. Oriented Response Networks. *ArXiv e-prints*, Jan. 2017.
- [279] N. E. R. Zimmermann, M. K. Horton, A. Jain, and M. Haranczyk. Assessing local structure motifs using order parameters for motif recognition, interstitial identification, and diffusion path characterization. *Frontiers in Materials*, 4, nov 2017.
- [280] A. Zunger. Inverse design in search of materials with target functionalities. *Nature Reviews Chemistry*, 2(4):0121, mar 2018.

Appendix A

Appendix for Realization of a
three-dimensional spin-anisotropic
harmonic honeycomb iridate

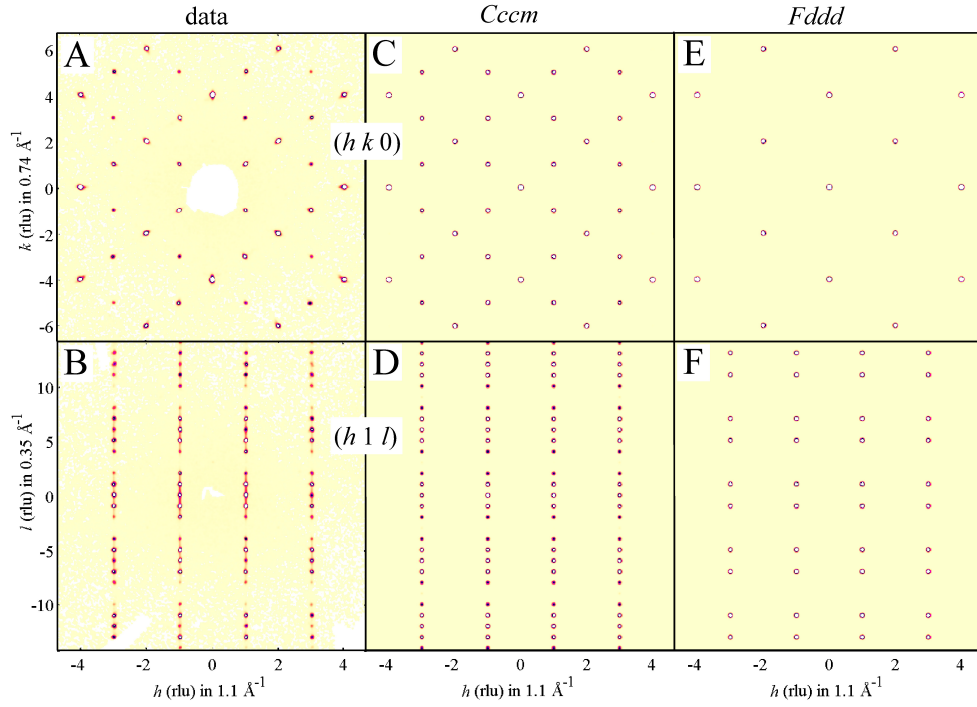


Figure A.1: X-ray diffraction pattern in the $(hk0)$ (top) and $(h1l)$ (bottom) planes. Raw data (AB) is well reproduced by calculations (CD) for the $Cccm$ structure (Table A.1), in contrast an $Fddd$ (hyper-honeycomb) structure (EF) can only explain the existence of less than half of the observed diffraction peaks.

Single Crystal Refinement

The very different magnetic ordering temperature of our flux-grown single crystals, $T_N = 38$ K, compared to 15 K [231] reported for the so-far-synthesized powders of Li_2IrO_3 (layered honeycomb crystal structure, monoclinic $C2/m$ unit cell [189]) suggested that the flux-grown samples may realize a polytype of Li_2IrO_3 with a different crystal structure. This was clearly revealed by x-ray diffraction measurements performed using a Mo-source Oxford Diffraction Supernova diffractometer. Several crystals were measured and the diffraction patterns were all consistent in terms of the unit cell and selection rules for the observed diffraction peaks. Here we report in detail the data on an approximate rhombus-shaped $\sim 35 \times 10^3 \mu\text{m}^3$ flux-grown crystal.

The lattice parameters of the monoclinic layered honeycomb crystal structure [189] could not account for the positions of over 2000 Bragg peaks measured in our diffraction experiment, which instead could be indexed with an orthorhombic unit cell with parameters given in Table A.1. Representative diffraction patterns are illustrated in Fig. A.1AB, where (h, k, l)

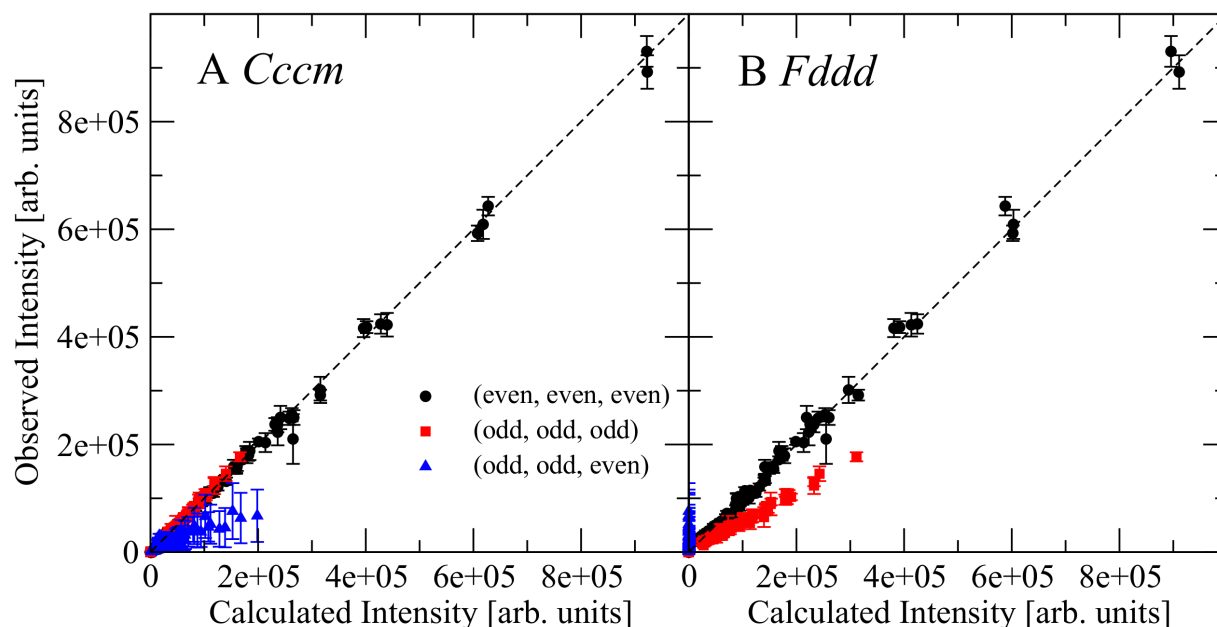


Figure A.2: Observed diffraction intensities plotted against those calculated in the refined (A) *Cccm* (Table A.1) and (B) *Fddd* structural models. The dashed lines indicate 1:1 agreement between data and model and error bars reflect the intensity uncertainties after averaging the observed intensities of reflections expected to be equivalent under orthorhombic symmetry. The three families of reflections discussed in the text are plotted as different symbols/colors (black circles, red squares, and blue triangles). Note that the *Fddd* model predicts zero intensity at the observed (odd, odd, even) reflections and largely overestimates the intensities of (odd, odd, odd) peaks.

refer to wavevector components in reciprocal lattice units of the orthorhombic unit cell. The highest-symmetry orthorhombic space groups that can account for all of the observed peaks in the diffraction patterns are *Cccm* (no. 66) and *Ccc2* (no. 37). Both have the same selection rule for allowed reflections for a general atomic position, $(hkl) : h + k$ even, $(0kl) : k$ and l even, $(h0l) : h$ and l even. Both have a *C*-centered unit cell, corresponding to a translation of $(\frac{1}{2}, \frac{1}{2}, 0)$, and *Ccc2* is obtained from *Cccm* by removing a mirror plane normal to the *c*-axis. In the final refinements of the crystal structure reported below, we did not find any significant atomic displacements and correspondingly no improvement in the goodness of fit when the crystal symmetry was lowered from *Cccm* to *Ccc2*, so in the following we discuss only the higher symmetry case.

The unit cell volume is approximately $4\times$ the unit cell volume of the layered honeycomb structure ($Z = 4$), which suggested that the present polytype has the same mass density, but with $Z = 16$ formula units per unit cell. Since iridium is by far the dominant x-ray scatterer with 77 electrons (oxygen 8 and lithium 3 electrons), we first attempted a preliminary fit to

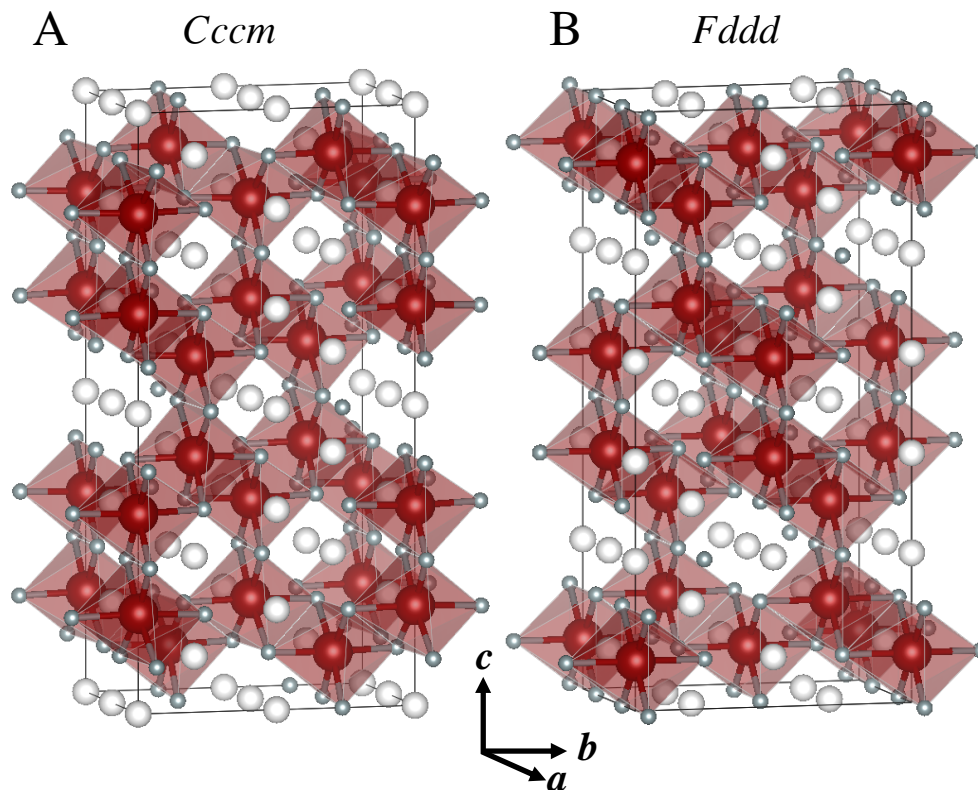


Figure A.3: Crystal structure models described in the text, (A) $Cccm$ (Table A.1) and (B) $Fddd$, large brown balls - Ir, medium light gray balls - Li, small gray balls - O.

the x-ray data assuming a simplified structural model composed solely of Ir ions located in general positions within the $Cccm$ space group symmetry. The iridium coordinates were set free to refine within the bounds of the orthorhombic unit cell. Remarkably, the refinement easily converged with Ir ions occupying two crystallographic sites with coordinates close to those listed in Table A.1. To test that this solution was reliable, and not an accidental local minimum in the least squares refinement, we employed simulated annealing techniques implemented in FullProf [210] to explore the full parameter space of the structural model against the full data set (treating each observed (h, k, l) reflection as an independent data point without imposing any symmetry constraints). By constructing a lattice with the dimensions of the orthorhombic unit cell $a \times b \times c$ but with lowered symmetry $P\bar{1}$, and populating it with eight iridium ions with atomic fractional coordinates free to vary within the full unit cell according to the annealing process, we found an unconstrained (except for inversion symmetry) yet highly reproducible iridium lattice that corresponded to a global

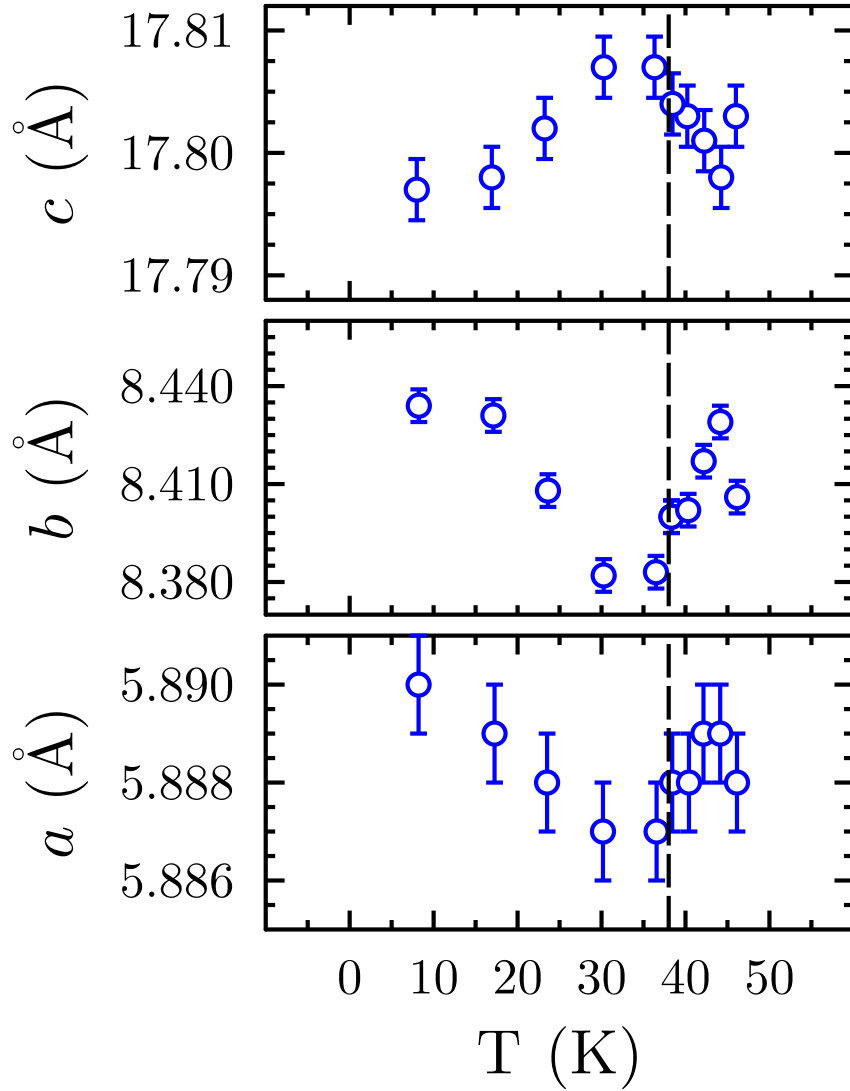


Figure A.4: Preliminary measurements of the change in the lattice parameters along the crystallographic a , b and c direction on cooling below the magnetic transition at T_N . We do not observe any changes in the crystallographic symmetry, but the elastic response in each direction is highly anisotropic, with the b -axis changing roughly 10 times more than the a -axis.

minimum in the parameter space. This structure was found to be in perfect agreement with the iridium framework of the initial refinement, confirming both the structural model and the space group, $Cccm$. In addition, the choice of space group symmetry was subjected to more rigorous testing by simulated annealing, which was systematically performed under symmetry constraints corresponding to sub-groups of $Cccm$ and $Fddd$ (see below), all of

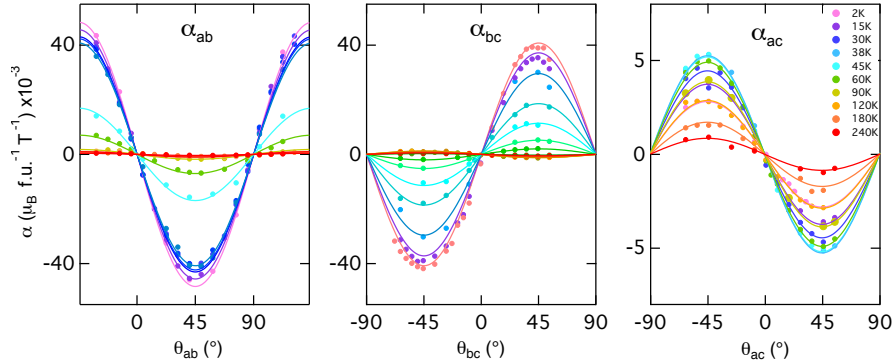


Figure A.5: The magnetic anisotropy extracted from the low field slope of the torque signal $\tau/\mu_0 H$, similar to that shown in Figure 3.4 B, taken for rotations through the three principal crystallographic planes and at different temperatures. The anisotropy is shown in units of μ_B per Ir, for (A) the $\chi_a - \chi_b$, (B) $\chi_a - \chi_c$ and (C) $\chi_b - \chi_c$. The only change of sign in the anisotropy is in (A) and an enlargement of this scale is shown in Figure 3D of the main text to emphasize this.

which converged to the $Cccm$ solution or failed, respectively.

Using the measured Bragg peak intensities, space group symmetry, and the identified iridium positions, we calculated the electron density maps in the unit cell (using Shelxl [177] and Wingx [84]). This revealed additional electron density pockets, which we identified as the location of oxygen ions. Lithium ions scatter x-rays very weakly (only 3 electrons) and their positions cannot be reliably identified using x-ray scattering techniques, especially in the presence of heavy elements such as iridium. However, assuming that the fundamental building blocks of the structure are edge-sharing IrO_6 and LiO_6 octahedra (as in the honeycomb polytype), one can readily determine idealized lithium positions (listed in Table A.1 and shown in Fig. A.3A) required to achieve this connectivity.

Assuming lithium ions to be fixed at the ideal positions, a full structural model was refined against the data set using FullProf [210]. Iridium and oxygen ions were located in the initial positions determined above, and their atomic coordinates were set free to vary within the constraints of $Cccm$ crystal symmetry. It became apparent that the structural model gave an excellent fit to most reflections, but over-estimated the diffraction intensity of a small subset. Specifically, the empirically-determined selection rules for observed (h, k, l) reflections give three families: (even, even, even) with $h + k + l = 4n$, n integer, (odd, odd, odd) except $l = 3 + 6n$, n integer, and (odd, odd, even). The intensities of these families of peaks are plotted in Fig. A.2A against the model calculation. It is clear that the model is in excellent agreement with the (even, even, even) and (odd, odd, odd) reflections. The model also explains the presence of the third family of reflections, the (odd, odd, even), but the observed intensity is weaker than predicted. In fact those reflections showed an asymmetry in the intensity not expected under orthorhombic symmetry, *i.e.* $I_{(\text{odd}, \text{odd}, \text{even})} \neq I_{(-\text{odd}, \text{odd}, \text{even})}$ (Fig. A.2A only shows the averaged (reduced) intensity of those reflections with the error

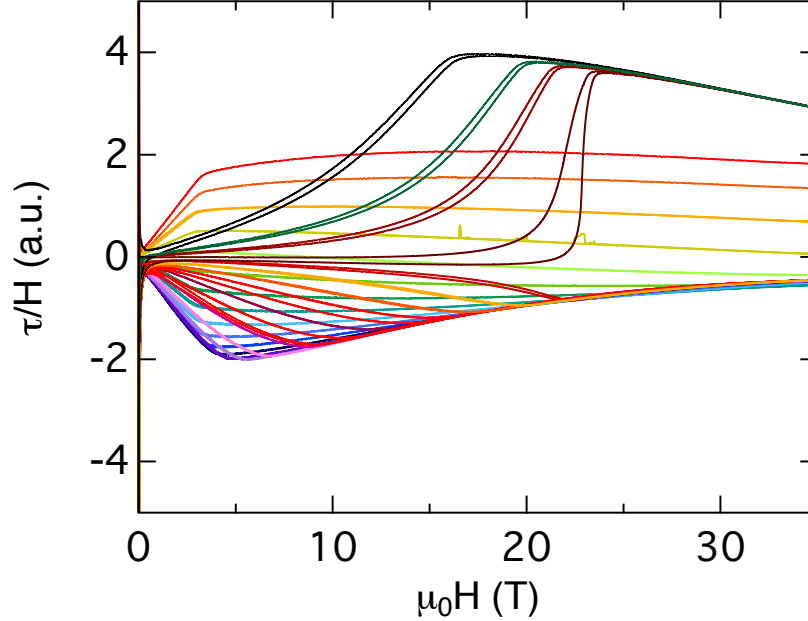


Figure A.6: Torque signal taken at magnetic fields up to 35 T at the National High magnetic Field Laboratory. The field H^* is extremely clear at all angles. At angles away from the principal axes the torque signal is very clearly linear and follows a $\sin 2\theta$ dependence described by equation A.4. The larger asymmetry in this data set compared to that measured in the superconducting magnet, is due to the larger field gradient experienced by the sample.

bars indicating the spread of values). The degrees of both the lowered average intensity and asymmetry were found to vary across a number of different samples measured, however, the excellent agreement to the (even, even, even) and (odd, odd, odd) reflections was robust and consistent across all samples tested. We propose that the discrepancies in (odd, odd, even) intensities are most likely due to sample-dependent structural stacking faults, as discussed later in this section. A final refinement was performed against the (even, even, even) and (odd, odd, odd) reflections with excellent reliability factors $R_{F^2} = 3.83\%$, $wR_{F^2} = 4.91\%$, and $R_F = 2.27\%$ [including also the (odd, odd, even) reflections in the refinement resulted only in very small changes in the oxygen positions, which we regard to be below the accuracy that can be reliably determined]. The obtained structural parameters from the final refinement are given in Table A.1; essentially the same results are obtained in refinement done using Sir-92 [24] and Shelxl [177]. The above refinement assumed stoichiometric Li_2IrO_3 with all atomic positions fully occupied. However, we have also tested for the possibility that each of the seven cation sites (Ir1-2, Li1-5) could have a mixed Li/Ir occupancy. In this test we constrain the total site occupancy to unity (i.e. no structural vacancies) with no constraint on the total Li:Ir atomic ratio (i.e. stoichiometry free to vary). Under these constraints a

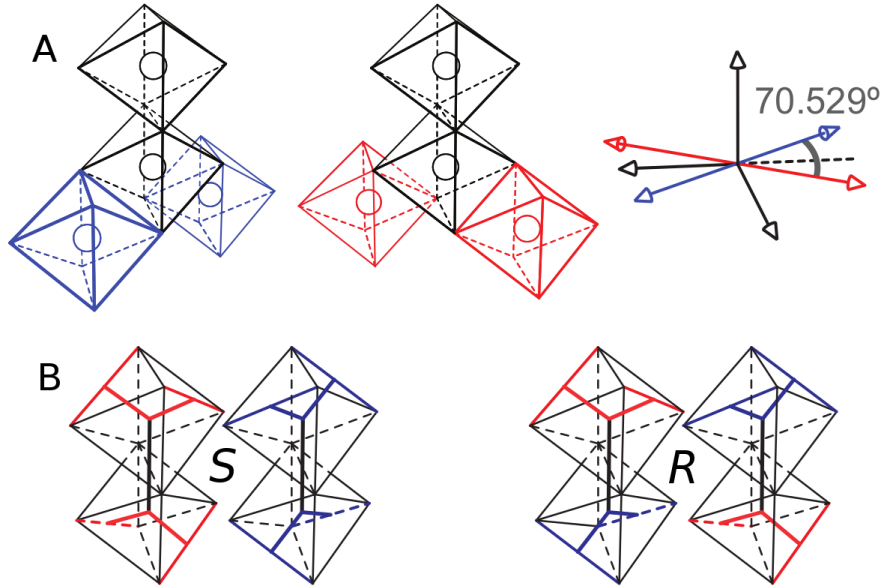


Figure A.7: (A) The two choices of edge shared bonds give rise to two kinds of links that are locally indistinguishable. These define two bonding planes (see Figure 3A of the main text) that are an angle $\phi_o \sim 70^\circ$ apart. (B) Links along the c -axis can either keep the same (S -links) or rotate (R -links) the honeycomb planes.

full refinement of Li/Ir occupancies on the cation sites lead to no significant improvement in the refinement parameters. Furthermore, the occupancies of the Li and Ir sublattices refined to their nominal values (Li only in Li1-5 sites and Ir only in Ir1-2 sites) within an error of less than 3%, further confirming the stoichiometric composition and the structural model in Table A.1. The obtained crystal structure is illustrated in Fig. A.3A. The full 3D x-ray diffraction pattern observed is well accounted for by this model and representative plots are shown in Fig. A.1CD. The refined structure has IrO₆ octahedra distorted from ideal cubic with non-equivalent Ir-O distances spanning a range of up to $\sim 7\%$ for each octahedron, comparable to the range of Ir-O distances reported for the IrO₆ octahedra in the layered honeycomb polytype [189].

The resulting Ir network show in Fig.1B-C of the main text is a novel arrangement of near-ideal honeycombs in three dimensions not reported before as far as we know in other $3d$ or $5d$ oxides. Ir honeycombs form parallel rows that alternate along the two diagonals of the unit cell in the ab plane, namely along $\mathbf{a} + \mathbf{b}$ at $z = 0$ and along $\mathbf{a} - \mathbf{b}$ at $z = 1/2$. This alternation leads to a 3D network of inter-connected honeycomb rows stacked along the c -axis, where all nearest-neighbor Ir-Ir links are nearly the same length ($\sim c/6$) and all Ir-Ir-Ir bond angles are close to 120° . The Ir positions are indeed very close to such an ideal lattice realized for Ir1 at $8k$ ($1/4, 1/4, 1/12$), Ir2 at $8i$ ($1/2, 1/2, 1/6$) and $c = \sqrt{3(a^2 + b^2)}$, compare with Table A.1 where the latter equation is satisfied to within 0.1%. This near-

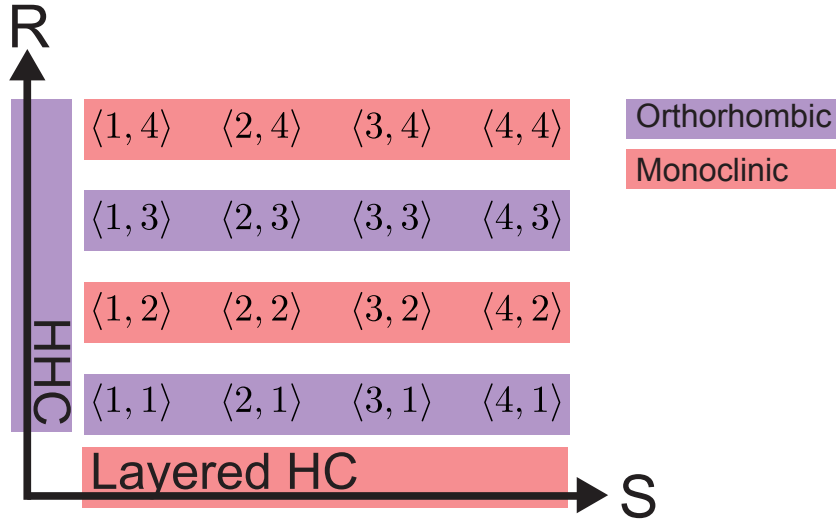


Figure A.8: The harmonic honeycomb family is rich in structural possibilities that tune symmetry (depending on whether the number of N_R and N_S links is odd or even) and dimensionality (the extent of the N_S links). This table summarizes this observation. Note we assume that the IrO_6 octahedra have ideal cubic symmetry. Complex distortions may create systems of lower symmetry than that indicated.

regularity of the Ir lattice is directly manifested in the observed x-ray diffraction pattern by a conspicuous absence of detectable scattering intensity along the c -axis for $l = 3 + 6n$, n integer as illustrated in Fig. A.1B, this is not due to a general symmetry-imposed selection rule of the space group, but is due to a near cancellation of intensity for a lattice built out of near-ideal honeycomb sections stacked along the c -axis.

The obtained iridium lattice can be thought of as being the $N = 1$ member of a regular series of periodic structures of alternating honeycomb sections of different widths ($N = 1, 2, 3, \dots, \infty$) as illustrated in Fig. 5B of the main text, with the layered honeycomb polytype ($C2/m$) being the $N = \infty$ end member. The $N = 1$ structure could be “transformed” into the honeycomb polytype by selectively mirror-imaging in the bc plane the iridium honeycomb rows centered at $z = 1/2$. In this case, iridium ions form infinite honeycomb layers in the $(\mathbf{a} + \mathbf{b}, \mathbf{c})$ plane and the unit cell along c is halved. It is clear from this construction why the reported repeating unit cell dimension of the layered honeycomb structure along this direction (labelled as $b_m = 8.9294 \text{ \AA}$ in the standard monoclinic cell notation [189]) is nearly half that of the c -axis repeat of the $N = 1$ polytype, $c = 17.8363(10) \text{ \AA}$, reported here.

For completeness we note that the different polytypes in the series plotted in Fig. 3.5B could be easily distinguished experimentally, as they have different symmetries and/or different unit cell sizes, and consequently distinct diffraction patterns. For illustration we consider the $N = 0$ hyper-honeycomb [127, 146] shown in Fig. 3.5B, $\mathcal{H}\langle 0 \rangle$. The periodic iridium atomic arrangement can be described by an orthorhombic unit cell of the same size $a \times b \times c$ and

Table A.1: Fractional atomic coordinates for ${}^{\mathcal{H}}(1)\text{-Li}_2\text{IrO}_3$ extracted from single-crystal x-ray data at 300 K ($Cccm$ space group, $a = 5.9119(3)$ Å, $b = 8.4461(5)$ Å, $c = 17.8363(10)$ Å, $Z = 16$). All sites are fully occupied and Li positions are fixed to nominal values such that edge-sharing IrO_6 and LiO_6 octahedra form a near-hexagonal arrangement in both $(\mathbf{a} + \mathbf{b}, \mathbf{c})$ and $(\mathbf{a} - \mathbf{b}, \mathbf{c})$ planes. The isotropic displacement parameter U for Li is also fixed to a value in the range found for the other atoms. Values in brackets show standard deviations in the fitted parameters.

Atom	Site	x	y	z	$U(\text{Å}^2)$
Ir1	$8k$	0.25	0.25	0.0836(2)	0.0124(4)
Ir2	$8i$	0.5	0.5	0.1670(3)	0.0206(6)
Li1	$8j$	0	0.5	0.3333	0.01
Li2	$8k$	0.75	0.25	0.25	0.0
Li3	$8k$	0.75	0.25	0.91667	0.01
Li4	$4c$	0.5	0.5	0.5	0.01
Li5	$4d$	0.5	0	0	0.01
O1	$16m$	0.77(1)	0.515(3)	0.087(4)	0.02(1)
O2	$8g$	0.72(2)	0.5	0.25	0.04(1)
O3	$8l$	0.00(1)	0.262(8)	0	0.006(9)
O4	$16m$	0.49(1)	0.262(6)	0.163(3)	0.006(9)

orientation of axes as for $N = 1$, but face-centered and with diamond glide planes. In the corresponding space group, $Fddd$ (no. 70), iridium ions occupy a single crystallographic site, $16g$ $(0, 0, z)$ (origin choice 1), with $z = 1/12$ assuming the c -axis Ir-Ir bond length is $c/6$.

Fig. A.1AB and EF show the comparison between data and the calculated diffraction pattern for a *generic* hyper-honeycomb structural model constructed such as to have hexagonal layers of edge-sharing IrO_6 and LiO_6 octahedra in the $(\mathbf{a} \pm \mathbf{b}, \mathbf{c})$ planes and 90° O-Ir-O and O-Li-O bonds. The atomic coordinates considered are Li1 $16g$ $(0, 0, 1/4)$, Li2 $16g$ $(0, 0, 5/12)$, O1 $32h$ $(1/4, 0, 1/6)$, O2 $16e$ $(1/4, 0, 0)$ and the full structure is plotted in Fig. A.3B. As illustrated in Fig. A.1EF the $Fddd$ space group has a much more restrictive selection rule for allowed reflections compared to $Cccm$, for example in the $(hk0)$ plane $h + k$ is required to be a multiple of 4 and both h and k to be even, as opposed to the less restrictive $h + k$ even for $Cccm$, and for $(h1l)$ both h and l odd, as opposed to h odd and l unrestricted for $Cccm$. The $Cccm$ selection rules can account for *all* the experimentally observed reflections, whereas an $Fddd$ unit cell could not account for the presence of the (odd, odd, even) reflections, such as the relatively strong (110), see Fig. A.1AE. Furthermore, refinement of the $Fddd$ structure against the intensities of reflections allowed in this symmetry, namely (even, even, even) and (odd, odd, odd), gives a statistically rather poor fit with $R_{F^2} = 21.4\%$, $wR_{F^2} = 36.2\%$, and $R_F = 13.3\%$. This becomes clear when comparing the calculated intensities to those

observed, shown in Fig. A.2B. The $Fddd$ model only reproduces the correct intensities for the (even, even, even) reflections, whereas the intensities of the (odd, odd, odd) reflections are calculated to be approximately double that observed. For completeness, the additional family of (odd, odd, even) reflections observed in the experimental data are also shown in Fig. A.2B, wrongly predicted to have exactly zero intensity in the $Fddd$ space group. These results, coupled with the conclusions drawn from the simulated annealing tests, conclusively show that the hyper-honeycomb $Fddd$ structural model (and lower-symmetry structures obtained by small distortions of an $Fddd$ parent structure) can be ruled out for the single crystals reported in this study.

Finally, we note that in addition to sharp Bragg peaks the x-ray diffraction pattern also revealed the presence of weak, but clearly visible diffuse scattering in the form of “rods” of scattering intensity in-between Bragg peaks along the l -direction, sharply defined in the h and k directions, as clearly seen in Fig. A.1B with the selection rule h odd and k odd. Whilst a quantitative refinement of the data including the diffuse scattering is beyond the scope of this present study, we propose that this diffuse scattering most likely originates from occasional structural faults in the nominal $Cccm$ atomic stacking sequence along the c -axis. The presence of diffuse scattering takes intensity away from the sharp Bragg peaks, and it is possible that some families of Bragg peaks are affected more than others; this might explain why the intensity of one particular family of reflections, namely the (odd, odd, even) peaks located on the diffuse scattering rods, appears weaker in experiment than predicted by a structurally-perfect $Cccm$ model considered in our refinement, see Fig. A.2A (blue triangles).

We have carried out extensive high-resolution SXD measurements at ~ 8 K to search signature of lowering of structural symmetry due to magnetic transition. These measurements were performed on the 6-ID-B undulator beamline at Advanced Photon Source using an incident photon energy of 11.215 keV and pyrolytic graphite analyzer. Only resolution-limited Bragg peaks allowed by the proposed space group were observed indicated the structure remained three-dimensionally ordered and fully coherent well below T_N . Furthermore, these measurements also ruled out any superlattice peaks (e.g. due to structural modulation, or magnetic order) at half-integer reciprocal-lattice points such as $(1/2, 0, 0)$, $(1/2, 1/2, 0)$. The temperature dependence of the orthorhombic lattice parameters around the magnetic transition $T_N = 38$ K was measured using $\theta - 2\theta$ scans to determine the 2θ location of strong structural Bragg peaks $(-2, 0, 6)$, $(0, 0, 12)$, and $(0, 2, 14)$ as a function of temperature between 8.4 - 45.1 K. Preliminary, data in Figure A.4 shows a small change of all orthorhombic lattice parameters around the 38 K magnetic transition and relaxation to comparable lattice parameters both below and above the transition. The percent change in lattice parameter appears to be an order of magnitude greater for the b -axis than for a or c , analogous to magnetic anisotropy seen in the susceptibility data.

Magnetic Characterization

A magnetically anisotropic material experiences a magnetic torque when its magnetization is not aligned with the applied magnetic field; the deflection of the cantilever in a uniform magnetic field is hence a direct measure of the magnetic anisotropy,

$$\boldsymbol{\tau} = \mathbf{M} \times \mathbf{H}. \quad (\text{A.1})$$

At small fields, where the magnetic response is linear, the magnetic anisotropy is captured by a susceptibility tensor χ_{ij} .

$$M_i = \chi_{ij}H_j \quad (\text{A.2})$$

The tensor is diagonal in the basis of the principal magnetic axes, which defines three principal components of magnetic susceptibility. For an orthorhombic crystal, these magnetic axes naturally coincide with the crystallographic directions, defining $\chi_{a,b,c}$. For example, for rotations in the $\mathbf{b-c}$ plane, the anisotropic magnetization $(M_b, M_c) = (\chi_b H_b, \chi_c H_c)$ creates a torque

$$\tau_a = M_b H_c - M_c H_b = (\chi_b - \chi_c) H_b H_c \quad (\text{A.3})$$

Defining θ as the angle between a crystallographic axis (c in this case) and the applied magnetic field, the torque can be rewritten as

$$\tau_a = (\chi_b - \chi_c) H^2 \sin\theta \cos\theta = \frac{(\chi_b - \chi_c) H^2 \sin 2\theta}{2} \quad (\text{A.4})$$

From this expression, the magnetic axes can be precisely identified from a complete angular dependence of the torque measurements (Figure 4B of the main text), with the amplitude of the $\sin 2\theta$ dependence being proportional to the magnetic anisotropy $\alpha_{bc} = (\chi_b - \chi_c)$. In ${}^{\mathcal{H}}\langle 1 \rangle$ -Li₂IrO₃ the magnetic axes are independent of temperature between room temperature and 1.5 K, but unusually, the sign of the anisotropy between the b and c axes, α_{bc} , changes at around 75 K (Figure 4D of the main text).

A convenient way to represent magnetization as observed by torque measurements is by plotting τ/H versus H (Figure 4B of the main text). This figure clearly demonstrates the linear dependence of magnetization at low fields with a slope that follows a $\sin 2\theta$ dependence with field orientation (colored curves). The softer component of magnetization appears to saturate at a field H^* , above which the linear response (equation A.4) is no longer valid. The finite torque at magnetic fields greater than H^* indicates the finite angle between M and H up to the highest measured magnetic fields. H^* is strongly dependent on the orientation of the crystal with respect to magnetic field. The largest kink field along the crystallographic a direction was measured at the NHMFL in Tallahassee. The observed overall negative slope at higher fields is due to a force component from a finite magnetic field gradient. A nonlinear torque signal was measured below H^* for magnetic fields aligned close to the hard susceptibility direction, χ_a , where the minimal torque condition is an unstable equilibrium (Figure 4B of the main text and Figure A.6).

In the harmonic honeycomb series each iridium atom occupies a local environment with uniaxial g -factor anisotropy that can be captured by a magnetic susceptibility χ_{\parallel} , parallel to and χ_{\perp} , perpendicular to the plane defined by its three nearest neighbor iridium atoms — the interlaced honeycomb planes. The measured high temperature magnetic anisotropy, α_{ij} , arises from the sum of this local anisotropy of the two honeycomb planes revealing that $\chi_{\parallel} > \chi_{\perp}$. Notably this is the opposite of the anisotropy $\chi_{\parallel} < \chi_{\perp}$ observed for the layered sodium iridate, $\mathcal{H}(\infty)$ -Na₂IrO₃ Ref. [232]. Superposition of both honeycomb planes leads to

$$\begin{aligned} M_a &= M_{\perp} \cos\phi/2 + M_{\parallel} \sin\phi/2 \\ M_b &= M_{\perp} \sin\phi/2 - M_{\parallel} \cos\phi/2 \end{aligned} \quad (\text{A.5})$$

where the magnetization parallel, M_{\parallel} , and perpendicular, M_{\perp} , to each of the planes can be written

$$\begin{aligned} M_{\perp} &= \chi_{\perp} H_{\perp} = \chi_{\perp} (H_a \cos\phi/2 + H_b \sin\phi/2) \\ M_{\parallel} &= \chi_{\parallel} H_{\parallel} = \chi_{\parallel} (H_a \sin\phi/2 - H_b \cos\phi/2) \end{aligned} \quad (\text{A.6})$$

Therefore, the geometric relation between the underlying pair of honeycomb planes results in three components of magnetization determined by only two microscopic parameters

$$\begin{aligned} M_a &= H_a [\chi_{\perp} \cos^2\phi/2 + \chi_{\parallel} \sin^2\phi/2] \\ M_b &= H_b [\chi_{\perp} \sin^2\phi/2 + \chi_{\parallel} \cos^2\phi/2] \\ M_c &= H_c \chi_{\parallel} \end{aligned} \quad (\text{A.7})$$

Using $\chi_{\pm} = (\chi_{\parallel} \pm \chi_{\perp})/2$ the anisotropic susceptibility of this family of structures can be simplified to

$$\begin{aligned} \chi_a &= \chi_+ - \chi_- \cos\phi \\ \chi_b &= \chi_+ + \chi_- \cos\phi \\ \chi_c &= \chi_+ + \chi_- \end{aligned} \quad (\text{A.8})$$

As a consequence, at high temperatures where g -factor anisotropy dominates, all three principal components of the magnetic susceptibility must order with $\chi_c > \chi_b > \chi_a$. The geometry of the undistorted, edge-sharing octahedra constrains the angle separating these two planes to $\phi = \arccos(1/3) \approx 70^\circ$ (Figure 3A of the main text). The geometric angle $\phi = \arccos 1/3$, which is also reflected in the crystal morphology, is directly apparent in the observed high temperature magnetic anisotropy, where $\chi_{a,b,c}$ are equally spaced,

$$\begin{aligned} \chi_a &= \chi_+ - (1/3) \chi_- \\ \chi_b &= \chi_+ + (1/3) \chi_- \\ \chi_c &= \chi_+ + \chi_- \end{aligned} \quad (\text{A.9})$$

This equal separation is observed as the ratios of the high temperature anisotropies saturating to the values of $\alpha_{ba}/\alpha_{ac} = -1/2$, $\alpha_{bc}/\alpha_{ac} = 1/2$, $\alpha_{bc}/\alpha_{ab} = 1$ (see Figure 3.3 B).

Kitaev quantum spin liquid

Every member of the harmonic honeycomb series is bonded by edge sharing IrO_6 octahedra. The edge-sharing geometry of the octahedra preserves the essential ingredients of the Kitaev model and this is universal for this family of structures. All three dimensional arrangements of edge-sharing octahedra maintain the interfering Ir-O₂-Ir exchange paths, where each of the three nearest neighbor Ir-Ir interactions predominantly couples a particular orthogonal component of spin (see Figure 4A of the main text). In the idealized limit of symmetric octahedra, such changes may compete primarily with the usual rotationally symmetric Heisenberg interactions. In the Kitaev limit where Heisenberg interactions may be set aside, the Hamiltonian becomes a sum of spin-anisotropic exchange terms

$$H_K = -K^c \sum_{\langle ij \rangle \in \hat{\mathbf{b}}_\perp} S_i^{\hat{\mathbf{b}}} S_j^{\hat{\mathbf{b}}} - K^h \sum_{\langle ij \rangle \in (\hat{\mathbf{a}} + \hat{\mathbf{c}})_\perp} S_i^{\hat{\mathbf{a}} + \hat{\mathbf{c}}} S_j^{\hat{\mathbf{a}} + \hat{\mathbf{c}}} - K^h \sum_{\langle ij \rangle \in (\hat{\mathbf{a}} - \hat{\mathbf{c}})_\perp} S_i^{\hat{\mathbf{a}} - \hat{\mathbf{c}}} S_j^{\hat{\mathbf{a}} - \hat{\mathbf{c}}}, \quad (\text{A.10})$$

where $S^{\hat{\mathbf{b}}}$ and $S^{\hat{\mathbf{a}} \pm \hat{\mathbf{c}}} = (S^{\hat{\mathbf{a}}} \pm S^{\hat{\mathbf{c}}})/\sqrt{2}$ are the spin operators in a set of three orthogonal directions, with $\hat{\mathbf{a}}$, $\hat{\mathbf{b}}$, $\hat{\mathbf{c}}$ being unit vectors along the orthorhombic crystallographic axes. Here we label each bond $\langle ij \rangle$ by the axis perpendicular to its Ir-O₂-Ir plane; for each bond, this normal vector lies along one of the directions $\{(\hat{\mathbf{a}} + \hat{\mathbf{c}}), (\hat{\mathbf{a}} - \hat{\mathbf{c}}), \hat{\mathbf{b}}\}$. The $\hat{\mathbf{b}}_\perp$ bonds are all oriented along the crystallographic c direction. Thus all the nearest neighbor Ir-Ir bonds can be divided into three classes, one for each component of spin: the $\hat{\mathbf{b}}$ component from the c -axis bonds, and the $\hat{\mathbf{a}} \pm \hat{\mathbf{c}}$ components from the h bonds defining each honeycomb plane (depicted in red and blue with corresponding \pm signs in Figure 4A of the main text). The exchange couplings K^h are constrained by the symmetry of the space group to be the same on the $(\hat{\mathbf{a}} \pm \hat{\mathbf{c}})_\perp$ bonds, but K^c , the coefficient of $S^{\hat{\mathbf{b}}}$ coupling, is symmetry-distinct from K^h .

The Hamiltonian in Equation A.10 was studied by Kitaev on the honeycomb lattice and shown to give an exactly solvable quantum spin liquid. The solution relies on the fact that spin algebra can be represented in an enlarged Hilbert space of Majorana fermions χ^α ($\alpha = 0, 1, 2, 3$) by mapping $S^\mu \rightarrow (i/2)\chi^0\chi^\mu$ (where $\mu = 1, 2, 3$) and implementing constraints to project back to the physical Hilbert space. As a result, each spin is represented in terms of two degrees of freedom — one a \mathcal{Z}_2 gauge field, the other a Majorana fermion moving in this field. The three-fold local connectivity of the honeycomb lattice together with the orthogonal Ising coupling of the Kitaev Hamiltonian (Equation A.10) freezes the gauge field fluctuations associated with the Hilbert space constraint, resulting in static \mathcal{Z}_2 fluxes. The problem then reduces to the motion of non-interacting particles in a fixed field. The ground state of these non-interacting fermions, expressed in terms of the underlying spins, is a complicated many-body superposition, and in particular is a quantum spin liquid.

In 2D the solution is possible because the honeycomb lattice contains the right number of hexagon plaquettes (minimal closed paths linking sites) to host the \mathcal{Z}_2 fluxes. This can be seen via Euler's theorem — which states that the number of minimal plaquettes plus the number of sites equals the number of links, on any 2D lattice. Threefold coordination means there are three bonds per two sites, and hence there is one flux degree of freedom for every two spins, as required by the solution. In 3D, there are too many minimal plaquettes

to host the required number of independent \mathcal{Z}_2 fluxes. However, a similar counting formula shows that the required number of independent gauge field degrees of freedom is matched by subtracting the number of enclosed volumes from the number of faces. Each enclosed volume gives a constraint; the independent flux constraints in 3D are not individual fluxes but rather unending flux lines, which form closed flux loops.

An additional difference in the 3D lattices is that, unlike the 2D honeycomb where every plaquette has six sites, in the harmonic honeycomb lattice the plaquettes vary in length, including 6, 10, 14 and so on. In particular, for the $\mathcal{H}\langle 1 \rangle$ -Li₂IrO₃ member there are two minimal plaquettes, 6 sites long and 14 sites long. The product of spin operators around each such plaquette forms an operator which commutes with the Hamiltonian. However products of such plaquette operators around an enclosed volume are reduced to the identity operation, constraining the flux lines to form closed loops. These gauge field fluxes remain static, enabling the spin-liquid solution to be extended to 3D for all members of this family [146, 127].

The ground state of the Hamiltonian described by Eq. A.10 contains no gauge-field fluxes. In this zero flux sector, the Hamiltonian is quadratic, diagonal in momentum space. Assuming $K^c = K^h = K$, the dispersion of Majorana Fermions is given by the eight eigenvalues of the tight-binding matrix

$$K \begin{pmatrix} 0 & 1 & 0 & 0 & 0 & 0 & 0 & V_2^* U_3^* \\ 1 & 0 & V_1^* & 0 & 0 & 0 & 0 & 0 \\ 0 & V_1 & 0 & 1 & 0 & 0 & 0 & 0 \\ 0 & 0 & 1 & 0 & V_1 & 0 & 0 & 0 \\ 0 & 0 & 0 & V_1^* & 0 & 1 & 0 & 0 \\ 0 & 0 & 0 & 0 & 1 & 0 & V_2^* & 0 \\ 0 & 0 & 0 & 0 & 0 & V_2 & 0 & 1 \\ V_2 U_3 & 0 & 0 & 0 & 0 & 0 & 1 & 0 \end{pmatrix} \quad (\text{A.11})$$

where $U_3 = \exp[i\mathbf{k} \cdot \mathbf{c}]$, $V_{1,2} = 1 + U_{1,2}$ and $U_{1,2} = \exp[i\mathbf{k} \cdot (\mathbf{a} \pm \mathbf{b})/2]$ with the $+/-$ sign corresponding to U_1, U_2 respectively. In the symmetric octahedra idealization where the Kitaev Hamiltonian is most likely to be relevant, the crystallographic vectors take the simple form $\mathbf{a} = (2, 2, 0)$, $\mathbf{b} = (0, 0, 4)$ and $\mathbf{c} = (-6, 6, 0)$ in the Ir-O Euclidean coordinate system, in units where the Ir-O distance is 1. The tight binding dispersion above is easily generalized to the other 3D lattices with the same \mathbf{a}, \mathbf{b} base-centered orthorhombic Bravais lattice vectors and arbitrarily long unit cells along \mathbf{c} , by appropriately cycling between V_1 and V_2 in the alternating off-diagonal elements of the matrix.

The resulting spectrum of the Majorana Fermions is gapless, and remains gapless for the entire region of parameter space with $K^c \leq 2K^h$ [146, 127]. The gapless fermion excitations form a 1D nodal contour within the 3D Brillouin zone, satisfied by the two equations $\mathbf{k} \cdot \mathbf{c} = 0$ and $\cos(\mathbf{k} \cdot \mathbf{a}/2) + \cos(\mathbf{k} \cdot \mathbf{b}/2) = 1/2$. For reference, note the BZ boundary satisfies the equations $\cos(\mathbf{k} \cdot \mathbf{c}) = -1$ or $\cos(\mathbf{k} \cdot \mathbf{a}/2) + \cos(\mathbf{k} \cdot \mathbf{b}/2) = 0$.

In the vicinity of the nodal contour the dispersion is linear ($\omega \sim |\mathbf{k}_\perp|$) in the two directions perpendicular to the nodal contour. Increasing K^c/K^h shrinks the nodal contour to a point,

at $K^c = 2K^h$; for $K^c > 2K^h$ the fermion spectrum is gapped.

If flux excitations proliferate, they will confine the fermions excitations in the spin liquid. In 2D, flux excitations are point objects and proliferate at any finite temperature. But in 3D, the fluxes form closed loop, with an energy cost proportional to the length of the flux loop; large flux loop cost arbitrarily high energy. Thus, in the 3D quantum spin liquid the fermions will survive in the deconfined phase until an entropy driven phase transition at finite temperature, separating the 3D quantum spin liquid and the classical paramagnet.

Other possible structures

To facilitate our description of the harmonic honeycomb family we develop a simple language based on their structural building blocks. Given a choice of one shared edge, there are two locally indistinguishable choices for the two remaining bonds, shown in Figure A.7 (A). Each Ir neighbor can then be in one of two planar environments, which we denote as the harmonic honeycomb plane (Figure 3A of the main text). The vertical (c -axis) bonds can then rotate the orientation of the planes (R -links) or keep them the same (S -links), shown in Figure A.7 (B). We emphasize that the Ir is always coordinated by three others in both kinds of bonds, just as in the layered honeycomb. In addition to the harmonic honeycomb family described in the main text, we mention a few other structural possibilities and their consequences here. The main text only describes a family of structures which have N links of the type S but only one R link. We can distinguish members of a more general structural family by different numbers of R and S links, and since the stoichiometry is unchanged we denote them ${}^{\mathcal{H}}\langle N_R, N_S \rangle\text{-Li}_2\text{IrO}_3$. For the $N_R = \text{odd}$ structures, the crystal structures are orthorhombic. If N_R is even the material is monoclinic, just as Na_2IrO_3 , which has the ${}^{\mathcal{H}}\langle 0, \infty \rangle\text{-Li}_2\text{IrO}_3$ structure. Note that even in this case, the $\sim 70^\circ$ internal bonding geometry is still evident in the angle between the monoclinic crystalline directions $-\mathbf{a}_m$ and \mathbf{c}_m . A material containing exclusively R links, ${}^{\mathcal{H}}\langle \infty, 0 \rangle\text{-Li}_2\text{IrO}_3$, is the ‘hyper-honeycomb,’ so named in analogy with the hyper-Kagome [185, 160, 127, 146]. By changing the number of S and R links we can therefore tune the global dimensionality and alternate the symmetry of the materials that are otherwise locally indistinguishable (see Figure A.8). Finally, we note that S and R links differ in another important regard: S links are inversion symmetric while R links are not. For structures containing the latter, this may lead to magnetic components in the Hamiltonian that break inversion symmetry, for example the Dzyaloshinsky-Moriya term [176, 82]. Note this is a local property in that the total space group for the systems may remain inversion symmetric.

Appendix B

Appendix for Ab initio Studies of Structural and Energetic Trends in the Harmonic Honeycomb Iridates

Table B.1: Lattice parameters for various levels of theory for $\mathcal{H}\langle 1\rangle$ and $\mathcal{H}\langle\infty\rangle$ Li_2IrO_3 and $\mathcal{H}\langle 1\rangle$ and $\mathcal{H}\langle\infty\rangle$ Na_2IrO_3 . All calculations for a given structure type are initialized with identical magnetic order. $U = 1.5$ eV. The percentage difference between the relaxed and experimental lattice parameter is indicated by the color of the cell.

Level of Theory	$\mathcal{H}\langle 1\rangle$ Li_2IrO_3			$\mathcal{H}\langle 1\rangle$ Na_2IrO_3		
	a (Å)	b (Å)	c (Å)	a (Å)	b (Å)	c (Å)
Experiment	5.91	8.45	17.84	–	–	–
PBE+SOC+U	5.96	8.53	18.02	6.48	9.10	19.02
PBE+SOC	6.01	8.75	17.17	6.46	9.11	19.13
PBE+U	6.01	8.73	16.99	6.46	9.12	19.10
PBE	6.01	8.76	17.03	6.45	9.13	19.17

Percent error color key: ≤ 1% ≤ 2% ≤ 3% > 3%

Table B.2: Total energy (eV) for constrained collinear magnetic orders on relaxed Li_2IrO_3 structures.

Mag. Order	$\text{Li}_2\text{IrO}_3^{\mathcal{H}} \langle \# \rangle$			
	0	1	2	∞
Ferro c	-35.199	-35.199	-35.199	-35.199
Ferro b	-35.195	-35.195	-35.195	-35.194
Ferro a	-35.194	-35.193	-35.194	-35.192
Néel c	-35.190	-35.191	-35.192	-35.193
Néel b	-35.195	-35.195	-35.194	-35.195
Néel a	-35.193	-35.194	-35.194	-35.194

Table B.3: Total energy (eV) for constrained collinear magnetic orders on relaxed Na_2IrO_3 structures.

Mag. Order	$\text{Na}_2\text{IrO}_3^{\mathcal{H}} \langle \# \rangle$			
	0	1	2	∞
Ferro c	-32.923	-32.910	-32.906	-32.908
Ferro b	-32.925	-32.911	-32.907	-32.910
Ferro a	-32.930	-32.918	-32.915	-32.915
Néel c	-32.927	-32.917	-32.913	-32.916
Néel b	-32.927	-32.917	-32.914	-32.917
Néel a	-32.925	-32.917	-32.912	-32.916

Table B.4: Bond lengths and angles for experimental and theoretical structures.

	Li_2IrO_3		Na_2IrO_3	
	Exp.	Theory	Exp.	Theory
Ir-Ir (Å)	2.97 ± 0.01	3.01 ± 0.01	3.13 ± 0.01	3.19 ± 0.01
Ir-O-Ir (°)	94 ± 3	94 ± 1	98.5 ± 0.5	100 ± 1

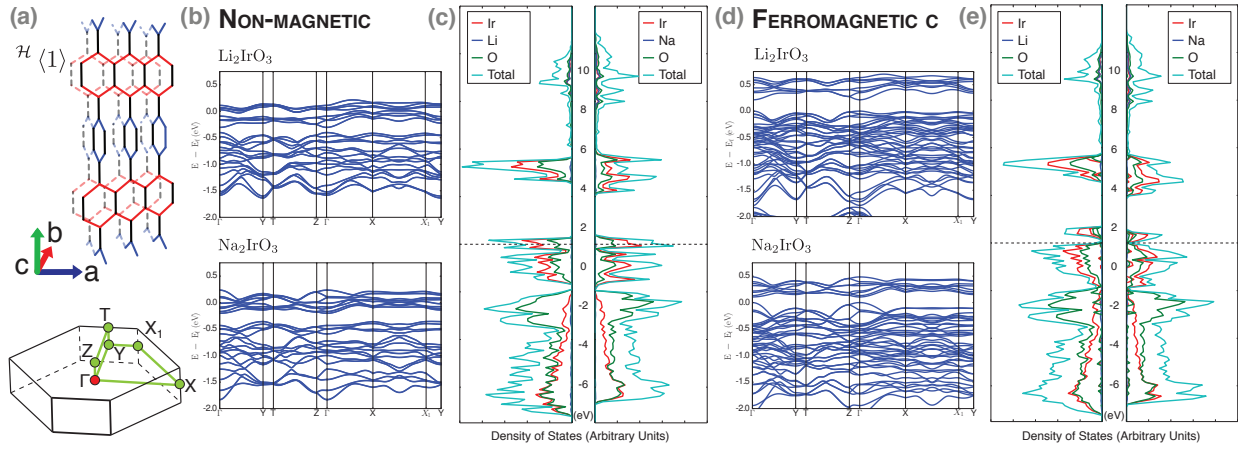


Figure B.1: Non-magnetic and ferromagnetic c band structures of relaxed unit cells of Li_2IrO_3 and Na_2IrO_3 $\mathcal{H}\langle 1 \rangle$ with PBE+SOC+U with path through k-space show at the bottom of (a). While the non-magnetic band structure is metallic (b), a gap opens up between $j = 1/2$ states with a magnetic order (d). The density of states for Li_2IrO_3 and Na_2IrO_3 $\mathcal{H}\langle 1 \rangle$ (and likewise for the entire harmonic honeycomb series) is dominated by oxygen p and iridium d orbitals (c and e).

Table B.5: Table of total energy, Ir-Ir bond lengths, and Ir-O-Ir bond angles for Li_2IrO_3 .

Series Member	$\mathcal{H}\langle 0 \rangle$		$\mathcal{H}\langle 1 \rangle$		$\mathcal{H}\langle 2 \rangle$		$\mathcal{H}\langle \infty \rangle$	
Ir-Ir Bond Lengths (\AA)	Ir1-Ir1	2.99684	Ir1-Ir1	3.00519	Ir1-Ir3	3.00367	Ir1-Ir1	3.01747
	Ir1-Ir1	3.00675	Ir1-Ir2	3.00499	Ir2-Ir2	3.00226	Ir1-Ir1	3.01011
			Ir2-Ir2	2.99884	Ir3-Ir3	3.00838		
Ir-O-Ir Bond Angles (Degrees)	Ir1-O1-Ir1	94.73	Ir1-O1-Ir2	94.64	Ir1-O1-Ir3	94.36	Ir1-O1-Ir1	94.63
	Ir1-O2-Ir1	93.17	Ir1-O2-Ir2	94.59	Ir1-O2-Ir3	94.57	Ir1-O2-Ir1	94.41
			Ir2-O3-Ir2	93.43	Ir3-O3-Ir3	94.06		
			Ir1-O4-Ir1	93.83	Ir1-O4-Ir2	94.23		
					Ir2-O5-Ir2	94.26		

Table B.6: Table of total energy, Ir-Ir bond lengths, and Ir-O-Ir bond angles for Na_2IrO_3 .

Series Member	$\mathcal{H}\langle 0 \rangle$		$\mathcal{H}\langle 1 \rangle$		$\mathcal{H}\langle 2 \rangle$		$\mathcal{H}\langle \infty \rangle$	
Ir-Ir Bond Lengths (\AA)	Ir1-Ir1	3.18524	Ir1-Ir1	3.19486	Ir1-Ir3	3.20029	Ir1-Ir1	3.18503
	Ir1-Ir1	3.19941	Ir1-Ir2	3.20077	Ir2-Ir2	3.20393	Ir1-Ir1	3.17998
			Ir2-Ir2	3.18584	Ir3-Ir3	3.18442		
Ir-O-Ir Bond Angles (Degrees)	Ir1-O1-Ir1	101.30	Ir1-O1-Ir2	101.27	Ir1-O1-Ir3	101.25	Ir1-O1-Ir1	100.38
	Ir1-O2-Ir1	100.11	Ir1-O2-Ir2	101.39	Ir1-O2-Ir3	101.40	Ir1-O2-Ir1	99.97
			Ir2-O3-Ir2	100.18	Ir3-O3-Ir3	100.08		
			Ir1-O4-Ir1	100.36	Ir1-O4-Ir2	100.27		
					Ir2-O5-Ir2	101.39		

Table B.7: Table of total energy, Ir-Ir bond lengths, and Ir-O-Ir bond angles for experimentally synthesized harmonic honeycomb iridates.

Series Member	Li_2IrO_3 $\mathcal{H}(\infty)$		Li_2IrO_3 $\mathcal{H}(0)$		Li_2IrO_3 $\mathcal{H}(1)$		Na_2IrO_3 $\mathcal{H}(\infty)$	
Ir-Ir Bond Lengths (Å)	Ir1-Ir1	2.97885	Ir1-Ir1	2.96502	Ir1-Ir1	2.98356	Ir1-Ir1	3.13793
	Ir1-Ir1	2.97870	Ir1-Ir1	2.96981	Ir1-Ir2	2.97575	Ir1-Ir1	3.12975
					Ir2-Ir2	2.96144		
Ir-O-Ir Bond Angles (Degrees)	Ir1-O1-Ir1	94.74	Ir1-O1-Ir1	95.07	Ir1-O1-Ir2	91.57	Ir1-O1-Ir1	97.97
	Ir1-O2-Ir1	95.33	Ir1-O2-Ir1	92.57	Ir2-O2-Ir2	96.89	Ir1-O2-Ir1	99.45
					Ir1-O3-Ir2	91.78		
					Ir1-O4-Ir2	95.90		

Table B.8: $\mathcal{H}(1)$ Li_2IrO_3 PBE+SOC+U lattice parameters for varying U. All calculations are initialized with the same magnetic order. The final magnetizations are not identical to one another. For PBE+SOC+U(0.25 eV) and PBE+SOC, the experimental lithium iridate structure is metallic. The relaxed PBE+SOC+U(0.25 eV) and PBE+SOC structures have gaps and relax to non-magnetic ground states.

U (eV)	a (Å)	b (Å)	c (Å)	Indirect Gap (meV)	Direct Gap (meV)
1.5	5.96	8.51	18.05	322	373
1.0	5.96	8.53	18.02	230	298
0.5	5.97	8.49	18.03	78	155
0.25	6.01	8.74	17.16	128	128
0	6.01	8.75	17.17	108	108

Table B.9: PBE+SOC+U for various initial magnetizations. All relaxations have a magnetic order. Magnetic orders were initialized with magnetic moments of 1 Bohr magneton on each iridium atom.

Initial magnetic order	a (Å)	b (Å)	c (Å)	eV per Li_2IrO_3
Random order 1	5.96	8.51	18.05	-35.20
Random order 2	5.96	8.51	18.05	-35.20
Ferromagnetic along c	5.96	8.54	18.01	-35.20
Non-magnetic	5.96	8.54	18.03	-35.20

Table B.10: PBE+U for various initial magnetizations. Calculations initialized with as a non-magnetic state relax to be non-magnetic and have similar lattice parameters to a non spin-polarized calculation.:

Initial Magnetic order	a (Å)	b (Å)	c (Å)	eV per Li_2IrO_3
Random order 1	5.97	8.62	17.50	-34.54
Random order 2	5.97	8.62	17.50	-34.51
Ferromagnetic along c	5.97	8.62	17.50	-34.54
Non-magnetic	6.02	8.72	16.99	-34.63
Non spin-polarized	6.01	8.73	16.99	-34.63

Appendix C

Appendix for Silver Benzeneselenolate
is a Self-Assembling Direct-Gap
Metal-Organic Chalcogenide
Assembly

C.1 General Information

Standard high vacuum, Schlenk line technique was employed for gram scale synthesis under dried nitrogen atmosphere. All reagents were obtained from commercial sources including dry toluene and tetrahydrofuran and were used without further purification. The reported yields are for isolated sample. Powder X-Ray diffraction studies were performed on a Bruker AXS D8 Discover GADDS X-Ray Diffractometer, operated at 35 kV and 40 mA at a wavelength of Co Ka, 1.79 Å. Scanning electron microscopy (SEM) images were collected on a Zeiss Gemini Ultra-55 Analytical Field Emission SEM with a secondary electron detector and at an accelerating voltage of 3 keV, and an FEI Phenom G1 Tabletop SEM. Samples of crystalline silver benzeneselenolate specimens were prepared by the drop casting of isopropanol suspensions onto a silicon wafer, which were allowed to settle followed by drying the surface with a stream of compressed air. Fluorescence spectra were obtained using an Edinburgh FLS980 spectrometer using an excitation wavelength of 380 nm.

C.2 Miscible Gram-Scale Synthesis of $[\text{AgSePh}]_{\infty}$

An oven dried round bottom flask equipped with a stir bar was charged with silver nitrate (1.4 g, 0.008 mol) and triphenylphosphine (4.4 g, 0.017 mol) in 250 mL of dry tetrahydrofuran. The solution was stirred for 16 h under nitrogen at ambient temperature giving a cloudy, white suspension. Diphenyl diselenide (1.3 g, 0.004 mol) in 80 mL of dry tetrahydrofuran was then added slowly to the flask at -50 C. The reaction was stirred while warming slowly to room temperature in which a deep yellow solution resulted. The solution is layered with 75 mL of diethyl ether and stirred rapidly until solution is clear and colorless and bright yellow crystals have precipitated. The solvent is decanted and the solid was purified by the addition of fresh isopropyl alcohol followed by sonication and centrifugation to separate the crystalline pellet and supernatant. The crystals are then dried under vacuum giving a canary yellow fine powder (2.3 g isolated). An additional SEM images of a typical morphology for the product is shown in Fig. S2.

C.3 Immiscible Interface Synthesis of $[\text{AgSePh}]_{\infty}$.

In a glass scintillation vial, 5 mL of 3 mM diphenyl diselenide in toluene solution was carefully layered over 5 mL of a 3 mM aq. silver nitrate solution and allowed to crystallize at room temperature for 3 days. Crystals are recovered by passing a substrate, glass or silicon, through the liquid interface into the aqueous phase, and then gently pulling the substrate at a 45 degree angle back into the organic phase. The crystals preferentially adhere to the solid substrate. Poor adhesion is noted when hydrophobic substrates are used; pristine silicon wafers gave poor results, as did gold, which becomes rapidly functionalized with benzeneselenolate monolayers on exposure to the organic solution. Gentle drying by forced air is generally acceptable for most analyses, although an absorbent laboratory wipe can be

APPENDIX C. APPENDIX FOR SILVER BENZENESSELENOLATE IS A SELF-ASSEMBLING DIRECT-GAP METAL-ORGANIC CHALCOGENIDE ASSEMBLY

used to wick residual liquids from the surface. Alternatively, suspensions of the crystals can be isolated by removing the aqueous layer from their reaction vessel using a glass pipette, and then decanting the toluene layer leaving behind the crystals. The product is then dispersed in isopropanol and sonicated briefly to remove any residual crystals off the sides of the glassware, and then pelletizes readily from isopropanol under centrifugation. The crystals are stored in the dark under vacuum (1 mg isolated per crystallization vial). Additional SEM images of typical morphologies for crystals covered by this method are collected in Figure S3.

C.4 Fluorescence Imaging Methods

Fluorescent images were acquired on a Zeiss LSM 710 confocal microscope with an Axio Observer.Z1 (Carl Zeiss Microimaging, Thornwood, NY). Crystalline $[\text{AgSePh}]_{\infty}$ was dried on glass coverslips (No. 1.5) and imaged using a 100 oil immersion objective (Plan-Apochromat, 1.40 NA). Confocal scans of the material were obtained using a 405 nm diode laser to excite the sample and a 585 nm wide pinhole. The emission spectrum was separated and the intensity of light between 400-700 nm (in 10 nm bins) was recorded on 32 detectors using the LSM 710 Linear Unmixing mode. The 32 images were imported to and analyzed using FIJI[218]. Isolated crystals were defined using the tracing tool in FIJI to detect the edges of the single crystal and then used to create a region of interest (ROI) around the crystal. For each ROI, the mean intensity, area, width and height was measured and recorded. Data were then exported to Origin 8.5.1 (Originlab, Northampton, MA) for analysis by linear regression and plotting. Atomic Force Microscopy (AFM) images were captured on a Cypher ES (Oxford Instruments). A budget Sensors TAP150G cantilever with a spring constant of 4.5 N/m was used in the repulsive tapping regime with an amplitude of 1.6 nm and a $\text{Asp}/A_0 = 0.08$. The z sensor was calibrated using an 18 nm step sample.

C.5 Calculation Methods

Density functional theory (DFT) calculations were performed using a plane-wave basis with the Vienna Ab Initio Simulations Package (VASP) [135, 137, 136]. We used a short-range hybrid functional of Heyd, Scuseria, and Ernzerhof (HSE) [141, 104, 103, 105] for band structure calculations; we used the local density approximation (LDA), the generalized gradient approximation of Perdew, Burke, and Ernzerhof (PBE) [193], and the vdW-df2 [79, 214, 147] functional to relax the experimental structure. Electron-ion interactions are treated with PAW pseudopotential [46, 138] with a 520 eV plane-wave cutoff; and the Brillouin zone was sampled with a Monkhorst-Pack mesh [175] of $15 \times 15 \times 3$ for PBE and df2 relaxations, and a $7 \times 7 \times 1$ mesh for the computationally more-demanding HSE calculations.

C.6 Calculation Details

Band structures for bulk and single layer $[\text{AgSePh}]_\infty$ and $[\text{AgSePh}]_\infty$ replaced with hydrogens are given in Figure C.5. The band structures is nearly identical between bulk and single layer $[\text{AgSePh}]_\infty$. The inorganic bands still present in $[\text{AgSePh}]_\infty$ replaced with hydrogens are similar to those of bulk and single layer $[\text{AgSePh}]_\infty$ with small changes to the band gap and effective masses at the direct gap.

Two symmetrically equivalent configurations of the benzene ligands are possible within the $2/c$ space group for the given refinement of $[\text{AgSePh}]_\infty$ [69]. We calculated that the two orientations differ in formation energy by 214 meV per formula unit with DFT-PBE and we use the lower energy structure for DFT-HSE calculations. Despite the energy difference, the band structures of these configurations are nearly indistinguishable. We calculated the electronic structure for the average of these two configurations and also observed that the band structure remained largely unaffected by change in the ligands orientation. The structural parameters for the configuration used for our DFT calculations is given in Figure C.7. The CIF for the original refinement containing both configurations as partial occupancies can be found in Cuthbert et. al [69].

DFT calculations were performed for bulk and single-layer $[\text{AgSePh}]_\infty$ in the lower energy of the two refined configurations (as described above) and single layer $[\text{AgSePh}]_\infty$ with the phenyls replaced with hydrogens. The hydrogens positions for the latter case are relaxed with DFT-PBE. The primitive cell was used for all calculations. The structure used for our calculations of the single layer unit cell is simply the conventional unit cell with one of the $[\text{AgSePh}]_\infty$ layers removed. There is a 14 Å distance between the single layers of $[\text{AgSePh}]_\infty$ and $[\text{AgSeH}]_\infty$ layers due to the periodic boundary conditions used in our VASP calculations.

To assess DFTs ability to reproduce the experimental structure, we relaxed the experimentally reported crystal structure,28 choosing the lower energy of the two possible phenyl configurations reported in space group 15, with LDA, PBE, and df2 functionals. (All df2 calculations were performed with PBE pseudopotentials.) A summary of the relaxation results, including percentage change in lattice parameters, variables describing the Ag lattice, and the dihedral angle between above and below plane phenyls, is given in Table C.2. The structures were relaxed until the stress on the unit cell was less than 0.5 kBar.

LDA gave the best agreement with experiment with isotropic changes in lattice parameters of less than 3%. The df2 with PBE pseudopotentials give anisotropic expansion of the b lattice parameters. PBE gave the worst agreement with experiment with 7% increases in a and b lattice parameters lying in the AgSe plane. df2 gives the best agreement with the dihedral angle between above and below layer phenyl ligands. However, the distortion of the Ag lattice shows poor description of the covalently bonded AgSe layer. The relaxations were insensitive to an increase in the basis energy cutoff and adding a $U = 3.5$ eV to Ag atoms.

The dihedral angle for the phenyl groups was determined by fitting Miller planes to a phenyl group from each orientation in VESTA and calculating the angle between the planes normal vector[173]. The band structure of the df2-relaxed structure shows a greater separation between bands of inorganic and organic character, with the bands of organic

APPENDIX C. APPENDIX FOR SILVER BENZENESELENOLATE IS A SELF-ASSEMBLING DIRECT-GAP METAL-ORGANIC CHALCOGENIDE ASSEMBLY

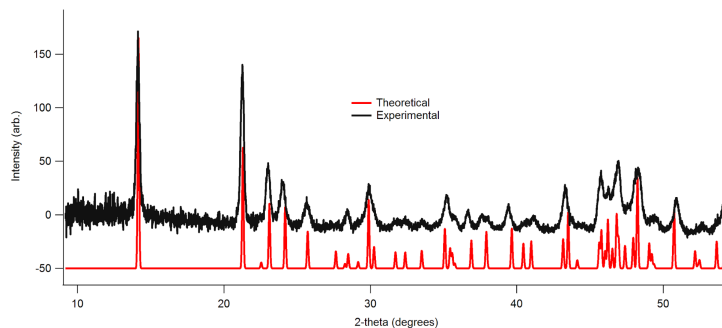


Figure C.1: Powder X-Ray diffractogram of $[\text{AgSePh}]_{\infty}$ overlapping the diffractogram calculated from Cuthbert et al. providing positive identification for silver benzeneselenolate.²⁸

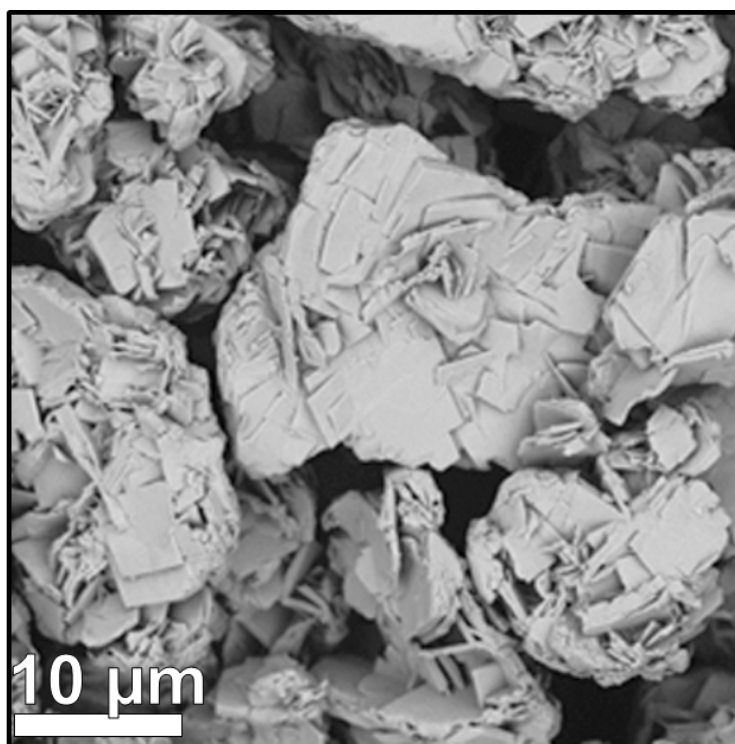


Figure C.2: Larger $[\text{AgSePh}]_{\infty}$ crystal sizes, having dimensions in excess of $20 \mu\text{m}$, are observed in the gram-scale-reaction product.

character moving away from the Fermi level. Otherwise, the bands remain largely unchanged. The effective masses of $[\text{AgSePh}]_{\infty}$ at the direct band gap were calculated using the EMC code^[85]. The band structures and densities of state were plotted using a locally modified version of pymatgen^[187].

APPENDIX C. APPENDIX FOR SILVER BENZENESELENOLATE IS A
 SELF-ASSEMBLING DIRECT-GAP METAL-ORGANIC CHALCOGENIDE ASSEMBLY

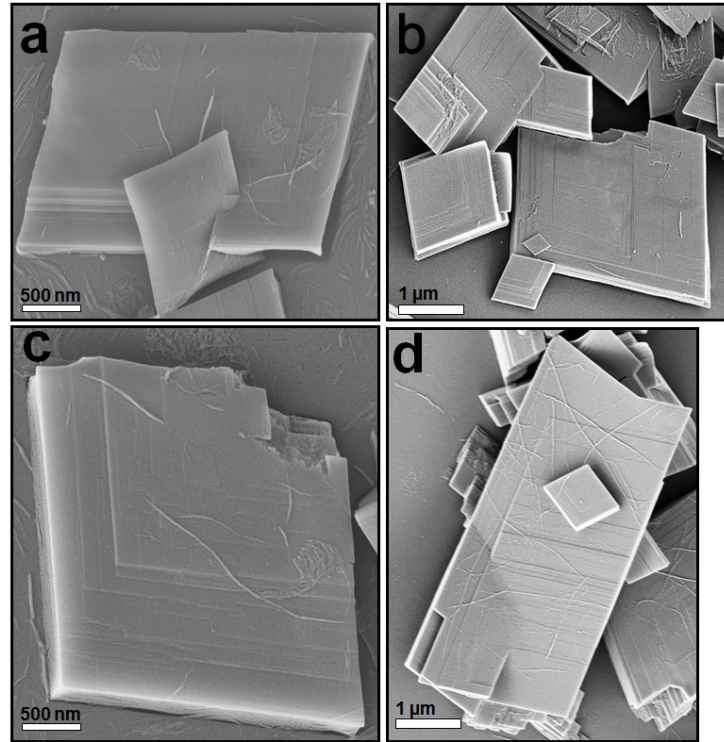


Figure C.3: Additional micrographs of $[\text{AgSePh}]_{\infty}$. Detail of step edges of the layered system down to single layer step edges are evident in the SEM micrographs.

Table C.1: Calculated effective masses at the direct gap of bulk, single and hydrogen-truncated $[\text{AgSePh}]_{\infty}$. The effective masses at the direct gap are similar for bulk and single layer $[\text{AgSePh}]_{\infty}$ and $[\text{AgSePh}]_{\infty}$ truncated with hydrogens. Only two principle directions are given for 2D single layer calculations.

Structure	Principle Direction 1		Principle Direction 2		Principle Direction 3	
Bulk	a	1.130	b	0.441	c^*	18.91
Single Layer	a	1.146	b	0.444	–	–
Truncated	a	0.466	b	0.298	–	–

APPENDIX C. APPENDIX FOR SILVER BENZENESELENOLATE IS A SELF-ASSEMBLING DIRECT-GAP METAL-ORGANIC CHALCOGENIDE ASSEMBLY

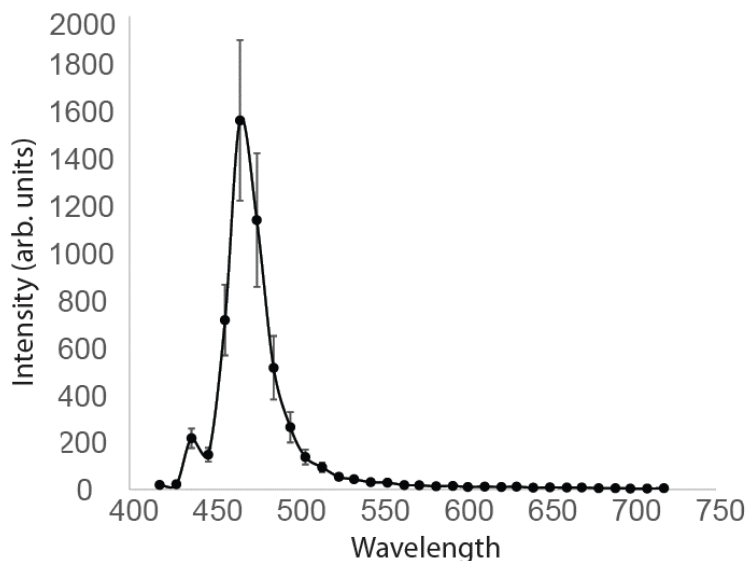


Figure C.4: Single particles of $[\text{AgSePh}]_{\infty}$ were selected from confocal microscopy images and their spectra were compared. Color was invariant regardless of size and aspect ratio. Thickness had no discernable effect but the precise thicknesses of crystals can be inferred only from total intensity. 100 isolated crystals were selected for this representation.

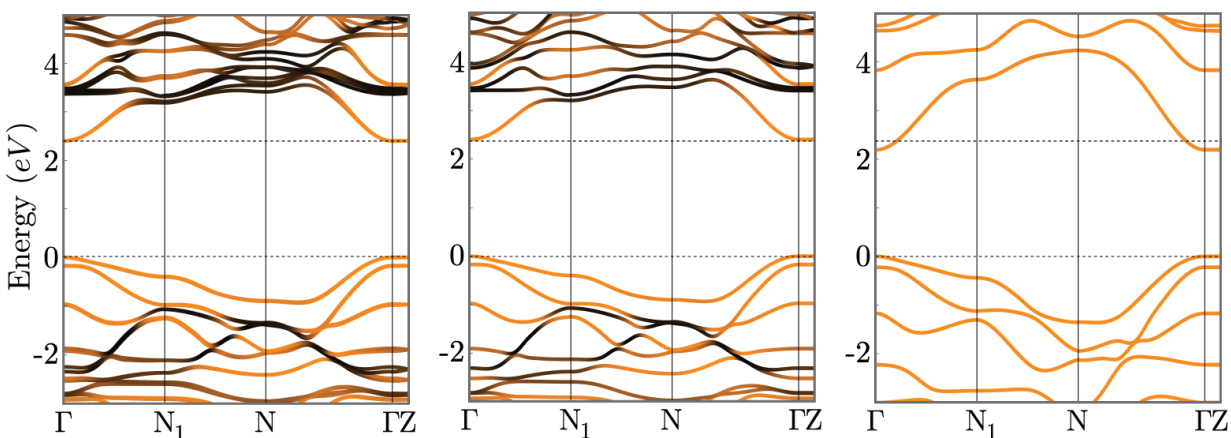


Figure C.5: HSE band structures for bulk and single-layer $[\text{AgSePh}]_{\infty}$ and single layer $[\text{AgSePh}]_{\infty}$ with the phenyls replaced with hydrogens. Dashed lines show the Fermi level (at 0 eV) and the HSE band gap for bulk and single-layer $[\text{AgSePh}]_{\infty}$. Color of band signifies the fraction of band occupations by inorganic atoms (Ag and Se) versus organic atoms (C and H). Bulk and single layer HSE band structures look identical. Single layer and hydrogen truncated AgSe look similar for Ag and Se dominated bands with small changes to the band gap and mobilities.

APPENDIX C. APPENDIX FOR SILVER BENZENESELENOLATE IS A SELF-ASSEMBLING DIRECT-GAP METAL-ORGANIC CHALCOGENIDE ASSEMBLY

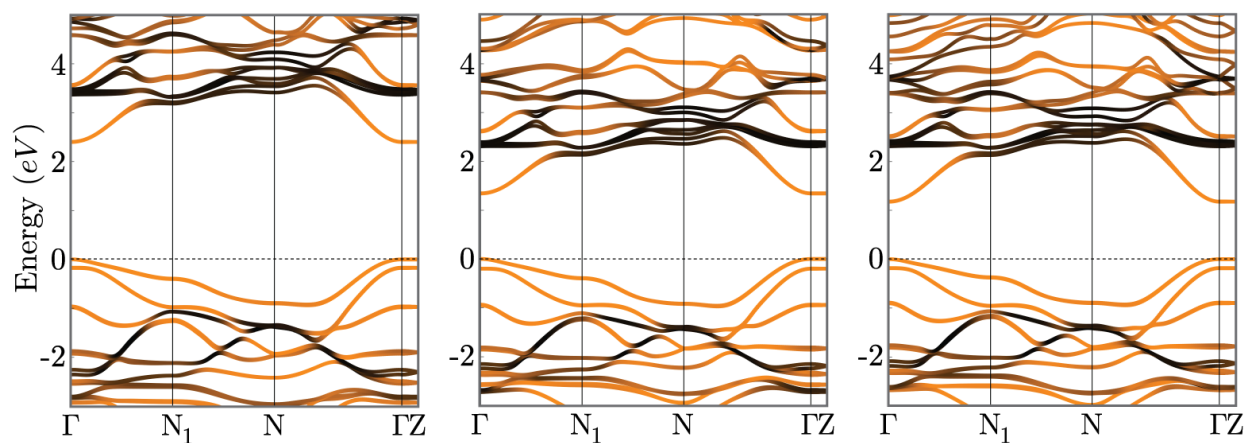


Figure C.6: HSE, PBE, and df2 band structures for bulk $[\text{AgSePh}]_\infty$. Dashed lines show the Fermi level. Color of band signifies the fraction of band occupations by inorganic atoms (Ag and Se) versus organic atoms (C and H). Band occupations and shape remain similar across these three levels of theory. N , N_1 and Z are along the primitive lattice vectors a^* , b^* and c^* , respectively.

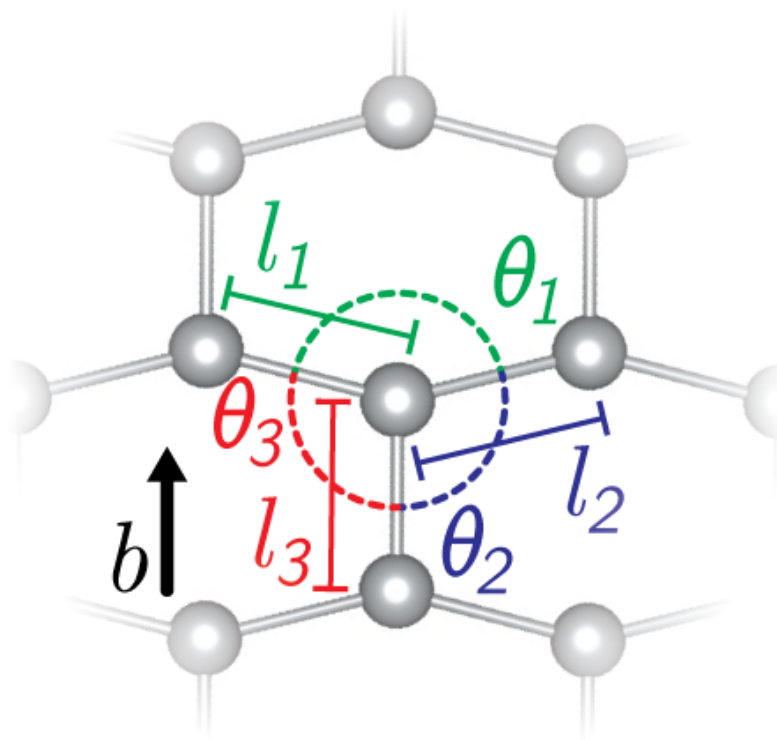


Figure C.7: Parameters of Ag lattice used in relaxation table.

APPENDIX C. APPENDIX FOR SILVER BENZENESELENOLATE IS A SELF-ASSEMBLING DIRECT-GAP METAL-ORGANIC CHALCOGENIDE ASSEMBLY

Table C.2: Relaxation Wyckoff tables:Lattice and Wyckoff position parameters for one phenyl configuration of Cuthberts crystal structure and DFT relaxations of that configuration.

Function	$\frac{a}{a_{exp}} - 1$	$\frac{b}{b_{exp}} - 1$	$\frac{c}{c_{exp}} - 1$	$\frac{\beta}{\beta_{exp}} - 1$	θ_1	$\theta_2 = \theta_3$	$l_1 = l_2$	l_3	Dihedral angle
Experiment	-	-	-	-	152	104	3.029	2.911	52
LDA	-1.17%	-1.97%	-2.62%	-0.65%	152	104	2.993	2.849	29
PBE	6.18%	7.86%	0.43%	-0.65%	170	95	3.132	3.656	28
df2	2.74%	10.54%	1.11%	-0.92%	154	103	3.099	3.332	38

Table C.3: Wyckoff table for experimental structure of $[\text{AgSePh}]_\infty$. Lattice and Wyckoff position parameters for one phenyl configuration of Cuthberts crystal structure.

Cuthbert				
Spacegroup: 15 (C2/c)				
a	b	c		
5.876	7.299	29.124		
α	β	γ		
90	95.79	90		
Label	x	y	z	Wyckoff letter
Ag1	0.5	0.381	0.25	e
Ag2	0.5	0.982	0.25	e
C1	0.671	0.186	0.141	f
C2	0.453	0.258	0.127	f
C3	0.369	0.267	0.081	f
C4	0.807	0.11	0.108	f
C5	0.496	0.191	0.049	f
C6	0.716	0.12	0.06	f
H1	0.439	0.199	0.018	f
H2	0.447	0.555	0.116	f
H3	0.802	0.08	0.037	f
H4	0.729	0.823	0.072	f
H5	0.363	0.3	0.15	f
Se1	0.792	0.182	0.205	f

APPENDIX C. APPENDIX FOR SILVER BENZENESELENOLATE IS A
 SELF-ASSEMBLING DIRECT-GAP METAL-ORGANIC CHALCOGENIDE ASSEMBLY

Table C.4: Wyckoff table for LDA Relaxation of experimental structure of $[\text{AgSePh}]_{\infty}$. Lattice and Wyckoff position parameters for one phenyl configuration of Cuthberts crystal structure relaxed with LDA.

LDA				
Spacegroup: 15 (C2/c)				
a	b	c		
5.807	7.155	28.361		
α	β	γ		
90	95.163	90		
Label	x	y	z	Wyckoff letter
Ag1	0.5	0.363	0.75	e
Ag2	0	0.262	0.75	e
C1	0.277	0.061	0.86	f
C2	0.058	0.02	0.873	f
C3	0.022	0.021	0.921	f
C4	0.457	0.103	0.893	f
C5	0.201	0.063	0.955	f
C6	0.419	0.104	0.941	f
H1	0.171	0.066	0.992	f
H2	0.627	0.141	0.882	f
H3	0.561	0.141	0.968	f
H4	0.351	0.483	0.931	f
H5	0.418	0.483	0.846	f
Se1	0.338	0.062	0.794	f

APPENDIX C. APPENDIX FOR SILVER BENZENESELENOLATE IS A
 SELF-ASSEMBLING DIRECT-GAP METAL-ORGANIC CHALCOGENIDE ASSEMBLY

Table C.5: Wyckoff table for PBE Relaxation of experimental structure of $[\text{AgSePh}]_{\infty}$. Lattice and Wyckoff position parameters for one phenyl configuration of Cuthberts crystal structure relaxed with PBE.

PBE				
Spacegroup: 15 (C2/c)				
a	b	c		
6.239	7.873	29.248		
α	β	γ		
90	95.166	90		
Label	x	y	z	Wyckoff letter
Ag1	0.5	0.328	0.25	e
Ag2	0	0.292	0.25	e
C1	0.259	0.061	0.356	f
C2	0.059	0.025	0.372	f
C3	0.036	0.028	0.419	f
C4	0.436	0.099	0.387	f
C5	0.212	0.066	0.45	f
C6	0.411	0.102	0.434	f
H1	0.193	0.07	0.487	f
H2	0.591	0.129	0.374	f
H3	0.549	0.134	0.458	f
H4	0.379	0.499	0.431	f
H5	0.422	0.494	0.347	f
Se1	0.29	0.06	0.29	f

APPENDIX C. APPENDIX FOR SILVER BENZENESSELENOLATE IS A
 SELF-ASSEMBLING DIRECT-GAP METAL-ORGANIC CHALCOGENIDE ASSEMBLY

Table C.6: Wyckoff table for df2 Relaxation of experimental structure of $[\text{AgSePh}]_{\infty}$. Lattice and Wyckoff position parameters for one phenyl configuration of Cuthberts crystal structure relaxed with df2.

df2				
Spacegroup: 15 (C2/c)				
a	b	c		
6.037	8.068	29.446		
α	β	γ		
90	94.904	90		
Label	x	y	z	Wyckoff letter
Ag1	0.5	0.393	0.25	e
Ag2	0.5	0.98	0.25	e
C1	0.665	0.188	0.139	f
C2	0.445	0.237	0.127	f
C3	0.365	0.237	0.081	f
C4	0.803	0.14	0.105	f
C5	0.502	0.188	0.047	f
C6	0.721	0.14	0.059	f
H1	0.439	0.188	0.011	f
H2	0.472	0.6	0.115	f
H3	0.829	0.099	0.034	f
H4	0.696	0.778	0.071	f
H5	0.339	0.278	0.152	f
Se1	0.787	0.186	0.204	f

Appendix D

A prototypical ferroelectric: BaTiO_3

BaTiO_3 is the prototypical ferroelectric. Well above room temperature, BaTiO_3 has a cubic perovskite structure in space group $Pm\bar{3}m$ (221), shown in Figure D.1. As temperature is lowered, BaTiO_3 undergoes several phase transitions to lower symmetry space groups that give rise to a spontaneous polarization, see Figure D.2 [273, 125]. BaTiO_3 has been known to be ferroelectric since 1946 [256, 266]. In its tetragonal phase, BaTiO_3 has a polarization is $26 \mu\text{C}/\text{cm}^2$ [263]. We use BaTiO_3 as a prototypical example for explaining how we conduct our automated ferroelectric search in Chapter 6 and Appendix F.

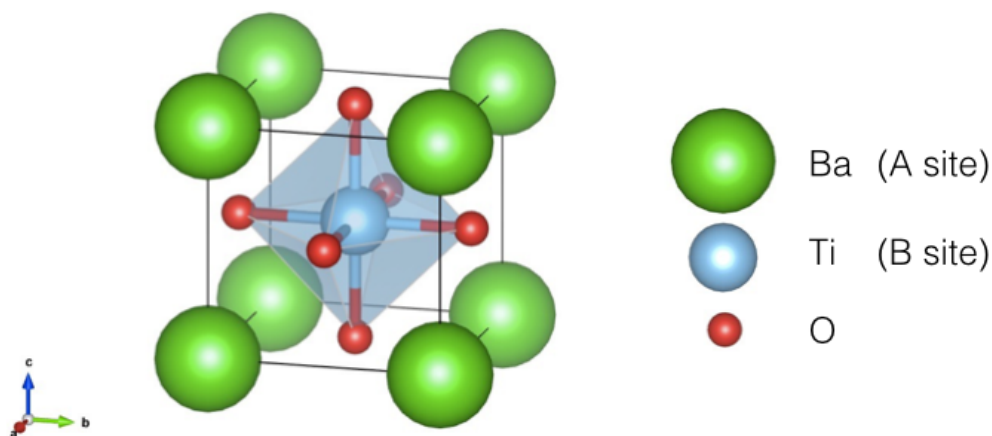


Figure D.1: BaTiO_3 is the quintessential ferroelectric. BaTiO_3 has a cubic perovskite crystal structure at high temperatures. Both the barium and titanium are octahedrally coordinated by oxygen. Octahedra of similar center element share corners.

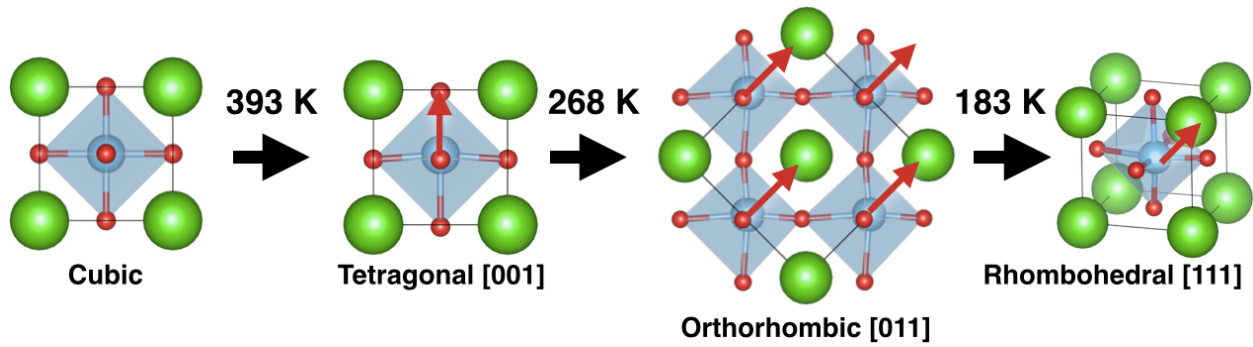


Figure D.2: BaTiO_3 goes through three phase transition as temperature is lowered: $Pm\bar{3}$ (221) \rightarrow $P4mm$ (99) \rightarrow $Amm2$ (38) \rightarrow $R3m$ (160). The red arrows in the diagram indicate the direction of the spontaneous polarization due to the displacement of the titanium atom and associated rearrangement of the oxygen atoms[273, 125].

Appendix E

Appendix for An Automatically Curated First-Principles Database of Ferroelectrics

Table E.1: Table of calculated versus experimentally measured polarizations as given in the Landolt-Börnstein - Group III: Condensed Matter - Ferroelectrics and Related Substances [227, 228, 229].

Workflow ID	Formula	Polarization Change	LB number	Exp	Exp Ref
wfid_1476040956.832394	O3PbTi	117.2	1A-11	75	[14, 245]
wfid_1476040982.95148	LiNbO3	84.1	2A-1	71	[264, 11]
wfid_1484444959.892999	NaNbO3	54.0	1A-1	12	[12]
wfid_1484444962.722730	KNbO3	51.6	1A-2	41.2	[10]
wfid_1484444953.778541	BaO3Ti	50.0	1A-10	26	[8]
wfid_1476040950.744757	KNbO3	47.7	1A-2	41.2	[10]
wfid_1476040947.794782	BaO3Ti	47.1	1A-10	26	[8]
wfid_1476040944.53976	BaO3Ti	46.3	1A-10	26	[8]
wfid_1476041110.265759	Bi2O9SrTa2	38.2	9A-12	5.8	[23]
wfid_1484444968.854031	Bi2Nb2O9Pb	37.3	9A-10	NA	[20]
wfid_1476040384.215156	CdO3Ti	37.0	1A-9	NA	[9]
wfid_1476041128.167316	Bi2O9SrTa2	37.0	9A-12	5.8	[23]
wfid_1476040759.946834	CdO3Ti	34.9	1A-9	NA	[9]
wfid_1476040393.450782	NaNbO3	31.9	1A-1	12	[12]
wfid_1476040403.435688	NaNbO3	31.9	1A-1	12	[12]
wfid_1476040428.848867	O3PbZr	23.5	1A-15	16	[15]
wfid_1476040441.814364	O5PTiTi	22.3	35A-13	NA	[106]
wfid_1476040425.250661	HfO3Pb	19.7	1A-16	Antiferroelectric	[13]
wfid_1476040435.561861	NbO4Sb	18.1	5A-2	19.7	[21]
wfid_1484694826.997820	Bi4O12Ti3	17.1	9A-15	50	[16]
wfid_1476041077.120822	Bi4O12Ti3	11.5	9A-15	50	[16]
wfid_1476040374.879552	CH4N2S	4.8	50A-1	3.5	[226]
wfid_1476040840.841892	O7Sr2Ta2	3.0	8A-6	1.9	[22]
wfid_1484445017.971658	B7IMn3O13	2.8	18A-20	NA	[19]
wfid_1476040471.728223	Cl4K2Zn	2.2	39A-9	0.135	[76]
wfid_1476040104.360695	Br4K2Zn	2.0	39A-16	3.0	[73]
wfid_1484445205.351382	B7ClCr3O13	1.6	18A-2	2.5	[17]
wfid_1484445029.449720	K2O4Se	0.7	39A-2	0.15	[74]
wfid_1484445193.941953	Cl4Rb2Zn	0.5	39A-10	0.16	[77]
wfid_1484445190.110462	Cl4K2Zn	0.5	39A-9	0.135	[76]
wfid_1484445186.170228	B7ClMg3O13	0.3	18A-1	0.08	[18]
wfid_1476040478.537387	Cl4Rb2Zn	0.3	39A-10	0.16	[77]
wfid_1476040475.325951	Cl4CoRb2	0.04	39A-7	0.15	[75]
wfid_1476040492.518912	H8N2O4S	0.02	39A-1	0.6	[72]

Table E.2: New high-quality candidates

Formula	Workflow ID	Polarization ($\mu\text{C}/\text{cm}^2$)	Energy Difference (eV)	Distortion max (Å)	Band Gap (eV)	Energy Above Hull (eV)	Subcategory
Ag2S	wfid_1476040932.225218	0.4	0.002	0.127	1.342	0.075	
Ag2S	wfid_1476041128.167316	27.5	-0.077	0.723	0.409	0.156	
Ag2S	wfid_1484444982.346272	45.3	0.089	0.956	1.342	0.075	
AgAl11O17	wfid_1476041161.431473	2.2	0.000	1.115	3.142	0.005	
AgC2O2	wfid_1476040384.215156	0.0	-0.002	0.328	0.980	0.016	
AlCH2NaO5	wfid_1476040789.617210	0.8	-0.001	0.082	5.030	-0.000	
AlCl4Hg2Sb	wfid_1484445042.637068	0.5	-0.000	0.738	0.835	0.030	
AlH3O3	wfid_1476040304.362065	1.1	0.009	0.398	4.963	0.004	Hydroxyls
AlH3O3	wfid_1484445287.593799	8.0	0.007	0.667	4.918	0.018	Hydroxyls
AuCl4K	wfid_1484445086.092903	0.3	0.000	0.072	1.451	0.003	
B13C2Li	wfid_1476041173.637876	0.8	-0.000	0.039	2.562	-0.021	
B2O6Zn3	wfid_1476040456.859630	0.1	-0.000	0.031	2.709	0.049	
Ba2F7Y	wfid_1484445183.339213	0.7	-0.062	1.262	6.501	0.111	
BaC2CaO6	wfid_1484445190.110462	1.3	-0.018	0.745	4.676	0.026	
BaCO3	wfid_1484444965.570570	1.0	-0.001	1.299	4.465	0.015	Oxocarbons
BaCl5La	wfid_1476040438.759718	26.3	0.013	1.526	4.150	0.009	
BiO3Y	wfid_1476040851.179557	9.9	0.037	0.650	2.057	0.074	
Br3CsGe	wfid_1476040104.360695	18.4	0.015	0.332	1.461	0.017	
C2HO2	wfid_1484445250.57163	3.4	-0.003	0.313	2.829	0.001	Oxocarbons
C2HgN2S2	wfid_1484444959.892999	0.9	-0.002	0.059	2.126	0.021	
C6Cu2H10N4S3	wfid_1476040837.97019	0.0	-0.007	0.946	2.733	0.035	
CCs4O4	wfid_1476040059.599818	1.7	-0.003	0.294	1.629	0.030	
CH4N2S	wfid_1476041035.850896	4.8	-0.006	0.770	3.293	0.006	
CHO2Ti	wfid_1476041077.120822	0.7	0.000	0.088	3.516	0.026	Oxocarbons
CK4O4	wfid_1476040355.151056	2.6	-0.001	0.167	2.232	0.144	
CK4O4	wfid_1484445253.438371	9.1	0.002	0.289	2.165	0.053	
CK4O4	wfid_1476040413.044763	14.6	-0.002	0.584	1.946	0.146	
CK4O4	wfid_1476040390.68687	16.6	0.006	0.608	1.989	0.049	
CLi4O4	wfid_1476040854.772923	0.1	0.071	0.221	4.738	-0.007	Oxocarbons
CLi4O4	wfid_1484445317.338075	16.6	0.003	0.236	4.149	0.168	Oxocarbons
CLi4O4	wfid_1476041081.548433	49.0	0.016	1.157	5.050	-0.023	Oxocarbons
CLi4O4	wfid_1476040950.744757	49.2	0.058	0.793	5.088	-0.023	Oxocarbons
CN2Pb	wfid_1476040496.278929	10.4	-0.003	0.189	1.728	0.039	
CNa4O4	wfid_1476040428.848867	3.6	-0.001	0.151	1.903	0.177	Oxocarbons
CNa4O4	wfid_1476040902.993927	12.5	-0.000	0.670	1.719	0.176	Oxocarbons
CNa4O4	wfid_1484444968.854031	39.2	0.010	1.277	2.184	-0.002	Oxocarbons
CNa4O4	wfid_1484445017.971658	39.2	0.026	0.999	2.184	-0.002	Oxocarbons
CNa4O4	wfid_1476040986.216576	56.3	0.153	1.356	2.162	0.022	Oxocarbons
CO4Rb4	wfid_1484444962.722730	0.6	-0.001	0.117	1.714	0.082	Oxocarbons
CO4Rb4	wfid_1484444978.482971	14.4	0.003	0.571	1.397	0.020	Oxocarbons
CO4Rb4	wfid_1476040478.537387	14.4	-0.004	0.746	1.395	0.020	Oxocarbons
Ca5ClO12P3	wfid_1476040897.624205	2.1	0.001	0.446	5.353	0.019	
CaF2	wfid_1476040844.52392	16.3	0.058	0.838	6.227	0.261	
Cd2ClP3	wfid_1484694771.994384	0.8	0.000	0.052	1.125	0.057	
Cl4GaHg2Sb	wfid_1476041044.880577	0.6	-0.001	0.802	0.754	0.049	
ClH3O5	wfid_1476040226.929827	5.2	0.047	1.187	5.381	0.007	
ClH4NO4	wfid_1476041121.199250	2.2	-0.001	0.903	5.255	0.001	
ClIn	wfid_1484445180.530019	3.7	0.000	0.039	1.450	0.081	
CrO3	wfid_1484445151.553442	0.4	0.021	1.413	1.588	0.039	
CrO9P3	wfid_1476040974.294686	1.1	0.001	0.276	3.161	0.034	
Cs2HgI4	wfid_1484445283.158561	0.3	-0.001	0.068	2.050	0.021	
Cs2O3Pb	wfid_1476040245.01667	7.2	0.000	0.288	1.391	0.033	
CuI	wfid_1484445295.230944	0.6	-0.002	0.121	1.099	0.188	
Er2F7K	wfid_1476040368.725338	1.5	0.000	0.183	6.924	0.074	Fluorides
F2HRb	wfid_1484445224.025729	1.5	-0.001	0.082	6.648	0.049	Fluorides

Table E.3: New high-quality candidates

Formula	Workflow ID	Polarization ($\mu\text{C}/\text{cm}^2$)	Energy Difference (eV)	Distortion max (Å)	Band Gap (eV)	Energy Above Hull (eV)	Subcategory
F2Pb	wfid_1476041088.40149	5.4	-0.003	0.098	4.396	0.105	
F3Nd	wfid_1484694880.421050	17.7	0.172	1.143	7.669	0.071	Fluorides
F3PbRb	wfid_1476040279.158189	4.0	0.033	0.776	3.804	0.083	
F5FeK2	wfid_1476040966.672844	0.5	-0.000	0.084	3.663	0.087	Fluorides
F5V	wfid_1476040393.450782	30.0	0.022	1.582	3.215	0.125	
F6LiV	wfid_1476040909.718858	1.2	-0.024	1.704	3.154	0.097	
FTl	wfid_1476041001.553476	6.4	0.029	0.498	3.149	0.114	
GaLuO3	wfid_1484445209.371670	8.2	0.021	0.344	2.894	0.045	Hexagonal manganite-like
GaO3Sc	wfid_1476040875.673476	10.4	0.014	0.416	3.115	0.051	Hexagonal manganite-like
H2Mg	wfid_1484445164.611735	30.9	-0.040	0.849	2.365	0.072	
H2MoO4	wfid_1476040207.31872	0.6	-0.001	0.381	3.426	-0.067	
H2O2Sr	wfid_1476041124.761330	1.2	0.003	0.257	3.984	0.012	Hydroxyls
H2O2Sr	wfid_1476040759.946834	1.2	-0.001	0.187	3.984	0.012	Hydroxyls
H2O4S	wfid_1476040460.586026	20.4	-0.003	0.983	6.140	0.003	
H2O4Sn3	wfid_1484445064.70045	1.3	-0.006	0.624	2.479	0.060	
H2O4U	wfid_1476041106.860617	2.9	0.087	1.465	1.909	0.049	Hydroxyls
H2O4U	wfid_1476040156.35457	2.9	-0.004	0.174	1.914	0.049	Hydroxyls
H3LaO3	wfid_1476040737.27481	17.9	-0.002	0.189	4.002	0.006	Hydroxyls
H3O3Pr	wfid_1476040371.699091	0.3	0.002	0.153	3.676	0.004	Hydroxyls
H3O3Y	wfid_1476040282.74358	7.8	-0.001	0.087	3.889	-0.008	Hydroxyls
H4O5S	wfid_1476041144.098790	0.8	-0.000	0.195	5.643	0.003	
HInO2	wfid_1476040139.05518	13.2	0.010	0.243	1.771	0.050	Hydroxyls
HK2NO6S2	wfid_1484445051.753689	3.2	0.006	0.595	5.261	0.009	
HNaO	wfid_1476040452.983312	10.7	0.002	0.198	2.982	-0.001	Hydroxyls
HNaO	wfid_1484445186.170228	10.7	0.001	0.196	2.982	-0.001	Hydroxyls
HORb	wfid_1476040489.133921	10.5	0.007	0.402	3.391	0.010	Hydroxyls
ILi6PS5	wfid_1476040187.488112	1.4	0.016	0.770	2.290	-0.009	
K2O7Zn6	wfid_1476040485.585687	2.6	-0.001	0.218	0.808	0.076	
K3S4Sb	wfid_1476040441.814364	1.0	0.008	0.736	2.158	0.019	
KLaS4Si	wfid_1476040464.155093	7.4	0.003	0.285	2.854	0.013	
LiO12P3Zr2	wfid_1476040894.532948	8.1	0.003	1.225	4.394	-0.020	
LiO4PV	wfid_1476040196.242976	0.0	-0.000	0.066	2.670	0.018	
LiO4PV	wfid_1476041131.850447	0.0	0.000	0.083	2.670	0.018	
MoO3	wfid_1476040193.378775	5.2	0.072	0.658	2.155	-0.105	
NaO11V6	wfid_1476040314.446703	2.4	0.010	0.271	0.987	0.050	
NbO5P	wfid_1484694927.058575	4.1	-0.001	0.159	2.249	0.002	
O23Rb6Si10	wfid_1476040149.329165	0.1	0.013	0.724	4.303	0.004	
O23Rb6Si10	wfid_1476040869.259479	0.5	0.008	0.653	4.221	0.010	
O2Si	wfid_1476040956.832394	0.0	0.004	0.570	5.606	0.008	
O2Si	wfid_1476040944.53976	0.0	-0.000	0.131	5.527	0.013	
O2Si	wfid_1476040094.757061	0.0	-0.003	0.846	5.388	0.008	
O2Si	wfid_1476040820.373005	0.0	-0.000	0.342	5.388	0.008	
O2Si	wfid_1484694862.160232	0.1	0.008	0.784	5.503	0.003	
O2Si	wfid_1476041095.479946	0.1	0.004	0.736	5.434	0.006	
O2Si	wfid_1484445313.916250	0.2	0.004	0.688	5.673	0.008	
O2Si	wfid_1476041154.194447	0.4	-0.010	1.296	5.592	0.014	
O3SbY	wfid_1476040753.50691	7.4	0.017	0.462	1.485	-0.018	Hexagonal manganite-like
O3ScY	wfid_1476040358.683542	6.5	0.010	0.321	3.152	-0.004	Hexagonal manganite-like
O3Te	wfid_1476041150.764661	0.4	0.002	0.505	0.550	0.679	
OPb	wfid_1484444945.05931	53.7	-0.002	0.531	2.257	0.096	

Table E.4: Known high-quality candidates

Formula	Workflow ID	Polarization ($\mu\text{C}/\text{cm}^2$)	Energy Difference (eV)	Distortion max (Å)	Band Gap (eV)	Energy Above Hull (eV)	Subcategory
Ag3IS	wfid_1476040471.728223	0.7	0.002	1.022	0.260	0.080	Proposed by Theory
Ag3IS	wfid_1476040762.919897	0.7	0.041	0.772	0.260	0.080	Proposed by Theory
Ag3IS	wfid_1476040109.318651	11.8	0.050	0.627	0.505	0.071	Proposed by Theory
Ag3IS	wfid_1476040331.097043	11.8	0.011	1.158	0.505	0.071	Proposed by Theory
Al2BaO4	wfid_1476040858.743894	0.3	0.004	0.560	4.079	0.002	Proposed by Theory
Al2BaO4	wfid_1476041047.628179	0.3	0.004	0.560	4.079	0.002	Proposed by Theory
Al2BaO4	wfid_1476040992.366616	0.3	0.004	0.559	4.079	0.002	Proposed by Theory
Al2CaH4O10Si2	wfid_1476040098.062674	4.2	0.005	0.752	5.056	0.004	
Al3F19Pb5	wfid_1476041165.857604	13.9	0.020	0.762	5.206	0.084	
AlBiO3	wfid_1476041098.970098	81.1	0.068	0.481	2.876	0.000	Perovskite
AlF7MgNa2	wfid_1476040117.949518	1.1	-0.000	0.208	6.660	0.063	
B2K3Nb3O12	wfid_1476040134.799732	0.1	0.004	0.220	2.373	0.005	
B3CaH5O8	wfid_1476041117.46294	0.6	0.004	0.957	5.591	-0.000	
B7ClCr3O13	wfid_1476040223.934313	1.6	-0.000	0.093	2.688	0.014	Boracite
B7ClMg3O13	wfid_1476040840.841892	0.3	0.010	0.491	5.695	0.004	Boracite
B7Mn3O13	wfid_1476041141.321099	2.8	0.005	0.471	3.696	0.012	Boracite
BaNiO3	wfid_1476040159.879894	3.7	0.000	0.046	1.480	0.050	
BaO3Ti	wfid_1476040217.741157	46.3	0.011	0.226	1.726	0.022	Perovskite
BaO3Ti	wfid_1484445022.713113	47.1	0.011	0.129	1.731	0.022	Perovskite
BaO3Ti	wfid_1476040190.49918	50.0	0.014	0.241	2.290	0.020	Perovskite
BaO5Ti2	wfid_1476041157.542583	15.3	0.003	0.168	2.142	0.041	
BeF4H8N2	wfid_1476040928.68650	0.6	0.011	0.549	6.640	0.022	N2H8SO4 family
BeF4H8N2	wfid_1484445148.273011	0.6	0.009	0.545	6.641	0.022	N2H8SO4 family
Bi2Nb2O9Pb	wfid_1476040947.794782	37.3	0.041	0.523	2.321	0.010	Perovskite
Bi2O9SrTa2	wfid_1476040415.883279	37.0	0.028	0.546	2.503	0.006	Perovskite
Bi2O9SrTa2	wfid_1476040872.620729	38.2	0.019	0.515	2.312	0.015	Perovskite
Bi4O12Ti3	wfid_1476040291.620895	11.5	0.023	0.487	1.616	0.052	Perovskite
Bi4O12Ti3	wfid_1476040275.56900	17.1	0.062	0.562	2.447	0.013	Perovskite
Bi4O12Ti3	wfid_1484445193.941953	58.2	0.062	0.566	2.368	0.014	Perovskite
BiCl8F4H3K6	wfid_1476040112.283926	0.1	-0.001	0.160	4.194	0.029	
BiInO3	wfid_1484445014.628732	63.7	0.466	0.817	2.749	0.039	Perovskite
BiInO3	wfid_1484444953.778541	63.7	0.011	1.400	2.749	0.039	Perovskite
BiO3Sc	wfid_1476040374.879552	6.5	0.323	0.726	2.675	0.029	
BiO3Sc	wfid_1484445145.139977	6.6	0.000	0.089	2.675	0.029	

Table E.5: Known high-quality candidates

Formula	Workflow ID	Polarization ($\mu\text{C}/\text{cm}^2$)	Energy Difference (eV)	Distortion max (\AA)	Band Gap (eV)	Energy Above Hull (eV)	Subcategory
Br4K2Zn	wfid_1476040115.133166	2.0	0.001	0.140	3.656	0.036	N2H8SO4 family
C3ClH10NO4	wfid_1476040269.225119	0.3	-0.000	0.275	5.608	-0.000	Proposed by Theory
Ca3Mn2O7	wfid_1476040396.862183	5.6	0.010	0.383	0.294	0.042	
Ca3Mn2O7	wfid_1484445029.449720	5.9	0.010	0.388	0.300	0.042	
CdO3Ti	wfid_1476040231.867950	34.9	0.003	0.147	2.405	0.092	Perovskite
CdO3Ti	wfid_1476040203.326613	37.0	0.003	0.121	2.458	0.093	Perovskite
Cl3CrRb	wfid_1476040445.577528	0.0	-0.001	0.115	0.502	0.032	
Cl3CrRb	wfid_1476040766.163640	0.0	0.007	0.357	0.502	0.032	
Cl3CsPb	wfid_1476040435.561861	2.3	0.006	0.575	2.418	0.028	
Cl4CoRb2	wfid_1484445157.56323	0.0	-0.001	0.251	0.831	0.021	N2H8SO4 family
Cl4K2Zn	wfid_1476041169.873380	0.5	0.013	0.698	4.509	0.040	N2H8SO4 family
Cl4K2Zn	wfid_1476041110.265759	2.2	0.000	0.112	4.412	0.053	N2H8SO4 family
Cl4Rb2Zn	wfid_1476040320.922919	0.3	-0.000	0.129	4.450	0.038	N2H8SO4 family
Cl4Rb2Zn	wfid_1476040953.684754	0.5	0.006	0.920	4.514	0.032	N2H8SO4 family
ClH	wfid_1476040295.440338	57.2	0.273	1.132	5.152	0.049	
CsF3Pb	wfid_1476040124.631808	0.7	0.004	0.449	3.383	0.077	Proposed by Theory
CsO4PZn	wfid_1476040056.258909	1.0	0.012	0.678	3.958	0.027	
F4MgSr	wfid_1484694929.994404	10.8	0.035	0.924	6.662	0.079	Proposed by Theory
H2KO4P	wfid_1484445095.317873	0.5	0.003	0.360	5.248	0.010	
H2KO4P	wfid_1476040475.325951	5.2	0.005	0.238	5.421	0.007	
H2O	wfid_1484694826.997820	13.5	-0.001	0.882	5.478	0.035	
H2O	wfid_1484445205.351382	13.5	0.000	0.833	5.478	0.035	
H2O4PRb	wfid_1484445276.419623	5.5	0.006	0.333	5.222	0.004	
H8N2O4S	wfid_1476041147.43703	0.0	0.007	1.267	5.073	0.000	N2H8SO4 family
HfO2	wfid_1476040425.250661	52.4	0.061	0.859	4.366	0.035	
HfO3Pb	wfid_1484445174.483678	19.7	-0.004	0.605	2.809	0.036	Perovskite
HfO3Sr	wfid_1476040963.135149	15.1	-0.000	0.114	3.744	0.045	
K2O4Se	wfid_1476040982.95148	0.7	0.000	0.404	3.630	0.016	N2H8SO4 family
KNbO3	wfid_1484445298.485748	47.7	0.011	0.226	1.472	0.013	Perovskite
KNbO3	wfid_1484444992.013915	50.4	0.013	0.177	2.311	0.010	Perovskite
KNbO3	wfid_1476040865.547657	51.6	0.013	0.218	2.058	0.011	Perovskite
LiNbO3	wfid_1476041051.123043	84.1	0.031	1.337	3.396	-0.004	Perovskite
LiNiO4P	wfid_1476040220.723663	0.2	-0.000	0.083	3.397	0.040	
MgO3Si	wfid_1476041102.78923	1.1	-0.005	1.522	4.663	0.025	
N6Pb	wfid_1476040079.687428	0.4	-0.000	0.229	2.303	0.021	
NaNbO3	wfid_1476040492.518912	31.9	0.021	0.493	2.402	0.002	Perovskite
NaNbO3	wfid_1484694837.128419	31.9	-0.000	0.683	2.402	0.002	Perovskite
NaNbO3	wfid_1476040743.679850	54.0	0.015	0.420	2.362	0.002	Perovskite
NbO4Sb	wfid_1476040403.435688	18.1	0.000	0.211	2.461	-0.002	
O2Zr	wfid_1476040756.894491	51.0	0.046	0.828	3.815	-0.065	
O3PbTi	wfid_1476040989.22333	117.2	0.039	0.581	1.861	0.045	Perovskite
O3PbZr	wfid_1476041014.627130	23.5	-0.004	0.356	2.868	-0.024	Perovskite
O5PTiTi	wfid_1484445106.855737	22.3	0.004	0.664	2.674	0.027	
O7Sr2Ta2	wfid_1476040410.139034	3.0	-0.000	0.088	2.943	0.012	

Appendix F

Isotropy Subgroups: How to check if two structure are continuously deformable

A nonpolar-polar structure pair are continuously deformable if the polar structure belongs to an isotropy subgroup of the nonpolar structure. Given a nonpolar-polar structure pair, one can determine if the polar structure is related to the nonpolar structure via an isotropy subgroup by checking the following:

First, we check that the point group of the polar space group is a subgroup of the point group of the nonpolar space group. An example relating the point groups of the phase transition of BaTiO_3 $Pm\bar{3}m \rightarrow R3m$ (see Figure F.1a) is given in F.1b.

Second, we determine the index of the group-subgroup relationship. The index tells us how many types of ferroelectric domains can form [178]. For some intuitive examples, let's consider the phase transitions of BaTiO_3 , shown in Figure D.2. The index for the cubic to tetragonal transition is 6, one for each face of a cube. The index for the cubic to orthorhombic transition is 12 one for each edge of a cube. The index for the cubic to rhombohedral transition is 8, one for each corner of the cube.

More formally, the definition of the index i is given by $i = i_t \times i_k$ where i_t is the *translationengleiche* (same translation) index and i_k is the *klassengleiche* (same symmetry) index [178]. i_t gives the reduction of point group operations and i_k gives the reduction in translation symmetry. For example, if the unit cell volume is doubled due to the transition, $i_k = 2$. If the number of point group operations is reduced by a third, $i_t = 3$.

For the BaTiO_3 examples, $i_k = 1$ because the ratio of the number of formula units per primitive unit cell for the polar to nonpolar structure is 1. i_t however varies because different numbers of symmetry operations are lost when the structure distorts to the polar space group. The table in Figure F.1c gives the indices for the maximal polar subgroups of $Pm\bar{3}m$ (221).

Third, we find chains of maximal subgroups compatible with the index of the group-subgroup relation for the nonpolar-polar structure pair. From these chains, we can determine

possible transformation matrices between the nonpolar to polar lattice.

Fourth, for each possible transformation matrix we must check whether the Wyckoff positions are compatible between the nonpolar structure in the low-symmetry setting and the polar structure. When a structure is transformed to a lower symmetry setting, the Wyckoff positions are said to “split”, meaning that due to the reduced symmetry, more symmetrically unique positions are required to describe the crystal structure.

Fifth, for the transformations that have compatible Wyckoff splitting, we transform the nonpolar lattice to the polar symmetry setting and compare to the polar lattice. If the lattices match within a generous tolerance of 3 Å and 10 degrees, we continue with the symmetry check.

Finally, we check the distance each atom has to move during the distortion. If the maximum distortion distance is within our tolerance of 1.5 Å, we store the distortion in our distortion database to then be computed with our first-principles workflow.

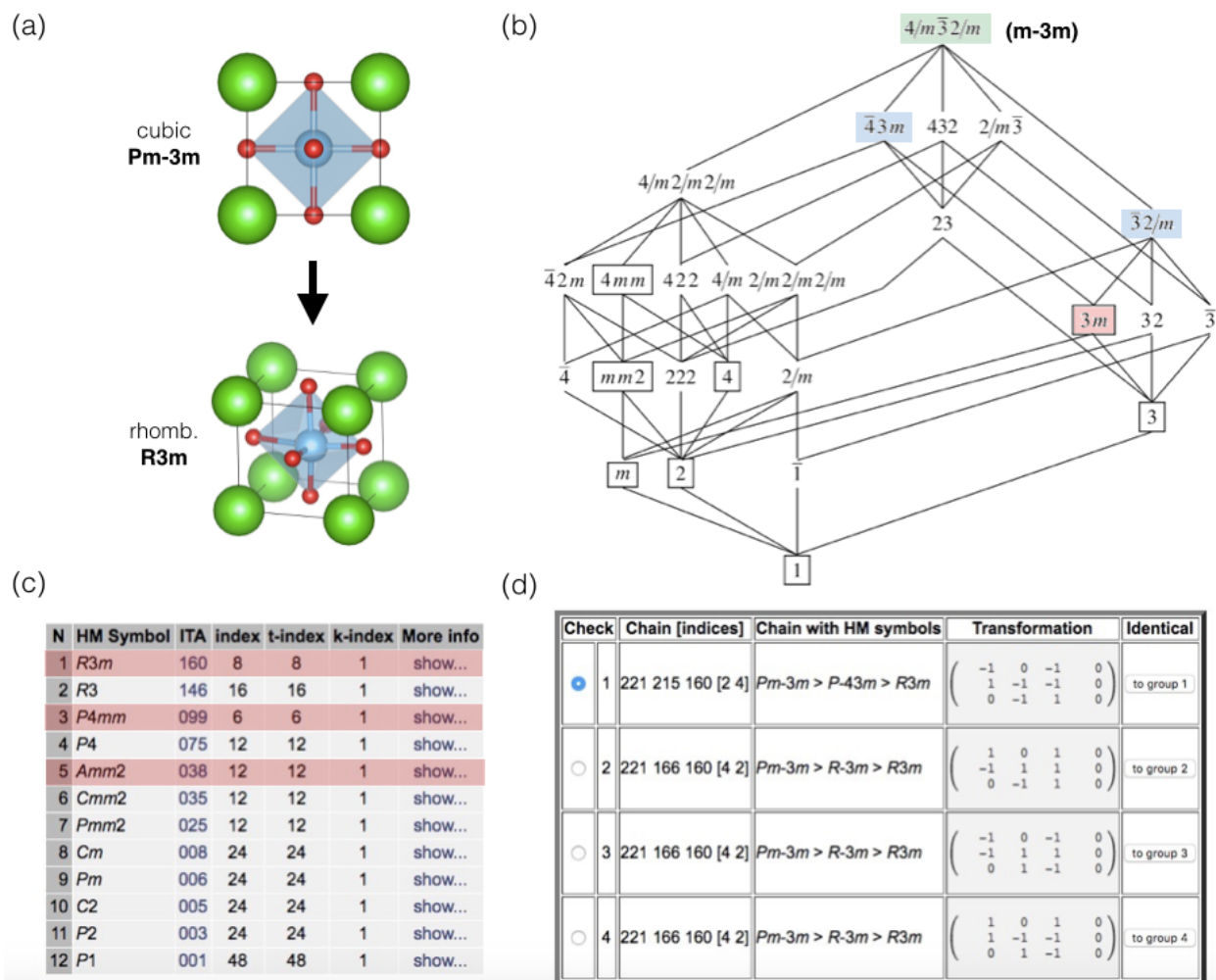


Figure F.1: Symmetry checks for isotropy subgroups the BaTiO_3 phase transition $Pm\bar{3}m$ (221) \rightarrow $R3m$ (160). a) cubic and rhombohedral BaTiO_3 structures. b) The maximal subgroup relations of the of the point group $4/m\bar{3}2/m$ (abbreviated as $m\bar{3}m$), modified from Figure 7.1 in [179] and reproduced with permission. The nonpolar point group ($4/m\bar{3}2/m$) is highlighted in green and the polar point group ($3m$) is highlighted in red. The point groups highlighted in blue ($\bar{4}3m$ and $\bar{3}2/m$) are the maximal subgroups between the nonpolar and polar point groups. c) A table, generated using the BCS tool CELLSUB (<http://www.cryst.ehu.es/cryst/cellsub.html>) [29], of the indices of the maximal polar subgroups of the cubic space group $Pm\bar{3}m$ with k -index of 1. We have highlighted those in red that correspond to subgroups shown in Figure D.2 d) A table of the possible transformation matrices for different chains of maximal subgroup from the nonpolar (221) to polar space group (160) for a group-subgroup index of 8. This table was generated using the BCS tool (<http://www.cryst.ehu.es/cryst/symmodes.html>) SYMMODES[56]. This transformation matrix is used to transform the lattice and Wyckoff positions.

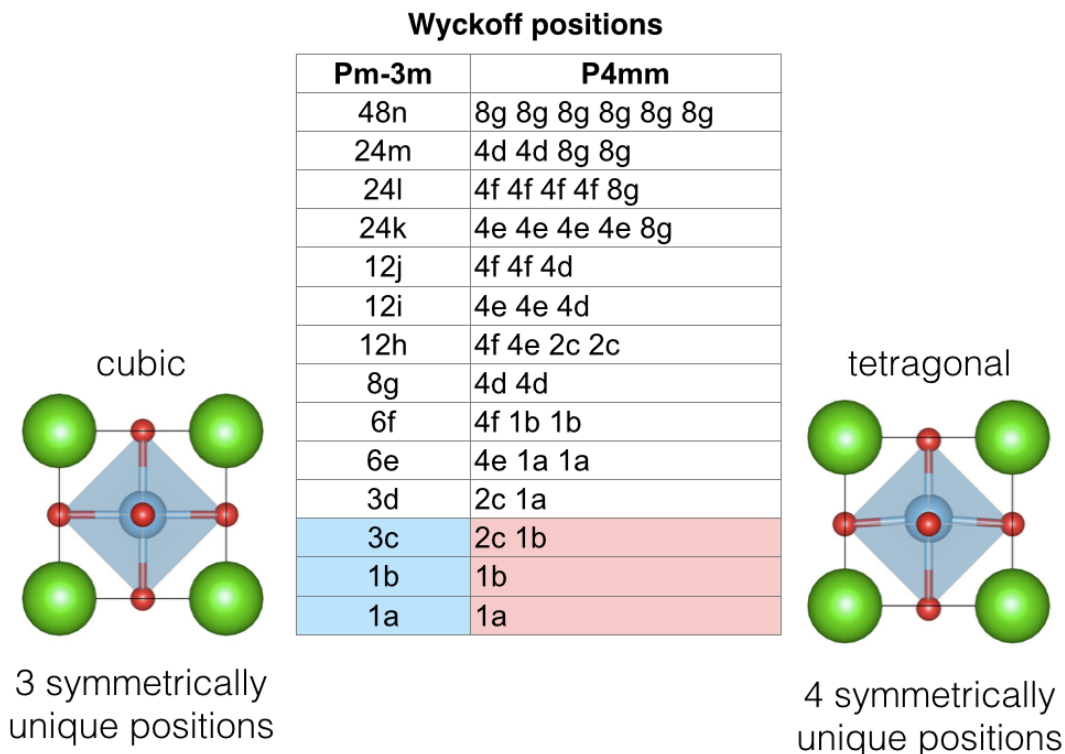


Figure F.2: Wyckoff splitting for BaTiO₃ from the cubic phase to tetragonal phase. While the cubic phase has 3 symmetrically unique positions, the tetragonal phase has 4.

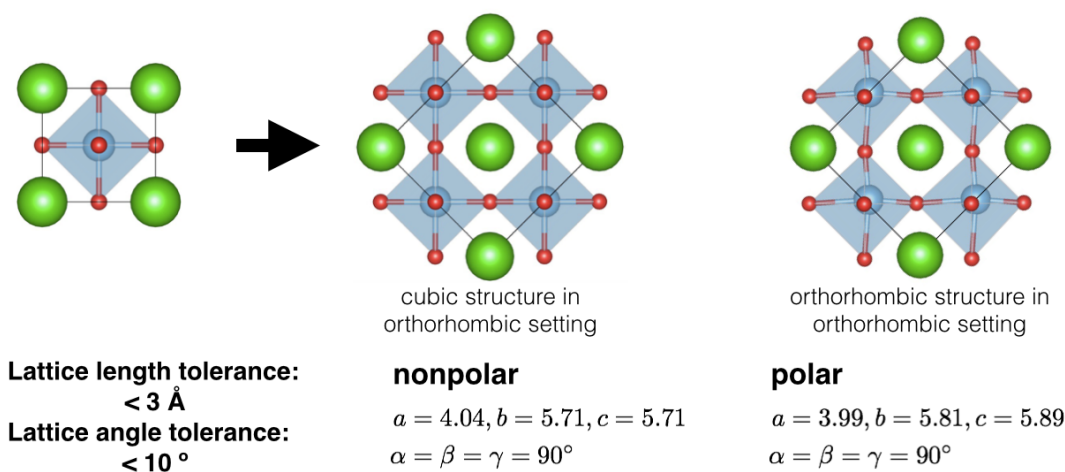


Figure F.3: Once we have possible transformation matrices for the group-subgroup relation of a given index that give the proper Wyckoff splitting, we transform the nonpolar lattice to the polar symmetry setting and compare to the polar lattice. If the lattices match within a generous tolerance of 3 Å and 10 degrees, we then check the distance the atoms have moved during the distortion.

Appendix G

A brief primer on deep learning

This section serves to give a quick introduction to the basics of deep learning. Deep learning is a subfield of machine learning where multiple layers of neural networks are used to learn complex functions.

In Figure G.1 and Chapter 7, we use diagrams inspired by Penrose notation [192] to depict neural networks. A neural network or *model* is a function with learnable parameters. For example, we can represent a model that learns the function $y = f(x)$ as Figure G.1a.

Fully-connected networks are commonly used and easy to mathematically write down. A single layer is composed of two components, a linear transformation and a nonlinear function. In this example, we use the hyperbolic tangent function. A one-layer fully-connected network is shown in Figure G.1b and written as:

$$y = \tanh(Wx + b) \tag{G.1}$$

where highlighted variables indicate **learned parameters**. Similarly, a two-layer fully-connected network is shown in Figure G.1c and written as:

$$y = \tanh(W_2 \tanh(W_1x + b_1) + b_2) \tag{G.2}$$

In this example, one can see the importance of having the nonlinear function. If it was not present, the two layer network expression could be re-written as a single layer with $W' = W_2W_1$ and $b' = W_2b_1 + b_2$. Networks with multiple layers can learn more complicated functions.

Fully-connected networks tend to become cumbersome when the input vector is large or when the input data has additional structure.

Convolutional neural networks (CNNs) are extensively used in image processing and computer vision. We build on this type of network in Chapter 7. CNNs take advantage of the adjacency information of pixels by scanning over an image with learned filters that are typically much smaller than the image (commonly 3×3 or 5×5 pixels in size). As the filter is scanned across the image (across convolution centers), the filter multiplies the portion of the

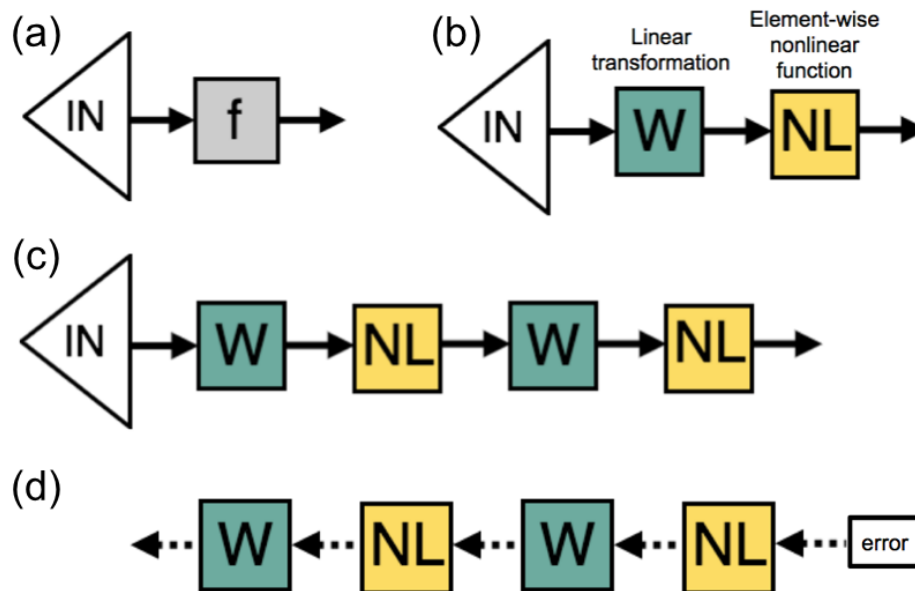


Figure G.1: Diagrams for example neural networks a) Diagram for an arbitrary function f . b) A one-layer fully-connected network. c) A two-layer fully-connected network. d) A diagram for backpropogation through a fully-connected network.

image it overlaps. This resulting matrix is summed to produce a pixel of the output image. This reuse of weights makes CNNs very efficient compared to fully-connected networks.

To evaluate a model’s performance, we have to define a cost function, this is also called the error or loss. The cost function is typically evaluated on the output of the model and is used to update learned parameters via a process called backpropogation.

Backpropogation requires a model to differentiable (or at least have gradients defined for each operation). One takes derivatives of the cost function with respect to the learnable parameters (using the chain rule) to obtain that gradients used to update those parameters. How these gradients are used depends on the optimizer used and hyperparameters of the optimizer such as the learning rate. For the most simple form of gradient descent, one simply updates the learned parameter by the gradients multiplied by a learning rate (typically 10^{-10} to 10^{-1}). More sophisticated optimizers often add in additional “physics” like momentum to better explore the loss surface.

For a deeper dive into deep learning, we recommend Ref. [94] and the course materials available at Ref [4].

Appendix H

Appendix for Tensor Field Networks

H.1 Proofs of general equivariance propositions

For equivariant \mathcal{L} , the following diagram is commutative for all $g \in G$:

$$\begin{array}{ccc} \mathcal{X} & \xrightarrow{\mathcal{L}} & \mathcal{Y} \\ \downarrow D^{\mathcal{X}}(g) & & \downarrow D^{\mathcal{Y}}(g) \\ \mathcal{X} & \xrightarrow{\mathcal{L}} & \mathcal{Y} \end{array}$$

If a function is equivariant with respect to two transformations g and h , then it is equivariant to the composition of those transformations:

$$\begin{aligned} \mathcal{L}(D^{\mathcal{X}}(gh)x) &= \mathcal{L}(D^{\mathcal{X}}(g)D^{\mathcal{X}}(h)x) \\ &= D^{\mathcal{Y}}(g)\mathcal{L}(D^{\mathcal{X}}(h)x) \\ &= D^{\mathcal{Y}}(gh)\mathcal{L}(x) \end{aligned}$$

for all $g, h \in G$ and $x \in \mathcal{X}$; that is, the following diagram is commutative:

$$\begin{array}{ccc} \mathcal{X} & \xrightarrow{\mathcal{L}} & \mathcal{Y} \\ \downarrow D^{\mathcal{X}}(g) & & \downarrow D^{\mathcal{Y}}(g) \\ \mathcal{X} & \xrightarrow{\mathcal{L}} & \mathcal{Y} \\ \downarrow D^{\mathcal{X}}(h) & & \downarrow D^{\mathcal{Y}}(h) \\ \mathcal{X} & \xrightarrow{\mathcal{L}} & \mathcal{Y} \end{array}$$

Composing equivariant functions $\mathcal{L}_1 : \mathcal{X} \rightarrow \mathcal{Y}$ and $\mathcal{L}_2 : \mathcal{Y} \rightarrow \mathcal{Z}$ yields an equivariant function $\mathcal{L}_2 \circ \mathcal{L}_1$:

$$\begin{aligned} \mathcal{L}_2(\mathcal{L}_1(D^{\mathcal{X}}(g)x)) &= \mathcal{L}_2(D^{\mathcal{Y}}(g)\mathcal{L}_1(x)) \\ &= D^{\mathcal{Z}}(g)\mathcal{L}_2(\mathcal{L}_1(x)) \end{aligned}$$

That is, the following is commutative:

$$\begin{array}{ccccc} \mathcal{X} & \xrightarrow{\mathcal{L}_1} & \mathcal{Y} & \xrightarrow{\mathcal{L}_2} & \mathcal{Z} \\ \downarrow D^{\mathcal{X}}(g) & & \downarrow D^{\mathcal{Y}}(g) & & \downarrow D^{\mathcal{Z}}(g) \\ \mathcal{X} & \xrightarrow{\mathcal{L}_1} & \mathcal{Y} & \xrightarrow{\mathcal{L}_2} & \mathcal{Z} \end{array}$$

H.2 Motivating point convolutions

We can represent input as a continuous function that is non-zero at a finite set of points (using Dirac δ functions):

$$V(\vec{t}) = \sum_{a \in S} V_a \delta(\vec{t} - \vec{r}_a)$$

A point convolution is then equivalent to applying an integral transform with kernel

$$F(\vec{t} - \vec{s}) \sum_{a \in S} \delta(\vec{t} - \vec{r}_a)$$

for some function F . This transform yields

$$\begin{aligned} \mathcal{L}(\vec{t}) &= \int d^3 \vec{s} F(\vec{t} - \vec{s}) \sum_{a \in S} \delta(\vec{t} - \vec{r}_a) \sum_{b \in S} V_b \delta(\vec{s} - \vec{r}_b) \\ &= \sum_{a \in S} \delta(\vec{t} - \vec{r}_a) \sum_{b \in S} F(\vec{r}_a - \vec{r}_b) V_b \\ &= \sum_{a \in S} \delta(\vec{t} - \vec{r}_a) \mathcal{L}_a \end{aligned}$$

where we define

$$\mathcal{L}_a := \sum_{b \in S} F(\vec{r}_a - \vec{r}_b) V_b$$

as in the main text.

H.3 Proof of equivariance of point convolution layer

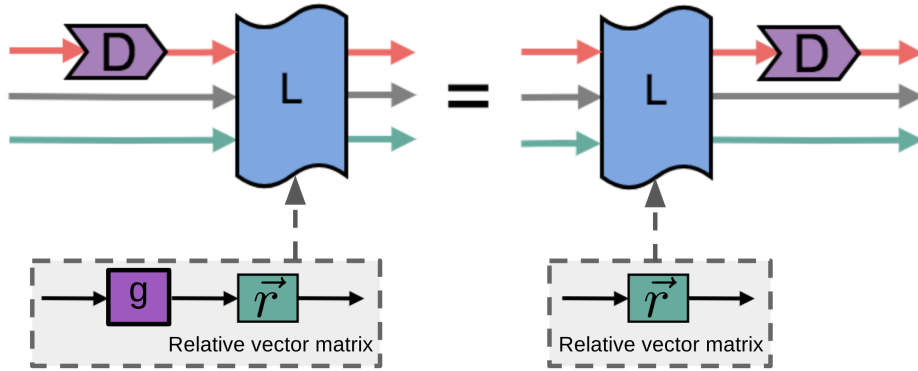


Figure H.1: Condition for layer rotation equivariance

Under a rotation $\vec{r}_a \mapsto \mathcal{R}(g)\vec{r}_a$, we know that $\vec{r}_{ab} \mapsto \mathcal{R}(g)\vec{r}_{ab}$ and

$$F_{cm}^{(l_f, l_i)}(\mathcal{R}(g)\vec{r}_{ab}) = \sum_{m'} D_{mm'}^{(l_f)}(g) F_{cm'}^{(l_f, l_i)}(\vec{r}_{ab}) \quad (\text{H.1})$$

because of the transformation properties of the spherical harmonics $Y_m^{(l)}$.

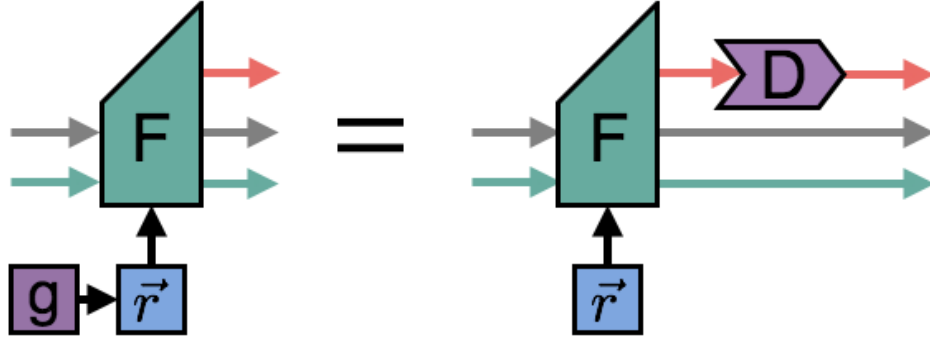


Figure H.2: Filter equivariance equation

Then

$$\begin{aligned}
& \mathcal{L}_{acm_O}^{(l_O)} \left(\mathcal{R}(g) \vec{r}_a, \sum_{m'} D_{m_I m'_I}^{(l_I)}(g) V_{acm'_I}^{(l_I)} \right) \\
&= \sum_{m_F, m_I} C_{(l_F, m_F)(l_I, m_I)}^{(l_O, m_O)} \\
&\quad \times \sum_{b \in S} F_{cm_F}^{(l_F, l_I)}(\mathcal{R}(g) \vec{r}_{ab}) \sum_{m'} D_{m_I m'_I}^{(l_I)}(g) V_{bcm'_I}^{(l_I)} \\
&= \sum_{m_F, m_I} C_{(l_F, m_F)(l_I, m_I)}^{(l_O, m_O)} \\
&\quad \times \sum_{b \in S} \left(\sum_{m'_F} D_{m_F m'_F}^{(l_F)}(g) F_{cm'_F}^{(l_F, l_I)}(\vec{r}_{ab}) \right) \\
&\quad \times \left(\sum_{m'_I} D_{m_I m'_I}^{(l_I)}(g) V_{bcm'_I}^{(l_I)} \right) \\
&= \sum_{m'_O} D_{m_O m'_O}^{(l_O)}(g) C_{(l_F, m_F)(l_I, m_I)}^{(l_O, m'_O)} \sum_{b \in S} F_{cm_F}^{(l_F, l_I)}(\vec{r}_{ab}) V_{bcm_I}^{(l_I)} \\
&= \sum_{m'_O} D_{m_O m'_O}^{(l_O)}(g) \mathcal{L}_{acm'_O}^{(l_O)}(\vec{r}_a, V_{acm_I}^{(l_I)}).
\end{aligned}$$

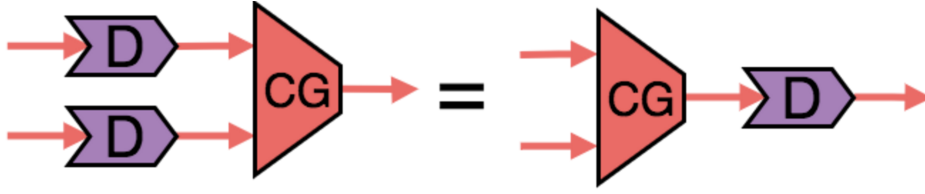


Figure H.3: Equivariance of Clebsch-Gordan coefficients. Note that each D may refer to a different irreducible representation.

H.4 Details for gravitational accelerations and moment of inertia tasks

Moment of inertia radial functions

We can write the moment of inertia tensor as

$$I_{ij} := \sum_{a \in \mathcal{S}} m_a T_{ij}(\vec{r}_a)$$

where

$$T_{ij}(\vec{r}) := R^{(0)}(r)\delta_{ij} + R^{(2)}(r) \left(\hat{r}_i \hat{r}_j - \frac{\delta_{ij}}{3} \right)$$

The expression that $R^{(2)}$ is multiplying is the 3D symmetric traceless tensor, which can be constructed from the $l = 2$ spherical harmonic. To get agreement with the moment of inertia tensor as defined in the main text, we must have

$$R^{(0)}(r) = \frac{2}{3}r^2 \quad R^{(2)}(r) = -r^2$$

Figure H.5 shows the excellent agreement of our learned radial functions for filters $l = 0$ and $l = 2$ to the analytical solution.

Point generation details and radial hyperparameters

The number of points is uniformly randomly selected from 2 through 10. The masses are scalar values that are randomly chosen from a uniform distribution from 0.5 to 2.0. The coordinates of the points are randomly generated from a uniform distribution to be inside a cube with sides of length 4 for gravity and 1 for moment of inertia.

We use 30 Gaussian basis functions whose centers are evenly spaced between 0 and 2. We use a Gaussian variance that is one half the distance between the centers. We use a batch size of 1. For the test set, we simply use more randomly generated points from the same distribution.

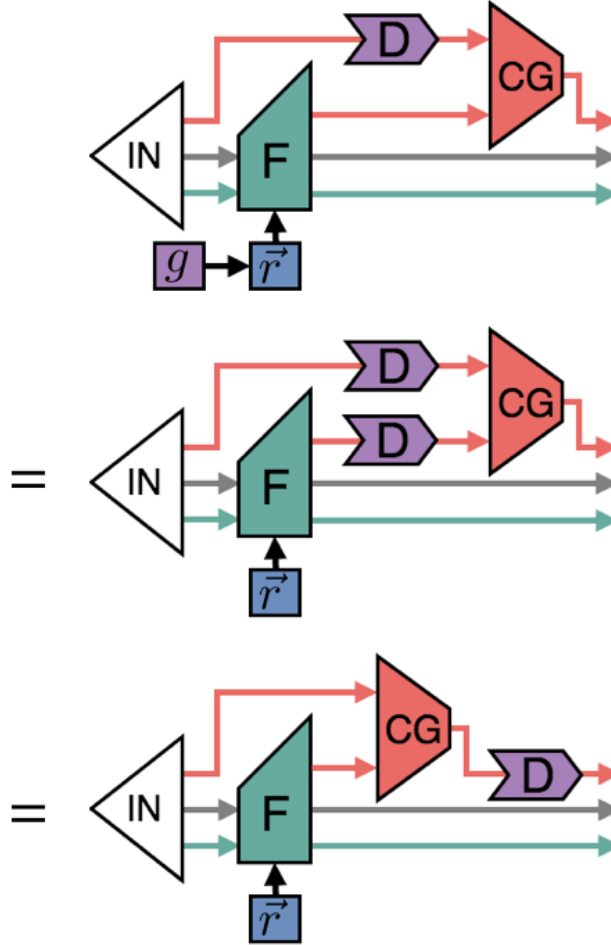


Figure H.4: Diagrammatic proof of point convolution rotation equivariance.

We note that $-1/r^2$ diverges as $r \rightarrow 0$. We choose a cutoff minimum distance at 0.5 distance because it is easy to generate sufficient examples at that distance with a few number of points per example. If we wanted to properly sample for closer distances, we would need to change how we generate the random points or use close to 1000 points per example.

H.5 Proof of weighted point-averaging layer equivariance

Let S be the set of points (not including the missing point at \vec{M}) with locations \vec{r}_a . Suppose that the output of the network is a scalar and a vector $\vec{\delta}_a$ at each point in S . We take

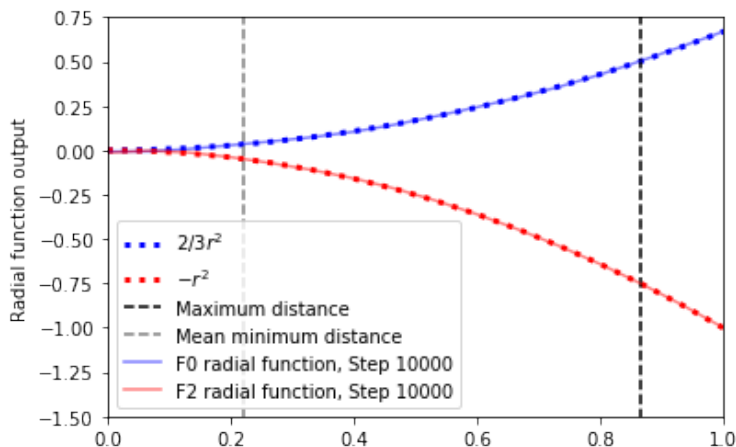


Figure H.5: Radial function learned by $l = 0$ and $l = 2$ filters for moment of inertia toy dataset. The filters learn the analytical radial functions. For a collection of randomly generated point sets, the mean minimum distance is the average of the minimum distance between points in each point set. Distances smaller than the mean minimum distance might not have been seen by the network enough times to correct the radial filter.

the softmax of the scalars over S to get a probability p_a at each point. Define the votes as $\vec{v}_a := \vec{r}_a + \vec{\delta}_a$, so the guessed point is

$$\vec{u} := \sum_{a \in S} p_a \vec{v}_a$$

This is the first operation that we have introduced that lacks manifest translation equivariance because it uses \vec{r}_a by itself instead of only using $\vec{r}_a - \vec{r}_b$ combinations. We can show that $\vec{r}_a \mapsto \vec{r}_a + \vec{t}$ implies

$$\vec{u} \mapsto \sum_{a \in S} \left[p_a (\vec{r}_a + \vec{t}) + p_a \vec{\delta}_a \right] = \vec{u} + \vec{t}$$

because the p_a sum to 1. This voting scheme is also rotation-equivariant because it is a sum of 3D vectors. The loss function

$$\text{loss} = (\vec{u} - \vec{M})^2$$

is translation-invariant because it is a function of the difference of vectors in 3D space and rotation-invariant because it is a dot product of vectors.

H.6 Missing point task accuracies and MAE by epoch

In Table H.1, we give the prediction accuracy and MAE on distance for the missing point task broken down by atom type. There are 1,000 molecules in each of the train and test

Table H.1: Performance on missing point task by atom type

Atoms	Number of atoms with given type in set	Accuracy (%) ($\leq 0.5 \text{ \AA}$ and atom type)	Distance MAE in \AA
Hydrogen			
5-18 (train)	7207	94.6	0.16
19	10088	93.2	0.16
23	14005	96.7	0.14
25-29	16362	97.7	0.15
Carbon			
5-18 (train)	5663	94.3	0.16
19	6751	99.9	0.10
23	7901	100.0	0.11
25-29	8251	99.7	0.17
Nitrogen			
5-18 (train)	1407	74.8	0.16
19	616	74.7	0.18
23	37	81.1	0.19
25-29	16	93.8	0.26
Oxygen			
5-18 (train)	1536	83.3	0.17
19	1539	80.2	0.21
23	1057	68.0	0.20
25-29	727	60.1	0.21
Fluorine			
5-18 (train)	50	0.0	0.18
19	6	0.0	0.07
23	0		
25-29	0		

sets; however, when comparing results by atom type, the relevant number to compare is the number of examples where a specific atom type is removed. In Figure H.6 and Figure H.7, we give the accuracy and distance MAE for the missing point task as a function of the number of training epochs (Tables 7.1 and H.1 contain the results after 225 epochs).

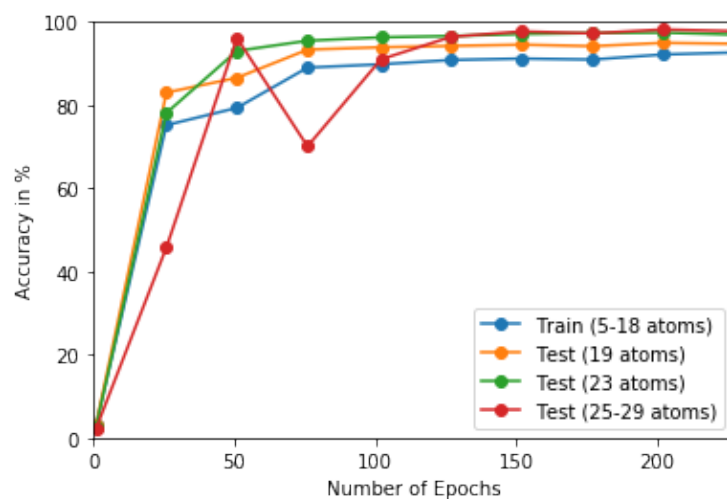


Figure H.6: Accuracy of missing point task by epoch of training

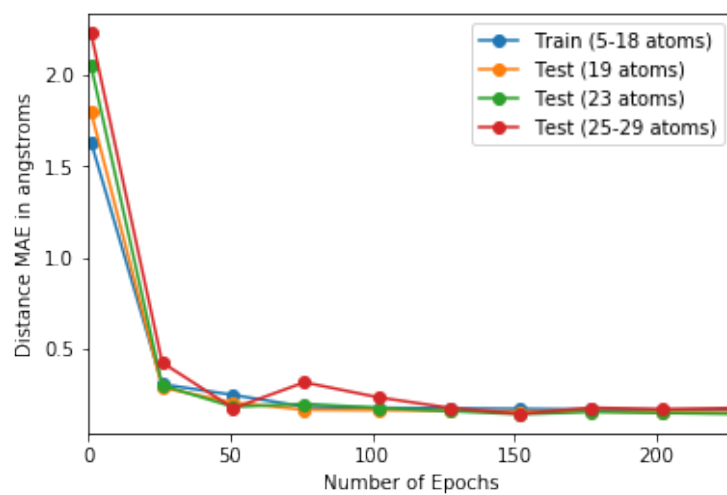


Figure H.7: Distance MAE of missing point task by epoch of training